JANUARY-MARCH 2022 VOL. 14 № 1 (52)

ISSN 2075-8251

ActaNaturae

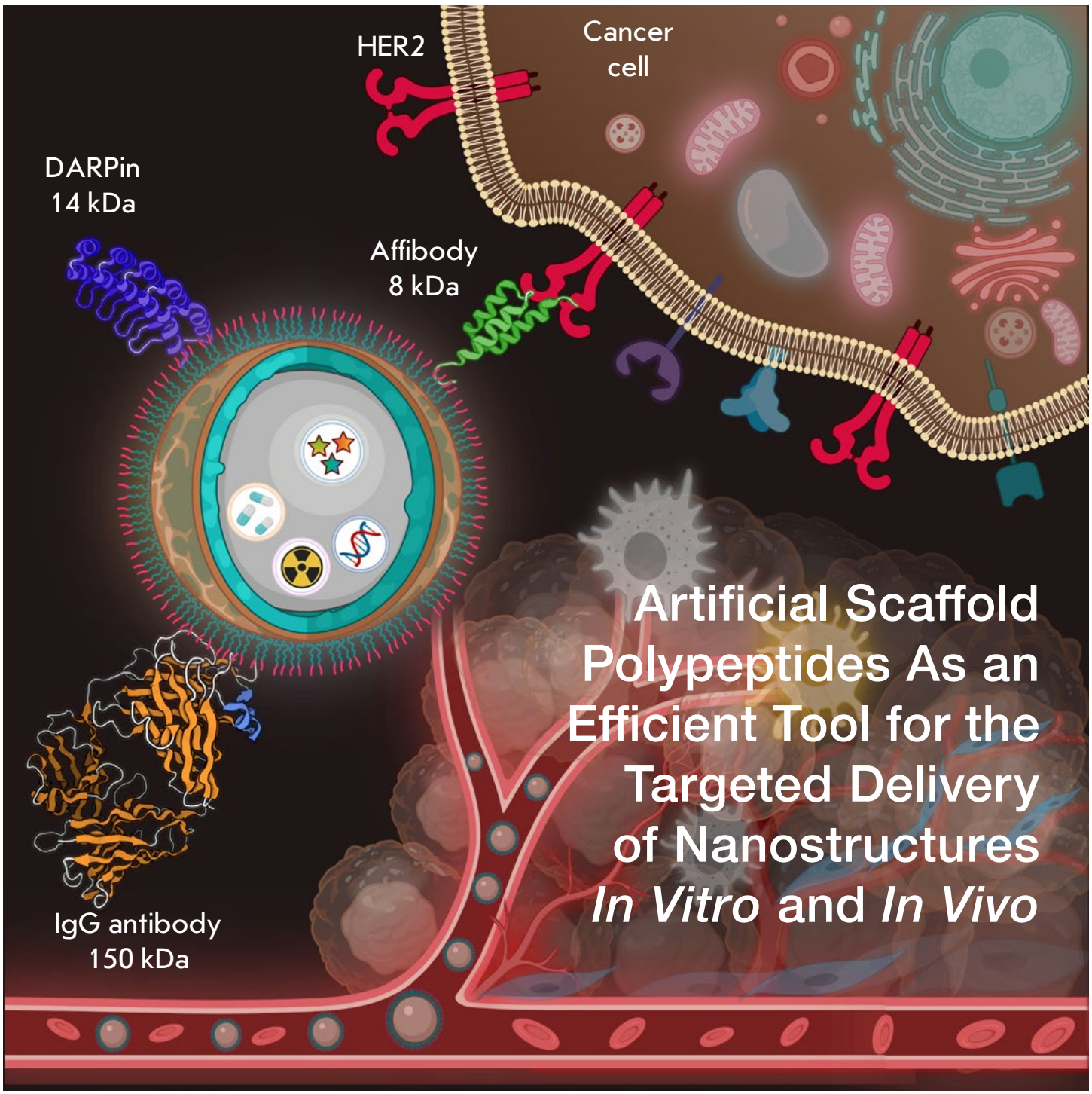

Artificial Scaffold Polypeptides As an Efficient Tool for the Targeted Delivery of Nanostructures *In Vitro* and *In Vivo*

III JOINT LIFE SCIENCES FORUM

VII RUSSIAN CONGRESS ON BIOCHEMISTRY & MOLECULAR BIOLOGY
♦
X RUSSIAN SYMPOSIUM "PROTEINS AND PEPTIDES"

Dagomys–Sochi, Russia ***April 3–7, 2022***

CONGRESS ORGANIZERS

- Russian Academy of Sciences
- Ivan Pavlov Russian Physiological Society
- Russian Biochemical Society (National Committee of Russian Biochemists)
- Russian Science Foundation

with the involvement of

- CIS Union of Physiological Societies

PROGRAM COMMITTEE CO-CHAIRS

Full Members of the Russian Academy of Sciences
Alexander Gabibov and **Mikhail Ostrovsky**

THE CONGRESS ABSTRACT BOOK IS AVALABLE FOR DOWNLOAD AT
http://www.rusbiochem.org/sbornik_tezisov.html

TO LEARN MORE ON APPLICATIONS ACCEPTED FOR ORAL OR POSTER PRESENTATION, PLEASE VISIT OUR WEBSITE AT
http://www.rusbiochem.org/page226.html

Any questions? Please contact us by e-mail: info@rusbiochem.org

WWW.RUSBIOCHEM.ORG

Fifty Years of Research on Protonophores: Mitochondrial Uncoupling As a Basis for Therapeutic Action

E. A. Kotova, Y. N. Antonenko

Protonophores, compounds performing electrogenic transmembrane H^+ transport, have been intensively studied over the past 50 years because of their ability to uncouple the electron transport chain from the ATP synthesis in mitochondria and chloroplasts. This review focuses on potential involvement of certain mitochondrial inner membrane proteins in the uncoupling. A conclusion has been drawn that it is important to thoroughly study the mechanism of action of uncoupling agents to make their pharmacological application more successful.

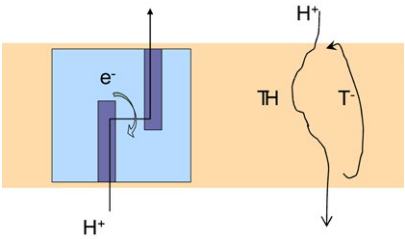

Schematic of the protonophoric effect of an anionic uncoupler T

Tandem Exon Duplications Expanding the Alternative Splicing Repertoire

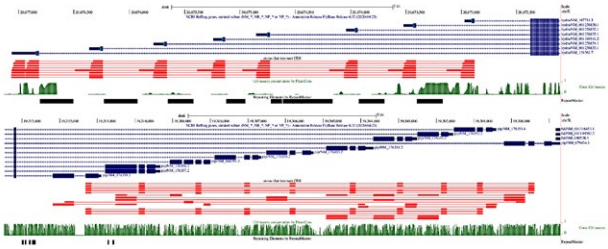

Genome Browser diagram of tandem exon duplications in *D. melanogaster* genes *hydra* and *pip*

T. M. Ivanov, D. D. Pervouchine

Tandem exon duplications involved in the mechanism of adaptive regulation of protein function play a crucial role in evolution of the eukaryotic genome. The paper addresses the problem of identifying tandem exon duplications in eukaryotic genes and demonstrates that tandemly duplicated exons are abundant in both the coding gene regions and the untranslated regions. A number of examples of tandem exon duplications have been provided; unannotated tandemly duplicated exons have been identified; and statistical evidence for their expression using large panels of RNA-seq experiments has been presented.

3D Models of Cellular Spheroids As a Universal Tool for Studying the Cytotoxic Properties of Anticancer Compounds *In Vitro*

A. S. Sogomonyan, V. O. Shipunova, V. D. Soloviev, V. I. Larionov, P. A. Kotelnikova, S. M. Deyev

A universal method for 3D cultivation of mammalian cells based on reusable molds has been developed; this method allows one to reproducibly produce multicellular spheroids with tight contacts to be used in molecular and cell biology, as well as for predicting the *in vivo* functional activity of various compounds.

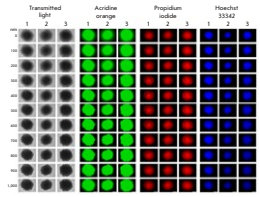

Imaging of SKOVip-kat spheroids

Effect of Additional Amino Acid Replacements on the Properties of Multi-point Mutant Bacterial Formate Dehyderogenase PseFDH SM4S

A. A. Pometun, P. D. Parshin, N. P. Galanicheva, L. A. Shaposhnikov, D. L. Atroshenko, E. V. Pometun, V. V. Burmakin, S. Yu. Kleymenov, S. S. Savin, V. I. Tishkov

Formate dehydrogenase from bacteria *Pseudomonas* sp. 101 (PseFDH) is of great fundamental and practical interest. A multipoint mutant PseFDH SM4S possessing improved catalytic parameters and increased temperature and chemical stability was used in this study. Five additional replacements enhancing the stability of the wild-type enzyme were introduced. A combination of the E170D replacement with the mutations introduced earlier was shown to have a synergistic effect: the mutant's thermal stability was twice as high as that of the wild-type enzyme.

Positions of Lys61, Ser131, Ser160, and Glu170 in the structure of apo-form of FDH from *Pseudomonas* sp. 101

ActaNaturae
JANUARY–MARCH 2022 VOL. 14 № 1 (52)
since april 2009, 4 times a year

Founders
Acta Naturae, Ltd,
National Research University
Higher School of Economics

Adress: 101000, Moscow, Myasnitskaya Ulitsa, 13, str. 4
Phone/Fax: +7 (495) 727 38 60
E-mail: actanaturae@gmail.com

Номер подписан в печать 30 марта 2022 г.
Тираж 15 экз. Цена свободная.
Отпечатано в типографии: НИУ ВШЭ,
г. Москва, Измайловское шоссе, 44, стр. 2

Indexed in Pubmed, Web of Science, Scopus, and RISC

Impact Factor: 1.845

CONTENTS

REVIEWS

RESEARCH ARTICLES

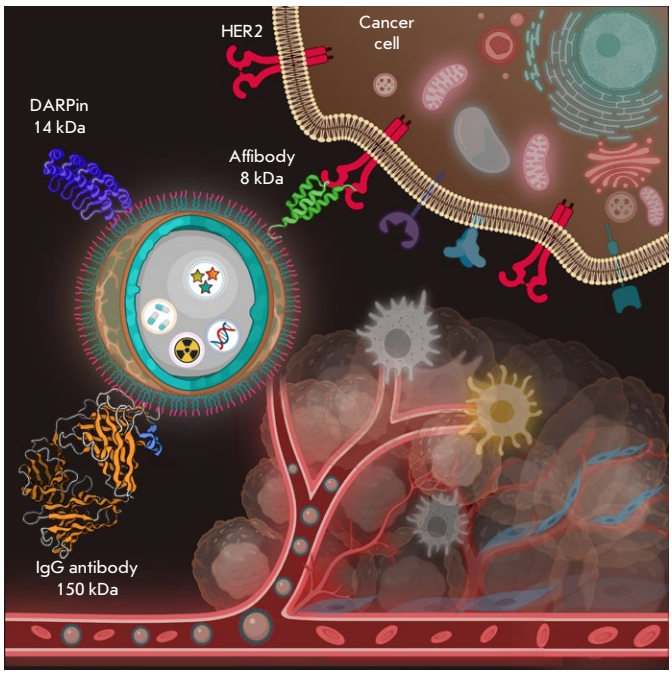

IMAGE ON THE COVER PAGE
(see the article by V. O. Shipunova et al.)

Fifty Years of Research on Protonophores: Mitochondrial Uncoupling As a Basis for Therapeutic Action

E. A. Kotova, Y. N. Antonenko*
Belozersky Institute of Physico-Chemical Biology, Lomonosov Moscow State University, Moscow, 119991 Russia
Received: October 19, 2021; in final form, December 21, 2021
*Email: antonen@belozersky.msu.ru
DOI: 10.32607/actanaturae.11610

ABSTRACT **Protonophores are compounds capable of electrogenic transport of protons across membranes. Protonophores have been intensively studied over the past 50 years owing to their ability to uncouple oxidation and phosphorylation in mitochondria and chloroplasts. The action mechanism of classical uncouplers, such as DNP and CCCP, in mitochondria is believed to be related to their protonophoric activity; i.e., their ability to transfer protons across the lipid part of the mitochondrial membrane. Given the recently revealed deviations in the correlation between the protonophoric activity of some uncouplers and their ability to stimulate mitochondrial respiration, this review addresses the involvement of some proteins of the inner mitochondrial membrane, such as the ATP/ADP antiporter, dicarboxylate carrier, and ATPase, in the uncoupling process. However, these deviations do not contradict the Mitchell theory but point to a more complex nature of the interaction of DNP, CCCP, and other uncouplers with mitochondrial membranes. Therefore, a detailed investigation of the action mechanism of uncouplers is required for a more successful pharmacological use, including their antibacterial, antiviral, anticancer, as well as cardio-, neuro-, and nephroprotective effects.**
KEYWORDS **uncouplers of oxidative phosphorylation, mitochondria, proton transport, bioenergetics.**
ABBREVIATIONS **DNP – 2,4-dinitrophenol; CCCP – carbonyl cyanide-m-chlorophenylhydrazone; BLM – bilayer lipid membrane; P-vs-U correlation – correlation of uncoupling efficiency in mitochondria and protonophoric activity in bilayer lipid membranes; CATR – carboxyatractyloside; mitoFluo – triphenyl-phosphonium cation–fluorescein conjugate.**

INTRODUCTION

The term protonophore was first used in a review by Skulachev published in 1970 [1], but protonophores were discovered several years earlier in the laboratories of Lehninger (1966 [2]), Skulachev [3], and Lieberman [4]. Those studies showed that some compounds previously identified as uncouplers of oxidative phosphorylation in mitochondria increase the proton conductivity of lipid membranes. This observation was in agreement with the Mitchell theory on the coupling of oxidation and phosphorylation in mitochondria through the electrochemical potential difference between protons [5]. In 1967, Mitchell observed proton transfer by some uncouplers in mitochondrial membranes [6]. As already mentioned, the term protonophore was coined in 1970 [1]; before that, uncouplers were called proton conductors, or H^+ carriers [2]. It is worth noting a study in 1967 [7] on an uncoupler-mediated increase in the proton conductivity of liposomes, but that study did not attract as much research attention as the publication in *Nature* [3]. Skulachev's group's priority in the discovery of protonophores was also confirmed by a publication in *Nature* in 1969 [8], which reported a quantitative correlation between protonophore activity in lipid membranes (planar bilayers, BLM) and stimulation of mitochondrial respiration in state 4 (P-vs-U-correlation) for many uncouplers of various chemical structures. This publication in 1969 [8] is now considered classic. It should be noted that the term ionophore, which denotes a compound that transports ions through membranes, had appeared earlier and was actively used

in Pressman's works in the mid-1960s [9]. However, Pressman focused on the transport of metal ions and did not use the term protonophore. At that time, Russian-language articles often used the term membrane-active complexone [10], which was later replaced by the term ionophore.

The listed studies caused an explosion of interest in protonophores and, together with subsequent studies, contributed significantly to proving the Mitchell chemiosmotic theory. It is worth noting that the P-vs-U correlation was immediately disputed in studies from another group [11], which reported significant deviations from the correlation for another set of compounds. Contradictions were added by Bakker et al., who showed that the P-vs-U correlation is much more stronger in liposomes than it is in planar BLMs [12]. However, the fundamental review [13] was published in 1980, which argued for the existence of a good P-vs-U correlation, while some of the contradictions were attributed to the physicochemical properties of the compounds used. Because the chemiosmotic theory was considered to have been proved by that time, the issue lost its relevance and became almost a closed one despite the fact that there was sufficient evidence of involvement of mitochondrial proteins in uncoupler effects. In particular, incubation of an azido derivative of DNP, (2-azido-4-nitrophenol (NPA), and an azido derivative of CCCP, 2-nitro-4-azidocarbonylcyanide phenylhydrazone (N3CCP), with mitochondria in response to illumination was shown to lead to covalent attachment of these compounds to a subunit of the ATPase complex [14] or a non-identified protein [15], respectively. Importantly, this covalent modification did not affect other mitochondrial proteins. But at that time, these studies were believed to contradict the Mitchell chemiosmotic theory; so they were not given sufficient attention. Interestingly, shortly after (in the 1990s), Skulachev's laboratory published papers that pointed to the sensitivity of the DNP and CCCP effect to inhibitors acting either through specific mitochondrial proteins or through nonidentified proteins [16, 17].

PROTONOPHORES AND LIPID MEMBRANES

Classical protonophores are organic acids with pKa close to physiological pH values, which have an extensive system of π-electrons delocalizing the negative charge that prevents penetration through the hydrophobic layer of the membrane (*Fig. 1*). This enables the anionic form of the protonophore (T^-) to cross the membrane in response to the application of a potential, then to be protonated (transforming into the TH form), and to move in the opposite direction, as a neutral form, along the concentration

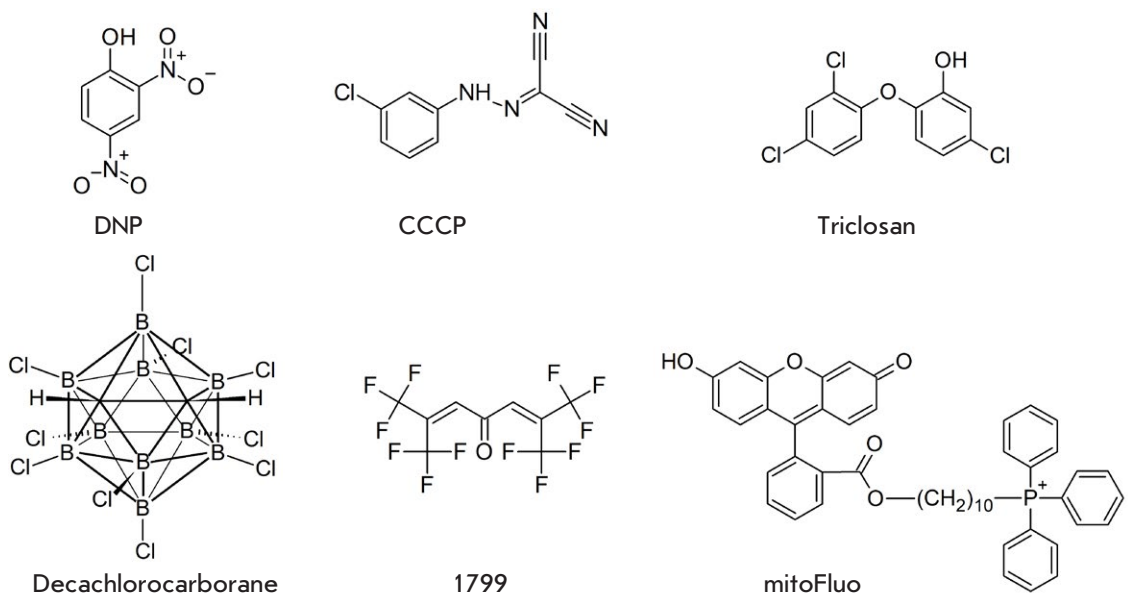

Fig. 1. Chemical structures of conventional protonophores (top row) and unconventional protonophores (bottom row). DNP – 2,4-dinitrophenol; CCCP – carbonyl cyanide-m-chlorophenyl hydrazone; triclosan – 2,2,4′-trichloro-2′-hydroxydiphenyl ether; decachlorocarborane; 1799 – α,α′-bis(hexafluoracetonyl)acetone; mitoFluo – a conjugate of fluorescein and the triphenylphosphonium cation

gradient. The cycle is completed by deprotonation of the TH form. Apart from phenols (DNP, pentachlorophenol, etc.), various hydrazones (CCCP, FCCP), benzimidazoles (TTFB and DTFB), dicoumarol, and salicylic acid were studied among the first protonophores. These compounds, which are weak aromatic acids, correspond well to the general protonophore structure described above. However, even the first tested uncouplers included untypical examples, such as decachlorocarborane [18] and compound 1799 (α,α'-bis(hexafluoracetonyl)acetone) [11]. Strictly speaking, these compounds are not aromatic; in addition, their ability to become deprotonated in an aqueous medium also raises serious questions. Recent studies have identified cationic [19–21] and zwitterionic protonophores [22–24].

INTERACTION BETWEEN PROTONOPHORES AND MITOCHONDRIAL MEMBRANE PROTEINS

Approximately 50 years have passed since the first studies on protonophores appeared, and many new small-molecule compounds with uncoupler properties have been identified. Many of them are described in the review [25], although the list is not complete and should be substantially expanded. Unfortunately, not all new compounds have been tested in lipid systems (BLM or liposomes), and even fewer compounds have been characterized under the same conditions. However, a lot of evidence enables significant advances in the refining of the P-vs-U correlation, compared to the first studies of the 1970s. For example, several compounds exhibiting a pronounced uncoupling effect on mitochondria but lacking protonophoric activity in lipid membranes were identified. The most known and physiologically important of these are fatty acids. It is important to emphasize that fatty acids, which increase the proton permeability of mitochondrial membranes [26, 27], have only a weak ability to increase the conductivity of planar BLMs: noticeable currents were found only in membranes formed from liposomes [28] according to the Montal method [29]. Fatty acids were shown to interact with the ADP/ATP antiporter [16, 30–32] and with other transport proteins of the SLC25 family [33], which leads to the catalysis of fatty acid anion transfer through the mitochondrial membrane. Many anti-inflammatory drugs [34] and a number of other compounds [35] have uncoupling properties. Therefore, the classical P-vs-U dependence may be significantly expanded. On the other hand, it may be concluded that the observed correlation of protonophore activity in BLMs and mitochondria is rather weak and hardly contradicts the involvement of proteins in protonophoric action in mitochondria.

Figure 2 presents this correlation according to [8], with the addition of several compounds to show the magnitude of possible deviations from the canonical P-vs-U dependence (red arrows).

Compounds that effectively uncouple mitochondria but barely increase the proton conductivity of BLMs also include a recently synthesized conjugate of fluorescein and triphenylphosphonium, called mitoFluo [22]. mitoFluo has a very weak protonophore effect on BLMs, which is expected because it can be either a cation or a zwitterion. Compared to anions, cations much less efficiently penetrate BLM owing to a dipole potential, i.e., a layer of oriented dipoles at the membrane–water interface [36–38]. Zwitterions carry not only a positive charge, but also a negative one, which should further reduce their permeability. To record the mitoFluo-induced BLM current, special synthetic lipids with ether rather than ester bonds

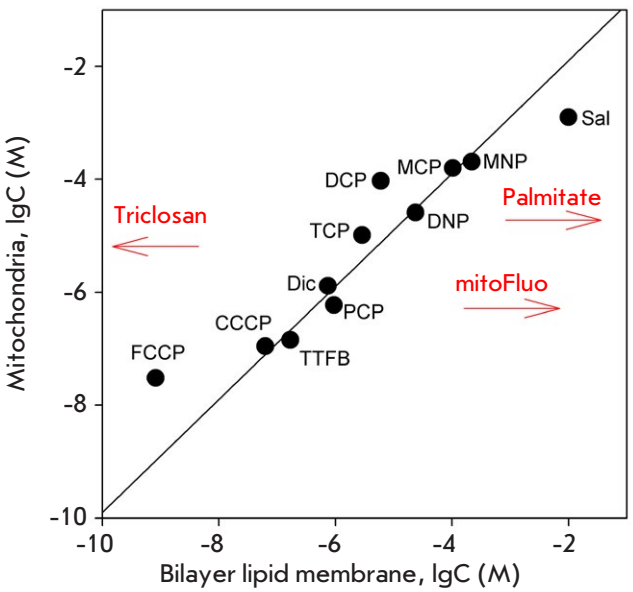

Fig. 2. Correlation between the ability of different compounds to uncouple oxidative phosphorylation in mitochondria and their protonophoric activity in the bilayer lipid membrane (BLM) (adopted from [8]). The Y axis shows the concentrations of compounds producing a two-fold stimulation of succinate oxidation in state 4 rat liver mitochondria; the X axis shows the concentrations required to increase the conductivity of a black lipid membrane by 5×10^{-9} $Ohm^{-1}\times cm^{-2}$. Red arrows mark the levels of effective concentrations of palmitate, mitoFluo, and triclosan according to [22, 40, 57]

and hydrocarbon residues were used. Previously, these lipids were shown to have a significantly reduced dipole potential of the membrane [39]. Even in BLMs prepared from this lipid, mitoFluo at pH 7 did not cause a proton current; the current appeared only as pH decreased and reached a maximum at pH 3 [22]. In this case, mitoFluo, which is an effective uncoupler in mitochondria, acts at submicromolar concentrations. Another group of compounds falling out of the P-vs-U correlation includes triclosan (2,2,4'-trichloro-2'-hydroxydiphenyl ether, *Fig. 2*, red left arrow). Unlike fatty acids or mitoFluo, triclosan is a potent protonophore in BLMs (its effective concentrations are significantly lower compared to those of CCCP) [40]. However, triclosan is a weak uncoupler in mitochondria, and tens of micromoles of this compound are required to stimulate mitochondrial respiration [41]. Triclosan is widely used as an antimicrobial agent and is added to various cosmetic products. Its extremely weak toxicity to animal cells is associated with its weak effect on the mitochondrial membrane. The structure of triclosan suggests that it is a common anionic phenolic uncoupler, with pKa = 7.9 [42].

As mentioned above, deviations from the P-vs-U correlation are traditionally explained by the interaction between uncouplers and proteins of the inner mitochondrial membrane, which may increase proton transfer due to accelerated transfer of the anionic form of the protonophore through the lipid part of the membrane [17, 35]. This concept is well illustrated by the induction of proton conductivity in the mitochondrial membrane by fatty acids, which is significantly suppressed by the addition of carboxyatractyloside (CATR), a specific inhibitor of the adenine nucleotide translocator in mitochondria [16, 31]. Fatty acid anions are supposed to interact with the ATP and/or ADP binding site and, thus, be transported across the membrane. High permeability of the lipid membrane for protonated fatty acids [43] enables these acids to perform the proton transfer cycle. Along with fatty acids, CATR, although to a lesser extent, inhibits the uncoupling effect of DNP in mitochondria [16, 44]. These data suggest that the DNP anion may also interact with the fatty acid binding site of the ADP/ATP translocator. Recently, interaction between DNP and the reconstituted translocator has been shown to be blocked when arginine 79 is replaced by serine in this protein [44].

The active interaction of uncouplers with proton pumps was known even before the studies of the late 1960s–early 1970s, because all the uncouplers known at that time exhibited a bell-shaped dependence of the respiration rate of mitochondria or submitochondrial particles (SMPs) on their concentration; i.e., stimulation of respiration at low concentrations of uncouplers was always followed by its inhibition at high concentrations of uncouplers [45, 46]. This phenomenon concerns the substrates of all major mitochondrial respiratory complexes. Further, the sites and the nature of this interaction were clarified. For example, in the case of complex I, this interaction correlates well with the hydrophobicity of the compounds, which could be explained by the existence of a hydrophobic region in the protein acting as a ubiquinone binding site [47]. In succinate dehydrogenase, the most active binding site for uncouplers is the ubiquinone pocket, with its affinity for pentachlorophenol reaching 2 μM [48]. Also, cytochrome oxidase was shown to have a CCCP binding site [49], interaction with which drastically changes the protein's affinity for oxygen [50]. Interestingly, methylation of a protonated group in uncouplers suppresses not only their uncoupling, but also their inhibitory effects [45, 51]. This important fact has not yet been explained; it indicates a close relationship between the inhibitory action and the uncoupling mechanism. It should be noted that some uncouplers are characterized by an unusually wide concentration bell [22, 52].

According to this concept, deviation of triclosan from the P-vs-U correlation in the opposite direction, compared to fatty acids, is due to the fact that most protonophores use certain proteins during the induction of proton conductivity in mitochondrial membranes. Because triclosan induces a greater BLM current than CCCP, while operating in mitochondria at larger concentrations than CCCP, the latter may be presumed to induce a proton current through some mitochondrial protein. This suggestion is supported by direct experiments on the interaction between the azido derivative of CCCP and mitochondrial proteins [15]. A recent study at our laboratory showed that the CCCP–triphenylphosphonium conjugate, which does not uncouple mitochondria, is able to block the uncoupling effect of CCCP [53]. The involvement of a protein in the uncoupling activity of CCCP is also evidenced by the strong inhibition of the CCCP effect on mitochondria by 6-ketocholestanol, which, on the contrary, can increase the CCCP-induced proton current in BLM due to an elevation of the membrane dipole potential [54]. Thus, the P-vs-U correlation in the case of conventional uncouplers is not directly related to the fact that uncouplers of oxidative phosphorylation are protonophores (i.e., proton carriers across the lipid part of the mitochondrial membrane). Apparently, this is also related to the strength of the interaction

between most of these compounds and some mitochondrial protein(s).

It should also be mentioned that the P-vs-U correlation appears clearly disturbed in a series of homologues of some uncouplers. For example, our laboratory showed that the protonophoric activity of uncouplers based on the popular fluorescent dye 7-nitrobenzo-2-oxa-1,3-diazole (NBD) with an alkyl substituent grows in planar BLMs and liposomes as the alkyl chain increases [55]. In mitochondria, the uncoupling activity reaches a maximum in the case of an octyl substituent, and a decyl derivative uncouples mitochondria much more weakly than an octyl one does [55]. Similarly, in a series of alkylrhodamines (CnR1), the protonophoric activity in liposomes [56] and BLMs increases as the alkyl chain is lengthened, while maximum uncoupling in mitochondria is observed with C4R1 [21]. The optimal alkyl chain length also indicates a possible involvement of the binding sites of mitochondrial proteins in the induction of proton leakage. Of note, uncoupling by fatty acids also has an optimum for the fatty acid length: among saturated fatty acids, palmitic acid causes maximum uncoupling, whereas longer acids are less active [57]. A recent study by Samartsev's laboratory showed that α,ω-hexadecanedioic acid stimulates mitochondrial respiration without inducing proton conductivity of the mitochondrial membrane [58]. This new phenomenon is to be studied and understood.

Thus, it may be concluded that the P-vs-U correlation is rather poor when comprising many of the new uncouplers discovered since the first studies in this field. However, it should be emphasized that the Mitchell theory, largely accepted by the scientific community owing to the P-vs-U correlation, cannot be questioned on this basis. The point is that the Mitchell theory has been proved by many direct experiments, such as the measurement of the generation of electric potentials by proton pumps [59] or the detection of ATP synthesis in liposomes with reconstructed bacteriorhodopsin and ATP synthase [60]. In addition, there is no doubt that the uncoupling effect of gramicidin A is mediated by the formation of a proton channel and induction of proton leakage in the inner mitochondrial membrane. The Mitchell theory puts emphasis not on the P-vs-U correlation but on the correlation between mitochondrial uncoupling (i.e., stimulation of respiration and ATP hydrolysis) and the protonophore activity of uncouplers, which is measured directly in mitochondria [61]. In the Mitchell theory, it is not important whether the uncoupler induces a proton current in the mitochondrial membrane via the lipid parts of the membrane or via some mitochondrial protein. Proton leakage in the mitochondrial membrane may be measured under deenergized conditions based on the swelling of mitochondria in a medium with potassium acetate in the presence of valinomycin or with ammonium nitrate without valinomycin [26]. This technique was used to show that fatty acids induce proton conductivity in the inner mitochondrial membrane at the same concentrations at which they stimulate mitochondrial respiration [26]. Thus, despite the fact that fatty acids fall out of the P-vs-U correlation, their induction of proton conduction in mitochondria only confirms the Mitchell theory.

Another question is the existence of a protonophore that acts in mitochondria without the involvement of proteins. As described above, the most popular uncouplers DNP and CCCP may hardly be considered such protonophores. Gramicidin A may be such a protonophore, but it transports not only protons, but also potassium and sodium ions, which makes it very toxic to cells. Perhaps, this role may be played by triclosan, an extremely active protonophore in BLMs, surpassing both CCCP and SF6847, the most potent known uncoupler [40]. However, triclosan causes a stimulation of mitochondrial respiration and their swelling in a medium with potassium acetate (in the presence of valinomycin) only at a concentration of 3–10 μM. Thus, triclosan strongly deviates from the P-vs-U correlation (*Fig. 2*, red arrow on the left). According to [40], this deviation from the P-vs-U correlation may be caused by the high hydrophobicity of triclosan, which complicates the penetration through the outer mitochondrial membrane. However, even this weak uncoupling activity may be due to the interaction of triclosan with some protein. In this regard, it should be mentioned that triclosan interacts with mitochondrial NADH dehydrogenase and inhibits it at higher concentrations (30–100 μM) [41].

PROTONOPHORES AND PROTON PUMPS

Above, we considered the mechanism of interaction between DNP and the ATP/ADP translocator, which contributes to the uncoupling effect of DNP on mitochondria [44]. According to our data, the translocator is also involved in the uncoupling effect of a new popular uncoupler BAM15 [62]. However, there may be also a universal mechanism of interaction between uncouplers and mitochondria, which differs from the direct proton transfer across the lipid part of the membrane. The following action mechanism of uncouplers may be proposed, which, on one hand, involves the ability to transfer protons across the lipid part of the membrane and, on the other hand, ex-

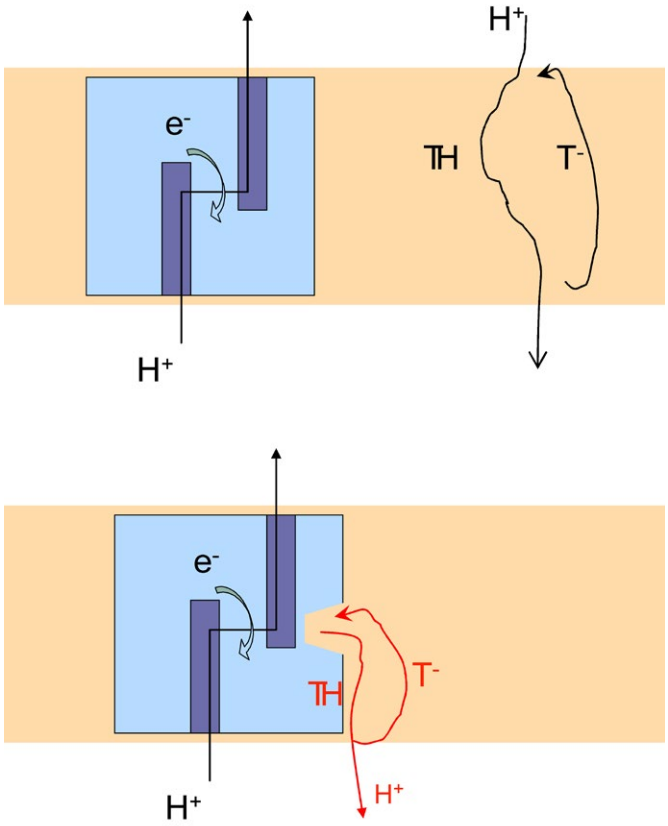

Fig. 3. Schematic of the protonophoric effect of an anionic uncoupler T (top) and a modified model of direct interaction between T and the proton channel of the proton pump (bottom). The protonophore T transfers protons as a protonated complex TH and comes back as an anionic form T^- via the deprotonation cycle at the membrane interface

plicitly requires their interaction with proton pumps. This mechanism may be characterized as capture ("stealing") of protons from the proton pump channels (lower diagram in *Fig. 3*). All proton pumps are known to have proton channels that are lined with appropriate amino acids to protect the proton from leakage into the aqueous phase. But nature did not need to protect the proton pathways from leakage into the lipid phase, because the hydrated proton is very hydrophilic, and there is a huge energy barrier to its transition into the lipid phase. Therefore, some channels of proton pumps (probably, most of these channels) may lack complete isolation from proton leakage in the hydrophobic layer of the membrane. Because protonophores are lipophilic acids, they are able to intercept the protons that are pumped out of the mitochondrial matrix during the transfer of electrons along the respiratory chain and return them to the matrix, even before they enter the intermembrane space. This causes an abortive proton cycle which is similar to classical uncoupling. This idea is consistent with a previously proposed mechanism of proton slips in proton pumps [63], which was discussed in connection with distortions of the membrane integrity caused by organic solvents or other rough effects. In addition, this concept explains the suppression of proton pumps at high concentrations of uncouplers because interaction with the proton channel of the mitochondrial pump at an increased concentration may lead to complete blocking of this channel, thereby causing inhibition of the enzyme. Because the structures of most mitochondrial proton pumps have already been established, a hypothesis of the mechanism of mitochondrial uncoupling may be tested using a bioinformatics analysis. Further research will show the validity of this hypothesis.

PROTONOPHORES AND MILD UNCOUPLING

Although the term protonophore is defined quite clearly (a protonophore is capable of electrogenically transferring a hydrogen cation through a hydrophobic phase), the use of this term for mitochondria encounters certain difficulties when combined with the term uncoupler. For example, should induction of leaks caused by detergents [64–66] or organic solvents [63] be called a protonophoric effect? In this case, a proton leak is also induced, but because there are leaks of other ions, it is hardly sensible to call this a protonophore effect. The question of whether penetrating organic cations accumulating in mitochondria, such as mitoQ and SkQ, are protonophores is more complicated. These cations are able to transport fatty acid anions across membranes and act as inducers of proton conductivity of the membranes in the presence of fatty acids, which are usually present in cells [67]. There are articles where the term protonophore is applied to mitoQ [25] and SkQ [68]. However, these cations are not capable of transporting protons across membranes; therefore, the term protonophore is not appropriate for them. On the other hand, they may be called uncouplers.

Another, rather controversial, concept associated with the use of uncouplers is the term "mild uncoupling". This term was proposed by Skulachev [17] and Starkov [69] to denote the mitochondrial state that is characterized by a reduced membrane potential, a reduced generation of reactive oxygen species (ROS), weak stimulation of respiration, and persistent high activity of ATP synthase. This state may be induced by mechanisms inherent to mitochon-

dria (uncoupling by endogenous fatty acids or UCP family proteins) or by the addition of a small concentration of uncouplers. The term mild uncoupling was introduced in connection with the discovery of a nonlinear dependence of ROS generation on the mitochondrial membrane potential [70]. Although the concept of mild uncoupling has not been quantified, it may be considered appropriate due to numerous examples of the therapeutic effect of low uncoupler concentrations in physiological models of various pathological conditions [71]. We will consider this issue in more detail when discussing the therapeutic effect of uncouplers.

APPLICATIONS OF PROTONOPHORES

The history of the investigation of protonophores dates back more than 50 years. In conclusion of our brief review, we would like to consider the practical application of protonophores. We should start with the history of DNP that was used as a remedy for obesity in the 1930s [72]. This was an over-the-counter drug that was used by more than 100,000 people, but it was prohibited in 1938 due to the side effects associated with hepatotoxicity and vision problems. Now, interest in DNP has re-emerged [73] due to the appearance of more complex DNP forms, such as ethyl ethers [74], which are converted into DNP mainly in the liver, or DNP complexes with nanoparticles [75]. These drugs show strong anti-diabetic activity in rats and are also effective against a non-alcoholic fatty liver disease. The clinical fate of protonophores, which are used as anthelmintic drugs, is more successful. These include salicylanilides: e.g., niclosamide. The action mechanism of these drugs is defined as the uncoupling of oxidative phosphorylation in worm cells [76, 77]. However, they have little effect on the human body because they are poorly absorbed in the gastrointestinal tract. Many protonophores also exhibit antimicrobial activity [78]. However, their general toxicity precludes their use as antibiotics. Strong protonophores such as triclosan, usnic acid [51], niclosamide [79], and pyrrolomycin [80] exhibit only a moderate toxic effect on eukaryotic cells with a very strong antimicrobial effect. Some anti-tuberculosis drugs also have a protonophoric effect [81–83]; usnic acid also has an anti-tuberculosis effect. In general, protonophores remain relevant for pharmacology and in some areas their potential is even growing.

We may also mention the insecticidal, herbicidal (pesticidal), and fungicidal effect of protonophores: dinitrophenol analogs, such as pentachlorophenol [84], 6-isobutyl-2,4-dinitrophenol (dinoseb) [85], fluazinam [86, 87], etc. We are talking about a fairly large production and a market for agriculture and the forestry industry (wood preservatives). However, in this review, of great importance is not the industrial application of protonophores but their potential significance for pharmacology. After many years of studying protonophores, a lot of data about their protective properties have been collected through animal disease models: they may be used as cardioprotectors [88], neuroprotectors [73, 89], nephroprotectors [90], radioprotectors [91], and exhibit antidiabetic activities [75, 92, 93], and the list goes on. Uncouplers may be used as anticancer agents [94]. Furthermore, low doses of DNP significantly increase the lifespan of rats [95], yeasts [96], and fruit flies [97]. As mentioned above, this protective effect is due to the ability of uncouplers to suppress the formation of ROS in mitochondria, which is largely controlled by the membrane potential [98]. Recent studies suggest that a decrease in the mitochondrial membrane potential in cells due to low concentrations of uncouplers may trigger a whole cascade of changes in the cell metabolism, which may lead to an increase in the mitochondrial mass in some cells [99, 100], activation of mitophagy [101], changes in the ratio of glycolysis to oxidative phosphorylation [102], and many others [89, 103]. The important role of calcium and cAMP in the alteration of cell metabolism is confirmed by the results of many studies [73, 100–103]. Gao et al. suggested that mild uncoupling may be used to call such a state where the dose of a used uncoupler does not lead to a decrease in the proliferative potential of cells but significantly affects some regulatory cascades, such as STAT3 [104].

Thus, a detailed study of the action mechanism of protonophores in mitochondria remains an important problem. Its solution may help towards a switch from animal experiments to the use of protonophores in clinical practice, not only as anthelmintic agents, but also as drugs effective against various common and severe diseases. ●

This study was supported by the Russian Science Foundation (grant No. 21-14-00062).
We are grateful to Academician V.P. Skulachev and Professor L.S. Yaguzhinsky for fruitful discussions of some aspects of this review.

REFERENCES

1. Skulachev V.P. // FEBS Lett. 1970. V. 11. № 5. P. 301–308.
2. Bielawski J., Thompson T.E., Lehninger A.L. // Biochem. Biophys. Res. Commun. 1966. V. 24. № 6. P. 948–954.
3. Skulachev V.P., Sharaf A.A., Liberman E.A. // Nature. 1967. V. 216. № 5116. P. 718–719.
4. Liberman E.A., Topali V.P. // Biochim. Biophys. Acta. 1968. V. 163. № 2. P. 125–136.
5. Mitchell P. // Biol. Rev. 1966. V. 41. № 3. P. 445–502.
6. Mitchell P., Moyle J. // Biochem. J. 1967. V. 104. № 2. P. 588–600.
7. Chappell J.B., Haarhoff K.N. // Biochemistry of mitochondria / Eds Slater E.C., Kaniuga Z., Wojtczak L. New York: Academic Press, 1967. P. 75–91.
8. Liberman E.A., Topaly V.P., Tsofina L.M., Jasaitis A.A., Skulachev V.P. // Nature. 1969. V. 222. № 5198. P. 1076–1078.
9. Pressman B.C. // Federation Proc. 1968. V. 27. № 6. P. 1283–1288.
10. Ovchinnikov Y.A., Ivanov V.T., Shkrob A.M. Membrane-active complexones. Amsterdam, New York: Elsevier, 1974.
11. Ting H.P., Wilson D.F., Chance B. // Arch. Biochem. Biophys. 1970. V. 141. № 1. P. 141–146.
12. Bakker E.P., van den Heuvel E.J., Wiechmann A.H., van Dam K. // Biochim. Biophys. Acta. 1973. V. 292. № 1. P. 78–87.
13. McLaughlin S., Dilger J.P. // Physiol. Rev. 1980. V. 60. № 3. P. 825–863.
14. Hatefi Y. // J. Supramol. Struct. 1975. V. 3. № 3. P. 201–213.
15. Katre N.V., Wilson D.F. // Arch. Biochem. Biophys. 1978. V. 191. № 2. P. 647–656.
16. Andreyev A.Y., Bondareva T.O., Dedukhova V.I., Mokhova E.N., Skulachev V.P., Volkov N.I. // FEBS Lett. 1988. V. 226. № 2. P. 265–269.
17. Skulachev V.P. // Biochim. Biophys. Acta. 1998. V. 1363. № 2. P. 100–124.
18. Liberman E.A., Topaly V.P., Silberstein A.Y. // Biochim. Biophys. Acta. 1970. V. 196. № 2. P. 221–234.
19. Schwaller M.A., Allard B., Lescot E., Moreau F. // J. Biol. Chem. 1995. V. 270. № 39. P. 22709–22713.
20. Gear A.R. // J. Biol. Chem. 1974. V. 249. № 11. P. 3628–3637.
21. Khailova L.S., Silachev D.N., Rokitskaya T.I., Avetisyan A.V., Lyamzaev K.G., Severina I.I., Il'yasova T.M., Gulyaev M.V., Dedukhova V.I., Trendeleva T.A., et al. // Biochim. Biophys. Acta-Bioenergetics. 2014. V. 1837. № 10. P. 1739–1747.
22. Denisov S.S., Kotova E.A., Plotnikov E.Y., Tikhonov A.A., Zorov D.B., Korshunova G.A., Antonenko Y.N. // Chem. Commun. 2014. V. 50. № 97. P. 15366–15369.
23. Rokitskaya T.I., Terekhova N.V., Khailova L.S., Kotova E.A., Plotnikov E.Y., Zorov D.B., Tatarinov D.A., Antonenko Y.N. // Bioconjug. Chem. 2019. V. 30. № 9. P. 2435–2443.
24. Terekhova N.V., Khailova L.S., Rokitskaya T.I., Nazarov P.A., Islamov D.R., Usachev K.S., Tatarinov D.A., Mironov V.F., Kotova E.A., Antonenko Y.N. // ACS Omega. 2021. V. 6. № 31. P. 20676–20685.
25. Childress E.S., Alexopoulos S.J., Hoehn K.L., Santos W.L. // J. Med. Chem. 2018. V. 61. № 11. P. 4641–4655.
26. Schonfeld P., Wieckowski M.R., Wojtczak L. // FEBS Lett. 2000. V. 471. № 1. P. 108–112.
27. Andreyev A.Y., Bondareva T.O., Dedukhova V.I., Mokhova E.N., Skulachev V.P., Tsofina L.M., Volkov N.I., Vygodina T.V. // Eur. J. Biochem. 1989. V. 182. № 3. P. 585–592.
28. Rupprecht A., Sokolenko E.A., Beck V., Ninnemann O., Jaburek M., Trimbuch T., Klishin S.S., Jezek P., Skulachev V.P., Pohl E.E. // Biophys. J. 2010. V. 98. № 8. P. 1503–1511.
29. Montal M., Mueller P. // Proc. Natl. Acad. Sci. USA. 1972. V. 69. № 12. P. 3561–3566.
30. Wojtczak L., Schonfeld P. // Biochim. Biophys. Acta. 1993. V. 1183. № 1. P. 41–57.
31. Bertholet A.M., Chouchani E.T., Kazak L., Angelin A., Fedorenko A., Long J.Z., Vidoni S., Garriti R., Cho J., Terada N., et al. // Nature. 2019. V. 571. № 7766. P. 515–520.
32. Kreiter J., Rupprecht A., Skulj S., Brkljako Z., Zuna K., Knyazev D.G., Bardakji S., Vazdar M., Pohl E. // Int. J. Mol. Sci. 2021. V. 22. № 5. P. 2490.
33. Samartsev V.N., Smirnov A.V., Zeldi I.P., Markova O.V., Mokhova E.N., Skulachev V.P. // Biochim. Biophys. Acta. 1997. V. 1319. № 2–3. P. 251–257.
34. Whitehouse M.W., Dean P.D. // Biochem. Pharmacol. 1965. V. 14. P. 557–567.
35. Lou P.H., Hansen B.S., Olsen P.H., Tullin S., Murphy M.P., Brand M.D. // Biochem. J. 2007. V. 407. № 1. P. 129–140.
36. Brockman H. // Chem. Phys. Lipids. 1994. V. 73. P. 57–79.
37. Liberman E.A., Topaly V.P. // Biophysics (Moscow). 1969. V. 14. P. 477–487.
38. Pickar A.D., Benz R. // J. Membrane Biol. 1978. V. 44. P. 353–376.
39. Gawrisch K., Ruston D., Zimmerberg J., Parsegian V.A., Rand R.P., Fuller N. // Biophys. J. 1998. V. 61. № 5. P. 1213–1223.
40. Popova L.B., Nosikova E.S., Kotova E.A., Tarasova E.O., Nazarov P.A., Khailova L.S., Balezina O.P., Antonenko Y.N. // Biochim. Biophys. Acta. 2018. V. 1860. № 5. P. 1000–1007.
41. Teplova V.V., Belosludtsev K.N., Kruglov A.G. // Toxicol. Lett. 2017. V. 275. P. 108–117.
42. Pemberton R.M., Hart J.P. // Analit. Chim. Acta. 1999. V. 390. № 1–3. P. 107–115.
43. Kamp F., Hamilton J.A. // Proc. Natl. Acad. Sci. USA. 1992. V. 89. № 23. P. 11367–11370.
44. Zuna K., Jovanovic O., Khailova L.S., Skulj S., Brkljako Z., Kreiter J., Kotova E.A., Vazdar M., Antonenko Y.N., Pohl E. // Biomolecules. 2021. V. 11. № 8. P. 1178.
45. Skulachev V.P., Sharaf A.A., Yagujzinsky L.S., Jasaitis A.A., Liberman E.A., Topali V.P. // Curr. Mod. Biol. 1968. V. 2. № 2. P. 98–105.
46. Wilson D.F., Merz R. // Arch. Biochem. Biophys. 1969. V. 129. № 1. P. 79–85.
47. Yaguzhinsky L.S., Smirnova E.G., Ratnikova L.A., Kolesova G.M., Krasinskaya I.P. // J. Bioenerg. Biomembr. 1973. V. 5. № 1. P. 163–174.
48. Afanas'eva E.V., Kostyrko V.A. // Biochemistry (Moscow). 1986. V. 51. № 5. P. 823–829.
49. Bona M., Antalik M., Gazova Z., Kuchar A., Davak V., Podhradsky D. // Gen. Physiol. Biophys. 1993. V. 12. № 6. P. 533–542.
50. Wilson D.F., Rumsey W.L., Green T.J., Vanderkooi J.M.

// J. Biol. Chem. 1988. V. 263. № 6. P. 2712–2718.
51. Antonenko Y.N., Khailova L.S., Rokitskaya T.I., Nosikova E.S., Nazarov P.A., Luzina O.A., Salakhutdinov N.F., Kotova E.A. // Biochim. Biophys. Acta. 2019. V. 1860. № 4. P. 310–316.
52. Kenwood B.M., Weaver J.L., Bajwa A., Poon I.K., Byrne F.L., Murrow B.A., Calderone J.A., Huang L., Divakaruni A.S., Tomsig J.L., et al. // Mol. Metab. 2014. V. 3. № 2. P. 114–123.
53. Iaubasarova I.R., Khailova L.S., Firsov A.M., Grivennikova V.G., Kirsanov R.S., Korshunova G.A., Kotova E.A., Antonenko Y.N. // PLoS One. 2020. V. 15. № 12. P. e0244499.
54. Starkov A.A., Bloch D.A., Chernyak B.V., Dedukhova V.I., Mansurova S.E., Severina I.I., Simonyan R.A., Vygodina T.V., Skulachev V.P. // Biochim. Biophys. Acta. 1997. V. 1318. № 1–2. P. 159–172.
55. Denisov S.S., Kotova E.A., Khailova L.S., Korshunova G.A., Antonenko Y.N. // Bioelectrochemistry. 2014. V. 98. P. 30–38.
56. Antonenko Y.N., Avetisyan A.V., Cherepanov D.A., Knorre D.A., Korshunova G.A., Markova O.V., Ojovan S.M., Perevoshchikova I.V., Pustovidko A.V., Rokitskaya T.I., et al. // J. Biol. Chem. 2011. V. 286. № 20. P. 17831–17840.
57. Samartsev V.N., Rybakova S.R., Dubinin M.V. // Biofizika. 2013. V. 58. № 3. P. 481–487.
58. Semenova A.A., Samartsev V.N., Dubinin M.V. // Biochimie. 2021. V. 181. P. 215–225.
59. Drachev L.A., Jasaitis A.A., Kaulen A.D., Kondrashin A.A., Liberman E.A., Nemecek I.B., Ostroumov S.A., Semenov A.Y., Skulachev V.P. // J. Biol. Chem. 1974. V. 249. № 455. P. 321–324.
60. Winget G.D., Kanner N., Racker E. // Biochim. Biophys. Acta. 1977. V. 460. № 3. P. 490–499.
61. Cunarro J., Weiner M.W. // Nature. 1973. V. 245. P. 36–37.
62. Firsov A.M., Popova L.B., Khailova L.S., Nazarov P.A., Kotova E.A., Antonenko Y.N. // Bioelectrochemistry. 2021. V. 137. P. 107673.
63. Luvisetto S., Pietrobon D., Azzone G.F. // Biochemistry. 1987. V. 26. № 23. P. 7332–7338.
64. Carafoli E., Rossi C.S., Gazzotti P. // Arch. Biochem. Biophys. 1969. V. 131. № 2. P. 527–537.
65. Brustovetsky N.N., Dedukhova V.I., Egorova M.V., Mokhova E.N., Skulachev V.P. // FEBS Lett. 1990. V. 272. № 1–2. P. 187–189.
66. Bragadin M., Dell'Antone P. // Arch. Environ. Contam. Toxicol. 1996. V. 30. № 2. P. 280–284.
67. Severin F.F., Severina I.I., Antonenko Y.N., Rokitskaya T.I., Cherepanov D.A., Mokhova E.N., Vyssokikh M.Y., Pustovidko A.V., Markova O.V., Yaguzhinsky L.S., et al. // Proc. Natl. Acad. Sci. USA. 2010. V. 107. № 2. P. 663–668.
68. Lyamzaev K.G., Tokarchuk A.V., Panteleeva A.A., Mulkidjanian A.Y., Skulachev V.P., Chernyak B.V. // Autophagy. 2018. V. 14. № 5. P. 921–924.
69. Starkov A.A. // Biosci. Rep. 1997. V. 17. № 3. P. 273–279.
70. Korshunov S.S., Skulachev V.P., Starkov A.A. // FEBS Lett. 1997. V. 416. № 1. P. 15–18.
71. Caldeira da Silva C.C., Cerqueira F.M., Barbosa L.F., Medeiros M.H., Kowaltowski A.J. // Aging Cell. 2008. V. 7. № 4. P. 552–560.
72. Colman E. // Regul. Toxicol. Pharmacol. 2007. V. 48. № 2. P. 115–117.
73. Geisler J.G. // Cells. 2019. V. 8. № 3. P. 280.
74. Perry R.J., Kim T., Zhang X.M., Lee H.Y., Pesta D., Popov V.B., Zhang D.Y., Rahimi Y., Jurczak M.J., Cline G.W., et al. // Cell Metabolism. 2013. V. 18. № 5. P. 740–748.
75. Perry R.J., Zhang D.Y., Zhang X.M., Boyer J.L., Shulman G.I. // Science. 2015. V. 347. № 6227. P. 1253–1256.
76. Kadri H., Lambourne O.A., Mehellou Y. // ChemMedChem. 2018. V. 13. № 11. P. 1088–1091.
77. Cojocaru A.F. // International Journal of Applied and Fundamental Research. 2019. V. 10. № 1. P. 11–22.
78. Lewis K., Naroditskaya V., Ferrante A., Fokina I. // J. Bioenerg. Biomembr. 1994. V. 26. № 6. P. 639–646.
79. Tharmalingam N., Port J., Castillo D., Mylonakis E. // Sci. Rep. 2018. V. 8. № 1. P. 3701.
80. Valderrama K., Pradel E., Firsov A.M., Drobecq H., Bauderlique-le Roy H., Villemagne B., Antonenko Y.N., Hartkoorn R.C. // Antimicrob. Agents Chemother. 2019. V. 63. № 10. e01450-19.
81. Hards K., McMillan D.G., Schurig-Briccio L.A., Gennis R., Lill H., Bald D., Cook G.M. // Proc. Natl. Acad. Sci. USA. 2018. V. 115. № 28. P. 7326–7331.
82. Garcia-Garcia V., Oldfield E., Benaim G. // Antimicrob. Agents Chemother. 2016. V. 60. № 10. P. 6386–6389.
83. Feng X., Zhu W., Schurig-Briccio L.A., Lindert S., Shoen C., Hitchings R., Li J., Wang Y., Baig N., Zhou T., et al. // Proc. Natl. Acad. Sci. USA. 2015. V. 112. № 51. P. E7073–E7082.
84. Pentachlorophenol: Chemistry, pharmacology, and environmental toxicology. New York: Plenum Press, 1978.
85. Palmeira C.M., Moreno A.J., Madeira V.M. // Toxicol. Appl. Pharmacol. 1994. V. 127. № 1. P. 50–57.
86. Hollingworth R.M., Gadelhak G.G. // Rev. Toxicol. 1998. V. 2. № 2. P. 253–266.
87. Clarke E.D., Greenhow D.T., Adams D. // Pesticide Sci. 1998. V. 54. № 4. P. 385–393.
88. Cadenas S. // Biochim. Biophys. Acta. 2018. V. 1859. № 9. P. 940–950.
89. Zorov D.B., Andrianova N.V., Babenko V.A., Pevzner I.B., Popkov V.A., Zorov S.D., Zorova L.D., Plotnikov E.Y., Sukhikh G.T., Silachev D.N. // Brain Sci. 2021. V. 11. № 8. P. 1050.
90. Plotnikov E.Y., Silachev D.N., Jankauskas S.S., Rokitskaya T.I., Chupyrkina A.A., Pevzner I.B., Zorova L.D., Isaev N.K., Antonenko Y.N., Skulachev V.P., Zorov D.B. // Biochemistry (Moscow). 2012. V. 7. № 9. P. 1029–1037.
91. Rai Y., Anita A., Kumari N., Singh S., Kalra N., Soni R., Bhatt A.N. // Biochim. Biophys. Acta. 2021. V. 1862. № 1. P. 148325.
92. Tao H.L., Zhang Y., Zeng X.G., Shulman G.I., Jin S.K. // Nature Medicine. 2014. V. 20. № 11. P. 1263–1269.
93. Kanemoto N., Okamoto T., Tanabe K., Shimada T., Minoshima H., Hidoh Y., Aoyama M., Ban T., Kobayashi Y., Ando H., et al. // Nat. Comm. 2019. V. 10. № 1. P. 2172.
94. Shrestha R., Johnson E., Byrne F.L. // Mol. Metab. 2021. V. 51. P. 101222.
95. Tainter M.L. // J. Pharm. Exp. Ther. 1938. V. 63. P. 51–57.
96. Barros M.H., Bandy B., Tahara E.B., Kowaltowski A.J. // J. Biol. Chem. 2004. V. 279. № 48. P. 49883–49888.
97. Padalko V.I. // Biochemistry (Moscow). 2005. V. 70. № 9. P. 986–989.
98. Zorov D.B., Juhascova M., Sollott S.J. // Physiol. Rev. 2014. V. 94. № 3. P. 909–950.
99. Cerqueira F.M., Laurindo F.R., Kowaltowski A.J. // PLoS One. 2011. V. 6. № 3. P. e18433.
100. Schlagowski A.I., Singh F., Charles A.L., Ramamoorthy T.G., Favret F., Piquard F., Geny B., Zoll J. // J. Appl. Physiol. 2014. V. 116. № 4. P. 364–375.

101. Berezhnov A.V., Soutar M.P., Fedotova E., Frolova M.S., Plun-Favreau H., Zinchenko V.P., Abramov A.Y. // J. Biol. Chem. 2016. V. 291. № 16. P. 8701–8708.
102. Shulman G.I., Petersen M.C., Vatner D.F. // Nat. Rev. Endocrinol. 2017. V. 13. № 10. P. 572–587.
103. Zorova L.D., Popkov V.A., Plotnikov E.Y., Silachev D.N., Pevzner I.B., Jankauskas S.S., Babenko V.A., Zorov S.D., Balakireva A.V., Juhascova M., et al. // Anal. Biochem. 2018. V. 552. P. 50–59.
104. Gao J.L., Zhao J., Zhu H.B., Peng X., Zhu J.X., Ma M.H., Fu Y., Hu N., Tai Y., Xuan X.C., et al. // Free Radic. Biol. Med. 2018. V. 124. P. 288–298.

Eukaryotic Ribosome Biogenesis: The 40S Subunit

A. A. Moraleva[1], A. S. Deryabin[1*], Yu. P. Rubtsov[1], M. P. Rubtsova[2*], O. A. Dontsova[1,2,3]
[1]Shemyakin-Ovchinnikov Institute of Bioorganic Chemistry of the Russian Academy of Sciences, Moscow, 117997 Russia
[2]Lomonosov Moscow State University, Faculty of Chemistry, Moscow, 119991 Russia
[3]Skolkovo Institute of Science and Technology, Moscow, 121205 Russia
*E-mail: deryabin95@mail.ru, mprubtsova@gmail.com
Received: July 29, 2021; in final form, February 02, 2022
DOI: 10.32607/actanaturae.11540

ABSTRACT **The formation of eukaryotic ribosomes is a sequential process of ribosomal precursors maturation in the nucleolus, nucleoplasm, and cytoplasm. Hundreds of ribosomal biogenesis factors ensure the accurate processing and formation of the ribosomal RNAs' tertiary structure, and they interact with ribosomal proteins. Most of what we know about the ribosome assembly has been derived from yeast cell studies, and the mechanisms of ribosome biogenesis in eukaryotes are considered quite conservative. Although the main stages of ribosome biogenesis are similar across different groups of eukaryotes, this process in humans is much more complicated owing to the larger size of the ribosomes and pre-ribosomes and the emergence of regulatory pathways that affect their assembly and function. Many of the factors involved in the biogenesis of human ribosomes have been identified using genome-wide screening based on RNA interference. This review addresses the key aspects of yeast and human ribosome biogenesis, using the 40S subunit as an example. The mechanisms underlying these differences are still not well understood, because, unlike yeast, there are no effective methods for characterizing pre-ribosomal complexes in humans. Understanding the mechanisms of human ribosome assembly would have an incidence on a growing number of genetic diseases (ribosomopathies) caused by mutations in the genes encoding ribosomal proteins and ribosome biogenesis factors. In addition, there is evidence that ribosome assembly is regulated by oncogenic signaling pathways, and that defects in the ribosome biogenesis are linked to the activation of tumor suppressors.**
KEYWORDS **nucleolus, ribosome biogenesis, ribosomopathy.**

INTRODUCTION

Ribosomes are molecular RNA–protein machines that ensure the translation of mRNA genetic information into proteins. Eukaryotic 80S ribosomes (S is the sedimentation constant) with a molecular mass of 4.3 MDa consist of two unequal subunits. The small subunit (40S or SSU) contains one 18S rRNA molecule and 33 ribosomal proteins (RPS or S). The large subunit (60S or LSU) comprises three rRNA molecules (25S/28S, 5.8S, and 5S) and usually 47 proteins (RPL or L) [1–4]. The subunits contain several functional regions that play different roles in the translation process (*Fig. 1*); the sequences of mature rRNAs and the general structure of ribosomes are evolutionarily conserved. Ribosome synthesis is a fundamental process for all forms of life, and its efficiency controls the proliferative and secretory status of the cell.

During ribosome biosynthesis, the ribosomal DNA (rDNA) is transcribed, the resulting rRNA precursors (pre-rRNAs) are processed into mature molecules, which involves ribosome biogenesis factors (RBFs) and ribosomal proteins (RPs), and, finally, all components are assembled into mature ribosomes. Only an accurate sequence of all these stages leads to the formation of functional ribosomes [5]. The most complex and interesting process is the biogenesis of three rRNAs – 18S, 5.8S, and 25S/28S – which are transcribed by RNA polymerase I (Pol I) as a single, long precursor [6, 7]. The need to coordinate rRNA synthesis and processing required the formation of a specialized structure within the nucleus: the nucleolus.

THE NUCLEOLUS IS A RIBOSOME ASSEMBLY FACTORY

Eukaryotic chromosomes usually occupy specific regions of the nucleus where genes are clustered for optimal use of the transcription machinery [8]. The synthesis of rRNA precursors and the early steps in ribosome assembly occur in a nucleus region called the nucleolus. The structural determinants of the nucleolus are nucleolar organizer regions (NORs), which

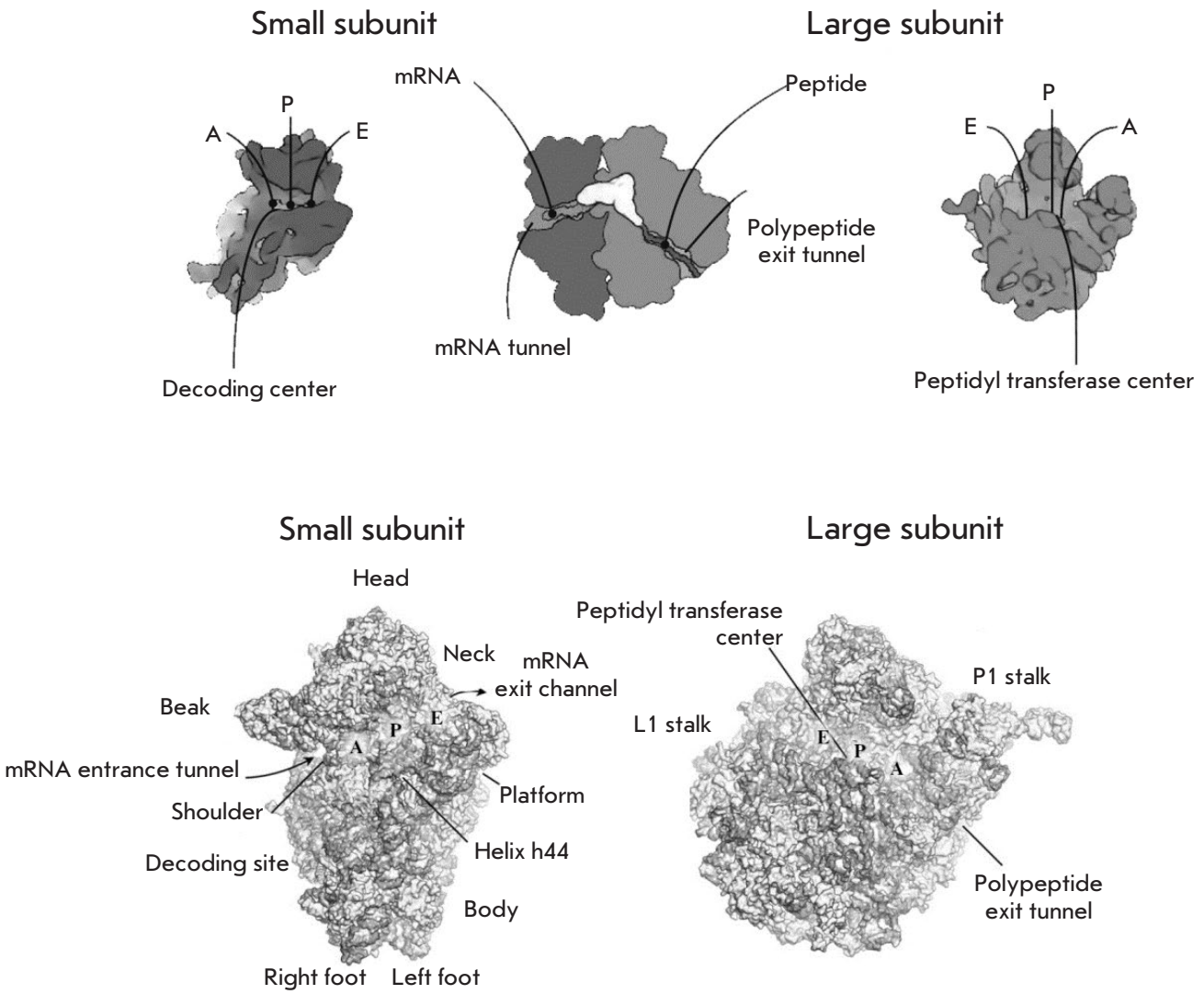

Fig. 1. Spatial structure of eukaryotic ribosome subunits. The main functional areas of the subunits are labeled. In the small subunit, these are: (1) the channel that accommodates mRNA during translation; (2) the decoding center where codon and anticodon pairing occurs, and (3) the tRNA binding sites (sites A, P, E). Site A (aminoacyl) is occupied by the incoming aminoacyl-tRNA; site P (peptidyl) accommodates tRNA with a growing polypeptide chain (peptidyl-tRNA); site E (exit) is the place where tRNA dissociates from the ribosome. The main functional domains of the large subunit are as follows: (1) tRNA binding sites (A, P, and E); (2) the peptide exit tunnel that extends over the body of the subunit; and (3) the peptidyl transferase center (PTC). PTC is responsible for peptide bond formation and is located at the beginning of the peptide exit tunnel, in a conserved region at the interface between two subunits, which is mainly composed of rRNA. The folding of rRNA into tertiary structures and their association with ribosomal proteins generates several characteristic regions in each subunit. The main ones in the 40S subunit are the head, neck, platform, body, left foot, right foot, shoulder, and beak, as well as helix h44 of the 18S rRNA, which houses the decoding center at its base. The main tRNA binding sites (A, P, and E) are located at the interface (on the surface). The mRNA entrance tunnel is located between the head and the shoulder. The exit channel, from where the 5′-end of the mRNA egresses, is located between the head and the platform. The decoding center is located at the interface surface and includes three domains from the head, shoulder, and the h44 helix of 18S rRNA. The main features of the large subunit are the central protuberance, L1 stalk, and P stalk. The tRNA binding sites (A, P, and E) are located on the interface side, along with PTC. The latter is adjacent to the entrance to the exit tunnel, from which the nascent polypeptide chain emerges [24]

are chromosomal regions where many rRNA gene repeats are grouped.

The intragenomic location of NORs depends on the species. In haploid budding yeast cells (*Saccharomyces cerevisiae*), the NOR occurs on chromosome 12. In humans, NORs occur on the acrocentric chromosomes 13, 14, 15, 21, and 22 [9–11]. Human rRNA gene arrays are unevenly located on the short arms of chromosomes in secondary constrictions between centromeres and telomeres [12, 13]. During eukaryotic division, nucleoli assemble in the end of mitosis and remain functionally active throughout the entire interphase, disintegrating at the beginning of the next mitosis. Ribosome production alters during the cell cycle, reaching a maximum in the G2 phase [14]. Nucleolar morphology significantly depends on the growth conditions and physiological status of the cell [15]. The nucleolar size correlates with the proliferative activity of the cell; nucleoli in rapidly dividing cells are larger than those in slowly dividing cells [16]. The nucleolar volume in most tumor cells is enlarged compared to that in their progenitors [17].

The nucleolus is the largest part of the nucleus, which is not separated by a membrane from the nucleoplasm; its volume accounts for 20–25% of the nucleus in higher eukaryotes. According to electron microscopy (EM), finer structures in the nucleolus correspond to the main stages of ribosome biogenesis. The fibrillar center (FC), a dense fibrillar component (DFC), and the granular component (GC) can be distinguished (*Fig. 2*).

Ribosome biogenesis is a vector process that begins with rRNA synthesis at the interface between FC and DFC, continues in DFC, and ends in GC. Thus, FCs contain rDNA, Pol I and DNA topoisomerase I subunits, and the upstream binding factor [18]. In DFC, synthesis and early stages of rRNA processing occur. For example, fibrillarin, Nopp140, and small nucleolar RNAs (snoRNAs) are involved in the early stages of rRNA processing and are localized in DFC [18–21]. Mutation in the main casein kinase 2 (CK2), a key protein of the granular component of human nucleophosmin (NPM/B23)) phosphorylation site leads to the detachment of GC from DC/DFC, which indicates a transition between the stages of pre-40S and pre-60S ribosome subunit assembly at the border between DFC and GC. The nucleolar stage of SSU and LSU precursor assembly in yeast, which continues with export to the nucleoplasm, takes a different amount of time. For example, SSUs leave the nucleolus approximately 10 min after the start of assembly, almost twice faster than LSUs [21–23]. The distribution of ribosome maturation stages over different structures of the nucleolus architecture in higher eukaryotes remains poorly understood.

Recently, new mechanisms that underly the nucleolus formation control have been proposed. They are based on the multiphase organization related to liquid–liquid phase separation [13]. Pre-rRNAs are supposed to recruit certain proteins, which leads to phase separation. The spatial separation and physical and compositional features of subnucleolar phases can optimize pre-rRNA processing, providing targeted transport and hierarchy of pre-ribosome assembly processes. Early stages of pre-rRNA processing and covalent modification of highly conserved rRNA residues (ribose and base methylation and pseudouridylation), which are essential for the structural organization of ribosomes and regulation of the translation process [24–26], occur in DFC (*Fig. 2*). The external GC acts as a temporary "quarantine" for misfolded nuclear proteins that accumulate under stressful conditions [13, 27].

Homologues of ~90% of yeast nucleolar proteins have been identified in the human nucleolus proteome [28]. According to the classification of nucleolar proteins functions, ~30% of them are associated with ribosome biogenesis [29]. Dysregulation of nucleolar proteins may lead to cell cycle arrest and apoptosis or, conversely, promote cell transformation and accelerate proliferation [30]. RPs also play an important role in the assembly process, as they are believed to stabilize the secondary rRNA structure, promoting the formation of cleavage-competent tertiary structures, and prevent misfolding. RPs from HeLa cells (32 proteins) may be classified into two categories depending on their involvement in the early or late stages of processing. The moment of RP attachment to pre-ribosomes correlates with their contribution at the stage of RNA precursor cleavage [6]. Pre-rRNA processing is a determining factor in the formation of mature functional ribosomes, and, in this review, we will focus on sequential maturation of the Pol I transcription product, a common precursor of 18S, 5.8S, and 25S/28S rRNAs.

RIBOSOME BIOGENESIS

Main processing stages and differences in the structure of yeast and human rRNA precursors

Transcription of rRNA genes leads to the formation of a pre-rRNA precursor (35S in yeast and 47S in human cells), which includes 18S, 5.8S, and 25S/28S rRNA sequences flanked with external transcribed spacers (5'-ETS and 3'-ETS) and separated by internal transcribed spacers (ITS1, between 18S and 5.8S; ITS2, between 5.8S and 25S/28S) (*Fig. 3*). During sequential maturation of pre-rRNAs, RNA intermediates are formed. Folding of long rRNAs is a difficult

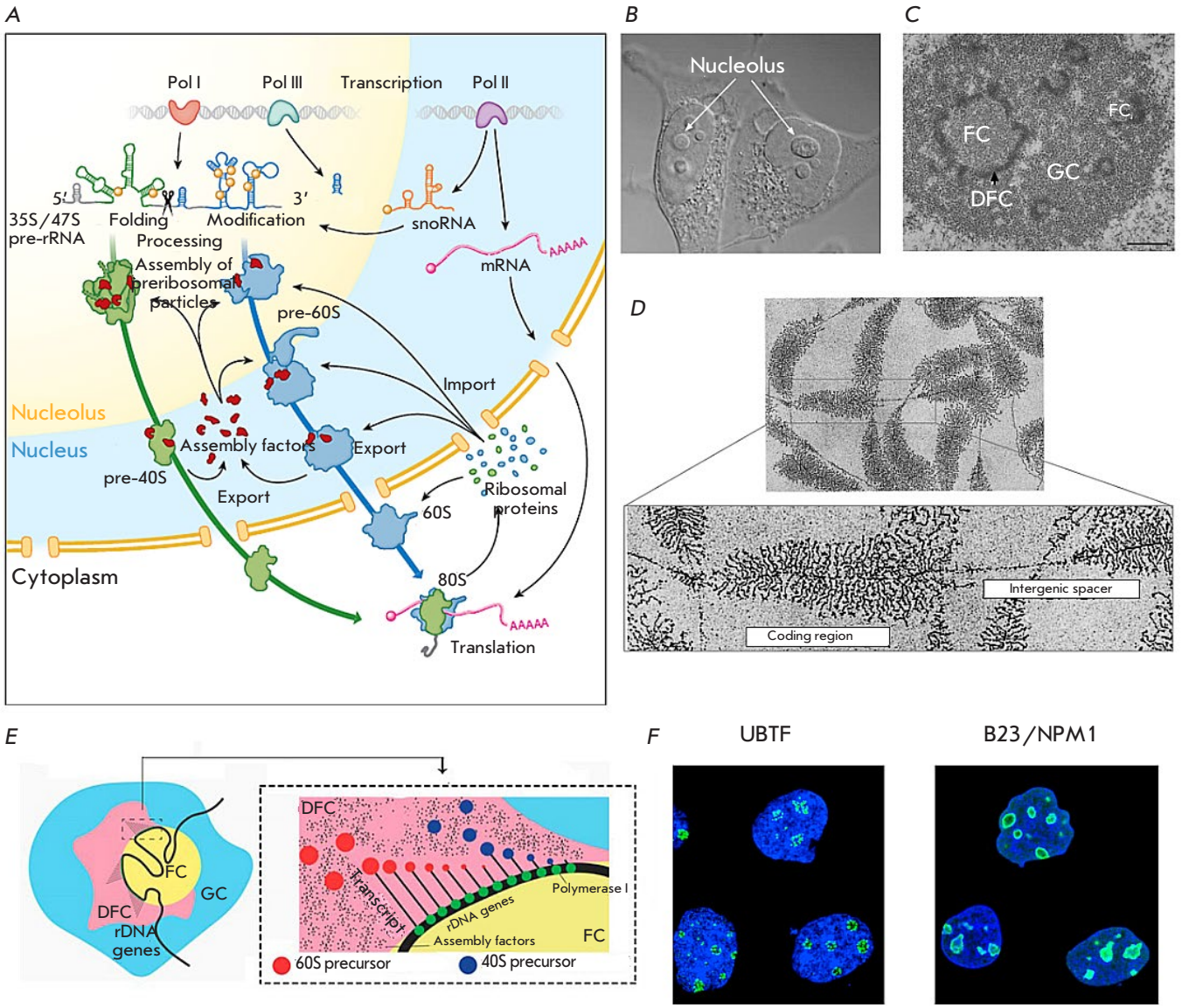

Fig. 2. Eukaryotic ribosome biogenesis. (*A*) General scheme [5]; (*B*) Nucleoli of HeLa cells, phase contrast [18]; (*C*) Electron micrograph of the HeLa cell nucleolus: granular component (GC), fibrillar center (FC), and dense fibrillar component (DFC) [19]; (*D*) Tandem repeats of ribosomal genes and transcribed rRNA of the newt oocyte were stained using the Miller method. (http://www.cellimagelibrary.org); (*E*) Mutual arrangement of subdivisions of human nucleoli [13]; (*F*) Localization of the ribosome processing factors UBTF in DFC and B23 in GC of the nucleoli of human A-43 cells stained with specific antibodies (https://www.proteinatlas.org/)

task, because their size allows these molecules to be in alternative stable non-functional structures. Unlike relatively weak interactions that maintain the spatial structure of proteins (e.g., alpha-helices and beta-sheets), approximately half of the folded rRNA structure is composed of the more stable A-form double helices [13]. Therefore, the existence of extended non-transcribed ETS and ITS spacers (about half of the primary rRNA transcript), which only complicate the structure of rRNA precursors, seems illogical. The role of external spacers is probably to reduce the risk of rRNA mutations owing to RNA polymerase errors, which more often occur in the 5'- and 3'-termini of transcripts. Although spacer sequences differ, their ends are evolutionarily conserved and fold into several hairpin structures [31]. The sequences of the noncoding spacer ITS1 are less conserved [32], which complicates any prediction of cleavage sites even in

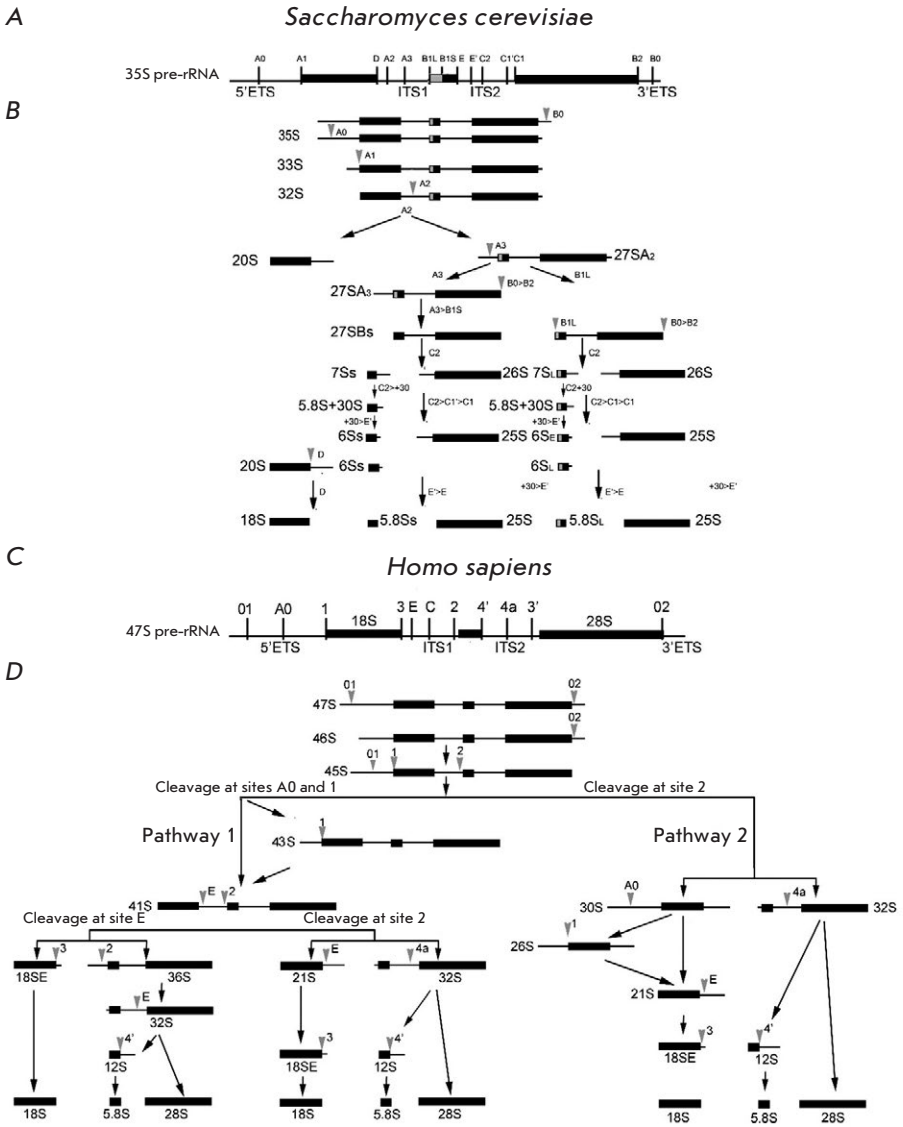

Fig. 3. Maturation pathways of the yeast 35S pre-rRNA transcript (*A*) and human 47S pre-RNA transcript (*C*). Three of the four rRNAs (18S, 5.8S, and 25S (in yeast)/28S (in humans)) are synthesized by Pol I as a single long transcript. The coding sequences of mature rRNAs are flanked by 5′- and 3′-ETS, ITS1, and ITS2 non-coding spacers. The schematic shows the relative position of known and predicted cleavage sites. (*B*) Processing of pre-rRNA in budding yeast. (*D*) A simplified schematic of human pre-rRNA processing. A primary transcript, 47S pre-rRNA, is initially cleaved at both ends at sites 01 and 02 to form the 45S precursor that is processed via two alternative pathways [6]. ">" (e.g., C2>C1′>C1) denotes sequential shortening of the appropriate 3′- or 5′-ends of the pre-rRNA by nucleases

closely related species. Mammalian ITS1 sequences are usually 2–3 times lengthier and possess a much higher G + C content than yeast ones (mice, 70.1%; yeast, 35.2%) [33, 34].

Because rRNA performs both structural and catalytic functions, it is not surprising that the key aspects of ribosomal subunit maturation include the formation of structural domains in rRNA, folding into the three-dimensional structure, and concomitant excision and removal of spacers from compound RNP complexes. In addition, the large subunit precursor pre-60S should include the 5S rRNA and its associated ribosomal proteins (*Fig. 3*) [6]. The RNA–protein composition of ribosomal precursor complexes is studied using a combination of biochemical approaches; in particular, Northern blotting, rapid amplification of cDNA ends (RACE) combined with DNA sequencing, Western blotting with antibodies to RPs and RAFs (ribosome assembly factor), as well as mass spectrometry and high-resolution cryo-electron microscopy (cryo-EM) to characterize secondary- and tertiary-structure elements. Combination of these methods enables mapping of the main pre-rRNA cleavage sites in yeast, mice, and humans [6, 35] and the elucidation of the protein–nucleic acid composition and 3D structure of individual complexes.

Saccharomyces cerevisiae ribosome biogenesis, rRNA processing

Figure 3A, B provides a schematic for cleavage and truncation of the ends of *S. cerevisiae* pre-rRNA. The RNase III homologue Rnt1 co-transcriptionally hydro-

lyzes 3'-ETS at the B0 site in primary 35S pre-rRNA transcripts [35–38]. Subsequent cleavage at the A0, A1, and A2 sites is interdependent (*Fig. 3B*), and in fast growing cells, co-transcriptional cleavage at ITS1 occurs in 50–70% of cases. Cleavage at A0, A1, and A2 is performed by the SSU processome containing snoRNA U3. The endonucleases Utp24 and Rcl1 hydrolyze pre-rRNAs at the A1 and A2 sites, respectively [39, 40]. The products 20S and 27SA2 further form SSU and LSU, respectively. 20S enters the cytoplasm, turning into 18S after cleavage at the D site by Nob1 nuclease (*Fig. 3*).

Maturation of the 27SA2 pre-rRNA leads to the formation of alternative 27SB forms which differ by additional 7–8 nucleotides at the 5'-end. The RNase MRP cleaves approximately 80% of 27SA2 at the A3 site, and Rat1–Rai1 (Rrp17) proteins truncate 27SA2 to the B1S site (probably, together with 5'–3'-exonuclease Xrn1). The remaining 20% of 27SA2 is cleaved by an unknown RNase at the B1L site, with hydrolysis at B1L and B2 occurring simultaneously (*Fig. 3*). Cleavage of 27S B1S and B1L at the C2 site within ITS2 results in the formation of 7S pre-rRNA (5.8S precursor) and 26S pre-rRNA (25S precursor). The RNA exosome, which comprises the Rrp6 and Ngl2 subunits and Rex exonuclease, truncates the 7S pre-rRNA to the E site which corresponds to the 3'-end of 5.8S. The 3'-end of 5.8S rRNA is finally formed in the cytoplasm, probably with involvement of Ngl2 that acts as a nuclease both in the nucleus and in the cytoplasm. Impairment of pre-rRNA processing kinetics at sites between A0 and A2 leads to aberrant rRNAs, which occurs upon knockdown of the genes of proteins essential for the processing of the 27SA2 pre-rRNA at the A3 site: Cic1, Erb1, Nop7, Nop12, and Nop1 (*Fig. 3*) [41]. Non-optimal growth conditions and mutations interfering with SSU or LSU synthesis affect the order of RNA cleavage [42], which leads to accumulation and cleavage of the 35S pre-rRNA immediately at the A3 site, but not at A0, A1, and A2, to form 23S, an aberrant product inappropriate for 18S rRNA maturation [43].

Processing of pre-rRNA and attachment of ribosomal proteins require many auxiliary RAFs, in particular RNA helicases, ribonucleases, GTPases, ATPases, RNA chaperones, and non-enzymatic proteins [44]. Some RAFs temporarily block transitions between the structures of subparticle precursors, preventing rRNA misfolding or premature binding of RAFs and RPs, which are required at later stages of assembly. As subunits mature structurally, RAF binding mimics the binding of translation factors or substrates (e.g., tRNA or mRNA) and prevents involvement of immature particles in translation initiation.

The earliest, large RNP–90S complex is formed co-transcriptionally. The structures of early intermediates were visualized using cryo-EM methods in [45, 46]. Simultaneously with transcription, rRNA undergoes covalent modifications, most of which occur in functionally important domains and are also believed to be essential for the rRNA structure [47]. In the three-dimensional structure of the human 80S ribosome, 130 rRNA modifications (methylation and pseudouridinylation) were revealed by cryo-EM [48]. Pseudouridinylation is performed by Cbf5, Gar1, Nop10, and Nhp2 synthases belonging to the H/ACA snoRNP class, while methylation of 2'-O-ribose is performed by C/D-box snoRNA proteins, such as Nop1 methyltransferase (fibrillarin in humans), Nop56–Nop58 heterodimer, and Snu13 [49, 50]. Probably, modifications occur during transcription and initial folding of pre-rRNAs because snoRNAs hybridize more efficiently to partially unfolded pre-rRNA. Some snoRNAs required for ribosome assembly do not modify pre-rRNAs but stabilize structures that benefit the assembly and maturation of pre-ribosomal particles. Subunit precursors are also modified by specific snoRNA-independent methyltransferases [5, 51] and acetylases [52].

The assembly of yeast ribosomes involves 19 RNA helicases, including DEAD-box and DEAH-box helicases, but their role in this process remains unclear [53]. Three helicases (Has1, Mtr4, and Prp43) are involved in the assembly of both subunits [54, 55]. The energy in this process is provided by GTPases (Bms1, Nog1, Nog2, Nug1, Lsg1, and Efl1), ATPases (Rio1, Rio2, and Fap7), and AAA ATPases (Mdn1, Drg1, and Rix7) [56]. The role of these factors is to maintain the irreversibility of the assembly processes.

Yeast ITS2 processing

ITS2 is a structural element that serves as the basis for several stages of 60S assembly, similar to 5'-ETS in the early stages of 18S rRNA maturation. Removal of ITS2 located between 5.8S and 25S rRNAs is considered one of the most difficult steps in ribosome assembly. Despite its short length (only a few hundred nucleotides), yeast ITS2 is highly structured and forms a dense and conserved core [57, 58]. An *in vivo* study of the pre-rRNA structure showed that ITS2 folds into a long hairpin structure with the C2 cleavage site at the stem end (*Fig. 4*) [59]. Disturbances of the hairpin sequence and structure block ITS2 processing, indicating its key importance in ribosome assembly [60, 61]. According to the cryo-EM structure, the pre-60S ITS2 base structure forms paws and involves several assembly factors [62–64]. There is a model where ITS2 rRNA and associated biogen-

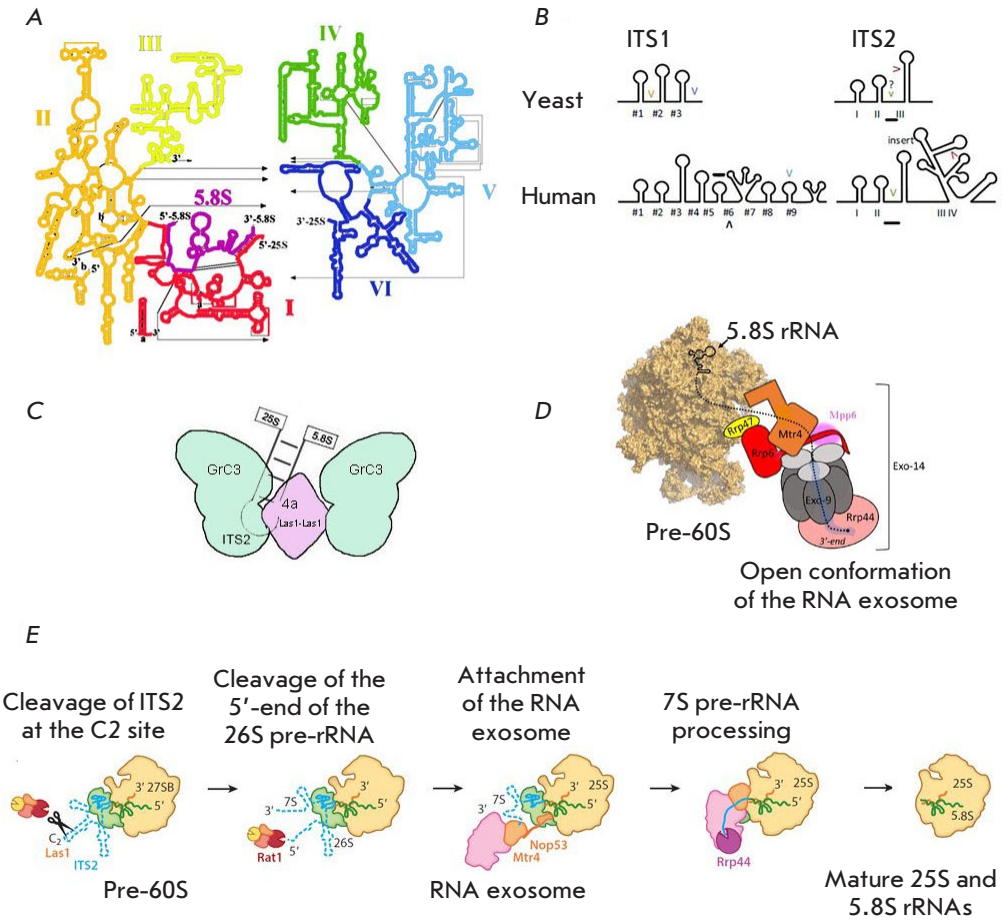

Fig. 4. Structure and maturation of yeast pre-rRNA. (*A*) The 25S rRNA contains six domains (I–VI). The 5.8S rRNA (shown in black) forms complementary interactions with domain I of the 25S rRNA (adopted from https://crw-site.chemistry.gatech.edu/). (*B*) Secondary structures of yeast and human ITS1 and 2. Cleavage sites are denoted by "V." Predicted sites are marked by "?"; the human exonuclease binding sites are underscored. (*C*) Model of ITS2 processing by RNase PNK [49, 52]. (*D*) Interaction of the nuclear RNA exosome with pre-60S [78]. (*E*) Removal of ITS2 from the pre-60S particle by RNA processing enzymes. Intermediates during ITS2 removal are shown [5]

esis factors (Nsa3, Nop7, Erb1, Rlp7, Nop15) facilitate hybridization of the 25S rRNA domain I and 5.8S. This model is supported by data indicating that mutations in these proteins inhibit ITS2 processing at early stages [65–68].

There are three phases of ITS2 processing: (1) cleavage and phosphorylation of the C2 site by the Las1–Grc3 complex, (2) hydrolysis of the 5'-end by Rat1 exonuclease, and (3) hydrolysis of the 3'-end by the RNA exosome (*Fig. 4*). Processing of ITS2 activates a tetrameric enzymatic complex consisting of two HEPN Las1 endonuclease and Grc3 polynucleotide kinase dimers (they function only as dimers; the level of the proteins is co-regulated) [69]. The N-terminal HEPN domain comprises the RφxxxH catalytic motif (φ is H, D, or N, and x is any amino acid) [70]. Depletion of mammalian LAS1L (Las1-like), an ortholog of yeast Las1, leads to inhibition of ITS2 processing and cell proliferation [71]. Depletion of yeast cells in Las1 also blocks ITS2 processing, which indicates conserved functions of Las1 in ITS2 processing in eukaryotes [69, 72]. C2 cleavage and phosphorylation are related processes; phosphorylation prevents re-ligation of C2 cleavage products: 7S pre-rRNA with 2'-3'-cyclophosphate and 26S pre-rRNA with 5'-hydroxyl [60, 61, 73]. Grc3 recruits the 5' → 3' exonuclease Rat1 (mammalian Xrn2) to the C2 site of the 26S pre-rRNA [61, 74, 75]. Rat1/Xrn2 (non-sequence-specific) hydrolyzes a single-stranded RNA with a terminal 5'-monophosphate in the 5' → 3' direction [76]. Yeast Rat1 and its activating cofactor, nuclease Rai1, form a dimeric complex that binds Las1–Grc3 via Grc3 [73] in pre-60S particles [73, 76, 77]. Binding between Rat1-Rai1 and Grc3 is rather weak, which implies additional interactions at the C2 site [60, 73, 78]. The amino acid sequences of Grc3/Nol9 and Rat1/Xrn2 are very conserved, suggesting conservation of Grc3-dependent recruitment of Rat1 to the C2 site. Details on a molecular interaction between Grc3/Nol9 and Rat1/Xrn2 are unknown, which complicates our understanding of the mechanism of ITS2 5'-end truncation.

The RNA exosome hydrolyzes the 3'-end of the 7S pre-rRNA after cleavage of the ITS2 5'-end (*Fig. 4*). The RNA exosome is a multisubunit 3' → 5' ribonuclease complex that hydrolyzes any known forms

of RNA [79, 80]. It comprises a core of 9 subunits (Exo-9) which form a two-layer ring with a central channel (*Fig. 4*) [78, 79, 81–83]. The Exo-9 core lacks catalytic activity and requires multiple partners to degrade RNA. The catalytic activity of the RNA exosome depends on the Rrp44 enzyme possessing the endonuclease and 3' → 5' exonuclease activities [84, 85]. Rrp44 binds the Exo-9 core to form the Exo-10 complex [79, 81] that interacts with additional 3' → 5' nuclease, Rrp6, to form Exo-11 [82, 86–89]. Additional proteins – Mpp6, Rrp47, and Rrp6 – recruit the Mtr4 cofactor, enhancing binding of the complex to pre-ribosomes, into the exosome. The interaction between Mtr4 and Nop53 or Utp18 directs Exo-11 to ITS2 and 5'-ETS, respectively (*Fig. 4E*) [90]. The helicase Mtr4 unwinds the ITS2 end in the 3' → 5' direction [91–93], enabling Rrp44 to hydrolyze the 3'-end of the 7S pre-rRNA. The resulting transcript encodes 5.8S with an additional 30 ITS2 nucleotide tag (*Fig. 4*) [92, 94, 95]. Further, Rrp6 nuclease cleaves ITS2 to form the 6S pre-rRNA [92]. A recent cryo-EM structure of the RNA–exosome revealed that it undergoes structural rearrangements upon binding to pre-60S [78, 96], forming a channel inside the RNA–exosome core, through which the 7S pre-rRNA reaches the Rrp44 exonuclease active site [78, 95, 96] (*Fig. 4*).

Human rRNA processing

Processing of human 18S rRNA includes more steps than those in yeast cells [23, 35] (*Fig. 3*). At the first stage of processing, the primary 47S transcript (*Fig. 3*) is truncated at both ends at the A0 (or 01) and 02 sites, which leads to the release of 5'- and 3'-ETS, respectively, and the formation of a 45S pre-rRNA precursor (*Fig. 3*) that is then truncated via two alternative pathways. In human cells, cleavage of the 47S pre-rRNA at the A0 and 02 sites is coordinated in time. Perturbation of this coordination leads to the accumulation of a 46S intermediate. The 45S pre-rRNA is processed via parallel pathways (1 and 2) to form numerous intermediates (*Fig. 3D*). Also, an important role in the processing (along with endonucleases) is played by exonucleases which truncate rRNA at the ends.

Some human pre-rRNA molecules are probably cleaved co-transcriptionally, as in yeast cells. In mammals, pre-rRNAs are supposed to be co-transcriptionally cleaved only at the A' site [97]. It is worth noting that there are conditions that favor one of the alternative pathways. For example, mutations in U3 or U8 snoRNAs disrupt the order of pre-rRNA cleavage [98]. The first 47S pre-rRNA cleavage occurs at site 01, located several hundred nucleotides downstream of the transcription start, at the 5'-ETS binding site for C/D snoRNA U3. The order of precursor cleavage also depends on the species and type of cells, physiological conditions, and cell cycle stages and is disturbed in disease [6, 99–101].

The key RAFs and RPs involved in pre-rRNA processing and an analysis of the differences in the yeast and human rRNA processing machineries will be addressed when considering the assembly of certain SSU and LSU precursors.

Although rRNA synthesis and maturation are the key events in the ribosome subunit biogenesis, there are other important aspects to this process: e.g., attachment of ribosomal proteins and RAFs at certain stages (*Fig. 5*). The ribosome assembly is based on four main principles: (1) a gradual decrease in the conformational freedom of pre-rRNA; (2) the sequence and temporal dynamics of binding of individual assembly factors provided by molecular mimicry and molecular switches; (3) the irreversibility of key checkpoints, which depends on energy consumption and enzymes that change the RNA length and structure; and (4) structural and functional correction of the active sites of both ribosomal subunits.

Assembly of 90S pre-rRNP

As the transcript is released from contact with Pol I, the 5'-ETS rRNA folds into stem–loop structures, providing a platform for the attachment of RAFs and RPs and for the folding of four SSU domains (*Fig. 6A*). Because these structures are formed co-transcriptionally, they provide binding sites for a number of RAF complexes, in particular the molecular chaperones UTP-A, UTP-B, and U3 snoRNA, ordering the assembly. At this stage, the hairpin structures formed by 5'-ETS play the main role (*Fig. 6A, B*) [44]. A significant variability in the primary structures of 5'-ETS and ITS in different species indicates the key role played by the spatial structure formed by these elements in ribosome biogenesis [102]. By pairing with rRNA bases, snoRNA U3 renders the rRNA structure rigid. In the 90S cryo-EM structure, a partially prominent complex of the 3'-terminal part of the U3 snoRNA with the main C/D-box factors (Nop1, Nop56, Nop58, Snu13, Rrp9) is observed. The single-stranded 5'-end of U3 penetrates deep into the SSU particle, hybridizing with the short, conserved nucleotide sequences of 18S rRNA and 5'-ETS (*Fig. 6B*). This process is accompanied by the formation of 5'- and 3'-loops and promotes excision of the 18S pre-rRNA owing to the formation of Box A and Box A' [44, 103–109] (*Fig. 6B*). The close proximity of these sites to the 5' region of snoRNA U3 provides a crucial spatial constraint that dictates the topology of the maturing particle. The complex comprising the

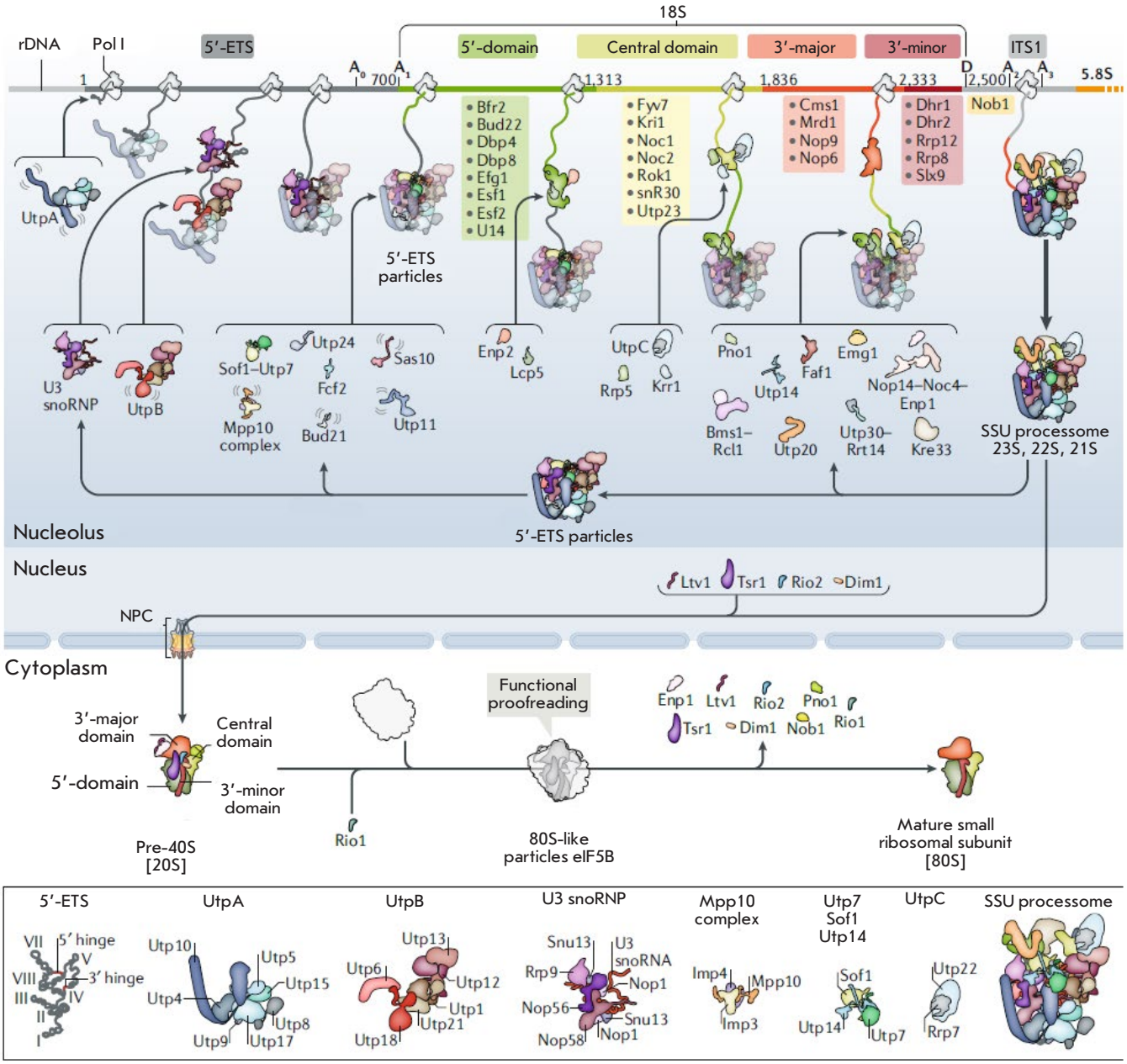

Fig. 5. The factors and complexes involved in the assembly of the yeast small subunit. The main stages of 40S subunit maturation in yeast are shown. (Top) rDNA with the main domains of the 18S rRNA: 5′-ETS, ITS1, 5′-central, 3′-major, and 3′-minor domains. Also, sites (A0, A1, D, and A2) are shown. (Below) Intermediate pre-ribosomal particles: 5′-ETS complex, SSU processome, and pre-40S. The intermediate components of pre-rRNA complexes are shown in square brackets under each particle. Assembly factors and complexes for which (not transparent) structures have been identified are depicted as cartoons, whereas those for which no structures are known are indicated only with text. Proteins that joined the growing SSU processome at an earlier stage are shown as transparent to highlight new components (not transparent). Adopted from [44]

folded 5′-ETS 18S pre-rRNA with an uncleaved A1 site and early RPs is incorporated into the structure formed by biogenesis factors (~60 proteins) and snoRNA U3 (*Fig. 6*, *Table*). Timely cleavage at the A1 and A2 sites requires U3-dependent formation of the 35S pre-rRNA conformation that prevents the formation of the central pseudoknot, a characteristic structure located at the decoding center in mature 18S rRNA (*Fig. 6*). A number of early RAFs (Utp11, Sas10, Mpp10, and Fcf2) (*Fig. 5*) limit the pre-rRNA domains

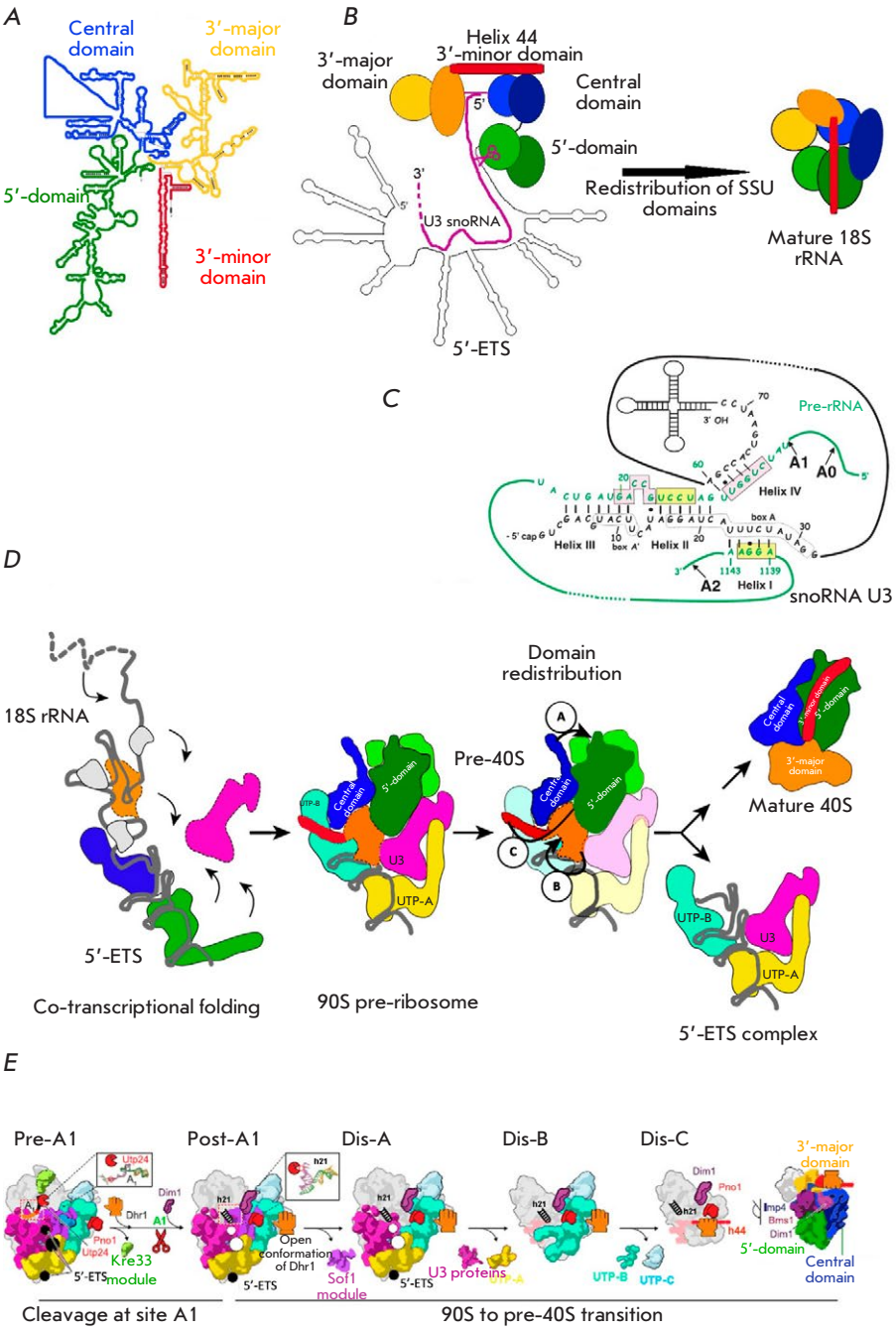

Fig. 6. Domain rearrangements during maturation of the 40S subunit. (*A*) The 18S rRNA contains the following domains: 5′-domain, central domain, 3′-major domain, and 3′-minor domain (adopted from https://crw-site.chemistry.gatech.edu/). (*B*) Schematic of the SSU processome (left) and mature 18S (right). 18S domains are shown in different colors: 5′-domain (green), central domain (blue), 3′-major domain (yellow), 3′-minor domain (red rectangle), and U3 RNA (pink line) [13]. (*C*) Base-pair interactions between the U3 snoRNA and the 18S region of the pre-rRNA in yeast. Three interactions between Box A and Box A′ in the U3 snoRNA and three 18S regions of the pre-rRNA, which are involved in the formation of the central pseudoknot structure in the mature 18S rRNA [23, 35]. (*D*) Model of 90S formation and its transformation into pre-40S. The snoRNP modules UTP-A (yellow), UTP-B (blue), and U3 (pink) bind co-transcriptionally to the 35S pre-rRNA. Further compaction leads to 90S complex formation. General folding of the 5′-domain of the 18S rRNA resembles the mature conformation, but transformation of the pre-40S preribosome 90S into the mature 40S subunit requires structural rearrangements in the central, 3′-major (orange), and 3′-minor (red) domains [23, 35]. (*E*) Schematic of 90S transformation into pre-40S upon cleavage at A1. Assembly factors and selected proteins are colored and labeled accordingly. The helicase Dhr1 is shown as a grasping hand representing open and closed conformations

inside the particle by binding either to the protein or to RNA elements. In the 90S pre-ribosome, only the 5′-domain has a conformation close to that of the mature one and, accordingly, contains RPs (*Fig. 6*). The central domain is only partially visible, and the 3′-terminal domains cannot be distinguished in the 90S structure. Thus, folding of the nascent 18S rRNA occurs in the direction from the 5′-end to the 3′-end but is blocked at intermediate stages involving additional RAFs (*Figs. 5, 6*). The 90S subparticle comprises the GTPase Bms1. After hydrolysis of GTP, this enzyme is believed to initiate the conformational changes necessary for pre-rRNA processing and transformation of 90S into the pre-40S subunit. According to this hypothesis, Bms1 is located at the interface of several pre-18S domains and comes into contact with several RAFs that stabilize the 90S intermediate (*Fig. 5*).

Approximately 18 out of 60 RAFs in the 90S particle are β-propeller proteins that mediate protein–protein interactions during the formation of macromo-

Small ribosomal subunit assembly factors [44]

Ribosome biogenesis factors of the SSU component in *Saccharomyces cerevisiae*					
Cluster number			Human	*S. cerevisiae*	Function
2	2	8	DDX47	Rrp3	DEAD-box-helicase
6	2	2	DDX49	Dbp8	DEAD-box-helicase
1	1	1	DDX42	Rok1	DEAD-box-helicase
1	1	1	EIF4A3	Fal1	DEAD-box-helicase
2			Rrp36	Rrp36	Structural
11	11		MYBBP1A	Pol5	Same
2	2		ABT1	Esf2	«
1	1	1	Esf1	Esf1	«
3			Utp23	Utp23	«
4	4	11	NOC2L	Noc2	«
8	3	3	RBM19	Mrd1	«
		2	C14orf21	Nop9	«
1			Rrp8	Rrp8	rRNA methyltransferase
				H/ACA components	
		2	Gar1	Gar1	Pseudouridine synthase cofactor
2	2		Nhp2	Nhp2	Pseudouridine synthase cofactor
			Nop10	Nop10	Pseudouridine synthase cofactor
				UtpA complex	
2	2	2	CIRH1A	Utp4	Structural
2	2	5	WDR43	Utp5	Same
2	2		HEATR1	Utp10	«
1	1	1	Utp15	Utp15	«
5	5	2	WDR75	Utp17/Nan1	«
				UtpB complex	
2	2	2	PWP2	Utp1/Pwp2	«
2	8	8	Utp6	Utp6	«
2	2	2	WDR3	Utp12	«
2	2	2	TBL3	Utp13	«
2	2		Utp18	Utp18	Structural, has the exosome binding motif
2	2	2	WDR36	Utp21	Structural
				U3 snoRNP	
2	2	2	Nop56	Nop56	BoxC/D snoRNP main component
2	2		Nop58	Nop58	BoxC/D snoRNP main component
2	2	2	FBL	Nop1	BoxC/D snoRNP main component
2	2	11	NHP2L1	Snu13	BoxC/D snoRNP main component
2	2	2	Rrp9	Rrp9	Specific factor of U3 snoRNA
				Mpp10 complex	
8	8	8	MPHOSPH10	Mpp10	Structural
2	2	2	Imp3	Imp3	Same
2	2	8	Imp4	Imp4	«
				Individual factors	
	2	8	DCAF13	Sof1	«
8	8	8	WDR46	Utp7	«
2		2	DNTTIP2	Fcf2	«
2	2	8	FCF1	Utp24	A1, A2 nuclease
1	2		UTP3	Sas10/Utp3	Structural, has the exosome binding motif
2	2	8	UTP11L	Utp11	Structural
				5'-domain	
2	2	8	AATF	Bfr2	Same
2	2	8	NOL10	Enp2	«
2	2	2	NOL6	Utp22	«
				Central domain	
2	8	8	RRP7A	Rrp7	«
8	8	4	PDCD11	Rrp5	«
1	2		Krr1	Krr1	«
1	2		BYSL	Enp1	«
				3'-main domain	
2	2	2	NOP14	Nop14	«
2	2	2	NOC4L	Noc4	«
7	7	7	Rrp12	Rrp12	«
1			NAT10	Kre33	Cytosine acetyltransferase/helicase
1	2	2	Bms1	Bms1	GTPase
2	2		Rcl1	Rcl1	Structural
1	1		EMG1	Emg1/Nep1	rRNA methyltransferase
4	4	4	RSL1D1	Utp30	Structural
6	6	6	Pno1	Pno1	Same
2	2	8	Utp20	Utp20	«
8	8	4	UTP14A	Utp14	Dhr1 binding
				Rrt14	«
				Faf1	«
				Dhr1	DEAH-box-helicase
2			Nob1	Nob1	D-site nuclease
	5	5	DHX33	Dhr2	DEAH-box helicase
1			DHX35		
1	1		C1orf107	Utp25	Structural
10	10	10	WBSCR22	Bud23	rRNA methyltransferase
			TRMT112	Trm112	Methyltransferase adapter
9	9	9	Ltv1	Ltv1	Structural
		4	Tsr1	Tsr1	Same
		4	RIOK1	Rio1	«
	10		RIOK2	Rio2	«
			CSNK1A1	Hrr25	Casein kinase
	4	8	DIMT1L	Dim1	rRNA demethylase

lecular complexes [110]. In addition, several proteins with Trp and Asp (WD) repeats in 90S bind directly to specific rRNA sites. Another large group of 90S RAFs are α-helical proteins. The large proteins Utp20 (~220 kDa) and Utp10 (~180 kDa) are linked to each other, reaching remote regions on the 90S particle with their long α-helices. For example, Utp10 extends from the base of 90S, where 5'-ETS is located, to the top of 90S (5'-domain), where it binds to the Utp20 wrapped around the head of the 90S particle (*Figs. 5, 6*). These distant contacts facilitate communication between different regions and/or promote recognition of a common conformation to coordinate maturation steps [5]. Some 90S biogenesis factors are partially or completely unfolded. These polypeptides are present both on the surface and deep in the 90S subparticles. A typical example is Mpp10, which winds around 90S and comes into contact with Imp3, Imp4, Bms1, Utp12, Utp13 (UTP-B), and some regions of the 18S rRNA (*Figs. 5, 6*). Similarly, Nop14 is in contact via its long N- and C-terminal regions with Noc4, Emg1, and Rcl1. These elements not only stabilize the 90S complex, but also participate in long-range interactions and/or in conformational sensing [5].

The last step in the 90S conversion is the detachment of the pre-40S complex. This step is closely related to cleavage of the 35S precursor at the A1 and A2 sites at the first stage of the 60S large subunit precursor biogenesis. Interestingly, Utp24 is in close proximity with the A1 site in the 90S particle but cannot perform its function because another RAF, Sof1, masks the A1 cleavage site. Thus, transition of the 90S pre-ribosome to the next stage of assembly requires significant conformational rearrangements that are a result of interaction between new RAFs (e.g., helicases) and the pre-ribosome and/or hydrolysis of macroergic bonds. In particular, several additional enzymes, such as Kre33 acetyltransferase or Nop1 and Emg1 methyltransferases, are present in the 90S particle. Although RNA helicases are involved in RNA structural rearrangements, including snoRNA dissociation, they are absent in the 90S complex. The 90S to pre-40S transition is stimulated by the helicase Dhr1/Ecm16, because the helicase appears to disrupt the base pairing between snoRNA U3 and pre-rRNA and to be involved in 5'-ETS cleavage [111, 112]. Many factors bind pre-rRNA transiently and only until cleavage at the A2 site. These include small RNAs (U14, snR10, and snR30 [113, 114]) and the proteins associated with each of the 18S rRNA subdomains [115–117], although their role remains poorly understood (*Fig. 5*).

The interaction of proteins, such as Mpp10, Utp11, and Sas10 (*Fig. 5*), and base pairing between the U3 snoRNA and the 5'-ETS and 18S rRNA (*Fig. 5*) provide additional particle stability, mainly acting as local stabilizers of RNA structural elements [31, 44]. Proteins containing helical repeats (Nop14, Noc4, Rrp5, Utp10, and Utp20) and playing mainly a structural role, as well as some enzymes, such as methyltransferase Emg1 [118], acetyltransferase helicase Kre33 [52], and GTPase Bms1 [31, 52], are located in the outer regions of the SSU processome. The temporal order in which enzymes act on the encapsulated pre-18S rRNA remains to be determined.

Transition from 90S pre-rRNP to 40S pre-rRNP: Release of 5'-ETS

Inhibition of the RNA exosome due to a mutation in Utp18 [53] or arrest of 90S assembly on the 3'-truncated pre-rRNA [46, 119, 120] stabilizes the complex of 5'-ETS RNA with UTP-A, UTP-B, U3 snoRNA, and other biogenesis factors, which is released during transition from the 90S to pre-40S subparticle [5, 53]. Degradation of 5'-ETS by the RNA exosome should lead to a recycling of biogenesis factors [90, 91].

Further maturation stages require coordinated cleavage at site A1 of 5'-ETS and A2 of ITS1, which acts as a signal for separation of the 18S rRNA and 5.8S/25S rRNA (*Fig. 6*) [5, 36, 44].

The dissociation of factors enables the formation of contacts between four 18S rRNA domains, which tightens the structure (*Fig. 6*). Cryo-EM structures showing the 90S to pre-40S transition revealed seven intermediate pre-ribosomal particles, Pre-A1, Post-A1, Dis-C, Dis-A, and Dis-B, which successively replace each other during biogenesis (*Fig. 6E*) [121].

In the Pre-A1 state, the helix h21 of the pre-18S rRNA occurs in its matured/correct position (*Fig. 6E*). Along with cleavage at the A1 site, structural changes result in the formation of the Post-A1 intermediate. Sequential dissociation of several assembly factor modules in the intermediate states Dis-C, Dis-A, and Dis-B leads to gradual simplification of the complex, with the main interactions in the 90S subparticle being preserved. Probably, the decisive step in the disassembly of a 90S intermediate depends on the degree of maturation of the pre-40S domains, which is reflected in its compaction degree. rRNA becomes more compact owing to the remodeling of rRNA and RNP, which enables the formation of the decoding center [44]. The degree of compaction may be a signal for disassembling the 5'-ETS scaffold, as seen from the structures preceding cleavage at A1 [90]. This suggestion is consistent with the dependence of cleavage at A1 on the activity of the helicase Mtr4 that probably remodels 5'-ETS [103]. Turning and displacement of RNA helixes, starting in the 3'-region of

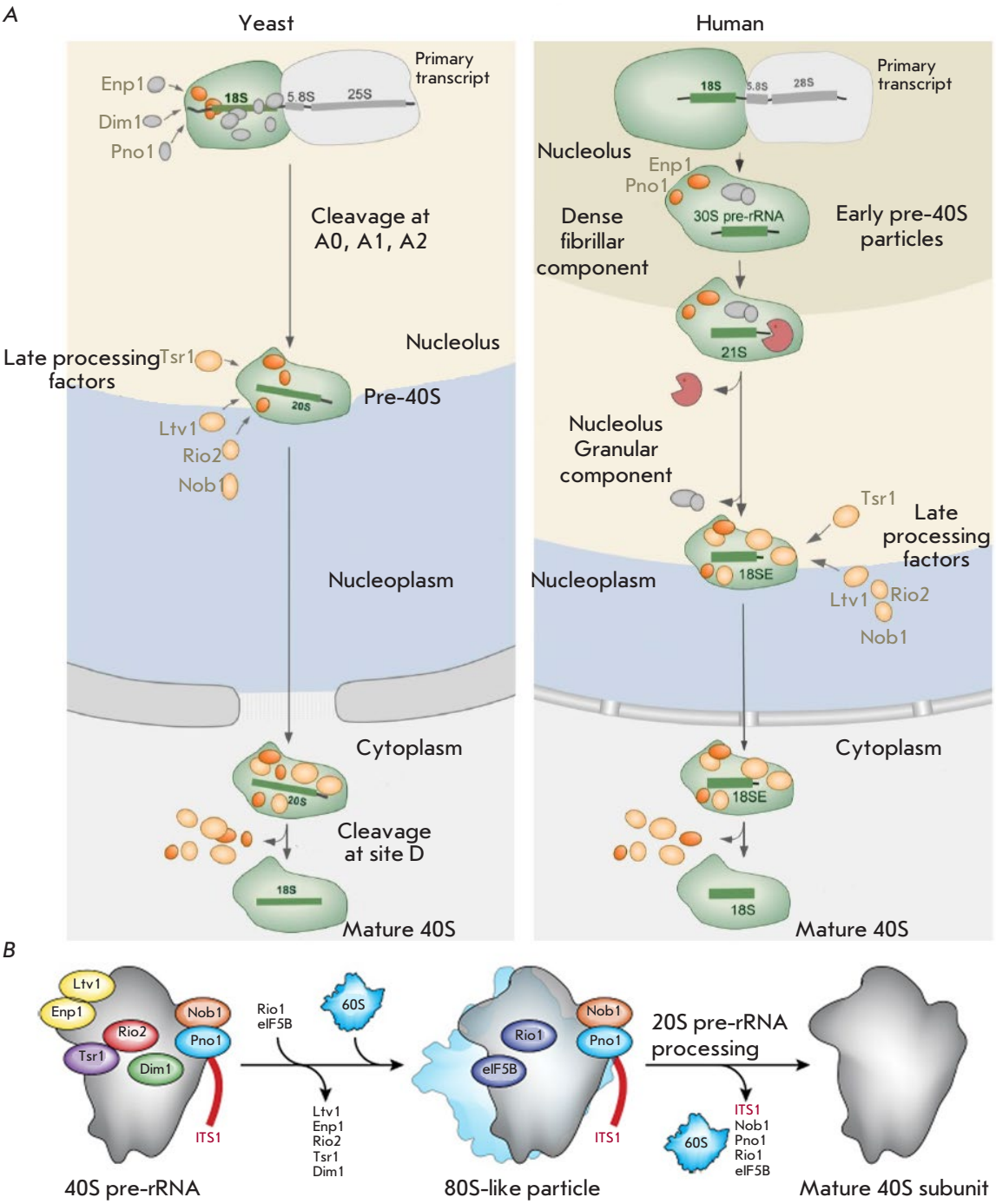

Fig. 7. Late maturation stages of the human and yeast ribosomal subunits and subcellular localization of the main assembly participants. (*A*) 40S pre-ribosome intermediates in *S. cerevisiae* (left) and *H. sapiens* (right). Stable identification of two additional pre-rRNAs (30S and 21S) in human cells indicates that there are at least two distinct early maturation stages that are not observed in yeast. Similar compositions of cytoplasmic pre-40S particles suggest similarities in late maturation in yeast and humans. (*B*) Schematic of quality control of the cytoplasmic pre-40S subunit. Only assembly factors with known binding sites are shown [125]

5'-ETS, enable movement of Pno1 and h45 and simultaneous attachment of the helicase Dhr1 that forms part of the rRNA helix h1 required for cleavage at A1 by Utp24 endonuclease. This complex process is accompanied by a dissociation of several factors, further destabilization of the intermediate 90S complex, and displacement of 5'-ETS. This results in release of RNA–protein complexes and the pre-40S formation (*Fig. 5*) [121].

Export of pre-40S particles

Within the 90S complex, the 20S pre-rRNA is formed (*Fig. 3*). It contains 18S rRNA and part of ITS1. The 20S pre-rRNA is a component of the earliest pre-40S particles. Pre-40S bind to several RAFs (nucleolar protein Tsr1 and cytoplasmic proteins Ltv1, Rio2, and Nob1 (*Fig. 5*)) and are rapidly transported into the cytoplasm. Due to their large size, pre-ribosomes move through the nuclear pores one at a time. The karyopherin Crm1/Xpo1, with the involvement of Ran/Gsp1, transports them into the cytoplasm in a GTP-dependent manner [122]. Rrp12, together with Crm1, binds to 90S and participates in 35S pre-rRNA processing at the A0 site [123]. A decrease in the level of Rrp12 or Crm1 causes accumulation of the pre-40S complex in the nucleoplasm [124]. At least three RAFs (Dim2, Ltv1, and Rio2) present in pre-40S particles contain predicted or functional nuclear export signals, but none of them alone is necessary for export. The functions of the other factors involved in the export of pre-40S subunits have not been identified.

Processing of pre-40S subparticles in the cytoplasm

According to biochemical and structural data, pre-40S particles have a relatively simple RAF composition upon transition to the mature 18S rRNA structure. The first cryo-EM structure of the pre-40S particle revealed almost formed 5'- and central (platform) domains, while the 3'-domain (head and beak regions) had not yet reached a mature conformation. The pre-40S subparticle entering the cytoplasm contains seven RAFs that promote late maturation events (*Fig. 7*). Two main events occur in the cytoplasm: beak-forming structural rearrangements and 20S pre-rRNA cleavage at the D site by the endonuclease Nob1. They are closely associated with quality control mechanisms and functional site checks, which ensure that ribosomal subunits are translationally competent [125]. Maturation of the beak is facilitated by the release of RAFs and export factors, stable attachment of several ribosomal proteins, and conformational rearrangement that results in the formation of the decoding site. Phosphorylation of the Ltv1 and Enp1 proteins by the kinase Hrr25 allows them to displace and properly place the mature Rps3 protein, which promotes Nob1-dependent 20S pre-rRNA cleavage at the D site [122].

CryoEM data of yeast and human pre-40S particles revealed a significant structural similarity in the positions of associated late RAFs, which occupy functionally important sites and block the formation of functional ribosomes [5, 126–128]. In particular, RAFs Tsr1, Enp1, Rio2, and Pno1/Dim2 jointly control incompletely formed sites in pre-40S: the decoding center and mRNA-binding groove (*Fig. 7*). In the early stages, Enp1 and Ltv1 occupy the binding site of ribosomal eS10 in the 3'-major domain (head and beak), dissociating upon phosphorylation by the protein kinase Hrr25 [5, 129–131]. The dissociation of Enp1/Ltv1 leads to attachment of eS31 and displacement of the C-terminal domain of uS3, which stabilizes the interaction between the 40S body and head [132]. The mechanism of timely cleavage of 20S pre-rRNA by the endonuclease Nob1 may be explained using cryo-EM structures. The RNA-binding protein Pno1 masks a cleavage site at the 3'-end of the mature 18S rRNA. Conformational rearrangement and interaction of the pre-40S subunit with the mature 60S subunit are the checking steps required for interaction with Nob1, which converts the 20S pre-rRNA into the 18S rRNA [5, 38, 133–137]. A Cryo-EM analysis of human, late pre-40S particles supports a model where Rio1-ATP interacts with the ribosomal protein RPS26 and displaces Dim2 from the 3'-end of the 20S pre-rRNA. This makes the pre-rRNA available for the interaction with Nob1 endonuclease. Hydrolysis of ATP and release of ADP lead to a dissociation of the Rio1–40S subunit complex. The locking mechanism with two keys, Rio1 and RPS26, guarantees consistency in the transformation of particles into translation-competent 40S sub-particles [138]. Coordination of 80S-like particle formation with final maturation of the 18S rRNA ensures that only correctly assembled 40S subunits participate in translation.

Thus, despite the abundance of data for *S. cerevisiae* and the high conservatism of eukaryotic ribosome biogenesis, the architecture of processing common to both subunits of the 90S precursor and 40S subunit precursor in higher eukaryotes has undergone significant changes, whose details are yet to be studied.

Further description of the large 60S subunit biogenesis will be presented in the next part of the review. ●

This work was supported by RFBR grant No. 20-04-00796 "Analysis of the protein-nucleic acid composition of ribosomal subunit assembly intermediates in genetically modified human cells".

REFERENCES

1. Ban N., Nissen P., Hansen J., Moore P.B., Steitz T.A. // Science. 2000. V. 289. № 5481. P. 905–920.
2. Jenner L., Melnikov S., de Loubresse N.G., Ben-Shem A., Iskakova M., Urzhumtsev A., Meskauskas A., Dinman J., Yusupova G., Yusupov M. // Curr. Opin. Struct. Biol. 2012. V. 22. № 6. P. 759–767.
3. Klinge S., Voigts-Hoffmann F., Leibundgut M., Ban N. // Trends Biochem. Sci. 2012. V. 37. № 5. P. 189–198.
4. Melnikov S., Ben-Shem A., Garreau De Loubresse N., Jenner L., Yusupova G., Yusupov M. // Nat. Struct. Mol. Biol. 2012. V. 19. № 6. P. 560–567.
5. Baßler J., Hurt E. // Annu. Rev. Biochem. 2019. V. 88. № 1. P. 281–306.
6. Mullineux S.T., Lafontaine D.L.J. // Biochimie. 2012. V. 94. № 7. P. 1521–1532.
7. Hadjiolov A.A., Nikolaev N. // Prog. Biophys. Mol. Biol. 1978. V. 31. P. 95–144.
8. Misteli T. // Sci. Am. 2011. V. 304. № 2. P. 66–73.
9. van Sluis M., McStay B. // Curr. Opin. Cell Biol. 2017. V. 46. P. 81–86.
10. Mangan H., Gailín M., McStay B. // FEBS J. 2017. V. 284. № 23. P. 3977–3985.
11. Henderson A.S., Warburton D., Atwood K.C. // Proc. Natl. Acad. Sci. USA. 1972. V. 69. № 11. P. 3394–3398.
12. Németh A., Längst G. // Trends Genet. 2011. V. 27. № 4. P. 149–156.
13. Correll C.C., Bartek J., Dundr M. // Cells. 2019. V. 8. № 8. P. 869.
14. Wang F., Ying C., Shang G., Jiao M., Hongfang Z. // Micron. 2013. V. 49. P. 15–20.
15. DiMario P.J. // Int. Rev. Cytol. 2004. V. 239. P. 99–178.
16. Thiry M., Lafontaine D.L.J. // Trends Cell Biol. 2005. V. 15. № 4. P. 194–199.
17. Montanaro L., Treré D., Derenzini M. // Am. J. Pathol. 2008. V. 173. № 2. P. 301–310.
18. Olson M.O.J. The Nucleolus. New York, NY. Springer New York, 2011. 414 c.
19. Dragon F., Compagnone-Post P.A., Mitchell B.M., Porwancher K.A., Wehner K.A., Wormsley S., Settlage R.E., Shabanowitz J., Osheim Y., Beyer A.L., et al. // Nature. 2002. V. 417. № 6892. P. 967–970.
20. Grandi P., Rybin V., Baßler J., Petfalski E., Strauß D., Marzioch M., Schäfer T., Kuster B., Tschochner H., Tollervey D., et al. // Mol. Cell. 2002. V. 10. № 1. P. 105–115.
21. Pöll G., Braun T., Jakovljevic J., Neueder A., Jakob S., Woolford J.L., Tschochner H., Milkereit P. // PLoS One. 2009. V. 4. № 12. P. 8249.
22. Henras A.K., Plisson-Chastang C., O'Donohue M.F., Chakraborty A., Gleizes P.E. // Wiley Interdiscip. Rev. RNA. 2015. V. 6. № 2. P. 225–242.
23. Rabl J., Leibundgut M., Ataide S.F., Haag A., Ban N. // Science. 2011. V. 331. № 6018. P. 730–736.
24. Laptev I., Shvetsova E., Levitskii S., Serebryakova M., Rubtsova M., Bogdanov A., Kamenski P., Sergiev P., Dontsova O. // RNA Biol. 2020. V. 17. № 4. P. 441–450.
25. Laptev I., Shvetsova E., Levitskii S., Serebryakova M., Rubtsova M., Zgoda V., Bogdanov A., Kamenski P., Sergiev P., Dontsova O. // Nucleic Acids Res. 2020. V. 48. № 14. P. 8022–8034.
26. Frottin F., Schueder F., Tiwary S., Gupta R., Körner R., Schlichthaerle T., Cox J., Jungmann R., Hartl F.U., Hipp M.S. // Science. 2019. V. 365. № 6451. P. 342–347.
27. Andersen J.S., Lam Y.W., Leung A.K.L., Ong S.-E., Lyon C.E., Lamond A.I., Mann M. // Nature. 2005. V. 433. № 7021. P. 77–83.
28. Boisvert F.-M., van Koningsbruggen S., Navascués J., Lamond A.I. // Nat. Rev. Mol. Cell Biol. 2007. V. 8. № 7. P. 574–585.
29. Moraleva A., Magoulas C., Polzikov M., Hacot S., Mertani H.C., Diaz J.-J., Zatsepina O. // Cell Cycle. 2017. V. 16. № 20. P. 1979–1991.
30. Barandun J., Chaker-margot M., Hunziker M., Molloy K.R., Chait B.T., Klinge S. // Nat. Struct. Mol. Biol. 2017. V. 24. № 11. P. 944–953.
31. Coleman A.W. // PLoS One. 2013. V. 8. № 11. P. 79122.
32. Wang M., Anikin L., Pestov D.G. // Nucleic Acids Res. 2014. V. 42. № 17. P. 11180–11191.
33. Grisendi S., Mecucci C., Falini B., Pandolfi P.P. // Nat. Rev. Cancer. 2006. V. 6. № 7. P. 493–505.
34. Tomecki R., Sikorski P.J., Zakrzewska-Placzek M. // FEBS Lett. 2017. V. 591. № 13. P. 1801–1850.
35. Woolford J.L., Baserga S.J. // Genetics. 2013. V. 195. № 3. P. 643–681.
36. Allmang C., Tollervey D. // J. Mol. Biol. 1998. V. 278. № 1. P. 67–78.
37. Lebaron S., Schneider C., van Nues R.W., Swiatkowska A., Walsh D., Böttcher B., Granneman S., Watkins N.J., Tollervey D. // Nat. Struct. Mol. Biol. 2012. V. 19. № 8. P. 744–753.
38. Bleichert F., Granneman S., Osheim Y.N., Beyer A.L., Baserga S.J. // Proc. Natl. Acad. Sci. USA. 2006. V. 103. № 25. P. 9464–9469.
39. Horn D.M., Mason S.L., Karbstein K. // J. Biol. Chem. 2011. V. 286. № 39. P. 34082–34087.
40. Granneman S., Petfalski E., Tollervey D. // EMBO J. 2011. V. 30. № 19. P. 4006–4019.
41. Osheim Y.N., French S.L., Keck K.M., Champion E.A., Spasov K., Dragon F., Baserga S.J., Beyer A.L. // Mol. Cell. 2004. V. 16. № 6. P. 943–954.
42. Venema J., Tollervey D. // Annu. Rev. Genet. 1999. V. 33. P. 261–311.
43. Klinge S., Woolford J.L. // Nat. Rev. Mol. Cell Biol. 2019. V. 20. № 2. P. 116–131.
44. Koš M., Tollervey D. // Mol. Cell. 2010. V. 37. № 6. P. 809–820.
45. Zhang L., Wu C., Cai G., Chen S., Ye K. // Genes Dev. 2016. V. 30. № 6. P. 718–732.
46. Sharma S., Lafontaine D.L.J. // Trends Biochem. Sci. 2015. V. 40. № 10. P. 560–575.
47. Natchiar S.K., Myasnikov A.G., Kratzat H., Hazemann I., Klaholz B.P. // Nature. 2017. V. 551. № 7681. P. 472–477.
48. Kiss T., Fayet-Lebaron E., Jády B.E. // Mol. Cell. 2010. V. 37. № 5. P. 597–606.
49. Watkins N.J., Bohnsack M.T. // Wiley Interdiscip. Rev. RNA. 2012. V. 3. № 3. P. 397–414.
50. Sharma S., Yang J., Watzinger P., Kötter P., Entian K.D. // Nucleic Acids Res. 2013. V. 41. № 19. P. 9062–9076.
51. Sharma S., Langhendries J.L., Watzinger P., Kotter P., Entian K.D., Lafontaine D.L.J. // Nucleic Acids Res. 2015. V. 43. № 4. P. 2242–2258.
52. Kornprobst M., Turk M., Kellner N., Cheng J., Flemming D., Koš-Braun I., Koš M., Thoms M., Berninghausen O., Beckmann R., et al. // Cell. 2016. V. 166. № 2. P. 380–393.
53. Rodríguez-Galán O., García-Gómez J.J., De la Cruz J. // Biochim. Biophys. Acta – Gene Regul. Mech. 2013. V. 1829. № 8. P. 775–790.
54. Martin R., Straub A.U., Doebele C., Bohnsack M.T. // RNA Biol. 2013. V. 10. № 1. P. 4–18.

55. Kressler D., Hurt E., Bergler H., Baßler J. // Biochim. Biophys. Acta – Mol. Cell Res. 2012. V. 1823. № 1. P. 92–100.
56. Schultz J., Maisel S., Gerlach D., Müller T., Wolf M. // RNA. 2005. V. 11. № 4. P. 361–364.
57. Joseph N., Krauskopf E., Vera M.I., Michot B. // Nucleic Acids Res. 1999. V. 27. № 23. P. 4533–4540.
58. Burlacu E., Lackmann F., Aguilar L.C., Belikov S., Nues R. Van, Trahan C., Hector R.D., Dominelli-Whiteley N., Cockroft S.L., Wieslander L., et al. // Nat. Commun. 2017. V. 8. № 1. P. 714.
59. Pillon M.C., Sobhany M., Borgnia M.J., Williams J.G., Stanley R.E., Baker D. // Proc. Natl. Acad. Sci. USA. 2017. V. 114. № 28. P. 5530–5538.
60. Fromm L., Falk S., Flemming D., Schuller J.M., Thoms M., Conti E., Hurt E. // Nat. Commun. 2017. V. 8. № 1. P. 1–11.
61. Wu S., Tutuncuoglu B., Yan K., Brown H., Zhang Y., Tan D., Gamalinda M., Yuan Y., Li Z., Jakovljevic J., et al. // Nature. 2016. V. 534. № 7605. P. 133–137.
62. Sanghai Z.A., Miller L., Molloy K.R., Barandun J., Hunziker M., Chaker-Margot M., Wang J., Chait B.T., Klinge S. // Nature. 2018. V. 556. № 7699. P. 126–129.
63. Kater L., Thoms M., Barrio-Garcia C., Cheng J., Ismail S., Ahmed Y.L., Bange G., Kressler D., Berninghausen O., Sinning I., et al. // Cell. 2017. V. 171. № 7. P. 1599–1610.
64. van Nues R.W., Rientjes J.M.J., Morré S.A., Mollee E., Planta R.J., Venema J., Raué H.A. // J. Mol. Biol. 1995. V. 250. № 1. P. 24–36.
65. van der Sande C.A.F.M., Kwa M., van Nues R.W., van Heerikhuizen H., Raué H.A., Planta R.J. // J. Mol. Biol. 1992. V. 223. № 4. P. 899–910.
66. Gadal O., Strauss D., Petfalski E., Gleizes P.E., Gas N., Tollervey D., Hurt E. // J. Cell Biol. 2002. V. 157. № 6. P. 941–951.
67. Adams C.C., Jakovljevic J., Roman J., Harnpicharnchai P., Woolford J.L. // RNA. 2002. V. 8. № 2. P. 150–165.
68. Castle C.D., Sardana R., Dandekar V., Borgianini V., Johnson A.W., Denicourt C. // Nucleic Acids Res. 2013. V. 41. № 2. P. 1135–1150.
69. Anantharaman V., Makarova K.S., Burroughs A.M., Koonin E.V., Aravind L. // Biol. Direct. 2013. V. 8. № 1. P. 8–15.
70. Castle C.D., Cassimere E.K., Lee J., Denicourt C. // Mol. Cell. Biol. 2010. V. 30. № 18. P. 4404–4414.
71. Schillewaert S., Wacheul L., Lhomme F., Lafontaine D.L.J. // Mol. Cell. Biol. 2012. V. 32. № 2. P. 430–444.
72. Gasse L., Flemming D., Hurt E. // Mol. Cell. 2015. V. 60. № 5. P. 808–815.
73. Wang M., Pestov D.G. // Nucleic Acids Res. 2011. V. 39. № 5. P. 1811–1822.
74. Geerlings T.H., Vos J.C., Raue H.A. // RNA. 2000. V. 6. № 12. P. 1698–1703.
75. Stevens A., Poole T.L. // J. Biol. Chem. 1995. V. 270. № 27. P. 16063–16069.
76. Xiang S., Cooper-Morgan A., Jiao X., Kiledjian M., Manley J.L., Tong L. // Nature. 2009. V. 458. № 7239. P. 784–788.
77. Pillon M.C., Lo Y.H., Stanley R.E. // DNA Repair (Amst.). 2019. V. 9. № 81. P.102653.
78. Chlebowski A., Lubas M., Jensen T.H., Dziembowski A. // Biochim. Biophys. Acta – Gene Regul. Mech. 2013. V. 1829. № 6–7. P. 552–560.
79. Januszyk K., Lima C.D. // Curr. Opin. Struct. Biol. 2014. V. 24. № 1. P. 132–140.
80. Lykke-Andersen S., Tomecki R., Jensen T.H., Dziembowski A. // RNA Biol. 2011. V. 8. № 1. P. 61–66.
81. Liu Q., Greimann J.C., Lima C.D. // Cell. 2006. V. 127. № 6. P. 1223–1237.
82. Zinder J.C., Lima C.D. // Genes Dev. 2017. V. 31. № 2. P. 88–100.
83. Schneider C., Leung E., Brown J., Tollervey D. // Nucleic Acids Res. 2009. V. 37. № 4. P. 1127–1140.
84. Lorentzen E., Conti E. // Methods Enzymol. 2008. V. 447. P. 417–435.
85. Wasmuth E.V., Januszyk K., Lima C.D. // Nature. 2014. V. 511. № 7510. P. 435–439.
86. Cristodero M., Böttcher B., Diepholz M., Scheffzek K., Clayton C. // Mol. Biochem. Parasitol. 2008. V. 159. № 1. P. 24–29.
87. Dziembowski A., Lorentzen E., Conti E., Séraphin B. // Nat. Struct. Mol. Biol. 2007. V. 14. № 1. P. 15–22.
88. Makino D.L., Schuch B., Stegmann E., Baumgärtner M., Basquin C., Conti E. // Nature. 2015. V. 524. № 7563. P. 54–58.
89. Thoms M., Thomson E., Baßler J., Griesel S., Hurt E. // Cell. 2015. V. 162. P. 1029–1038.
90. De la Cruz J., Kressler D., Tollervey D., Linder P. // EMBO J. 1998. V. 17. № 4. P. 1128–1140.
91. Allmang C., Kufel J., Chanfreau G., Mitchell P., Petfalski E., Tollervey D. // EMBO J. 1999. V. 18. № 19. P. 5399–5410.
92. Jia H., Wang X., Anderson J.T., Jankowsky E. // Proc. Natl. Acad. Sci. USA. 2012. V. 109. № 19. P. 7292–7297.
93. Allmang C., Petfalski E., Podtelejnikov A., Mann M., Tollervey D., Mitchell P. // Genes Dev. 1999. V. 13. № 16. P. 2148–2158.
94. Kummer E., Ban N. // Biochemistry. 2018. V. 57. № 32. P. 4765–4766.
95. Schuller J.M., Falk S., Fromm L., Hurt E., Conti E. // Science. 2018. V. 360. № 6385. P. 219–222.
96. Sloan K.E., Bohnsack M.T., Schneider C., Watkins N.J. // RNA. 2014. V. 20. № 4. P. 540–550.
97. Langhendries J.L., Nicolas E., Doumont G., Goldman S., Lafontaine D.L.J. // Oncotarget. 2016. V. 7. № 37. P. 59519–59534.
98. Hadjiolova K.V., Nicoloso M., Mazan S., Hadjiolov A.A., Bachellerie J.P. // Eur. J. Biochem. 1993. V. 212 № 1. P. 211–215.
99. Gerbi SA, Borovjagin AV. Pre-Ribosomal RNA Processing in Multicellular Organisms. Madame Curie Bioscience Database. Austin, TX: Landes Bioscience, 2000–2013.
100. Belin S., Beghin A., Solano-Gonzàlez E., Bezin L., Brunet-Manquat S., Textoris J., Prats A.C., Mertani H.C., Dumontet C., Diaz J.J. // PLoS One. 2009. V. 4. № 9. P. 7147.
101. Coleman A.W. // Trends Genet. 2015. V. 31. № 3. P. 157–163.
102. Sun Q., Zhu X., Qi J., An W., Lan P., Tan D., Chen R., Wang B., Zheng S., Zhang C., et al. // Elife. 2017. V. 6. e22086.
103. Cheng J., Kellner N., Berninghausen O., Hurt E., Beckmann R. // Nat. Struct. Mol. Biol. 2017. V. 24. № 11. P. 954–964.
104. Dutca L.M., Gallagher J.E.G., Baserga S.J. // Nucleic Acids Res. 2011. V. 39. № 12. P. 5164–5180.
105. Puchta O., Cseke B., Czaja H., Tollervey D., Sanguinetti G., Kudla G. // Science. 2016. V. 352. № 6287. P. 840–844.
106. Beltrame M., Henry Y., Tollervey D. // Nucleic Acids Res. 1994. V. 22. № 20. P. 5139–5147.
107. Marmier-Gourrier N., Cléry A., Schlotter F., Senty-Ségault V., Branlant C. // Nucleic Acids Res. 2011. V. 39. № 22. P. 9731–9745.
108. Barandun J., Hunziker M., Klinge S. // Curr. Opin Struct. Biol. 2018. V. 49. P. 85–-93.

109. Rout M.P., Field M.C. // Annu. Rev. Biochem. 2017. V. 86. P. 637–657.
110. Zhu J., Liu X., Anjos M., Correll C.C., Johnson A.W. // Mol. Cell. Biol. 2016. V. 36. № 6. P. 965–978.
111. Sardana R., Liu X., Granneman S., Zhu J., Gill M., Papoulas O., Marcotte E.M., Tollervey D., Correll C.C., Johnson A.W. // PLoS Biol. 2015. V. 13. № 2. e1002083.
112. Hierlmeier T., Merl J., Sauert M., Perez-Fernandez J., Schultz P., Bruckmann A., Hamperl S., Ohmayer U., Rachel R., Jacob A., et al. // Nucleic Acids Res. 2013. V. 41. № 2. P. 1191–1210.
113. De La Cruz J., Karbstein K., Woolford J.L. // Annu. Rev. Biochem. 2015. V. 84. P. 93–129.
114. Krogan N.J., Peng W.T., Cagney G., Robinson M.D., Haw R., Zhong G., Guo X., Zhang X., Canadien V., Richards D.P., et al. // Mol. Cell. 2004. V. 13. № 2. P. 225–239.
115. McCann K.L., Charette J.M., Vincent N.G., Baserga S.J. // Genes Dev. 2015. V. 29. № 8. P. 862–875.
116. Ferreira-Cerca S., Pöll G., Gleizes P.E., Tschochner H., Milkereit P. // Mol. Cell. 2005. V. 20. № 2. P. 263–275.
117. Shi Z., Fujii K., Kovary K.M., Genuth N.R., Röst H.L., Teruel M.N., Barna M. // Mol. Cell. 2017. V. 67. № 1. P. 71–83.
119. Chaker-Margot M., Hunziker M., Barandun J., Dill B.D., Klinge S. // Nat. Struct. Mol. Biol. 2015. V. 22. № 11. P. 920–923.
119. Hunziker M., Barandun J., Petfalski E., Tan D., Delan-Forino C., Molloy K.R., Kim K.H., Dunn-Davies H., Shi Y., Chaker-Margot M., et al. // Nat. Commun. 2016. V. 7. № 12090. P. 1–10.
120. Cheng J., Lau B., La Venuta G., Ameismeier M., Berninghausen O., Hurt E., Beckmann R. // Science. 2020. V. 369. № 6509. P. 1470–1476.
121. Hutten S., Kehlenbach R.H. // Trends Cell Biol. 2007. V. 17. № 4. P. 193–201.
122. Moriggi G., Nieto B., Dosil M. // PLoS Genet. 2014. V. 10. № 12. e1004836.
123. Nieto B., Gaspar S.G., Moriggi G., Pestov D.G., Bustelo X.R., Dosil M. // Nat. Commun. 2020. V. 11. № 1. P. 156.
124. Nerurkar P., Altvater M., Gerhardy S., Schütz S., Fischer U., Weirich C., Panse V.G. // Int. Rev. Cell Mol. Biol. 2015. V. 319. P. 107–140.
125. Strunk B.S., Loucks C.R., Su M., Vashisth H., Cheng S., Schilling J., Brooks C.L., Karbstein K., Skiniotis G. // Science. 2011. V. 333. № 6048. P. 1449–1453.
126. Larburu N., Montellese C., O'Donohue M.F., Kutay U., Gleizes P.E., Plisson-Chastang C. // Nucleic Acids Res. 2016. V. 44. № 17. P. 8465–8478.
127. Johnson M.C., Ghalei H., Doxtader K.A., Karbstein K., Stroupe M.E. // Structure. 2017. V. 25. № 2. P. 329–340.
128. Schäfer T., Maco B., Petfalski E., Tollervey D., Böttcher B., Aebi U., Hurt E. // Nature. 2006. V. 441. № 7093. P. 651–655.
129. Ghalei H., Schaub F.X., Doherty J.R., Noguchi Y., Roush W.R., Cleveland J.L., Elizabeth M., Karbstein K. // J. Cell Biol. 2015. V. 208. № 6. P. 745–759.
130. Mitterer V., Gantenbein N., Birner-Gruenberger R., Murat G., Bergler H., Kressler D., Pertschy B. // Sci. Rep. 2016. V. 6. № 1. P. 1–11.
131. Scaiola A., Peña C., Weisser M., Böhringer D., Leibundgut M., Klingauf-Nerurkar P., Gerhardy S., Panse V.G., Ban N. // EMBO J. 2018. V. 37. № 7. e98499.
132. Turowski T.W., Lebaron S., Zhang E., Peil L., Dudnakova T., Petfalski E., Granneman S., Rappsilber J., Tollervey D. // Nucleic Acids Res. 2014. V. 42. № 19. P. 12189–12199.
133. Strunk B.S., Novak M.N., Young C.L., Karbstein K. // Cell. 2012. V. 150. № 1. P. 111–121.
134. Ferreira-Cerca S., Kiburu I., Thomson E., Laronde N., Hurt E. // Nucleic Acids Res. 2014. V. 42. № 13. P. 8635–8647.
135. Belhabich-Baumas K., Joret C., Jády B.E., Plisson-Chastang C., Shayan R., Klopp C., Henras A.K., Henry Y., Mougin A. // Nucleic Acids Res. 2017. V. 45. № 18. P. 10824–10836.
136. Ghalei H., Trepreau J., Collins J.C., Bhaskaran H., Strunk B.S., Karbstein K. // Mol. Cell. 2017. V. 67. № 6. P. 990–1000.
137. Plassart L., Shayan R., Montellese C., Rinaldi D., Larburu N., Pichereaux C., Lebaron S., O'donohue M.-F., Kutay U., Marcoux J., et al. // eLife. 2021. V. 10. e61254.
138. Sleeman J.E. // Philos. Trans. A. Math. Phys. Eng. Sci. 2004. V. 362. № 1825. P. 2775–2793.

Chemiluminescence Detection in the Study of Free-Radical Reactions. Part 2. Luminescent Additives That Increase the Chemiluminescence Quantum Yield

L. A. Romodin*
The A. I. Burnazyan Federal Medical Biophysical Center of the Federal Medical Biological Agency of Russia, Moscow, 123098 Russia
*E-mail: rla2904@mail.ru
Received March 3, 2020; in final form, June 11, 2020
DOI: 10.32607/actanaturae.11427

ABSTRACT **The present review examines the use of chemiluminescence detection to evaluate the course of free radical reactions in biological model systems. The application of the method is analyzed by using luminescent additives that enhance the luminescence thanks to a triplet–singlet transfer of the electron excitation energy from radical reaction products and its emission in the form of light with a high quantum yield; these additives are called chemiluminescence enhancers or activators. Examples of these substances are provided; differences between the so-called chemical and physical enhancers are described; coumarin derivatives, as the most promising chemiluminescence enhancers for studying lipid peroxidation, are considered in detail. The main problems related to the use of coumarin derivatives are defined, and possible ways of solving these problems are presented. Intrinsic chemiluminescence and the mechanism of luminescence accompanying biomolecule peroxidation are discussed in the first part of the review.**
KEYWORDS **free radical reactions, apoptosis, ferroptosis, chemiluminescence, lipid peroxidation, reactive oxygen species, chemiluminescence enhancers, coumarin derivatives.**
ABBREVIATIONS **DTMC – 7-(4,6-dichloro-1,3,5-triazinylamino)-4-methylcoumarin; C-314 – coumarin-314 – quinolizidine[5,6,7-*gh*]3-ethoxycarbonylcoumarin; C-334 – coumarin-334 – quinolizidine[5,6,7-*gh*]3-acetylcoumarin; C-525 – coumarin-525 – quinolizidine[5,6,7-*gh*]3,2'-benzimidazolylcoumarin; EES – electronically excited state; ROS – reactive oxygen species; EEE – electronic excitation energy.**

INTRODUCTION

Due to the extremely low intensity of intrinsic chemiluminescence, the mechanisms of which are described in the first part of the review [1], it is quite difficult to detect. In addition, it is often necessary to study reactions that include the formation and participation of specific radicals such as lipid peroxidation processes; i.e., to evaluate the presence of lipid radicals in the system under study. However, the method used to detect intrinsic chemiluminescence is nonspecific.

In order to increase the chemiluminescence intensity, specific substances that enhance it are added to the system. These substances are called chemiluminescence enhancers or activators. A subgroup of these substances is called chemiluminescent probes. However, this term is often used randomly. From the chemical point of view, the correct terms would be a chemiluminescent reagent and luminescent additive. The ambiguity of the term activator has to do with the fact that it is generally interpreted as the ability of a particular compound to interact chemically, while the specific meaning of the word is the active part of a concentration. The monograph [2] presents a short list of terms related to the topic of chemiluminescence. This list contains the term initiator, which is considered "a chemically active substance that creates primary active centers and thereby increases the rate of the reaction that provides active products and changes the quantum yield of excitation." The term activator may also fall under this definition. It should be noted that luminescent additives in biological systems come in aqueous solution with a pH of ~7, where they can exhibit low solubility. leading to their aggregation. The interaction of phagocytes with additive microparticles activates the production of reactive oxygen species (ROS) [3, 4]; thus, the term activator

can be used in this system in relation to the additives under discussion.

The term activator can be used when describing systems with chemically initiated electron-exchange luminescence: e.g., chemiluminescence of oxalate esters [5]. Introduction of a fluorophore with a low ionization potential to the system leads to electron transfer from this compound to the intermediate. This is followed by reverse electron transfer, leading to fluorophore excitation, which then becomes a chemiluminescence emitter. However, a luminescent additive is most often called an activator. The definition of the latter in that case is a compound that has a high quantum yield of emission and enhances luminescence owing to physical migration of the energy of the electronically excited state (EES) without a change in the excitation quantum yields of radical reaction products and the reaction speed [2, 6, 7].

The increase in luminescence in the presence of these substances is the result of electronic excitation energy (EEE) migration from the reaction products to the additive, which (or its product of interaction with the radical reaction product, i.e. the excitation donor) is a more efficient light emitter than the excited donor compound. In 1963, R.F. Vasil'ev studied the mechanism of chemiluminescence enhancement upon addition of anthracene derivatives to the ketone products of free radical oxidation of hydrocarbon substrates in the triplet EES [8]. The resulting excited molecules of anthracene derivatives were not in the triplet but singlet EES. Thus, a fundamental photophysical process that is widely used to enhance luminescence in chemiluminescent systems, namely physical enhancement of chemiluminescence as a result of a triplet–singlet energy transfer in the liquid phase, was studied in detail [8]. It should be noted that chemiluminescence enhancement in the presence of anthracene derivatives had been demonstrated a year earlier [9]. However, the enhancement mechanism had not been elucidated, yet. An analysis of the action of anthracene and its derivatives showed that anthracene itself is less effective than its halogenated derivatives: in particular 9,10-dibromoanthracene [9–11]. The corresponding value of the exclusion coefficient of the triplet–singlet transition, which is calculated as the ratio of the reaction rate constant to the diffusion rate constant, is 10^{-2} [11].

Chemiluminescence enhancement can be schematically represented as follows:

$P^* \xrightarrow{k_1} P + h\nu$ (non-activated chemiluminescence with a quantum yield of Q_{lum1}).

P^* + enhancer (activator) $\rightarrow P$ + enhancer$^* \xrightarrow{k_{3enh}}$
$\xrightarrow{k_{3enh}} P$ + enhancer + $h\nu$. (1)

This is activated chemiluminescence with a quantum yield of Q_{lum2}. Note that $Q_{lum1} << Q_{lum2}$.

An important chemiluminescence enhancer characteristic is not only the chemiluminescence quantum yield value, but also the same value multiplied by the molar extinction coefficient of the given compound, since this multiplication is directly proportional to the luminescence intensity [12].

R.F. Vassil'ev and V.A. Belyakov provided the basis for our understanding of the triplet–triplet and triplet–singlet EES energy transfer for the quantitative study of chemiluminescent reactions [11]. In particular, the relationship between the rates of EEE migration from the radical reaction product (EEE donor), EEE acceptor (chemiluminescence enhancer) concentration (let us denote it by A), and chemiluminescence intensity in the absence (J_0) and presence (J) of the excitation acceptor has been determined:

$$\frac{1}{\frac{J}{J_0}-1} = \frac{1}{\frac{Q_{LumEnh}\cdot k_{TS}}{Q_{LumPr}\cdot\left(k_{TT}+k_{TS}\right)}-1} + \frac{1}{\frac{Q_{LumEnh}\cdot k_{TS}}{Q_{LumPr}\cdot\left(k_{TT}+k_{TS}\right)}-1}\cdot\frac{1}{\left(k_{TT}+k_{TS}\right)\cdot t_{P^*}\cdot A}, \quad (2)$$

where Q_{LumEnh} is the quantum yield of the luminescence enhancer (EEE acceptor), Q_{LumPr} is the quantum yield of the excited product of the radical reaction (EEE donor), t_{P^*} – average donor excitation lifetime in the absence of EEE acceptor, k_{TT} is the rate constant of the triplet–triplet EEE transfer (chemiluminescence quenching), and k_{TS} is the rate constant of the triplet–singlet EEE transfer to the acceptor molecule. The rate constant of the triplet–triplet transfer, which does not result in luminescence, is higher than that of the triplet–singlet transfer [11]. The non-emissive triplet–triplet energy transfer is more pronounced in 1,2-dioxetanone decomposition than in the case of 1,2-dioxetane, which determines the lower emission efficiency of the activated decomposition of dioxetanone compared to that of dioxetane [13].

However, different chemiluminescence enhancers have different mechanisms of receiving the EEE from the radical reaction products. There are two groups of chemiluminescence enhancers. There is some ambiguity in their terminology that should be mentioned. Luminescent additives of the first group react chemically with the participants and products of a free radical reaction and result in the EES, with a quantum yield much higher than that of intrinsic chemiluminescence. According to the terminology proposed by A.I. Zhuravlyov [2], these substances are called chemiluminescent probes. Yu.A. Vladimirov calls these

substances chemical activators of chemiluminescence [6]. From the chemical point of view, a chemiluminescent reagent would be a better term for these substances, since they substitute the reaction pathways of ROS, resulting in ultra-weak chemiluminescence under natural conditions, with other pathways leading to higher chemiluminescence. Substances of the second group of luminescent additives generate the EES without interacting chemically with the system components. Representatives of the Yu.A. Vladimirov scientific school [6, 14–16] call these substances physical activators of chemiluminescence, thus extending the term activator to both groups of chemiluminescent reagents. The authors of [2] use the term activator to designate physical chemiluminescence activators only.

However, it is important to note that the above classification is largely theoretical: most luminescent additives cannot be clearly assigned to a specific group. This is because the chemiluminescence mechanism for most of them is not fully understood. The simple fact of an increase in the intensity of detected chemiluminescence in response to introduction of an additive does not allow one to classify this additive as either a chemical or physical activator.

We should mention that chemiluminescence enhancers were divided into two groups in one of the first studies involving them [10]. Activators were characterized as either bad activators, those without chemical stability and capable of quenching luminescence at high concentrations, or good activators, those with chemical stability and a chemiluminescence enhancement coefficient that increases monotonically with an increase in concentration (see the formula for calculating the luminescence enhancement coefficient in [10]).

EXAMPLES OF SUBSTANCES THAT ENHANCE CHEMILUMINESCENCE

The phenomenon of chemiluminescence enhancement was first observed upon using anthracene derivatives [8–10]. Later, dibromoanthracene, which is a physical chemiluminescence enhancer, was used to study the decomposition of polymers during their oxidation by a peroxide compound [17]; dibromoanthracene and 9,10-diphenylanthracene were utilized to explore the chemiluminescence of a ascorbate- and hemoglobin-dependent brain [18]. Anthracene was used to study dioxetane and dioxetanone decomposition accompanied by EES generation [13].

Luminol (5-amino-2,3-dihydro-1,4-phthalazinedione) is the most common chemiluminescent reagent [19–28]. In the first half of the 20th century, luminol was known as a substance that could generate chemiluminescence upon oxidation [29]. Luminol was first used as a chemiluminescence activator in the biological system by R.C. Allen *et al.* when studying the immune response of polymorphonuclear leukocytes in 1972 [30].

The mechanism of luminescence generated by luminol oxidation involves the formation of 4-hydroperoxy-1-oxy-5-aminophthalazin-4-olate, a hydroperoxide product of luminol interaction with ROS [31], chloramines in the case of hydrogen peroxide [32], and oxidized peroxidase forms at certain stages of the peroxidase catalytic cycle [6]. This compound is then naturally converted to 2,3-peroxydi[hydroxymethyleneyl]phenylamine containing an endoperoxide moiety that is eventually cleaved to form a EES hydroaminophthalate ion. This ion emits a photon when returning to its ground state (the mechanism of luminol interaction with various substances is described in detail in [6, 31, 33, 34]). Aside from luminol, isoluminol, which activates luminescence through a similar mechanism, is sometimes used [35–37].

Luminol is utilized to evaluate total antioxidant activity based on its reaction with 2,2'-azobis(2-amidinopropane) [38, 39] and in various chemiluminescent methods for hydrogen peroxide detection (see review [40]). Some techniques use several substances as chemiluminescent reagents at once. For instance, addition of fluorescein to the system increases the chemiluminescence intensity in the presence of luminol [41]. An increase in luminescence intensity upon addition of some phenols to the horseradish peroxidase–H_2O_2–luminol system was also reported [42]. At the same time, so-called non-enhancer phenols inhibit chemiluminescence in the horseradish peroxidase–H_2O_2–luminol–4-iodophenol system [43]. These phenols, except for 4-iodophenol, compete with each other as luminol substrates. Luminol remains the most often used substance to determine the immune reactivity of leukocytes [37, 44, 45]; it is also utilized to study lipid peroxidase reactions [24]. The widespread use of luminol is due to the high quantum yield of its luminescence. However, the chemiluminescence enhanced by luminol is nonspecific. Therefore, it is impossible to determine exactly what free radical reactions – and in what proportions – take place in the sample when using laminol.

There are even more specific chemiluminescent reagents, such as the luciferin–luciferase system [46] (luciferase can also have other substrates bedsides luciferin [46]). It is utilized to detect ATP molecules [47]. This system can be also used to solve a large number of other tasks.

Another specific chemical chemiluminescent reagent is coelenterazine (2-(4-hydroxybenzyl)-6-(4-

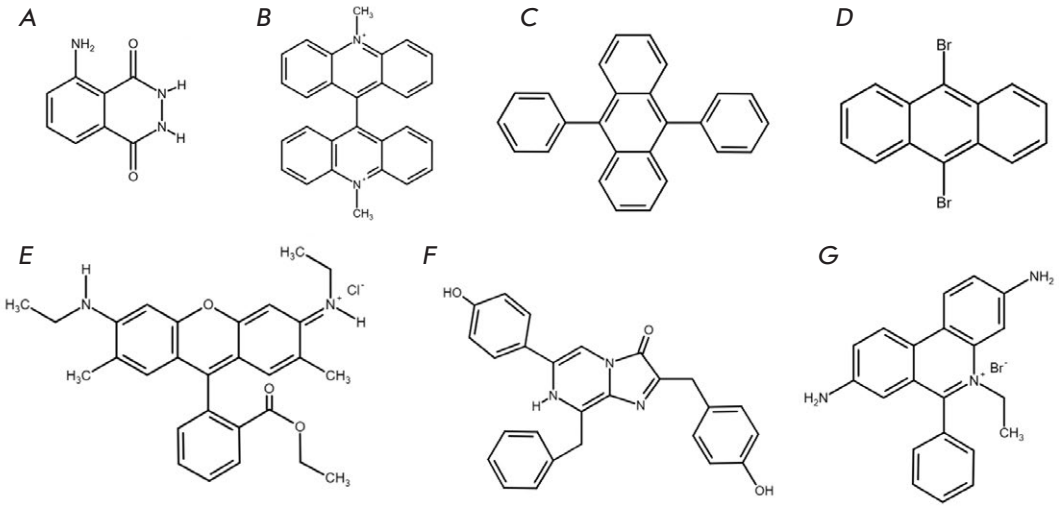

Fig. 1. Structural formulas of the substances used as chemical enhancers (activators) of chemiluminescence: luminol (*A*), lucigenin (*B*), 9,10-diphenylanthracene (*C*), 9,10-dibromanthracene (*D*), rhodamine 6G (*E*), coelenterazine (*F*), and ethidium bromide (*G*)

hydrophenol)-8-benzyl-3,7-dihydroimidazo[1,2-alpha] pyrazine-3-one), which is used to evaluate the level of the superoxide radical $O_2^{\cdot-}$.

Lucigenin is one of the most frequently used reagents to detect the superoxide radical [6, 48]. It can also be applied to the study of xanthine and hypoxanthine oxidation by xanthine oxidase [49] to detect the superoxide radical formed as the result of NADPH oxidase activity [49–52] and in ether mitochondria of intact cells [53] or an isolated mitochondrial suspension [54, 55]. Lucigenin-based techniques have recently been developed to detect dopamine [56] and glutathione [57]. In both cases, lucigenin was part of a relatively complex test system (the hypothetical mechanisms of lucigenin-dependent chemiluminescence activation in various systems are discussed in detail in the review [6]).

Fluorescein, which has a high quantum yield of the triplet state [58], is also utilized as a chemiluminescent reagent in one of the hydrogen peroxide detection-based methods [40].

Deamination of amino acids during their oxidation by H_2O_2 in the presence of Fe^{2+} ions was studied with the use of ethidium bromide as a chemiluminescent reagent [59]. An increase in the ethidium bromide concentration up to 100 μM in the system under study was shown to be accompanied by a growth in luminescence intensity and its further drop at higher concentrations of ethidium bromide. Furthermore, 1 mM ethidium bromide significantly inhibited amino acid oxidation.

Despite the fact that chemiluminescent probes often cause a greater increase in luminescence, since they are directly involved in the processes occurring in the system under study, they are not suitable for fundamental research, including the study of lipid peroxidation processes. Physical enhancers of chemiluminescence that increase the luminescence quantum yield owing to the resonance transfer of the EEE of reaction products without chemically interacting with the reaction participants and products should be used in that case [60–62]. This approach is fully consistent with the principle of non-interference with the system under study.

Figure 1 presents the formulas of some of the substances used as luminescent reagents in a number of studies.

SEARCH FOR PHYSICAL ENHANCERS OF THE CHEMILUMINESCENCE ACCOMPANYING LIPID PEROXIDATION

The interaction of a chemiluminescent probe with components of the system under study presents a serious problem when using these probes in fundamental research. This is because the analyzed chemiluminescent signal is received not from the lipid substrate–peroxidase–hydrogen peroxide system but from the lipid substrate–peroxidase–hydrogen peroxide–chemiluminescence activator system. These data cannot be considered completely adequate for application to living organisms.

An important contribution to our understanding of the chemiluminescence enhancers used in free radical reactions involving lipids was made by V.S. Sharov. In the 1980s, the possibility of using various lanthanides to enhance chemiluminescence was studied. It was suggested that this process is based on intermolecular energy transfer from the products formed in free radical reactions of peroxides to the 4f shell of the lanthanide ion [63]. An example is the data presented in [64]; this led to the conclusion that Tb^{3+} ions can be used as a physical enhancer of chemiluminescence to

study lipid peroxidation reactions. Before that, europium complexed with tetracycline was shown to increase chemiluminescence intensity in lipid peroxidation [65]. However, lanthanide ions are not suitable for research in biological systems due to the following reasons. Chemiluminescence quenching was discovered as early as in the 1980s when using lanthanide ions in biological model systems. This was explained by the fact that lanthanide ions can easily form complexes with the buffer components, which often leads to the loss of their ability to enhance chemiluminescence [65].

In addition, the study of the mechanism of chemiluminescence enhanced by Eu^{3+} ions complexed with 2,2-dimethyl-6,6,7,7,8,8,8-heptafluoro-3,5-octanedione in the presence of dimethyldioxirane (a model organic peroxide) showed that the lanthanide complex reacts chemically with this organic peroxide. The NMR analysis of the resulting mixture and the photophysical characteristics of the isolated reaction product differed from those of the initial europium chelate. Similar results were also obtained for Eu^{3+} ion complexed with 2-thenoyltrifluoroacetone, 2,2,6,6-tetramethyl-3,5-heptanedione (dipivaloylmethane), and tris[3-(trifluoromethylhydroxymethylene)*d*-camphorate]; in the case of the complex with the latter compound in the excess of dimethyldioxirane, chemiluminescence not characteristic of the Eu^{3+} ion but due to an unknown emitter was observed [66].

Apparently, the chemiluminescence of lanthanide chelates can be a result of their interaction with organic peroxides [67]. This conclusion is supported by the assumption that the dioxirane intermediate plays a key role in chemiluminescence generation in the solid-phase reaction between potassium peroxymonosulfate and europium nitrate hexahydrate in the presence of acetone vapor, although the Eu^{3+} ion is the direct emitter [66, 67]. It should also be noted that the Nd^{3+} and Yb^{3+} ions act as chemiluminescence activators, similarly to Eu^{3+} ions in the decomposition of organic peroxides [66].

However, it is important to add that it is the complex of lanthanide ions, but not the ions emitting photons by receiving the EEE from the chelating agent, that is called the chemical activator [66, 67].

Therefore, when searching for an optimal chemiluminescence enhancer, it is necessary to use substances that can undergo triplet–singlet transitions with a high degree of probability. This is due to the fact that the products formed in the disproportionation of lipid peroxide radicals are in the triplet EES [11]. Despite the indicated disadvantages, the abovementioned lanthanide complexes have the required characteristic. This requirement is also met by low-molecular-weight organic substances containing conjugated cyclic groups. An example is the histological dye Nile blue, which is used as an enhancer of chemiluminescence accompanying Fe^{2+}-induced oxidation of lipids [68].

Rhodamine 6G, a xanthene family substance, was used as a physical chemiluminescence activator with a high quantum yield to study tetraoxane decomposition by Fe^{2+} inorganic salts (the comparison of the kinetic dependences of the activated and intrinsic chemiluminescence for the system is presented as evidence) [69]. Coumarin derivatives have similar properties. Such quinolizidine derivatives of coumarin as coumarin-314 (C-314), coumarin-334 (C-334), and coumarin-525 (C-525) act as chemiluminescence enhancers in lipid peroxidation reactions [16, 60–62, 70]. Because of the selective chemiluminescence enhancement caused by free radical reactions involving lipids, these substances are most suitable for studying lipid peroxidation processes.

Coumarin derivatives and their use in chemiluminescence detection

Coumarins are a group of organic compounds that includes unsaturated aromatic lactones: 5,6-benzo-α-pyrone (*cis*-ortho-hydroxycinnamic acid lactone) derivatives (coumarin or 5,6-benzo-pyran-2-one) [71]. Many members of this group are used as laser dyes [72]. Coumarin derivatives with a substitution at the 7th position (7-hydroxy-4-methylcoumarin and 7-amino-4-methylcoumarin are provided as an example) are effective fluorophores that emit in the visible region [12].

Studies using coumarin derivatives as indicators or part of an indicator system deserve special attention. The structural formulas of the coumarin derivatives used as chemiluminescence enhancers are shown in *Fig. 2*. The coumarin derivative obtained by condensing nitromethane with coumarinyl aldehyde can selectively detect specific cyanide anions [73]. Nucleophilic aromatic substitution of hydrogen with cyanide in the coumarin molecule changes its color and increases the fluorescence intensity (excitation wavelength 365 nm) to an extent that the fluorescence can be observed even with the naked eye. The detection limit is < 3 μM cyanide (dissolved in a acetonitrile medium): the coumarin group generates a bright blue fluorescent signal. The substances 6,7-dihydroxy-4-methyl-8-formylcoumarin and 3,4-benzo-7-hydroxy-8-formylcoumarin can also be used as chromogenic and fluorescent chemosensors to detect cyanide anions and Cu^{2+} cations [74]. DTMC (7-(4,6-dichloro-1,3,5-triazinyl-2-amino)-4-methylcoumarin) was proposed for the chemiluminescent determination of hydrogen per-

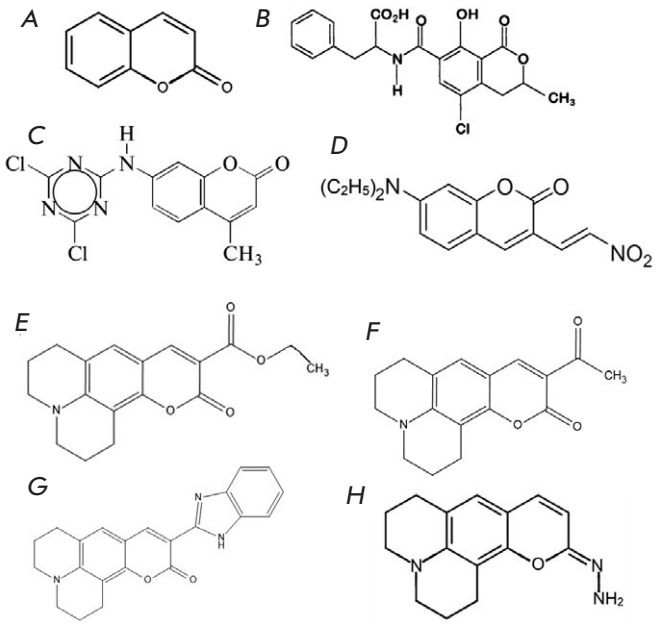

Fig. 2. Coumarin (*A*) and its derivatives: ochratoxin A (*B*), DTMC (*C*), 3-(2-nitrovinyl), 7-(diethylamino)coumarin (*D*), C-314 (*E*), C-334 (*F*), C-525 (*G*), and PFM4 (*H*)

oxide by the chemiluminescent method [75]. The detection limit for hydrogen peroxide is 4×10^{-8} mol/L. However, this method requires high pH values of the medium (11.4).

PFM (1-diethylaminobenzo[4,3-e]-pyran-2-hydrazone) was proposed for formaldehyde detection [76]. A year later, a more efficient fluorogenic substrate, PFM4, was proposed (*Fig. 2H*) [77]. PFM4 was used to successfully assess the accumulation of formaldehyde in the lysosomes of cells treated with endoplasmic reticulum stress inducers [77].

A 1995 study analyzed the effect of various enhancers on the intensity of the chemiluminescence generated in the Fe^{2+}-induced peroxidation of phospholipids in egg yolk liposomes. The C-525 dye (2,3,5,6-1H,4H-tetrahydro-9-(2'-benzimidazolyl)-quinolysin-(9,9a,1-GH)) showed the most potent effect: it increased the chemiluminescence intensity more than 2,000-fold without affecting the reaction kinetics at a concentration of 4 μM [62]. The mechanism of luminescence enhancement in this case is, apparently, the energy transfer from the ketone molecule in the EES (the primary product of peroxyl radical recombination) to a fluorescent level of C-525 [60]. Meanwhile, it should be taken into account that C-525 contains a purine group, whose interaction with free radicals under certain conditions triggers an antioxidant action of the substance [78]. The specific chemiluminescence activator of the superoxide radicals 2-methyl-6-[*p*-methoxyphenyl]-3,7-dihydroimidazo[1,2-a]pyrazine-3-one has a similar disadvantage [79, 80].

However, despite its structure, C-525 is quite often used as a chemiluminescence activator; e.g., when detecting lipid hydroperoxides in the lipid substrate–Fe^{2+} system [16]. Experiments in a similar system based on C-334 showed that the chemiluminescence of the system containing cytochrome *c* complexed with cardiolipin is due to the lipoperoxidase and quasi-lipoxygenase activity of this nanoparticle, but not to the activity of non-heme iron via the Fenton reaction [81].

The studies of the EES of coumarin derivatives should also be mentioned. Detection of photogeneration of C-314 radical cations by using nanosecond laser excitation at wavelengths > 400 nm in benzene, acetonitrile, and dichloromethane made it possible to detect the triplet EES of C-314 with maximum absorption at 550 nm and a lifetime of 90 μs in benzene, which is easily quenched by oxygen [82]. No excited state was detected in an aqueous solution; however, relatively long-lived (160 μs in air-equilibrated solutions) free C-314 radical cations with maximum absorbance at 370 nm were identified. In addition, these free C-314 radical cations are quenched by phenolic antioxidants; the rate constant for this reaction is $> 10^9$ $M^{-1}s^{-1}$ [82]. According to [82], this reaction is based on the mechanism of electron transfer between the phenolic antioxidant and C-314 radical cation with potential ionic pair formation.

A study of C-314 solvation in an aqueous solution in the presence of a surfactant [83] revealed two well-differentiated interfacial phases (water/air). The author of the review showed that C-314, C-334, and C-525 do not dissolve in water at concentrations > 50 μM; the optimal concentration range for a coumarin derivative in the system is 20–25 μM. According to [83], surfactant addition promotes C-314 solvation. Two different positions of C-314 molecules relative to the surfactant spatial domains were revealed; they were due to large fluctuations in the surfactant concentration taking place in a small coverage area commonly called the two-dimensional gas–liquid coexistence region [83].

The mechanisms of action of various antioxidants such as β-carotene, tocopherol, rutin, and ascorbate in suppressing the lipid peroxidation triggered by free Fe^{2+} ions were studied using C-525-induced chemiluminescence [84]. The physicochemical properties of low-density plasma lipoproteins were elucidated by using the method of enhanced C-525 chemiluminescence. An increase in the amplitude of the fast luminescent flash was shown for oxidized lipoproteins in a

Fe^{2+}-containing solution [61]. Free-radical oxidation of cardiolipin complexed with cytochrome *c* was studied by detecting C-525-enhanced chemiluminescence [70].

Of special interest are the results obtained when comparing coumarin C-525 and chlorophyll-α as chemiluminescence enhancers [72]. The luminescence quantum yield was much higher in the case of C-525. A 2- to 3-fold increase in chemiluminescence accompanying the tert-butyl hydroperoxide-induced oxidation of microsomes from rat liver and peroxidation of liposomal lipids was observed. Coumarin derivatives activate chemiluminescence owing to the energy transfer from carbonyls in the triplet EES formed in the peroxide radical reaction through the Russell mechanism and dioxetane decomposition.

A very significant disadvantage of quinolizidine derivatives of coumarin should be mentioned: C-525 loses its ability to luminesce in the blood serum [55]. This is considered to be due to the binding of C-525 to serum albumins.

It has been repeatedly reported that C-314, C-334, and C-525 are fluorogenic substrates that do not react with mixture components [16, 60–62, 70]. Although these data were obtained in a non-enzymatic lipid peroxidation system [62], they were automatically projected on systems where this process is triggered by peroxidase. This was so despite the report by V.S. Sharov *et al.* in 1996 showing that C-525 is unsuitable for studying lipid peroxidation catalyzed by horseradish peroxidase due to the C-525 instability in this system [72].

The data indicating that quinolizidine derivatives of coumarin serve as substrates in the peroxidase reaction were confirmed in [85, 86], which showed a statistically significant decrease in the concentration of C-314, C-334, and C-525 during the peroxidase reaction catalyzed by cytochrome *c* complexed with cardiolipin. A decrease in the concentration of coumarin derivatives in enzymatic lipid peroxidation reduces the chemiluminescence intensity, which can lead to erroneous data interpretation: a researcher can draw a wrong conclusion about a decrease in lipid peroxidation intensity. For instance, in the case of the study of antioxidants, such a false interpretation could lead to an erroneous conclusion about an affective suppression of lipid peroxidation by the test substance. In order to avoid this trap, one should multiply the intensity values recorded by the chemiluminometer by correction factors for a decrease in the concentration of coumarin derivatives for the corresponding time points, from the beginning of the reaction when conducting an experiment on measuring the coumarin-enhanced chemiluminescence accompanying lipid peroxidation. These coefficients should be calculated using a mathematical function inverse to the decreasing function of the proportion of the concentration of coumarin derivatives, depending on the reaction time.

One should also make certain that the reaction between a coumarin derivative and peroxidase is not accompanied by luminescence. Otherwise, it is also necessary to add additional coefficients to the formula for calculating the correction factors that balance the contribution to the luminescence values recorded by the device due to the reaction between the chemiluminescence enhancer and peroxidase, not related to the luminescence accompanying lipid peroxidation.

Correction of the chemiluminescence curves obtained using the discussed correction functions allows one to return them to the form they would have had in the case of a constant concentration of the chemiluminescence enhancer in the system. Thus, it becomes possible to adequately assess enzymatic lipid peroxidation reactions in the test sample. ●

The author of this review would like to thank N.P. Lysenko, Professor of the Department of Radiobiology and Biophysics n.a. A.D. Belov of K.I. Skryabin Moscow State Academy of Veterinary Medicine and Biotechnology, for help in preparing the English version of the article and Yu.A. Vladimirov, Head of the Department of Medical Biophysics, Faculty of Fundamental Medicine of M.V. Lomonosov Moscow State University, and Academician of the Russian Academy of Sciences, for information on chemiluminescence activation mechanisms and recommendations regarding scientific literature analysis.

REFERENCES

1. Romodin L.A. // ActaNaturae. 2021. V. 13. № 3(50). P. 90–100.
2. Zhuravlyov A.I., Zubkova S.M. Antioxidants. Free radical pathology, aging. Second edition, revised and enlarged. Moscow: White Alves, 2014. 304 p.
3. Piryazev A.P., Azizova O.A., Aseichev A.V., Dudnik L.B., Sergienko V.I. // Bull. Exp. Biol. Med. 2013. V. 156. № 1. P. 101–103.
4. Meier B., Radeke H.H., Selle S., Habermehl G.G., Resch K., Sies H. // Biol. Chem. Hoppe-Seyler. 1990. V. 371. № 10. P. 1021–1025.
5. Bryant P.D., Capomacchia A.C. // J. Pharm. Biomed. Analysis. 1991. V. 9. № 10–12. P. 855–860.

6. Vladimirov Yu.A., Proskurnina E.V. // Advances in biological chemistry. 2009. V. 49. P. 341–388.
7. Bajmatov V.N., Farhutdinov R.R., Bagautdinov A.M. Chemiluminescent methods for the study of free radical oxidation in agriculture, veterinary medicine and animal husbandry. Ufa: Publishing House "Health of Bashkortostan", 2009. 104 p.
8. Vassil'ev R.F. // Nature. 1963. V. 200. № 4908. P. 773–774.
9. Vassil'ev R.F. // Nature. 1962. V. 196. № 4855. P. 668–669.
10. Vasil'ev R.F., Vichutinskij A.A., Cherkasov A.S. // Doklady Akademii nauk of the USSR. 1963. V. 149. № 1. P. 124–127.
11. Belyakov V.A., Vassil'ev R.F. // Photochem. Photobiol. 1970. V. 11. № 3. P. 179–192.
12. Martynov V.I., Pahomov A.A., Popova N.V., Deev I.E., Petrenko A.G. // ActaNaturae. 2016. V. 8. № 4(31). P. 33–46.
13. Augusto F.A., Frances-Monerris A., Fdez Galvan I., Roca-Sanjuan D., Bastos E.L., Baader W.J., Lindh R. // Physical Chemistry Chemical Physics: PCCP. 2017. V. 19. № 5. P. 3955–3962.
14. Vladimirov Yu.A., Potapenko A.Ya. Physico-chemical foundations of photobiological processes: a textbook for medical and biological specialists universities. Moscow: High School, 1989. 199 p.
15. Vladimirov Yu.A., Proskurnina E.V., Izmajlov D.Yu. // Bull. Exp. Biol. Med. 2007. V. 144. № 3. P. 390–396
16. Volkova P.O., Alekseev A.V., Dzhatdoeva A.A., Proskurnina E.V., Vladimirov Yu.A. // MSU Bulletin, Series 2: Chemistry. 2016. V. 57. № 1. P. 41–52.
17. Phillips D., Anissimov V., Karpukhin O., Shlyapintokh V. // Photochem. Photobiol. 1969. V. 9. № 2. P. 183–187.
18. Prat A.G., Turrens J.F. // Free Radical Biol. Med. 1990. V. 8. № 4. P. 319–325.
19. Zhao C., Cui H., Duan J., Zhang S., Lv J. // Analyt. Chem. 2018. V. 90. № 3. P. 2201–2209.
20. Zhang A., Guo W., Ke H., Zhang X., Zhang H., Huang C., Yang D., Jia N., Cui D. // Biosensors Bioelectronics. 2018. V. 101. P. 219–226.
21. Saqib M., Qi L., Hui P., Nsabimana A., Halawa M.I., Zhang W., Xu G. // Biosensors Bioelectronics. 2018. V. 99. P. 519–524.
22. Mayer M., Takegami S., Neumeier M., Rink S., Jacobi von Wangelin A., Schulte S., Vollmer M., Griesbeck A.G., Duerkop A., Baeumner A.J. // Angewandte Chemie. 2018. V. 57. № 2. P. 408–411.
23. Li F., Ma W., Liu J., Wu X., Wang Y., He J. // Analyt. Bioanalyt. Chem. 2018. V. 410. № 2. P. 543–552.
24. Vladimirov Yu.A., Proskurnina E.V., Dyomin E.M., Matveeva N.S., Lyubickij O.B., Novikov A.A., Izmajlov D.Yu., Osipov A.N., Tihonov V.P., Kagan V.E. // Biochemistry (Moscow). 2009. V. 74. № 3. P. 372–379.
25. Dyomin E.M., Proskurnina E.V., Vladimirov Yu.A. // Moscow University Bulletin. Series 2: Chemistry. 2008. V. 49. № 5. P. 354–360.
26. Mostafa I.M., Halawa M.I., Chen Y., Abdussalam A., Guan Y., Xu G. // Analyst. 2020. V. 145. №7. P. 2709–2715.
27. Habibullin R.R., Fedosov A.V. // Bashkir chemistry journal. 2006. V. 13(2). P. 106–107.
28. Zhang X., Zhang H., Xu S., Sun Y. // Analyst. 2014. V. 139. № 1. P. 133–137.
29. Huntress E., Stanley L., Parker A. // J. Am. Chem. Soc. 1934. V. 56. № 1. P. 241–242.
30. Allen R.C., Stjernholm R.L., Steele R.H. // Biochem. Biophys. Res. Commun. 1972. V. 47. № 4. P. 679–684.
31. Roshchupkin D.I., Belakina N.S., Murina M.A. // Biophysics. 2006. V. 51. № 1. P. 99–107.
32. Murina M.A., Belakina N.S., Roshchupkin D.I. // Biophysics. 2004. V. 49. № 6. P. 1099–1105.
33. Arnhold J., Mueller S., Arnold K., Sonntag K. // J. Biolumin. Chemilumin. 1993. V. 8. № 6. P. 307–313.
34. Mueller S., Arnhold J. // J. Biolumin. Chemilumin. 1995. V. 10. № 4. P. 229–237.
35. Proskurnina E.V., Dzhatdoeva A.A., Lobichenko E.N., Shalina R.I., Vladimirov Yu.A. // Journal of Analytical Chemistry. 2017. V. 72. № 7. P. 639–644.
36. Ji X., Wang W., Li X., Chen Y., Ding C. // Talanta. 2016. V. 150. P. 666–670.
37. Dahlgren C., Bjornsdottir H., Sundqvist M., Christenson K., Bylund J. // Meth. Mol. Biol. 2020. V. 2087. P. 301–324.
38. Seliverstova E.Yu., Sazykin I.S., Hmelevcova L.E., Majorov E.L. // Journal of Health and Life Sciences. 2014. №4. P. 26–34.
39.Vladimirov Yu.A., Proskurnina E.V., Izmajlov D.Yu. // Biophysics. 2011. V. 56. № 6. P. 1081–1090.
40. Caplev Yu.B. // Journal of Analytical Chemistry. 2012. V. 67. № 6. P. 564–572.
41. Navas Diaz A., Gonzalez Garcia J.A., Lovillo J. // J. Biolumin. Chemilumin. 1997. V. 12. № 4. P. 199–205.
42. Hodgson M., Jones P. // J. Biolumin. Chemilumin. 1989. V. 3. № 1. P. 21–25.
43. Candy T.E., Jones P. // J. Biolumin. Chemilumin. 1991. V. 6. № 4. P. 239–243.
44. Torabi R., Ghourchian H. // Sci. Repts. 2020. V. 10. № 1. P. P. 594.
45. Chen M.S., Lu P.K., Lin W.C., Shin H.C., Sie S.R., Sheu S.M. // Lipids. 2020. V. 55. № 1. P. 45–52.
46. Lee J., Muller F., Visser A. // Photochem. Photobiol. 2019. V. 95. № 3. P. 679–704.47.
47. Dubyak G.R. // Meth. Enzymol. 2019. V. 629. P. 81–102.
48. Greenlee L., Fridovich I., Handler P. // Biochemistry. 1962. V. 1. P. 779–783.
49. Storch J., Ferber E. // Analyt. Biochem. 1988. V. 169. № 2. P. 262–267.
50. Bhunia A.K., Han H., Snowden A., Chatterjee S. // J. Biol. Chem. 1997. V. 272. № 25. P. 15642–15649.
51. Irani K., Xia Y., Zweier J.L., Sollott S.J., Der C.J., Fearon E.R., Sundaresan M., Finkel T., Goldschmidt-Clermont P.J. // Science. 1997. V. 275. № 5306. P. 1649–1652.
52. Allen R.C. // Meth. Enzymol. 1986. V. 133. P. 449–493.
53.Rembish S.J., Trush M.A. // Free Rad. Biol. Med. 1994. V. 17. № 2. P. 117–126.
54. Dzhatdoeva A.A., Polimova A.M., Proskurnina E.V., Vladimirov Yu.A. // Bulletin of Russian State Medical University. 2016. №1. P. 49–55.
55. Matveeva N.S. Activated chemiluminescence as a method for studying free radical reactions in cells and tissues. Dissertation for the degree of Candidate of Sciences in Biological Sciences, Biophysics specialty. Moscow: 2012, Lomonosov Moscow State University. 204 p.
56. Lan Y., Yuan F., Fereja T.H., Wang C., Lou B., Li J., Xu G. // Analyt. Chem. 2019. V. 91. № 3. P. 2135–2139.
57. Halawa M.I., Wu F., Zafar M.N., Mostafa I.M., Abdussalam A., Han S., Xu G. // J. Materials Chem. B. 2019. V. 8(16). P. 3542–3549.
58. Demissie A.A., Dickson R.M. // J. Phys. Chem. A. 2020. V. 124. № 7. P. 1437–1443.
59. Voejkov V.L., Baskakov I.V. // Biophysics. 1995. V. 40. № 6. P. 1150–1157.
60. Sharov V.S., Dremina E.S., Vladimirov Iu.A. // Biofizika. 1995. V. 40. № 2. P. 428–433.

61. Vladimirov Iu.A., Sherstnev M.P., Azimbaev T.K. // Biofizika. 1995. V. 40. № 2. P. 323–327.
62. Vladimirov Y.A., Sharov V.S., Driomina E.S., Reznitchenko A.V., Gashev S.B. // Free Rad. Biol. Med. 1995. V. 18. № 4. P. 739–745.
63. Sharov V.S., Vladimirov Yu.A. // Biophysics. 1982. № 27. P. 327–329.
64. Sharov V.S., Vladimirov Yu.A. // Biophysics. 1984. V. 29. № 3. P. 394–397.
65. Sharov V.S., Suslova T.B., Deev A.I., Vladimirov Yu.A. // Biophysics. 1980. № 25. P. 923–924.
66. Safarov F.E. Chemiluminescence of lanthanide complexes in reactions with organic peroxides. Abstract of the dissertation for the degree of candidate of chemical sciences, Physical chemistry specialty. Ufa: 2011.
67. Kazakov D.V., Kazakov V.P., Safarov F.E., Ostahov S.S., Ahmadeeva G.H. // Bashkir chemistry journal. 2007. V. 14. № 1. P. 69–70.
68. Sherstnyov M.P., Azimbaev T.K., Vladimirov Yu.A. // Biophysics. 1995. № 40. P. 531–535.
69. Galimov D.I., Nazyrov T.I., Bilalova S.R., Gazeeva D.R., Bulgakov R.G. // Bulletin of Bashkir University. 2015. V. 20(3). P. 841–844.
70. Vladimirov Yu.A., Dyomin E.M., Proskurnina E.V., Osipov A.N. // Biochemistry (Moscow) Supplement. Series A: Membrane and Cell Biology. 2009. V. 3. № 4. P. 467–477.
71. Isolation and analysis of natural biologically active substances. Tomsk: Publishing House of Tomsk University, 1987. 184 p.
72. Sharov V.S., Briviba K., Sies H. // Free Rad. Biol. Med. 1996. V. 21. № 6. P. 833–843.
73. Kim G.J., Kim H.J. // Tetrahedron Lett. 2010. V. 51. № 10. P. 185–187.
74. Nikolaeva O.G., Revinskij Yu.V., Tihomirova K.S., Dmitrieva O.I., Dubonosov A.D., Bren' V.A. // Science in the South Russia. 2018. V. 14. №2. P. 14–19.
75. Ma Q., Ma H., Wang Z., Su M., Xiao H., Liang S. // Talanta. 2001. V. 53. № 5. P. 983–990.
76. Liang X.G., Chen B., Shao L.X., Cheng J., Huang M.Z., Chen Y., Hu Y.Z., Han Y.F., Han F., Li X. // Theranostics. 2017. V. 7. № 8. P. 2305–2313.
77. Liang X.G., Cheng J., Qin S., Shao L.X., Huang M.Z., Wang G., Han Y., Han F., Li X. // Chem. Commun. 2018. V. 54. № 85. P. 12010–12013.
78. Jiang J., Bakan A., Kapralov A.A., Silva K.I., Huang Z., Amoscato A.A., Peterson J., Garapati V.K., Saxena S., Bayir H., et al. // Free Rad. Biol. Med. 2014. V. 71. P. 221–230.
79. Tampo Y., Tsukamoto M., Yonaha M. // FEBS Lett. 1998. V. 430. № 3. P. 348–352.
80. Imada I., Sato E.F., Miyamoto M., Ichimori Y., Minamiyama Y., Konaka R., Inoue M. // Analyt. Biochem. 1999. V. 271. № 1. P. 53–58.
81. Romodin L.A., Vladimirov Yu.A., Lysenko N.P., Zarudnaya E.N. // Izvestia MAAO. 2018. V. 42(1). P. 102–106.
82. Aspee A., Alarcon E., Pino E., Gorelsky S.I., Scaiano J.C. // J. Phys. Chem. A. 2012. V. 116. № 1. P. 199–206.
83. Pantano D.A., Sonoda M.T., Skaf M.S., Laria D. // J. Phys. Chem. B. 2005. V. 109. № 15. P. 7365–7372.
84. Vasiljeva O.V., Lyubitsky O.B., Klebanov G.I., Vladimirov Yu.A. // Membr. Cell Biol. 1998. V. 12. № 2. P. 223–231.
85. Romodin L.A., Shangin S.V., Vladimirov Yu.A., Lysenko N.P., Hramov A.P. // Izvestia MAAO. 2018. V. 42. № 1. P. 118–123.
86. Romodin L.A., Vladimirov Yu.A., Shangin S.V. et al. Isoquinoline Coumarin Derivatives as Chemiluminescence Activators in Reactions of Lipid Peroxidation // Biophysics. 2020. V. 65. № 4. P. 577–586.

Immunogenic Cell Death in Cancer Therapy

O. S. Troitskaya[1*], D. D. Novak[1,2], V. A. Richter[1], O. A. Koval[1,2]
[1]Institute of Chemical Biology and Fundamental Medicine, Siberian Branch of the Russian Academy of Sciences, Novosibirsk, 630090 Russia
[2]Novosibirsk State University, Novosibirsk, 630090 Russia
*E-mail: troitskaya_olga@bk.ru
Received July 16, 2021; in final form, December 20, 2021
DOI: 10.32607/actanaturae.11523

ABSTRACT **Apoptosis plays a crucial role in chemotherapy-induced cell death. The conventional theory holding that apoptosis needs to be immunologically silent has recently been revised, and the concept of immunogenic cell death (ICD) has been proposed. This review describes the main features of ICD induction. These ICD markers are important for the effectiveness of anticancer therapy, as well as for basic research into cell death regulation. The mechanism of the "vaccination effect" of dying cancer cells undergoing ICD has been fully described, including the activation of specific antitumor response after re-challenge by the same living tumor cells. This review also discusses the whole set of molecular events attributing cell death to immunogenic type: the exposure of calreticulin and the heat shock protein HSP70 to the outer surface of the cell membrane and the release of the nuclear protein HMGB1 and ATP into the extracellular space. ICD inducers of various nature (chemotherapy drugs, cytotoxic proteins, and oncolytic viruses), as well as physical methods, are classified in the current review.**
KEYWORDS **Immunogenic cell death (ICD), HMGB1, calreticulin, antitumor vaccination, chemotherapy, apoptosis-inducing proteins, oncolytic viruses, cold plasma jet.**
ABBREVIATIONS **APCs – antigen-presenting cells; ATP – adenosine triphosphate; CAP – cold atmospheric plasma; CRT – calreticulin; CTLs – cytotoxic T lymphocytes; DAMPs – danger-associated molecular patterns; ER – endoplasmic reticulum; HMG – high-mobility group; HSP – heat shock protein; ICD – immunogenic cell death; IL – interleukin; LPC – lysophosphatidylcholine; MHC – major histocompatibility complex; PS – phosphatidylserine; ROS – reactive oxygen species; TLR – Toll-like receptor; TNF – tumor necrosis factor; VV – vaccinia virus.**

INTRODUCTION

The long-held theory that tumor cells can be successfully eliminated only when they die via apoptosis, without activation of the immune system, has recently been revised. The "dual-action strategy" is one of the successful antitumor approaches outside of surgical intervention. In this strategy, on the one hand, an antitumor drug directly induces the death of most cancer cells, while, on the other, the dying cells activate the immune system and elicit a specific immune response to the tumor antigens, resulting in the destruction of the remaining tumor cells. These criteria are met by immunogenic cell death (ICD) inducers (this class includes antitumor drugs) and approaches that involve various mechanisms of action: conventional chemotherapeutics, protein-based drugs, oncolytic viruses, photodynamic and radiation therapies, as well as cold atmospheric plasma. Immunogenic cell death can be detected based on the activation of a certain combination of damage-associated molecular patterns (DAMPs) from dying tumor cells, which contributes to their recognition and uptake by antigen-presenting cells. The exposure of calreticulin and the heat shock protein HSP70 on the outer surface of the cell membrane, as well as the release of the nuclear protein HMGB1 and ATP into the extracellular space, is considered the key molecular event that allows one to talk about ICD induction [1, 2]. Tumor antigen processing and presentation by dendritic cells trigger the activation of antigen-specific T lympho-

cytes, thus eliciting an adaptive immune response against these antigens [3]. The activation of immunogenic cell death of tumor cells contributes to the eliciting of an adaptive immune response. Cells on the ICD pathway exhibit an anticancer vaccination effect when transplanted to syngeneic immunocompetent animals [4]. The development of a specific immune response against the antigens released by the dying tumor cells enables the use of therapeutic ICD inducers, both to assume control over metastatic tumors and to elaborate approaches to antitumor immunization [5].

THE GENERAL CONCEPT OF IMMUNOGENIC CELL DEATH

The concept of tumor immunotherapy relies on the immune system's ability to recognize transformed cells and affect their growth and proliferation. Physiological cell death occurs via apoptosis, which can be induced either by the organism's intrinsic growth and life-sustaining programs by exposure to external factors [6]. Chromatin condensation, nucleus fragmentation with the plasma membrane remaining intact, and the emergence of apoptotic bodies are the morphological markers of apoptotic cell death, while plasma membrane integrity is disrupted during necrosis, resulting in the release of DAMPs activating the immune system and triggering an inflammatory response [7]. The proteins HMGB1, MRP8, calgranulins A and B, and MRP14 are the best studied DAMPs.

The differences in the antitumor properties of oxaliplatin and doxorubicin observed in experiments on immunodeficient and immunocompetent tumor-bearing mice have inspired scientists to search for an explanation to the phenomenon. Scheffer *et al.* [8] have put forward a hypothesis that when animals are subjected to antitumor vaccination with dying tumor cells, the repertoires of antigens from dying and intact cells may differ. Immunocompetent mice were transplanted with tumor cells: in some of those, apoptosis was induced by γ-irradiation, while in others necrosis was induced by freeze/thaw cycles. It was shown that when living tumor cells had subsequently been transplanted to the same mice, only animals vaccinated with apoptotic cells did not develop tumors in 75–100% of cases. Meanwhile, transplantation of living tumor cells did not result in tumor development in only 0–30% of animals vaccinated with necrotic cells on the same protocol. An immunohistochemical analysis of the vaccination site showed that the area had been infiltrated by $CD4^+$ and $CD8^+$ T cells and dendritic cells after the injection of apoptotic cells, which was an indication of a strong T-cell response, while the necrotic cell vaccine caused infiltration predominantly by macrophages [8]. Therefore, cells in which apoptosis was induced by γ-irradiation were found to exhibit an immunogenic potential. Tumor cells in which apoptosis was induced by anthracycline derivatives (e.g., doxorubicin) transplanted to mice were shown to stimulate the maturation of dendritic cells and subsequently elicit an immune response against tumor cells *in vivo* [4]. It was revealed by a comparison of the antitumor effects of treating immunocompetent and immunodeficient tumor-bearing mice with oxaliplatin or cardiac glycosides that the elimination of tumor cells occurs in immunocompetent mice, thus proving the role played by the immune system in the antitumor effects of these drugs [9, 10]. The apoptosis which causes the aforementioned effects is known as immunogenic apoptosis. A search for the molecular markers of immunogenic apoptosis showed that it is typically characterized by the secretion of DAMPs recognized by dendritic cells, followed by processing and presentation of antigens from the dying cells. This results in the activation of specific T cells and formation of long-lasting antitumor immunity [5].

THE MECHANISM OF IMMUNOGENIC CELL DEATH INDUCTION

The role played by the endoplasmic reticulum in ICD induction

Doxorubicin, mitoxantrone, and γ-irradiation were the first efficient inducers of immunogenic cell death to appear on the scene. The ability of these antitumor drugs to trigger ICD was found to depend on their ability to induce endoplasmic reticulum (ER) stress [11]. The exposure of ER chaperones, primarily calreticulin (CRT), to the outer plasma membrane is the fundamental event in immunogenic cell death induction. When exposed to certain stimuli, the cell can trigger an integrated stress response, a complex molecular mechanism aiming to preserve cellular homeostasis [12]. In particular, anthracycline-induced ER stress stimulates PERK, which phosphorylates the translation initiation factor eIF2α [13]. Inactivation of eIF2α is accompanied by partial activation of caspase 8 and cleavage of B-cell receptor-associated protein 31 (BAP31) and conformational activation of the Bax and Bak proteins; in turn, it triggers translocation of ER chaperones to the outer cell membrane [11]. For most ICD inducers, the translocation of chaperones to the outer membrane does not occur directly but results from their transport from ER to the Golgi apparatus, mediated by vesicle-associated membrane protein 1 (VAMP1) and synaptosomal-associated protein 25 (SNAP25), and requires concomitant production of reactive oxygen species (ROS) [11, 14, 15].

According to Garg et al. [16], if the ER-to-Golgi transport is blocked, the exposure to ICD inducers reduces the secretion of ATP into the extracellular space, while not causing CRT exposure, which suggests that calreticulin and ATP follow the ER-to-Golgi transport pathway to reach the plasma membrane. The ICD-induced translocation of CRT to the outer plasma membrane is apparently regulated by multiple factors: the CXCL8 chemokine ligand [17], the changes in the Ca^{2+} levels in the ER [18], caspase 2 [19], long non-coding RNAs (e.g., ncRNA-RB1 and miR-27a) [20], and plasma membrane integrins, at least under some conditions [21]. CRT and other ER chaperones on the cell surface contribute to the uptake of these dying cells or their fragments; they are referred to as "eat-me" signals for antigen-presenting cells (APCs) [16]. Furthermore, the exposure of CRT apparently stimulates type I IFN secretion by antigen-presenting cells [22], which may also contribute to the immunogenicity of regulated cell death.

It has been shown that simultaneous elevation in the cellular level of ROS and induction of ER stress activate the signal pathways that help transport DAMPs into the extracellular space [11, 23]. Interestingly, immunogenicity decreases in the presence of antioxidants, thus indicating that ROS are crucial for ICD induction [11, 24]. It was later found that cisplatin, which alters the cellular redox metabolism, cannot trigger ICD, because it is unable to induce ER stress [25]. Furthermore, the simultaneous ER stress and ROS production increases the amount of various, released DAMPs, which eventually becomes a crucial factor for the immunogenicity of dying tumor cells [16, 26]. Thus, etoposide causes only exposure of HSP70 and ATP secretion but neither induces ER stress nor triggers ICD [23, 27, 28].

Classification of ICD

Two types of ICD inducers are currently distinguished depending on whether they trigger apoptosis through ER, or apoptotic cell death and ER stress occur independently [29]. Such agents as doxorubicin or mitoxantrone can be classified as type I ICD inducers (i.e., agents that trigger apoptosis through non-ER targets and stimulate the ICD-associated immunogenicity through the secondary or "side" stress effects of the ER). Contrariwise, type II ICD inducers selectively target the ER components and can induce immunogenic apoptosis by directly altering the ER homeostasis and triggering ER stress (e.g., photodynamic therapy). Therefore, ER stress triggered by type I ICD inducers can differ qualitatively from that triggered by type II inducers, since it can be less severe and capable of initiating the transducing survival-promoting signals [29].

In addition to immunogenic apoptosis, other types of programmed cell death include autophagy, necroptosis, and pyroptosis involving activation of some ICD markers. *Table 1* lists the variants of immunogenic cell death and their specific features.

Table 1. Comparison of different types of programmed cell death in cells manifesting immunogenicity

Type of cell death	DAMPs characteristic of ICD	"Eat-me" signals	Inflammation	Immunogenicity	Terminal cellular events
Apoptosis	Ecto-CRT, secretion of HMGB1 and ATP	Ecto-CRT, HSP70, HSP90, exposure of PS	-	+	Nonlytic pathway, DNA fragmentation and apoptotic bodies
Autophagy	Release of HMGB1 and ATP	Secretion of LPC, exposure of PS	-	+	Nonlytic pathway, autophagic bodies
Necroptosis	Long genomic DNA, IL-6 [30], ATP, and HMGB1 [31]	Secretion of LPC, exposure of PS, low level of ecto-CRT [31]	+	++	Nonlytic pathway, loss of plasma membrane integrity, swelling of cellular organelles
Pyroptosis	Release of HMGB1, ATP, IL-1α, IL-1β, IL-6, IL-18, and TNF-α	Exposure of PS	+	++	Lytic pathway, plasma membrane rupture, release of the cell contents

Note. The degree of immunogenicity for each type of cell death was assessed as + and ++ depending on the intensity of "eat-me" signals and the level of DAMP release [30].

Immunogenic cell death cascade

The key molecular events required for immunogenic cell death to take place have been identified (*Fig. 1*). The first event of the ICD cascade is the exposure of a complex formed by two proteins, calreticulin and disulfide isomerase ERp57, on the surface of dying tumor cells [11]. Both proteins are normally located in the ER lumen and are translocated to the cell surface within a few hours after stimulation with ICD inducers. CRT exposure can be detected before the translocation of phosphatidylserine (PS) to the outer membrane of a dying cell. CRT translocation from the ER is an initiating "eat-me" signal for phagocytic cells. Calreticulin exposed on the cell membrane interacts with the CD91 receptors on the surface of dendritic cells, thus stimulating the uptake of dying cells [29, 32].

Another molecular feature of ICD that can be observed after the CRT exposure consists in the translocation of heat shock proteins (such as HSP70 or HSP90, which can bind to the CD91 receptor on the dendritic cell surface like calreticulin) from the nucleus to the cell surface, which stimulates their activation and maturation [33].

Twelve to 18 hours after the initiation of CRT exposure, non-histone chromatin-binding nuclear protein HMGB1 is released into the intercellular space. This protein binds to the TLR4 receptors in dendritic cells, which is required to ensure optimal TLR4-dependent processing and presentation of tumor antigens to T cells by dendritic cells [34]. During chemotherapy or radiation therapy, dendritic cells receive a signal through TLR4 and its adapter, MyD88, to start efficient processing and cross-presentation of antigen from dying tumor cells [35]. The final molecular event in the ICD cascade is the release of ATP into the extracellular space, which is the "find-me" signal and is required for productive maturation of dendritic cells. The dying cells mark their presence through chemotactic factors known as "find-me" signals that are needed so that phagocytic cells (neutrophils, monocytes, and tissue macrophages) could quickly find and efficiently destroy them [36]. The release of ATP from dying cells into the intercellular space activates the P2X7 purinergic receptors on dendritic cells and causes P2X7/NLRP3 receptor-dependent activation of the inflammasome in dendritic cells, thus contributing to proteolytic maturation and the release of proinflammatory cytokines such as interleukin IL-1β. IL-1β is essential for the activation of antigen-specific $CD8^+$ T cells producing IFNγ [3]. Moreover, IL-1β is involved in the activation of the innate immunity factors, development of inflammation, and the early stages of the immune response [34, 37].

If the cascade of immunogenic apoptosis is successful, a population of antigen-specific T cells is expected to emerge: when being re-challenged with tumor cells of this type, antigen-specific T cells will recognize the respective antigens and destroy cancer cells (*Fig. 2*). The possibility of inducing the cascade of events for immunogenic apoptosis in tumor cells using antitumor drugs has enabled us to develop an antitumor vaccination strategy where cells with induced immunogenic cell death are the "vaccine."

THE ENDOGENIC FACTORS INVOLVED IN IMMUNOGENIC CELL DEATH

Calreticulin (CRT)

Approximately 30% of all cell proteins and peptides are synthesized in the ER, where they interact with enzymes and chaperons, including calreticulin, calnexin, glucose-regulated protein Grp94, thiol oxidoreductases PDI, and protein disulfide isomerase ERp57. All these molecules are involved in the formation of the functional conformation of proteins [38]. CRT, calnexin, and ERp57 constitute the chaperone complex responsible for the folding of the synthesized proteins transported through the ER and their quality control.

Another important function of the ER is storing and releasing Ca^{2+} ions [39]. Calreticulin, a unique Ca^{2+}-binding chaperone, is one of these proteins [40]. Cells with downregulated CRT expression are characterized by protein misfolding and accumulation of misfolded proteins [40]. Overexpression of CRT increases the Ca^{2+} content in intracellular depots [41].

It is assumed that the cell surface CRT plays a role in antigen presentation, activation of the complement system [42], apoptotic cell removal [43], immunogenicity of dying cancer cells [23], wound healing [44], and thrombospondin signaling [45]. CRT acts as a secondary ligand on the cell surface, being essential for recognition during phagocytosis and stimulating LRPs (low-density lipoprotein receptor-bound proteins) on the surface of engulfing cells. The protein resides on the outer surface of the plasma membrane in many cell types, where it may contribute to antigen processing and mediate cell–cell adhesion [40]. Being normally located in the lumen of the endoplasmic reticulum, CRT is translocated to the outer cell membrane in the form of a complex with ERp57 as a result of ER stress via exocytosis (*Fig. 3*). The ER-to-membrane transport of CRT depends on the interaction between vesicle-associated SNARE (V-soluble N-ethylmaleimide-

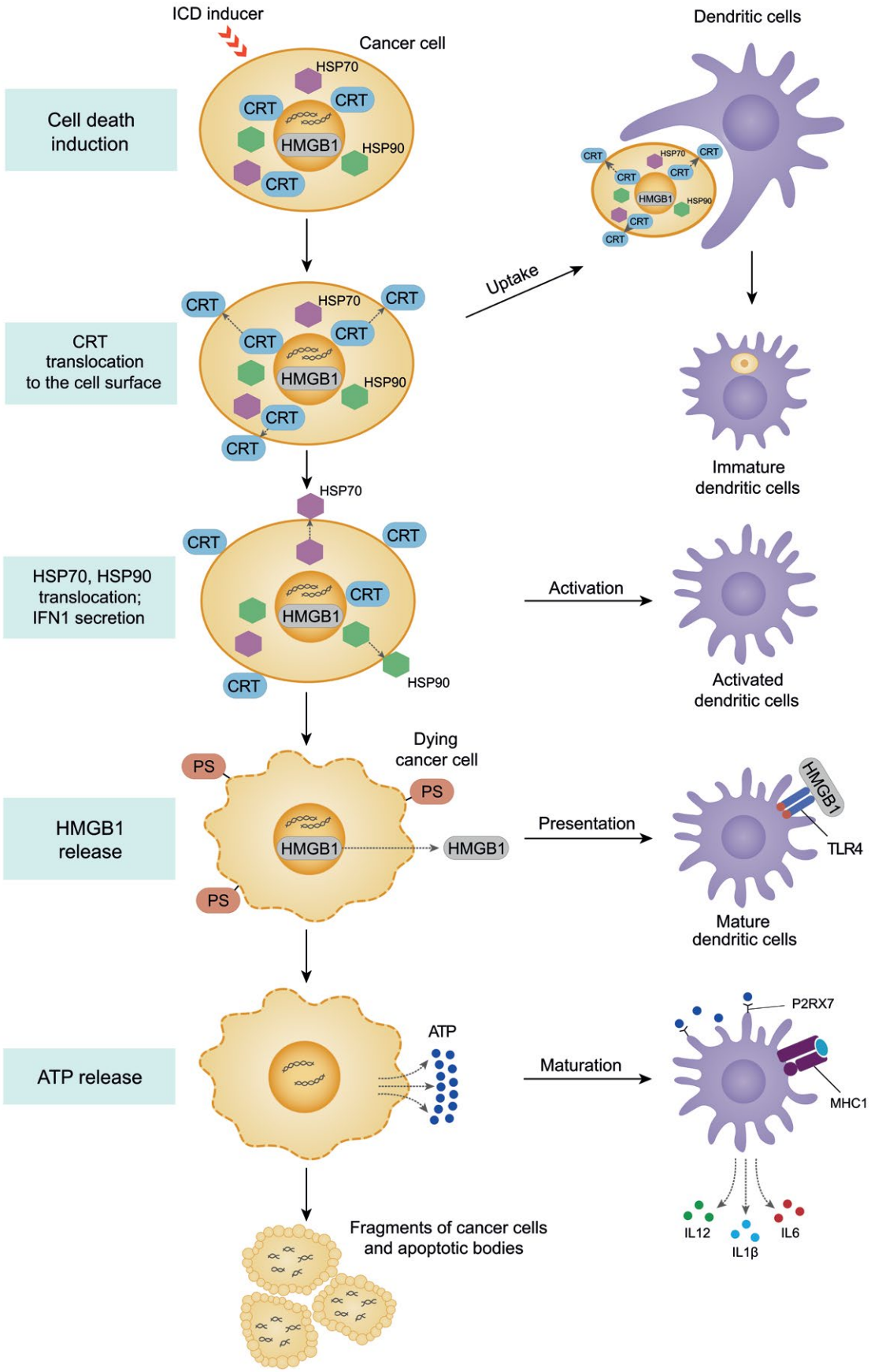

Fig. 1. Sequential events of immunogenic cell death and activation of antigen-presenting dendritic cells

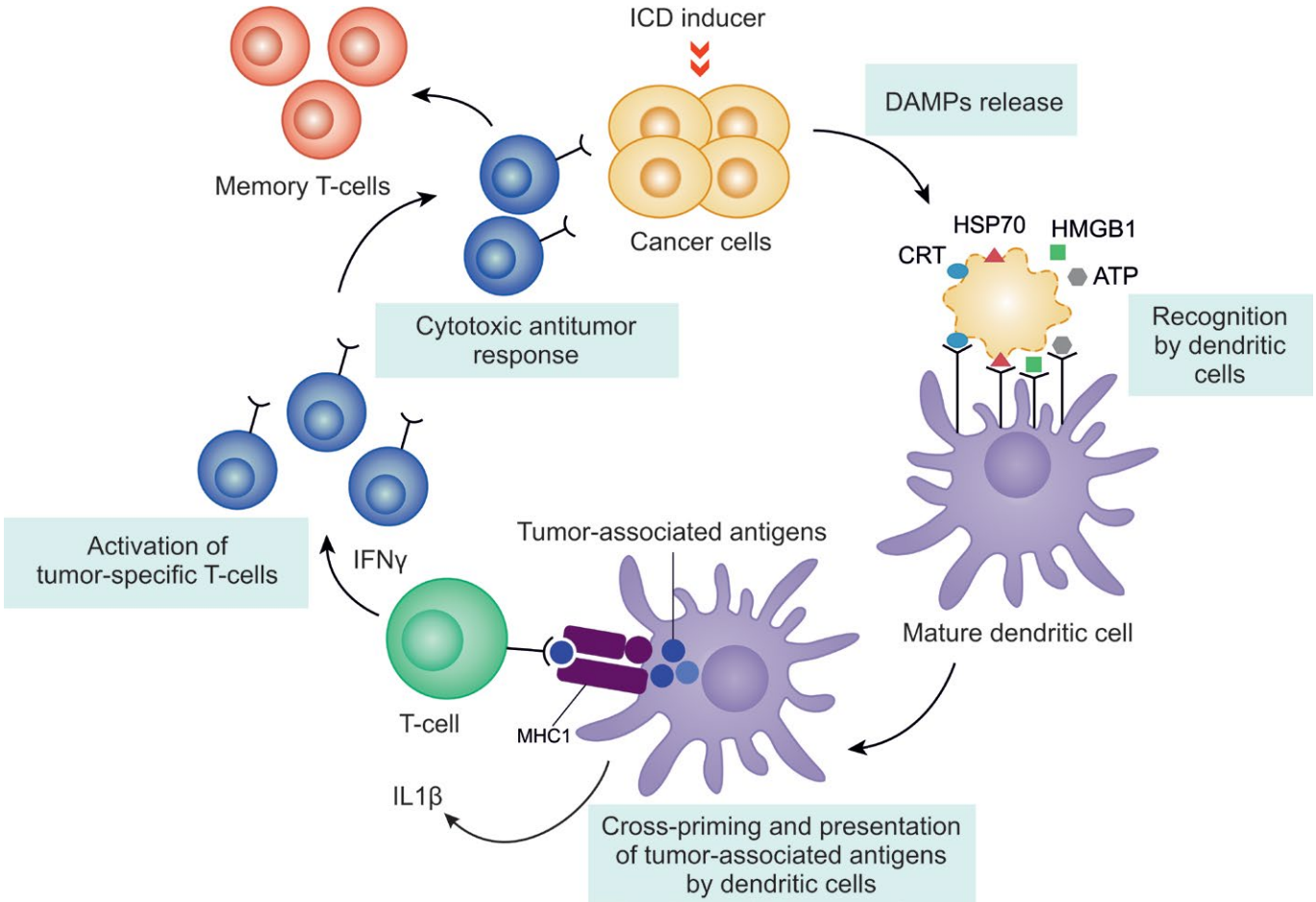

Fig. 2. A simplified scheme of the induction of immunogenic cell death

sensitive factor attachment protein receptor) proteins and the SNARE proteins on the cell membrane [11, 21]. Calreticulin on the outer plasma can bind to the CD91 receptors in dendritic cells, thus causing phagocytosis of dying cells [46].

The signaling function of ATP in the activation of the immune system

Dying cells mark their presence by releasing chemotactic factors (known as "find-me" signals) and through the "eat-me" signals that act as ligands for uptake. Several factors that can act as "find-me" signals have been proposed, including ATP, UTP, the chemokine fractalkine (CX3CL1), lysophosphatidylcholine (LPC), and S1P [47]. Apoptotic cells are converted to secondary necrotic cells when their scavenging is disrupted, which causes chronic inflammation and the development of autoimmune diseases [35].

The release of ATP into the extracellular space is typical of both immunogenic apoptosis and necro-

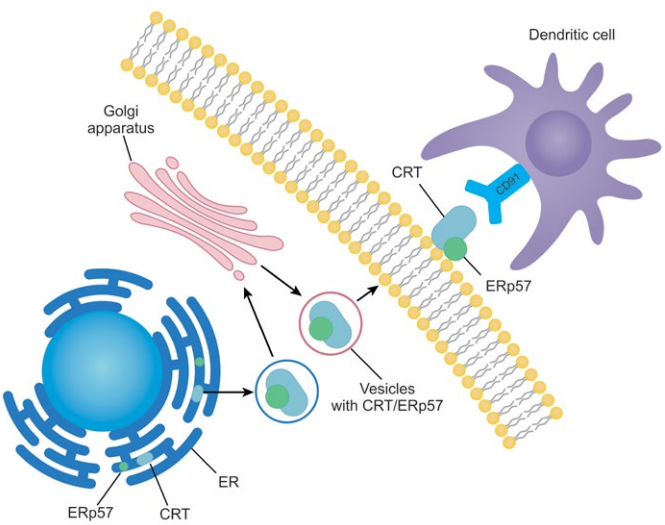

Fig. 3. The exposure of calreticulin (CRT) on the cell surface and its recognition by dendritic cells

sis, accompanied by cell lysis. However, there exist several differences between these processes. The first difference is related to the amount of released ATP. During apoptosis, less than 2% of cellular ATP reaches the extracellular space [48]. The characterization of ATP as a mediator of inflammation largely rests on its ability to activate the ionotropic nucleotide receptor P2X7, which, in turn, causes the activation of the inflammasome and release of proinflammatory cytokines [49]. The enormous release of ATP during necrosis activates the inflammasome and the inflammation process. Nonetheless, the ATP concentration required to activate purinergic P2X7 receptors is no less than 100 μM, significantly higher than that required to activate chemotactic receptors such as P2Y2 (< 1 μM) [50]. Interestingly, lower ATP concentrations can actually exhibit an anti-inflammatory effect by inhibiting the secretion of inflammatory cytokines, as well as promoting the release of anti-inflammatory cytokines [35]. Hence, ATP cannot be regarded as a universal signal of inflammation development.

The non-histone chromatin-associated nuclear protein HMGB1 and its functions in the cell

The HMGB1 protein belongs to the HMG (High mobility group) family: the family of nuclear non-histone proteins required to maintain chromatin architecture. Inside the cell, HMGB1 interacts with p53, TBR, Oct14, Hox, steroid hormone receptors, and many viral proteins and efficiently regulates gene expression [51]. HMGB1 can migrate between the cytoplasm and the cell nucleus depending on the phase of the cell cycle. Lymphoid cells contain HMGB1 both in the cytoplasm and in the nucleus [52].

The emergence of HMGB1 in the intercellular space is considered a marker of sudden damage or necrosis, since chromatin is damaged irreversibly in this case. In the mechanical damage foci, HMGB1 interacts with the receptor for advanced glycation end products (RAGE), thus enhancing the production of TNF, IL-1, IL-8, MCP1, CDF1α, and other factors, recruiting healthy stem cells to the damage focus [53]. HMGB1 can be secreted in cells both actively and passively. The active secretion of HMGB1 is related to the dissociation from the complex with chromosome damage resulting from histone acetylation, HMGB1 hyperacetylation, and monomethylation of HMGB1. Passive diffusion of HMGB1 is observed during necrosis. However, in the case of normal (non-immunogenic) apoptosis, HMGB1 is not released from the tightly packed apoptotic cell nuclei [54]. According to Luo et al. [54], the release of HMGB1 from necrotic tumor cells treated with doxorubicin, which causes necrosis when used at high concentrations [55], contributes to the resumption of tumor growth and metastasis development via the RAGE system activation pathway.

Heat shock proteins HSP70 and HSP90

Transcription activation of a number of chaperones belonging to the class of inducible HPS proteins or heat shock proteins is a common response to cellular stress, including stress induced by chemotherapeutics. Heat shock proteins protect the cell against death by refolding the damaged proteins or directing the damaged proteins to proteasomes for degradation [34].

In mammals, HSP70 is involved in protein formation, stabilization, and transport across the mitochondrial and nuclear envelopes [56]. Chaperone HSP90 performs a number of functions in the cell, including protein folding and stabilization under heat shock; it also promotes protein degradation [57]. Chaperone HSP90 stabilizes many of the proteins that are responsible for tumor growth and is involved in the regulation of adhesion, invasion, metastasis, angiogenesis, and apoptosis; therefore, HSP90 inhibitors are studied as potential antitumor agents [58].

Furthermore, the heat shock proteins HSP70 and HSP90 can form complexes with peptide antigens, including tumor-targeting peptides, which is a necessary and sufficient source of antigens for presentation to T cells. Unbound peptide antigens cannot elicit the T-cell response in $CD8^+$ lymphocytes, unlike the antigens bound to heat shock proteins. *In vivo* experiments conducted on mice have demonstrated that the complexes formed between antigens, on the one hand, and HSP70 and HSP90, on the other, can be a source of antigens for efficient cross-presentation by dendritic cells [59].

In Vivo INDUCTION OF IMMUNOGENIC CELL DEATH UPON PROPHYLACTIC VACCINATION

Today, there exist several models for *in vivo* ICD studies. The "gold standard" for evaluating the ability of dying cells to trigger adaptive immunity involves prophylactic vaccination of immunocompetent syngeneic animals [5]. In this approach, tumor cells are exposed *in vitro* to a potential ICD inducer and then transplanted subcutaneously as a vaccine containing no immunological adjuvants. One to two weeks later, the animals are re-challenged with viable tumor cells of the same type at the minimum dose required for the formation of tumor nodules; tumor growth is monitored for 40–60 days (*Fig. 4*) [4, 35, 60]. Not only is the percentage of tumor-free mice taken into account for assessing the vaccination effectiveness, but allowance is also usually made for

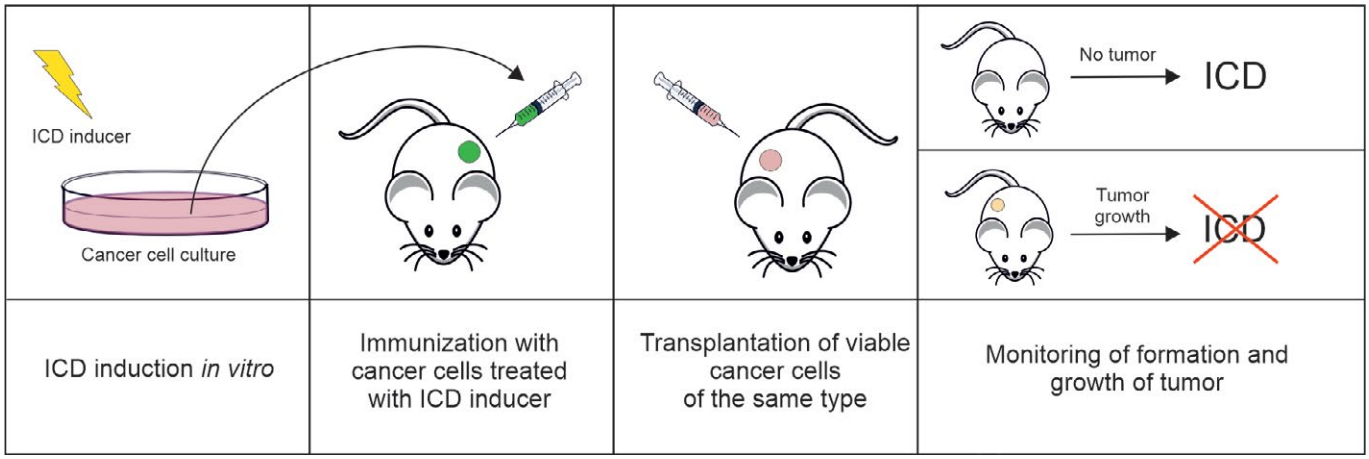

Fig. 4. The classical scheme of antitumor vaccination with mouse tumor cells treated with a potential ICD inducer, followed by re-vaccination with viable tumor cells of the same type

the tumor growth rate if tumors develop regardless of the vaccine-induced adaptive immunity. The specificity of the development of an antitumor response is confirmed by the fact that at the end of the experiment, tumor-free vaccinated mice were re-challenged with syngeneic cancer cells of a different line, which are expected to cause neoplastic progression in 100% of mice. The potentiated effectiveness of therapy with any inducer of regulated death of tumors growing in immunocompetent mice compared to immunodeficient ones indicates that this inducer has the potential to trigger ICD. However, this experimental design does not allow one to distinguish between ICD induction and non-ICD immunostimulation. Some antitumor drugs (such as docetaxel, cisplatin, 5-fluorouracil, gemcitabine, etc.) do not induce ICD but mediate immunomodulatory effects in the tumor microenvironment by having a direct impact on immune cell populations. Although these immunomodulatory effects are crucial for maximizing the clinical effectiveness of therapy, they are not related to ICD induction [12, 61].

An equivalent approach to the *in vivo* evaluation of ICD in immunocompetent syngeneic systems can consist in measuring the growth of a tumor located far from the tumor structure treated using local ionizing radiation or intratumoral delivery of anticancer therapy [62]. This approach is also effective when the tumor is accessible only to cytotoxic T lymphocytes (CTLs) (e.g., in the case of brain metastases in a patient receiving chemotherapy agents that cannot cross the blood–brain barrier) [63]. The models of the so-called "latent response" (i.e., regression of tumor lesions located far away from the site of the ionizing radiation treatment of the primary tumor in patients) proved useful in this situation [64]. This *ex vivo* modeling of ICD induction allows one to characterize DAMPs released by tumor cells in response to *in situ* stress, perform immunological profiling of the APCs and CTLs that underlie the *in vivo* initiation and implementation of antitumor immunity, and identify the sequences of the triggered ICD cascades and their correspondence to the observed responses *in vitro*.

DRUGS INDUCING IMMUNOGENIC CELL DEATH

Chemotherapeutics

Induction of immunogenic cell death was first demonstrated for doxorubicin, an anthracycline drug [4]. Some chemotherapeutic agents can also induce ICD (selected drugs are listed in *Table 2*) [9, 65–67].

Peptides exhibiting antitumor activity

Peptide LTX-315. Some peptides exhibiting an antitumor activity can also induce ICD. Thus, such cationic amphiphilic synthetic peptide as LTX-315 permeabilizes the inner mitochondrial membrane and causes necrotic cell death [74]. Intratumoral injections of LTX-315 completely eliminate murine B16 melanoma, while mice treated with the drug exhibit

Table 2. Chemotherapeutics inducing immunogenic apoptosis

Chemotherapeutics	Types of tumor cells	Markers of ICD induction, DAMPs	Vaccination effectiveness, %
Anthracyclines (doxorubicin, daunorubicin, and idarubicin), doxorubicin-loaded liposomes[4, 68]	Murine CT26 colon carcinoma	CRT exposure, ER stress, eIF2α phosphorylation, HMGB1 release, ATP secretion	Doxorubicin, 80 Daunorubicin, 35 Idarubicin, 45
Oxaliplatin [9, 69–71]	Murine CT26 colon carcinoma, RKO and HCT116 human colorectal carcinoma	CRT exposure, HMGB1 release	Oxaliplatin, 80
Microtubule inhibitors (colchicine, CMQ, FMQ, nocodazole, epothilone B, Taxotere)[67, 72]	Murine CT26 colon carcinoma	ER stress, CRT exposure, PERK-dependent phosphorylation of eIF2α	Nocodazole, 80
Cardiac glycosides (digoxin DIG, digitoxin DIGT) [65, 73]	MCA205 mouse fibrosarcoma, murine B16 melanoma	CRT exposure, HMGB1 release, ATP secretion	DIG/DIGT + cisplatin – 70–90 DIG/DIGT + mitomycin – 60–90

resistance to subsequent injections of live B16 melanoma cells. Peptide LTX-315 activates all the key molecular markers of ICD: CRT exposure, release of HMGB1 and ATP, as well as interferon response without activation of cellular caspases, which suggests that cell death occurs via the non-apoptotic pathway [74, 75].

The antitumor peptide RT53 belonging to the CPP class. The synthetic antitumor peptide RT53 belonging to the CPP class (high-permeability proteins) causes tumor cell death through unregulated necrosis with markers of ICD [76]. It was shown that after vaccination with RT53-treated B16F10 melanoma cells, only 25% of mice had no tumors at the re-transplantation site [77]. The development of antitumor immunity induced by RT53 peptide was also confirmed in C57BL/6 mice prophylactically vaccinated with RT53-treated MCA205 mouse fibrosarcoma cells: only the tumor growth rate decreased, but tumors at the re-transplantation site were not completely eliminated [76].

RIG-1-like helicases. The group of peptide inducers of ICD also includes RIG-1-like helicases. In contrast to LTX-315 and RT53, the RIG-like helicase RIG1 triggered apoptosis of Panc02 mouse pancreatic tumor cells with markers of ICD. Along with the conventional set of ICD markers, increased production of interferons and some proinflammatory cytokines was observed. Importantly, dendritic cells in the spleen efficiently engulf tumor cells treated with RIG-1 and present tumor-associated antigens to naïve CD8+ T cells [78].

Recombinant analog of lactaptin (RL2). Recent studies have shown that a recombinant analog of the human milk pro-apoptotic protein lactaptin (RL2) [79, 80] can induce ICD *in vitro* by activating the whole cascade of immunogenic cell death markers and elicit an antitumor immune response in the prophylactic vaccination model [81]. Thus, in experiments on immunocompetent C3H/He mice, 43% of mice vaccinated with RL2-treated MX-7 murine rhabdomyosarcoma cells did not develop a tumor nodule after they had been re-challenged. It is also worth mentioning that the growth rate of tumors that had actually developed was significantly lower compared to the control group. Ethyl pyruvate, an indoleamine 2,3-dioxygenase inhibitor, used in combination with cells incubated in the presence of RL2 potentiated the vaccination effect of RL2-treated cells by up to 60% [81].

Oncolytic viruses in ICD induction

It has been demonstrated that the death of cells infected with some unmodified oncolytic viruses, such as the Newcastle disease virus, measles virus, vaccinia virus (VV), and coxsackievirus B3, occurs with the activation of typical ICD markers [82–84]. The abilities of the human adenovirus, Semliki Forest

virus, and wild-type VV to induce ICD were compared. All three viruses were found to stimulate the release of ICD markers, as well as the activation and maturation of dendritic cells; however, only the tumor cells infected with the Semliki Forest virus stimulated T-helper type 1 (Th1) maturation and induced antigen-specific T-cell activation [85]. Dendritic cells phagocytizing tumor cells infected with VV were unable to elicit a T-cell response. On the other hand, attenuated VV strains activated the STING- and Batf3-dependent pathways in dendritic cells and induced potent antitumor immunity [86]. Therefore, modification of the VV genome can be considered as a strategy to overcome the immunosuppression characteristic of wild-type VV. Heinrich et al. [84] showed that when incubated with human melanoma cells, the JX-594 (Pexa-Vec) virus causes exposure of CRT, HMGB1 release, and dendritic cell activation/maturation. The VV-GMCSF-Lact recombinant virus causes the death of tumor cells of different histological origins with markers of ICD [87, 88]. It has been revealed recently that glioma therapy with the Newcastle disease virus elicits an adaptive immune response against glioma cells, being a component of the antitumor response [89]. The recombinant adenovirus carrying the CD40 ligand transgene induces a type 1 T-helper response, resulting in the activation of cytotoxic T cells and reducing immunosuppression [90].

Physico-chemical approaches to antitumor therapy with an ICD-inducing potential

It has been demonstrated that various approaches involving physical impact (e.g., ionizing radiation, photochemotherapy, photodynamic therapy, near-infrared photoimmunotherapy, high hydrostatic pressure, thermal shock, nano-pulsed stimulation, hyperthermia, and cold plasma irradiation) can induce the death of tumor cells with markers of ICD [12].

Radiation therapy. Radiation therapy is among the methods of local tumor treatment; however, ionizing radiation also causes the elimination of tumor cells in distant metastases, thus indicating that radiation activates the immune system [91]. *In vitro* experiments have shown that radiation therapy induces a dose-dependent death of triple-negative breast cancer cells with exposure of CRT and release of ATP and HMGB1 [92]. In order to potentiate the immunogenic component of radiotherapy, it is also used in combination with clinically effective chemotherapeutics, causing immunogenic cell death (e.g., oxaliplatin or paclitaxel) [92].

Hyperthermia. It has been shown that exposure to heat shock above 42°C (hyperthermia) can induce a cascade of events that trigger ICD *in vitro* and elicit immunogenicity in mice. Thus, prophylactic vaccination with CT26 tumor cells exposed to heat shock (47°C) significantly inhibits tumor growth in the site of living cells inoculation and increases the survival chances of vaccinated animals [93].

Nano-pulse stimulation. It has been shown that nano-pulse stimulation leads to complete regression of weakly immunogenic metastatic 4T1-Luc murine mammary carcinoma [94]. Another interesting observation is that spontaneous metastases to distant organs were detected less frequently even in animals in whom tumor had not regressed completely. After nano-pulse stimulation and tumor regression, all mice became resistant to re-challenging with tumor cells and exhibited a vaccination-like effect. Nano-pulse stimulation was shown to induce antitumor immunity, stimulate the maturation of memory T cells, cause the destruction of the tumor microenvironment, and reduce the number of immunosuppressive cells in the tumor microenvironment and blood.

Cold atmospheric plasma (CAP). Cold atmospheric plasma (CAP) is one of the novel, promising directions in the therapy of malignancies. Cold atmospheric plasma treatment leads to selective death of melanoma cells [95], intestinal [96] and lung cancer cells [97, 98], pancreatic [99], gastric [100] and breast cancer cells [101], as well as glioblastoma cells [102] *in vitro*.

Cold atmospheric plasma irradiation can also trigger immunogenic cell death. Death of Hmel1 MM melanoma cells and PANC-1 pancreatic tumor cells treated with a CAP-irradiated culture medium was shown to be accompanied by CRT exposure and ATP release, which suggests that plasma-activated media can potentially be used as an inducer of cell death through activation of innate immunity [103]. Even a CAP-irradiated phosphate buffer can trigger the ICD cascade *in vitro* [104]. Direct treatment of tumor cells with CAP can also trigger ICD by inducing the exposure of calreticulin and HSP70 on the outer membrane, as well as secretion of ATP and HMGB1 [105]. It was also found that *in vitro* CAP treatment of tumor cells causes the release of ICD-specific DAMPs; 30% of mice vaccinated with CAP-irradiated CT26 cells did not develop tumors at the site of re-challenging with live tumor cells, while 90% of the tumors that developed in vaccinated mice were smaller compared to the average tumor size in the control group [106]. *In vivo* cold plasma irradia-

tion of MX-7 rhabdomyosarcoma tumors transiently increased the serum levels of HMGB1 in tumor-bearing animals [105].

Hence, some physical methods of cancer therapy can be regarded as ICD inducers and the contribution of the antitumor immune response to tumor therapy effectiveness in patients can be evaluated.

SUPPRESSION OF THE ANTITUMOR IMMUNE RESPONSE UPON ICD INDUCTION

Along with the endogenous factors that activate the immune system, there are several mechanisms that serve to suppress the immune response through inhibitory signals. As a tumor progresses, it acquires a number of properties that allow it to evade the immune system [107]. The tumor microenvironment prevents the penetration of tumor infiltrating lymphocytes by limiting the nutrient supply and by releasing inhibitory signals. Plasmacytoid dendritic cells, tumor-associated macrophages and myeloid-derived suppressor cells secreting anti-inflammatory cytokines and expressing immunosuppressive metabolic enzymes (such as inducible nitric oxide synthase (iNOS), indoleamine 2,3-dioxygenase (IDO), tryptophan 2,3-dioxygenase (TDO), and arginase) play an important role in the development of the immunosuppressive tumor microenvironment [108, 109]. The reduction in the tryptophan level because of the action of IDO1 and the simultaneous increase in the level of its metabolites stimulate the immunosuppressive properties of the tumor and its microenvironment mainly through the development of APC- and T-cell-mediated immune tolerance, as well as immune cell death [110]. This suppression of the T-cell metabolism can inhibit the effector activity of T cells, while simultaneously stimulating regulatory T cells and acting as a barrier to effective immunotherapy. Rapid depletion of nutrients such as glucose and accumulation of metabolic products such as lactate or kynurenine, which directly inhibit T cells, are characteristic of tumors [111]. Along with signals such as CRT, which recruit cells that exhibit phagocytic activity, tumor cells can display molecules that are antagonistic to "eat-me" signals (CD47 molecules) on their surface, resulting in the suppression of calreticulin-mediated phagocytosis. The interaction between CD47 and the SIRPα receptor on dendritic cells is a signal that inhibit phagocytosis [112]. Activation of the aforementioned mechanisms can potentially interfere with the ICD cascade and protect tumor cells against attacks on the immune system.

CONCLUSIONS

Immunogenic cell death is a unique response that is initiated by cellular stress and ends in cell death, accompanied by the active secretion or passive release of numerous alarmins. The ICD plays a crucial role in fighting a cancer thanks to its ability to trigger the antitumor immune response, potentiating the therapeutic effect of chemotherapeutics and radiation therapy agents. Detailed research into the molecular markers of ICD will allow us to better predict the *in vivo* activation of the antitumor immune response by using specific antitumor drugs and approaches. ●

This review was prepared with the support of the Russian Foundation for Basic Research (RFBR) No. 19-34-90134 (Postgraduate students), the Russian Science Foundation (RSF) No. 19-19-00255 and the project of basic budget financing of the Ministry of Science and Higher Education of the Russian Federation No. 0245-2019-0001.

REFERENCES

1. Vacchelli E., Aranda F., Eggermont A., Galon J., Sautès-Fridman C., Cremer I., Zitvogel L., Kroemer G., Galluzzi L. // Oncoimmunology. 2014. V. 3. № 1. P. e27878.
2. Bogdanova I.M., Ponomarenko E.A. // Immunology. 2015. V. 36. № 3. P. 158–161.
3. Vacchelli E., Senovilla L., Eggermont A., Fridman W.H., Galon J., Zitvogel L., Kroemer G., Galluzzi L. // Oncoimmunology. 2013. V. 2. № 3. P. e23510.
4. Casares N., Pequignot M.O., Tesniere A., Ghiringhelli F., Roux S., Chaput N., Schmitt E., Hamai A., Hervas-Stubbs S., Obeid M., et al. // J. Exp. Med. 2005. V. 202. № 12. P. 1691–1701.
5. Kepp O., Senovilla L., Vitale I., Vacchelli E., Adjemian S., Agostinis P., Apetoh L., Aranda F., Barnaba V., Bloy N., et al. // Oncoimmunology. 2014. V. 3. № 9. P. e955691.
6. Galluzzi L., Bravo-San Pedro J.M., Vitale I., Aaronson S.A., Abrams J.M., Adam D., Alnemri E.S., Altucci L., Andrews D., Annicchiarico-Petruzzelli M., et al. // Cell Death Differ. 2015. V. 22. № 1. P. 58–73.
7. Davidovich P., Kearney C.J., Martin S.J. // Biol. Chem. 2014. V. 395. № 10. P. 1163–1171.
8. Scheffer S.R., Nave H., Korangy F., Schlote K., Pabst R., Jaffee E.M., Manns M.P., Greten T.F. // Int. J. Cancer. 2003. V. 103. № 2. P. 205–211.
9. Tesniere A., Schlemmer F., Boige V., Kepp O., Martins I., Ghiringhelli F., Aymeric L., Michaud M., Apetoh L., Barault L., et al. // Oncogene. 2010. V. 29. № 4. P. 482–491.
10. Menger L., Vacchelli E., Adjemian S., Martins I., Ma Y., Shen S., Yamazaki T., Sukkurwala A.Q., Michaud M., Mignot G., et al. // Sci. Transl. Med. 2012. V. 4. № 143. P. 143ra99.

11. Panaretakis T., Kepp O., Brockmeier U., Tesniere A., Bjorklund A.-C., Chapman D.C., Durchschlag M., Joza N., Pierron G., van Endert P., et al. // EMBO J. 2009. V. 28. № 5. P. 578–590.
12. Galluzzi L., Vitale I., Warren S., Adjemian S., Agostinis P., Martinez A.B., Chan T.A., Coukos G., Demaria S., Deutsch E., et al. // J. Immunother. Cancer. 2020. V. 8. № 1. P. e000337.
13. Bezu L., Sauvat A., Humeau J., Gomes-da-Silva L.C., Iribarren K., Forveille S., Garcia P., Zhao L., Liu P., Zitvogel L., et al. // Cell Death Differ. 2018. V. 25. № 8. P. 1375–1393.
14. Garg A.D., Agostinis P. // Immunol. Rev. 2017. V. 280. № 1. P. 126–148.
15. Rufo N., Garg A.D., Agostinis P. // Trends in Cancer. 2017. V. 3. № 9. P. 643–658.
16. Garg A.D., Krysko D.V., Verfaillie T., Kaczmarek A., Ferreira G.B., Marysael T., Rubio N., Firczuk M., Mathieu C., Roebroek A.J.M., et al. // EMBO. 2012. V. 31. № 5. P. 1062–1079.
17. Sukkurwala A.Q., Martins I., Wang Y., Schlemmer F., Ruckenstuhl C., Durchschlag M., Michaud M., Senovilla L., Sistigu A., Ma Y., et al. // Cell Death Differ. 2014. V. 21. № 1. P. 59–68.
18. Tufi R., Panaretakis T., Bianchi K., Criollo A., Fazi B., Di Sano F., Tesniere A., Kepp O., Paterlini-Brechot P., Zitvogel L., et al. // Cell Death Differ. 2008. V. 15. № 2. P. 274–282.
19. Moserova I., Truxova I., Garg A.D., Tomala J., Agostinis P., Cartron P.F., Vosahlikova S., Kovar M., Spisek R., Fucikova J. // Oncoimmunology. 2017. V. 6. № 1. P. e1258505.
20. Colangelo T., Polcaro G., Ziccardi P., Muccillo L., Galgani M., Pucci B., Rita Milone M., Budillon A., Santopaolo M., Mazzoccoli G., et al. // Cell Death Dis. 2016. V. 7. № 2. P. e2108–e2108.
21. Liu C.-C., Leclair P., Pedari F., Vieira H., Monajemi M., Sly L.M., Reid G.S., Lim C.J. // Front. Oncol. 2019. V. 9. P. 411.
22. Chen X., Fosco D., Kline D.E., Kline J. // Oncoimmunology. 2017. V. 6. № 4. P. e1278332.
23. Obeid M., Tesniere A., Ghiringhelli F., Fimia G.M., Apetoh L., Perfettini J.-L., Castedo M., Mignot G., Panaretakis T., Casares N., et al. // Nature Medicine. 2007. V. 13. № 1. P. 54–61.
24. De Boo S., Kopecka J., Brusa D., Gazzano E., Matera L., Ghigo D., Bosia A., Riganti C. // Mol. Cancer. 2009. V. 8. P. 108.
25. Martins I., Kepp O., Schlemmer F., Adjemian S., Tailler M., Shen S., Michaud M., Menger L., Gdoura A., Tajeddine N., et al. // Oncogene. 2011. V. 30. № 10. P. 1147–1158.
26. Garg A.D., Krysko D.V., Vandenabeele P., Agostinis P. // Oncoimmunology. 2012. V. 1. № 5. P. 786–788.
27. Fucikova J., Kralikova P., Fialova A., Brtnicky T., Rob L., Bartunkova J., Spisek R. // Cancer Research. 2011. V. 71. № 14. P. 4821–4833.
28. Martins I., Tesniere A., Kepp O., Michaud M., Schlemmer F., Senovilla L., Séror C., Métivier D., Perfettini J.-L., Zitvogel L., et al. // Cell Cycle. 2009. V. 8. № 22. P. 3723–3728.
29. Krysko D.V., Garg A.D., Kaczmarek A., Krysko O., Agostinis P., Vandenabeele P. // Nat. Rev. Cancer. 2012. V. 12. № 12. P. 860–875.
30. Inoue H., Tani K. // Cell Death Differ. 2014. V. 21. № 1. P. 39–49.
31. Yatim N., Jusforgues-Saklani H., Orozco S., Schulz O., Barreira da Silva R., Reis e Sousa C., Green D.R., Oberst A., Albert M.L. // Science. 2015. V. 350. № 6258. P. 328–334.
32. Bedard K., Szabo E., Michalak M., Opas M. // Int. Rev. Cytol. 2005. V. 245. P. 91–121.
33. Pawaria S., Binder R.J. // Nat. Commun. 2011. V. 2. № 1. P. 521.
34. Zitvogel L., Apetoh L., Ghiringhelli F., Kroemer G. // Nat. Rev. Immunol. 2008. V. 8. № 1. P. 59–73.
35. Apetoh L., Ghiringhelli F., Tesniere A., Obeid M., Ortiz C., Criollo A., Mignot G., Maiuri M.C., Ullrich E., Saulnier P., et al. // Nat. Med. 2007. V. 13. № 9. P. 1050–1059.
36. Chekeni F.B., Ravichandran K.S. // J. Mol. Med. (Berl.). 2011. V. 89. № 1. P. 13–22.
37. Vacchelli E., Galluzzi L., Eggermont A., Galon J., Tartour E., Zitvogel L., Kroemer G. // Oncoimmunology. 2012. V. 1. № 4. P. 493–506.
38. Lewin B., Cassimeris W., Lingappa P., Poppe, D. Cell. Transl. from eng. M.: Binom. 2011. 952 p.
39. Corbett E.F., Michalak M. // Trends Biochem. Sci. 2000. V. 25. № 7. P. 307–311.
40. Michalak M., Groenendyk J., Szabo E., Gold L.I., Opas M. // Biochem. J. 2009. V. 417. № 3. P. 651–666.
41. Mery L., Mesaeli N., Michalak M., Opas M., Lew D.P., Krause K.H. // J. Biol. Chem. 1996. V. 271. № 16. P. 9332–9339.
42. Gao B., Adhikari R., Howarth M., Nakamura K., Gold M.C., Hill A.B., Knee R., Michalak M., Elliott T. // Immunity. 2002. V. 16. № 1. P. 99–109.
43. Gardai S.J., McPhillips K.A., Frasch S.C., Janssen W.J., Starefeldt A., Murphy-Ullrich J.E., Bratton D.L., Oldenborg P.-A., Michalak M., Henson P.M. // Cell. 2005. V. 123. № 2. P. 321–334.
44. Gold L.I., Rahman M., Blechman K.M., Greives M.R., Churgin S., Michaels J., Callaghan M.J., Cardwell N.L., Pollins A.C., Michalak M., et al. // J. Investig. Dermatol. Symp. Proc. 2006. V. 11. № 1. P. 57–65.
45. Goicoechea S., Pallero M.A., Eggleton P., Michalak M., Murphy-Ullrich J.E. // J. Biol. Chem. 2002. V. 277. № 40. P. 37219–37228.
46. Asadzadeh Z., Safarzadeh E., Safaei S., Baradaran A., Mohammadi A., Hajiasgharzadeh K., Derakhshani A., Argentiero A., Silvestris N., Baradaran B. // Cancers (Basel). 2020. V. 12. № 4. P. 1047.
47. Medina C.B., Ravichandran K.S. // Cell Death Differ. 2016. V. 23. № 6. P. 979–989.
48. Elliott M.R., Chekeni F.B., Trampont P.C., Lazarowski E.R., Kadl A., Walk S.F., Park D., Woodson R.I., Ostankovich M., Sharma P., et al. // Nature. 2009. V. 461. № 7261. P. 282–286.
49. Bours M.J.L., Swennen E.L.R., Di Virgilio F., Cronstein B.N., Dagnelie P.C. // Pharmacol. Ther. 2006. V. 112. № 2. P. 358–404.
50. Trautmann A. // Sci. Signal. 2009. V. 2. № 56. P. e6.
51. Agresti A., Bianchi M.E. // Curr Opin Genet. Dev. 2003. V. 13. № 2. P. 170–178.
52. Landsman D., Bustin M. // Bioessays. 1993. V. 15. № 8. P. 539–546.
53. Scaffidi P., Misteli T., Bianchi M.E. // Nature. 2002. V. 418. № 6894. P. 191–195.
54. Luo Y., Chihara Y., Fujimoto K., Sasahira T., Kuwada M., Fujiwara R., Fujii K., Ohmori H., Kuniyasu H. // Eur. J. Cancer. 2013. V. 49. № 3. P. 741–751.
55. Vu M., Kassouf N., Ofili R., Lund T., Bell C., Appiah S. // International Journal of Oncology. 2020. V. 57. № 1. P. 113–121.
56. Hartl F.U. // Nature. 1996. V. 381. № 6583. P. 571–579.
57. Buchner J. // Trends in Biochemical Sciences. 1999. V. 24. № 4. P. 136–141.
58. Wu J., Liu T., Rios Z., Mei Q., Lin X., Cao S. // Trends Pharmacol Sci. 2017. V. 38. № 3. P. 226–256.

59. Binder R.J., Srivastava P.K. // Nat. Immunol. 2005. V. 6. № 6. P. 593–599.
60. Dudek-Perić A.M., Ferreira G.B., Muchowicz A., Wouters J., Prada N., Martin S., Kiviluoto S., Winiarska M., Boon L., Mathieu C., et al. // Cancer Res. 2015. V. 75. № 8. P. 1603–1614.
61. Galluzzi L., Buqué A., Kepp O., Zitvogel L., Kroemer G. // Cancer Cell. 2015. V. 28. № 6. P. 690–714.
62. Twyman-Saint Victor C., Rech A.J., Maity A., Rengan R., Pauken K.E., Stelekati E., Benci J.L., Xu B., Dada H., Odorizzi P.M., et al. // Nature. 2015. V. 520. № 7547. P. 373–377.
63. Quail D.F., Joyce J.A. // Cancer Cell. 2017. V. 31. № 3. P. 326–341.
64. Ngwa W., Irabor O.C., Schoenfeld J.D., Hesser J., Demaria S., Formenti S.C. // Nat. Rev. Cancer. 2018. V. 18. № 5. P. 313–322.
65. Menger L., Vacchelli E., Adjemian S., Martins I., Ma Y., Shen S., Yamazaki T., Sukkurwala A.Q., Michaud M., Mignot G., et al. // Science Translational Medicine. 2012. V. 4. № 143. P. 143ra99-143ra99.
66. Spisek R., Charalambous A., Mazumder A., Vesole D.H., Jagannath S., Dhodapkar M.V. // Blood. 2007. V. 109. № 11. P. 4839–4845.
67. Senovilla L., Vitale I., Martins I., Tailler M., Pailleret C., Michaud M., Galluzzi L., Adjemian S., Kepp O., Niso-Santano M., et al. // Science. 2012. V. 337. № 6102. P. 1678–1684.
68. Huang F.-Y., Lei J., Sun Y., Yan F., Chen B., Zhang L., Lu Z., Cao R., Lin Y.-Y., Wang C.-C., et al. // OncoImmunology. 2018. V. 7. № 7. P. e1446720.
69. Zhu H., Shan Y., Ge K., Lu J., Kong W., Jia C. // Cell Oncol. (Dordr.). 2020. V. 43. № 6. P. 1203–1214.
70. Sun L., Shen F., Tian L., Tao H., Xiong Z., Xu J., Liu Z. // Adv. Mater. 2021. V. 33. № 18. P. e2007910.
71. Liu X., Jiang J., Chang C.H., Liao Y.-P., Lodico J.J., Tang I., Zheng E., Qiu W., Lin M., Wang X., et al. // Small. 2021. V. 17. № 14. P. e2005993.
72. Wen C.-C., Chen H.-M., Chen S.-S., Huang L.-T., Chang W.-T., Wei W.-C., Chou L.-C., Arulselvan P., Wu J.-B., Kuo S.-C., et al. // Journal of Biomedical Science. 2011. V. 18. № 1. P. 44.
73. Xiang Y., Chen L., Li L., Huang Y. // ACS Appl. Mater. Interfaces. 2020. V. 12. № 1. P. 1606–1616.
74. Forveille S., Zhou H., Sauvat A., Bezu L., Müller K., Liu P., Zitvogel L., Pierron G., Rekdal O., Kepp O., et al. // Cell Cycle. 2015. V. 14. № 21. P. 3506–3512.
75. Eike L.-M., Yang N., Rekdal O., Sveinbjørnsson B. // Oncotarget. 2015. V. 6. № 33. P. 34910–34923.
76. Pasquereau-Kotula E., Habault J., Kroemer G., Poyet J.-L. // PLoS ONE. 2018. V. 13. № 8. P. e0201220.
77. Jagot-Lacoussiere L., Kotula E., Villoutreix B.O., Bruzzoni-Giovanelli H., Poyet J.-L. // Cancer Res. 2016. V. 76. № 18. P. 5479–5490.
78. Duewell P., Steger A., Lohr H., Bourhis H., Hoelz H., Kirchleitner S.V., Stieg M.R., Grassmann S., Kobold S., Siveke J.T., et al. // Cell Death Differ. 2014. V. 21. № 12. P. 1825–1837.
79. Koval O.A., Tkachenko A.V., Fomin A.S., Semenov D.V., Nushtaeva A.A., Kuligina E.V., Zavjalov E.L., Richter V.A. // PLoS ONE. 2014. V. 9. № 4. P. e93921.
80. Semenov D.V., Fomin A.S., Kuligina E.V., Koval O.A., Matveeva V.A., Babkina I.N., Tikunova N.V., Richter V.A. // Protein J. 2010. V. 29. № 3. P. 174–180.
81. Troitskaya O., Varlamov M., Nushtaeva A., Richter V., Koval O. // Molecules. 2020. V. 25. № 12. P. 2804.
82. Donnelly O.G., Errington-Mais F., Steele L., Hadac E., Jennings V., Scott K., Peach H., Phillips R.M., Bond J., Pandha H., et al. // Gene Ther. 2013. V. 20. № 1. P. 7–15.
83. Miyamoto S., Inoue H., Nakamura T., Yamada M., Sakamoto C., Urata Y., Okazaki T., Marumoto T., Takahashi A., Takayama K., et al. // Cancer Res. 2012. V. 72. № 10. P. 2609–2621.
84. Heinrich B., Klein J., Delic M., Goepfert K., Engel V., Geberzahn L., Lusky M., Erbs P., Preville X., Moehler M. // OTT. 2017. V. 10. P. 2389–2401.
85. Ma J., Ramachandran M., Jin C., Quijano-Rubio C., Martikainen M., Yu D., Essand M. // Cell Death Dis. 2020. V. 11. № 1. P. 48.
86. Dai P., Wang W., Yang N., Serna-Tamayo C., Ricca J.M., Zamarin D., Shuman S., Merghoub T., Wolchok J.D., Deng L. // Sci. Immunol. 2017. V. 2. № 11. P. eaal1713.
87. Koval O., Kochneva G., Tkachenko A., Troitskaya O., Sivolobova G., Grazhdantseva A., Nushtaeva A., Kuligina E., Richter V. // BioMed Research International. 2017. V. 2017. P. 1–14.
88. Kochneva G., Sivolobova G., Tkacheva A., Grazhdantseva A., Troitskaya O., Nushtaeva A., Tkachenko A., Kuligina E., Richter V., Koval O. // Oncotarget. 2016. V. 7. № 45. P. 74171–74188.
89. Koks C.A., Garg A.D., Ehrhardt M., Riva M., Vandenberk L., Boon L., De Vleeschouwer S., Agostinis P., Graf N., Van Gool S.W. // Int. J. Cancer. 2015. V. 136. № 5. P. E313–325.
90. Diaconu I., Cerullo V., Hirvinen M.L.M., Escutenaire S., Ugolini M., Pesonen S.K., Bramante S., Parviainen S., Kanerva A., Loskog A.S.I., et al. // Cancer Res. 2012. V. 72. № 9. P. 2327–2338.
91. Golden E.B., Demaria S., Schiff P.B., Chachoua A., Formenti S.C. // Cancer Immunol. Res. 2013. V. 1. № 6. P. 365–372.
92. Golden E.B., Frances D., Pellicciotta I., Demaria S., Helen Barcellos-Hoff M., Formenti S.C. // Oncoimmunology. 2014. V. 3. P. e28518.
93. Adkins I., Sadilkova L., Hradilova N., Tomala J., Kovar M., Spisek R. // Oncoimmunology. 2017. V. 6. № 5. P. e1311433.
94. Guo S., Jing Y., Burcus N.I., Lassiter B.P., Tanaz R., Heller R., Beebe S.J. // Int. J. Cancer. 2018. V. 142. № 3. P. 629–640.
95. Zirnheld J.L., Zucker S.N., DiSanto T.M., Berezney R., Etemadi K. // IEEE Trans. Plasma Sci. 2010. V. 38. № 4. P. 948–952.
96. Georgescu N., Lupu A.R. // IEEE Trans. Plasma Sci. 2010. V. 38. № 8. P. 1949–1955.
97. Schweigert I., Zakrevsky D., Gugin P., Yelak E., Golubitskaya E., Troitskaya O., Koval O. // Applied Sciences. 2019. V. 9. № 21. P. 4528.
98. Golubitskaya E.A., Troitskaya O.S., Yelak E.V., Gugin P.P., Richter V.A., Schweigert I.V., Zakrevsky D.E., Koval O.A. // Acta Naturae. 2019. V. 11. № 3. P. 16–19.
99. Liedtke K.R., Bekeschus S., Kaeding A., Hackbarth C., Kuehn J.-P., Heidecke C.-D., von Bernstorff W., von Woedtke T., Partecke L.I. // Scientific Reports. 2017. V. 7. № 1. P. 8319.
100. Chen Z., Lin L., Cheng X., Gjika E., Keidar M. // Biointerphases. 2016. V. 11. № 3. P. 031010.
101. Kumar N., Attri P., Choi E.H., Uhm H.S. // RSC Adv. 2015. V. 5. № 19. P. 14670–14677.
102. Conway G.E., Casey A., Milosavljevic V., Liu Y., Howe O., Cullen P.J., Curtin J.F. // British Journal of Cancer. 2016. V. 114. № 4. P. 435–443.
103. Azzariti A., Iacobazzi R.M., Di Fonte R., Porcelli L., Gristina R., Favia P., Fracassi F., Trizio I., Silvestris N., Guida

G., et al. // Sci. Rep. 2019. V. 9. № 1. P. 4099.
104. Van Loenhout J., Flieswasser T., Freire Boullosa L., De Waele J., Van Audenaerde J., Marcq E., Jacobs J., Lin A., Lion E., Dewitte H., et al. // Cancers. 2019. V. 11. № 10. P. 1597.
105. Troitskaya O., Golubitskaya E., Biryukov M., Varlamov M., Gugin P., Milakhina E., Richter V., Schweigert I., Zakrevsky D., Koval O. // IJMS. 2020. V. 21. № 14. P. 5128.
106. Lin A.G., Xiang B., Merlino D.J., Baybutt T.R., Sahu J., Fridman A., Snook A.E., Miller V. // OncoImmunology. 2018. V. 7. № 9. P. e1484978.
107. Baryshnikov A.Y. // Practical oncology. 2003. V. 4. № 3. P. 127–130.
108. Gabrilovich D.I., Ostrand-Rosenberg S., Bronte V. // Nat. Rev. Immunol. 2012. V. 12. № 4. P. 253–268.
109. Munn D.H. // Science. 1998. V. 281. № 5380. P. 1191–1193.
110. Soliman H., Mediavilla-Varela M., Antonia S. // The Cancer Journal. 2010. V. 16. № 4. P. 354–359.
111. Beckermann K.E., Dudzinski S.O., Rathmell J.C. // Cytokine Growth Factor Rev. 2017. V. 35. P. 7–14.
112. Chao M.P., Jaiswal S., Weissman-Tsukamoto R., Alizadeh A.A., Gentles A.J., Volkmer J., Weiskopf K., Willingham S.B., Raveh T., Park C.Y., et al. // Sci. Transl. Med. 2010. V. 2. № 63. P. 63ra94.

Artificial Scaffold Polypeptides As an Efficient Tool for the Targeted Delivery of Nanostructures *In Vitro* and *In Vivo*

V. O. Shipunova*, S. M. Deyev
Shemyakin-Ovchinnikov Institute of Bioorganic Chemistry of the Russian Academy of Sciences, Moscow, 117997 Russia
*E-mail: viktoriya.shipunova@phystech.edu
Received August 4, 2021; in final form, December 20, 2021
DOI: 10.32607/actanaturae.11545

ABSTRACT **The use of traditional tools for the targeted delivery of nanostructures, such as antibodies, transferrin, lectins, or aptamers, often leads to an entire range of undesirable effects. The large size of antibodies often does not allow one to reach the required number of molecules on the surface of nanostructures during modification, and the constant domains of heavy chains, due to their effector functions, can induce phagocytosis. In the recent two decades, targeted polypeptide scaffold molecules of a non-immunoglobulin nature, antibody mimetics, have emerged as much more effective targeting tools. They are small in size (3–20 kDa), possess high affinity (from subnano- to femtomolar binding constants), low immunogenicity, and exceptional thermodynamic stability. These molecules can be effectively produced in bacterial cells, and, using genetic engineering manipulations, it is possible to create multispecific fusion proteins for the targeting of nanoparticles to cells with a given molecular portrait, which makes scaffold polypeptides an optimal tool for theranostics.**
KEYWORDS **nanoparticles, DARPins, affibody, anticalins, scaffold proteins, ADAPT, HER2, HER1, EGFR, EpCAM, conjugation, targeted delivery.**
ABBREVIATIONS **ADP – adenosine diphosphate; LSPR – localized surface plasmon resonance; MAPK – mitogen-activated protein kinase; MRI – magnetic resonance imaging; MNPs – magnetic nanoparticles; PMAO – poly(maleic anhydride/1-octadecene); PEG – polyethylene glycol; PET – positron emission tomography; RNAse – ribonuclease; ADAPT – albumin-binding domain-based scaffold protein; Bs-C-Mms6 – fusion protein of barstar with C-Mms6; DARP – designed ankyrin repeat protein; DARP 9_29–Bn – fusion protein of DARPin 9_29 with barnase; DARP-LoPE – fusion protein of DARPin 9_29 with LoPE; DOTA – dodecanetetraacetic acid; EDC – 1-ethyl-3-(3-dimethylaminopropyl) carbodiimide; eEF2 – eukaryotic elongation factor 2; EGF-1R – insulin-like growth factor 1 receptor; EpCAM – epithelial cell adhesion molecule; EPR – enhanced permeability and retention effect; HER2 – human epidermal growth factor 2 receptor; IgE – immunoglobulin E; IgG – immunoglobulin G; NHS – hydroxysuccinimide; PE, ETA – pseudomonas exotoxin A of *Pseudomonas aeruginosa*; PRINT – particle replication in nonwetting templates; ScFv – a single-chain fragment of the light and heavy chains of immunoglobulin; SBP – silica binding peptide; SPIO – superparamagnetic nanoparticles; TNF-α – tumor necrosis factor; VEGF-A – vascular endothelial growth factor.**

1. INTRODUCTION

Developing novel, highly sensitive diagnostic tools and targeted cancer therapies, as well as improving on the existing ones, is among the main drivers of developments in modern nanobiomedicine. Targeted drug delivery is the key issue in theranostics, with respect to the novel approaches to the design of drugs that would simultaneously act as early diagnostic tools, therapeutic agents, and tools for the monitoring of treatment effectiveness [1, 2].

Nanoparticles differing in their nature are promising objects for the design of theranostic agents (*Fig. 1*). Nanoparticles possess a broad range of unique characteristics: they are small in size, boast

a high ratio of surface area to the number of bulky atoms and can form nanoparticle–ligand complexes, including those with compounds larger than their own size (such as proteins, various drugs, etc.) and selectively deliver them to a specific target, thus implementing the targeted delivery strategy. These, and many other, advantages make nanoparticles excellent diagnostic and therapeutic agents in various areas of medicine (in particular, for the detection and optical imaging of malignant tumors and targeted drug delivery). However, several factors limit the successful implementation of nanobiocomplexes in clinical practice. In particular, constructs that are characterized by minimal toxicity, high specificity in target recognition, and maximum therapeutic and targeting efficacy are not always available. Meanwhile, such complexes are expected to be characterized by low immunogenicity so as to make possible the performing of multiple courses of therapy.

More than 20 nanoparticle-based drugs are currently used for tumor treatment, and a number of agents are in the late phases of clinical trials. The efficacy of these drugs (e.g., liposomal doxorubicin Myocet (non-PEGylated liposomal formulation) or Caelix (polyethylene glycol-coated liposomal doxorubicin)) or micellar paclitaxel (Genexol-PM) is based on the effect of enhanced permeability and retention (EPR) of tumor vessels. Because there is high demand for oxygen and blood supply, a new vascular network develops in the tumor. This network is constituted by defective endothelial cells with wide fenestrations (up to 4 μm); the vessels do not possess a smooth muscle layer, and endothelial cells lack angiotensin II receptors. Due to the impaired lymphatic efflux observed in the 150- to 200-μm tumor cell aggregates surrounded by this vascular network, molecules and nanostructures with a size of up to 150 nm can stay near the tumor and exert their therapeutic effect.

However, the EPR effect is characterized by significant heterogeneity (both between different tumor models and even within the same tumor) and is pronounced much stronger in rodents with tumor xenografts than it is in human tumors. This is related to the slower tumor growth rate in humans and formation of a normal vascular network with a well-developed lymphatic efflux compared to rapidly proliferating tumors in rodents [3, 4]. Meanwhile, even for a really strong EPR effect (e.g., for rapidly progressive Kaposi sarcoma), only a small number of injected nanoparticles (< 0.7%) get inside a tumor [5]. The following nanobiomedicine-related problems are yet to be solved: the treatment of aggressive metastatic cancer [6], integration of the methods of personalized noninvasive diagnosis and therapy [7], and the generation of physiologically relevant xenograft animal models [4].

There exist different approaches to targeted drug delivery to the tumor, which mainly consist in improving the efficiency in their binding to cancer cells, endothelial cells or immune cells [8], as well as drug internalization by the cell and its controlled release (including upon exposure to external factors: light, pH, temperature, electromagnetic fields, etc.) [9–13]. The nanostructure surface is modified using targeting agents of differing nature, such as antibodies and their derivatives [14, 15], transferrin, the epidermal growth factor, lectins [16], molecules based on DNA/RNA (aptamers and protein–nucleic acids), low-molecular-weight compounds (folic acid, saccharides (e.g., galactosamine)), etc.

The application of these molecules elicits a full range of undesirable effects. Thus, the large size of IgG antibodies often prevents an efficient use of the surface of modified nanostructures; the heavy chain constant domains exhibit effector functions that can induce phagocytosis and cause inflammation without being involved in selective target recognition, or induce undesirable *in vivo* immunomodulation. The size of an antibody limits the diffusion of its molecules deep inside a tumor.

Targeted polypeptide scaffold molecules of a non-immunoglobulin nature, which are produced by phage, cell surface, or ribosome display techniques, appear to be more efficient tools in targeting nanostructures to target cells. These polypeptides are produced by mutagenesis of the protein motifs involved in the protein–protein interactions in living systems. Affibodies and DARPins are the most vivid examples of this group of targeting compounds (*Fig. 1*).

2. THE MAIN STRUCTURAL CHARACTERISTICS OF SCAFFOLD PROTEINS AND THEIR ADVANTAGES OVER FULL-LENGTH ANTIBODIES

The hybrid technology for producing monoclonal antibodies, which was described by Georges Köhler and César Milstein and for which they were awarded the Nobel Prize in Physiology or Medicine in 1984, has enabled significant advances in the implementation of the concept of the "magic bullet." This concept was formulated by Paul Ehrlich and consists in developing an efficient way to deliver a therapeutic agent exclusively to the disease site without affecting healthy tissues or triggering undesired harmful effects. More than eight dozen antibodies have been clinically tested and approved for clinical use. However, even these antibodies cause a broad range of undesirable effects,

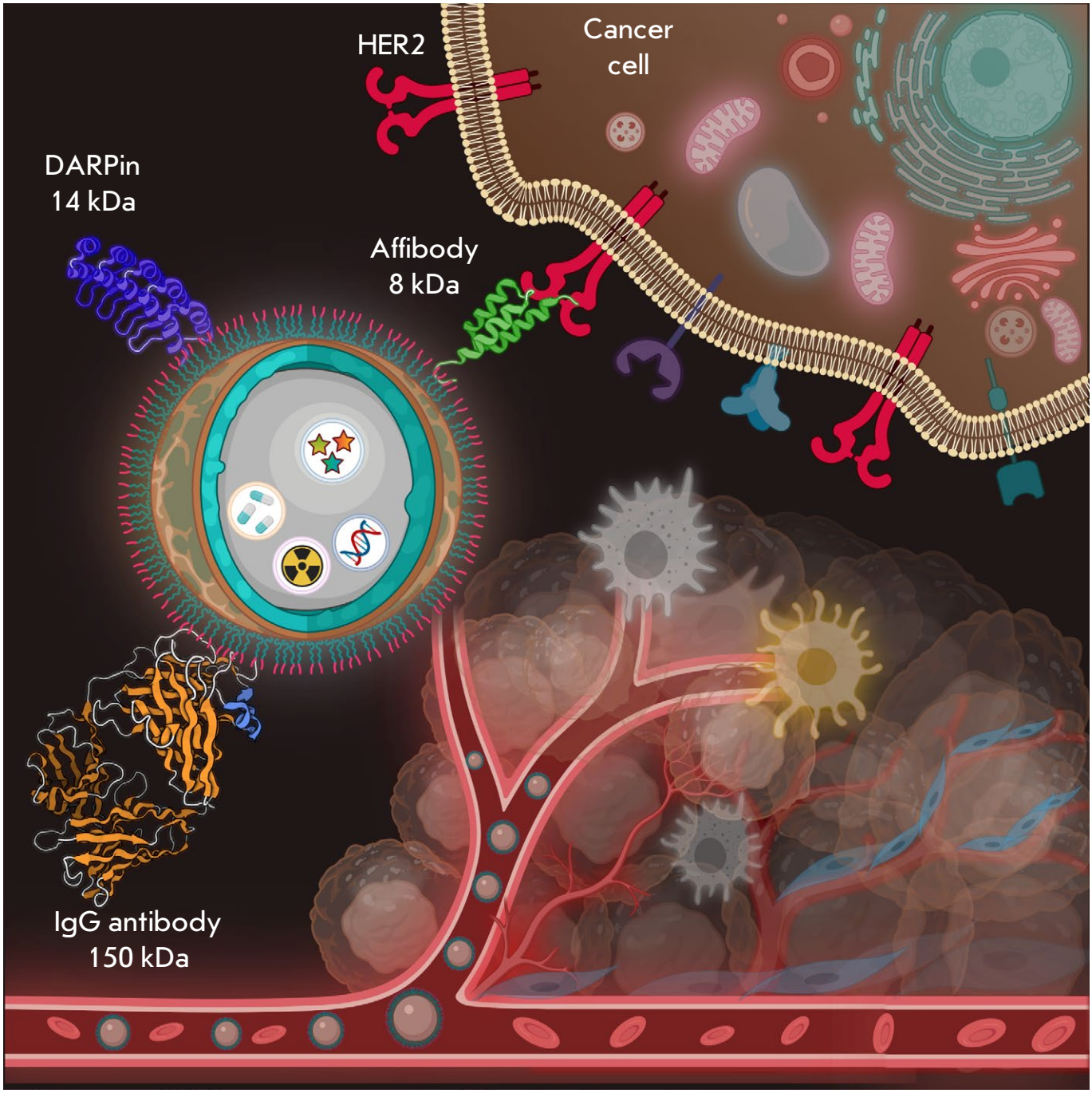

Fig. 1. Nanoparticles as a platform for the design of theranostics tools. The scheme shows a core–shell nanoparticle, which is a matrix for loading both diagnostic (fluorescent or radioactive) and therapeutic compounds (chemotherapeutic substances and genes). The nanoparticle surface is modified with various targeting compounds: antibodies (IgG, 150 kDa) or scaffold polypeptides (DARPins (14 kDa) or affibodies (8 kDa)) are conventionally used. The diagram shows the nanostructures targeting the HER2 tumor marker, which is overexpressed on the surface of human breast cancer cells. The plot was created using Biorender.com

which has inspired intensive efforts in synthetic biology focusing on the design of recognition scaffold proteins.

Various recognition scaffold proteins have been designed over the past 20 years, largely thanks to the synthetic library technology. Similar to antibodies, these proteins have a conserved scaffold region and a variable recognition region. Specifically binding scaffold proteins are usually designed using combinatorial libraries that contain sets of genes differing in their variable regions. In particular, proteins based on the domains of lipocalin, zinc fingers, Src homology domains, PDZ domains, Kunitz-type serine protease inhibitor domains, cystatins, DNA-binding protein Sac7d, A-domains of various membrane receptors, gamma-B-crystallin and ubiquitin-binding domains, etc. are being developed. More than 20 classes of antibody mimetics have been designed thus far; the key ones are listed in *Table*.

The aforementioned proteins are small in size (8–20 kDa) and are characterized by high affinity for molecular targets (subnano–femtomolar binding constants), as well as optimal biochemical and thermodynamic characteristics. They remain stable for a long time at high temperatures (up to 80°C), low pH (up to pH 2), and upon exposure to chaotropic agents. The incorporation of cysteine residues into these proteins both yields dimers with target characteristics and allows one to perform regioselective protein modification using various compounds via disulfide bond formation. The low immunogenicity of proteins due to their synthetic nature allows one to use them for therapeutic purposes, especially when a single therapy course is insufficient for achieving remission and repeated injection of the drug is needed.

All classes of these proteins have free N- and C-termini lying outside the recognition sequence, which enables efficient chemical conjugation of the proteins to the polymers on the nanoparticle surface, as well as the production of genetically engineered constructs (such as fusion proteins consisting of scaffolds and protein toxins) for therapeutic applications. The small size of scaffolds makes it possible to significantly increase the number of their molecules tethered to the nanoparticle surface compared to IgG. Only DARPins, affibodies and albumin-binding domain (ABD) derivatives are commonly used today for the delivery of nanoparticles to molecular targets (*Fig. 2*). A number of studies focusing on the engineering of nanoparticles for targeted delivery based on repebodies [49–51], affimers [52], affitins [53–55], and knottins [56] have also been conducted.

3. DARPINS AS A TOOL FOR THE TARGETED DELIVERY OF NANOPARTICLES

DARPins (Designed Ankyrin Repeat Proteins), or ankyrin repeat proteins, are unique tools for solving problems related to personified medicine and fundamental research in molecular and cellular biology [57, 58]. These proteins are based on ankyrin repeats: a series of tightly packed repeats, each consisting of approximately 33 amino acid residues. In turn, each repeat consists of two α-helices connected by a short loop and one β-turn joining this repeat to the next one. Proteins with ankyrin repeats form a dexiotropic solenoid that contains a long hydrophobic backbone and a hydrophilic surface accessible to the solvent [59]. They often mediate protein–protein interactions inside the cell (e.g., when acting as cytoskeleton proteins, transcriptional initiators or cell cycle regulators). Proteins carrying four to six repeats commonly occur in nature, but sometimes the number of repeats can exceed 29. Seven amino acid residues in the repeat (six residues in the β-turn and one in the helix) form the binding surface. When constructing recombinant libraries, random substitutions are inserted into the codons encoding these residues. DARPins are often selected using the ribosome display technology. DARPins are typically formed by two or three (sometimes four) repeats sequentially located between the N- and C-termini. The molecular weight of these scaffold proteins depends on the number of repeats and is 14–18 kDa if a scaffold protein consists of two or three repeats. DARPins are extremely thermostable proteins that can withstand quite harsh conditions: heating to 90°C and exposure to proteases or chaotropic agents. DARPins specific for membrane-bound tumor markers (EpCAM, VEGF-A, HER2, as well as for the maltose-binding protein, MAP kinase, caspase 2, IgE antibody, and CD4) have been obtained [35, 60–62].

Since DARPins have a rather rigid framework and recognizing surface, steric challenges often occur upon target recognition. A novel, similar class of compounds, LoopDARPins, with soft protruding recognizing loops that do not disrupt the structure of the scaffold protein, has been designed to solve this problem [63].

3.1. DARPins conjugated to magnetic nanostructures for targeted drug delivery

A series of studies [64–68] have demonstrated that magnetic nanostructures represented by superparamagnetic iron oxide nanoparticles can be successfully modified with the DARPin G3 and DARPin 9_29 molecules [69], which selectively recognize the clinically relevant tumor marker HER2 (human epider-

The key representatives of scaffold proteins (antibody mimetics)

Proteins	Protein platform: a scaffold	Molecular weight, kDa	Representative references
Avimers	Domain A of extracellular receptors	4	[17, 18]
Adhirons	Phytocistatin domain	10	[19]
Adnectins (monobodies)	Fibronectin type III domain (FN3)	10	[20–22]
Atrimers	Tetranectin CTLD	60–70	[23]
Anticalins	Lipocalin domains	20	[24, 25]
Affibodies	Z domain of protein A derived from the Staphylococcus aureus cell wall	6	[26]
Affilins	Gamma-B-crystallin/ubiquitin domains	20 /10	[27, 28]
Affimers	Domains of cystatin, a cysteine protease inhibitor	12	[29, 30]
Affitins (Nanofitins)	Domains of DNA-binding protein Sac7d	7	[31–33]
DARPins	Drosophila ankyrin repeat	14–18	[34–37]
Knottins	Disulfide-rich peptide toxins	3	[38]
OBodies	Aspartyl-tRNA synthetase anticodon recognition domain	10	[39]
Kunitz domain polypeptides	Kunitz domain of serine proteases	6	[40]
Pronectins	Human fibronectin domain 14	75	[41]
Repebodies	Leucin-rich repeats of variable lymphocyte receptors	3–30	[42]
Fynomers	SH3-domain of Fyn kinase (Src homology domain)	7	[43]
Centyrins	FN3 domains of tenascin C	9	[44]
ADAPT (ABD-Derived Affinity Proteins)	Albumin-binding domain of protein G	5	[45]
NanoCLAMP (nano-CLostridial Antibody Mimetic Proteins)	Carbohydrate-binding domain of hyaluronidase of *Clostridium perfringens* hyaluronidase	16	[46]
ARM (Armadillo Repeat Proteins)	Drosophila proteins carrying the armadillo domain	39	[47]
PDZ proteins	PSD-95/Discs-large/ZO-1 domains	10	[48]

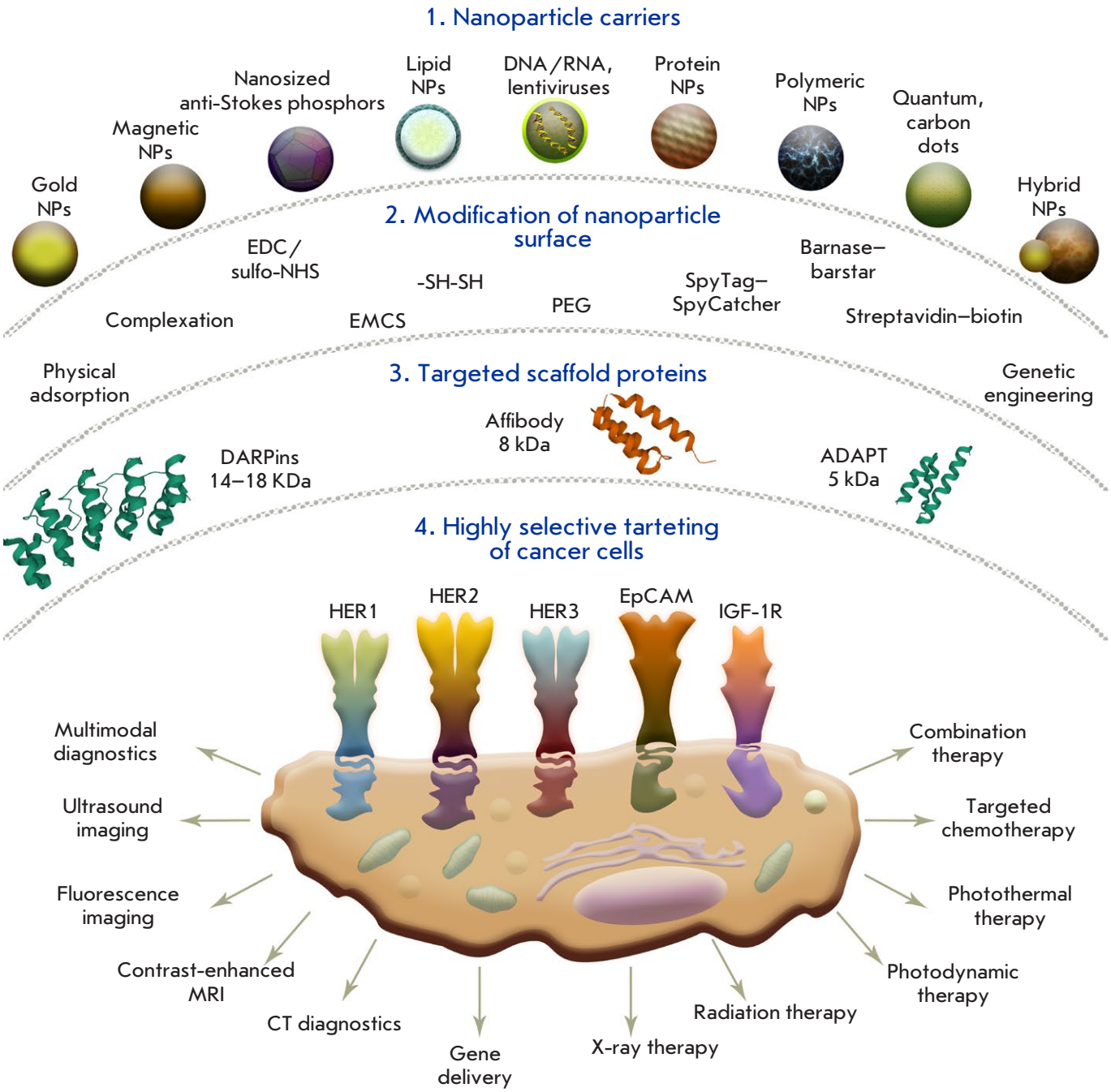

Fig. 2. Artificial scaffold polypeptides for the targeted delivery of nanocarriers to target cells. **1** – A wide range of nanoparticles that are used for diagnostic and therapeutic applications. **2** – Methods for surface modification with targeting molecules: physical adsorption, chemical conjugation, protein adapter systems, and genetic engineering. **3** – Scaffold proteins already used for the targeted delivery of nanoparticles: DARPins, affibodies, and ADAPT. **4** – Targeted delivery of nanoparticles to the receptors of cancer cells for different applications: diagnostics, including the multimodal one, and therapy, including the combined one

mal growth factor receptor 2). DARPin_G3 binds to the domain IV of the HER2 receptor (residing in close proximity to the membrane) with K = 0.070 nM [61], while DARPin_9.29 binds to domain I of the HER2 receptor (being most distant from the membrane) with K = 3.8 nM [34].

The *ERBB2* gene encoding HER2 plays an important role in the development of malignant tumors in humans. This gene is amplified in approximately 20–30% of all breast cancer cases and in many other types of malignant tumors. HER2 overexpression often correlates with a high metastatic potential and chemotherapy resistance of the tumor; it also presages a high risk of disease recurrence and a reduced overall survival rate for patients.

The HER2 molecule is already used as a target for the targeted therapy of breast and gastric cancer with humanized anti-HER2 antibodies: trastuzumab (Herceptin, Herclon) and pertuzumab (Perjeta, Omnitarg) [70, 71]. Unfortunately, the mechanisms related to the recruitment of complement molecules and cytotoxic leukocytes to cancer cells are insufficient to completely eliminate the tumor: so, targeted agents containing additional toxic compounds are needed. Thus, trastuzumab conjugated to a microtubule assembly inhibitor (trastuzumab emtansine, Kadcyla), which actually increases the effectiveness of the therapy for HER2-positive tumors, is used to treat HER2-positive breast and gastric cancer.

There is an urgent need for novel therapies for this disease that would be more effective. HER2-targeted nanoparticles exhibiting diagnostic and therapeutic properties seem to be among the most promising tools in our efforts to develop novel cancer treatment strategies.

Magnetic nanoparticles conjugated to DARPin G3 and DARPin 9_29 have proved to be effective for the theranostics of HER2-positive tumors. Thus, magnetic nanoparticles–DARPin G3 complexes targeting HER2 on the surface of the SK-BR-3 human breast adenocarcinoma cell line were obtained via chemical conjugation. This has enabled *in vivo* fluorescence and magnetic resonance imaging of HER2-overexpressing tumors [64].

Chemical conjugation of DARPin 9_29 to magnetic particles did not result in selective binding of nanoparticles to the target cells [67, 68]. Direct conjugation of small molecules to the nanoparticle surface seems to cause such problems as (1) partial protein denaturation on the nanoparticle surface, (2) binding through multiple amino groups and non-oriented attachment, and (3) steric hindrance upon target recognition. These problems have been solved using protein adapter systems. In particular, the high-affinity barnase:barstar protein pair was used as a mediator between the nanoparticle surface and the DARPin molecule.

The barnase-barstar pair is a unique tool for the design of multifunctional biomedical agents [72–74]. Barstar (10 kDa) is a natural inhibitor of barnase, a bacterial ribonuclease (12 kDa). These proteins are characterized by an extremely high affinity (the binding constant $K_b \sim 10^{14}$ M^{-1}) and fast interaction kinetics (the complexation rate constant $k_{on} \sim 10^8$ $M^{-1}s^{-1}$), while the absence of these proteins in mammalian cells allows one to use them in the bloodstream without any potential complications related to competitive binding to endogenous blood components. Their small size and high binding constant make these proteins the ideal "molecular glue" in designing various self-assembling structures based on different modules, where one module (e.g., the therapeutic one) contains one component of the system (e.g., barstar), while the other module (e.g., DARPin) contains the other component (e.g., barnase). This "LEGO" approach allows one to avoid the standard problems related to chemical conjugation of the components to the nanostructures and obtain biologically active structures simply by mixing the components (e.g., nanoparticle–barstar + barnase–DARPin).

In particular, a novel, universal method for the biomodification of nanostructures of different nature has been developed; this method consists in using peptides that bind the solid phase and the barnase:barstar protein module [68]. It involves non-covalent modification of the nanoparticle surface with a peptide binding the SiO_2 surface of nanoparticles $(VKTQATSREEPPRLPSKHRPG)_4VKTQTAS$ (silica-binding peptide, SBP) genetically fused to barstar (SBP-Bs). The efficiency of the proposed method was confirmed by the obtaining fluorescent and magnetic nanoparticles modified with DARPin 9_29 recognizing the HER2 tumor marker and by targeted delivery of these nanoparticles to the HER2-overexpressing cancer cells. Fusion proteins consisting of the SiO_2-binding polypeptide and barstar (SBP-Bs), as well as those formed by DARPin 9_29 and barnase (DARPin 9_29-Bn), were produced and characterized to implement this approach. In both proteins, the functional modules are connected by a protease-resistant flexible peptide linker to preserve their functional activity. The targeted nanoparticles were obtained by self-assembly of two components: nanoparticles with barstar and the targeted DARPin with barnase. This approach turned out to be much more efficient in the recognition of the tar-

get (HER2 on the cell surface) compared to chemical conjugation.

This approach is rather versatile: the components of the adapter system containing barnase or barstar can be easily replaced. Twelve methods for the targeted delivery of nanoparticles modified with targeted polypeptides through barnase:barstar in different ways have been described [68]. The C-terminal motif of the Mms6 protein, one of the magnetosome membrane proteins in magnetotactic bacteria, was also used as a polypeptide that mediates protein binding in the barnase:barstar adapter system to the nanoparticle surface [67]. The self-assembled constructs based on MNPs-Bs-C-Mms6-DARP 9_29-Bn magnetite nanoparticles were used for targeted delivery to HER2-overexpressing SK-BR-3 cells. These constructs were shown to be efficient for selective *in vitro* labeling and imaging of HER2-positive cells [65, 67].

3.2. Modification of gold nanostructures with DARPins

Nanosized objects acquire unusual quantum chemical properties differing from those of large samples, making it possible to design multifunctional therapeutic and diagnostic tools [75–78]. One of such interesting properties is the effect of localized surface plasmon resonance (LSPR) in gold and silver nanostructures, as well as in hybrid ones (e.g., core–shell nanostructures).

The LSPR phenomenon relies on the resonant excitation of plasmons (quasiparticles being quanta of free-electron vibrations at the interface between two phases having different refractive indices provided that the total internal reflection condition is met). If the conditions of LSPR are met, the intensity of the reflected light drops abruptly as the energy of the incident electromagnetic wave is transformed into plasmon energy. The absorbed energy can be converted into thermal energy: so, the hyperthermal properties of the sample with LSPR are implemented, which can be used in the therapy of tumors whose cells are highly sensitive to heating.

Basic research addresses the properties of LSPR nanostructures (mainly formed by gold and silver, as well as other, less conventional materials, such as aluminum, copper, palladium, and platinum). In particular, gold nanoparticles sized 5 nm and modified with DARP 9_29 have been obtained [79]. The non-covalent stabilization of uncoated gold nanoparticles using DARP 9_29 molecules has given rise to colloidally stable complexes containing target molecules capable of selective recognition of the surface of HER2-expressing cancer cells. A similar modification method has been used to produce gold nanorods 50 nm long and 7 nm in diameter for *in vitro* targeted delivery to HER2-positive cells and their selective destruction by photothermically induced local hyperthermia upon 20-min excitation (wavelength, 850 nm; intensity, 30 mW/cm^2) [80]. The efficiency of the designed targeted nanorods for local hyperthermia has been confirmed by the fact that irradiation caused almost 100% death of exclusively HER2-overexpressing cells, while non-irradiated cells and cells exhibiting negligible HER2 expression remained fully viable.

3.3. Modification of upconversion nanoparticles with DARPins

Upconversion nanoparticles (nanosized anti-Stokes phosphors) are photoluminescent nanoparticles that convert lower-energy electromagnetic radiation (having a longer wavelength) into higher energy electromagnetic radiation (having a shorter wavelength) [81–85]. Nanosized anti-Stokes phosphors are $NaYF_4$ crystals doped with rare-earth elements: namely, Yb^{3+}, Er^{3+}, and Tm^{3+}. These nanostructures absorb several low-energy photons and re-emit one high-energy photon, thus implementing the upconversion phenomenon, where the emission wavelength is shifted toward shorter wavelengths (the blue shift or anti-Stokes shift) while most fluorescence processes in living systems involve the Stokes shift (the red shift). Nanosized phosphors are synthesized in such a way that excitation occurs in the biotissue transparency window (~ 980 nm), while emission occurs in the short-wave range suitable for most imaging devices to work with living objects both *in vitro* and *in vivo*. Nanosized anti-Stokes phosphors are excellent labels for *in vivo* imaging, since their long-lasting photoluminescence and time-resolved signal acquisition make it possible to completely eliminate biotissue autofluorescence and record a real signal without noise with a high sensitivity, so that even a single particle can be registered.

The $NaYF_4$:Yb,Er,Tm/$NaYF_4$ core/shell nanosized phosphors were coated with anti-HER2 DARPin DARPin 9_29 and used for targeted delivery to a HER2-positive cancer cell culture and for the imaging of tumor xenografts in animals for at least 24 h. A comprehensive preclinical study of the overall and specific toxicity of these nanostructures was performed, including an assessment of their allergenic, immunotoxic, and reprotoxic properties. The experimental results suggest that both non-targeted and targeted nanosized phosphors are functional, non-cytotoxic, biocompatible and safe for *in vitro* imaging of cells and *in vivo* imaging of tumors [86–88].

In order to ensure an additional therapeutic modality of nanophosphors, their surface was modified with the DARPin 9_29 protein fused with a low-immunogenicity fragment of the pseudomonad exotoxin A, LoPE, using genetic engineering techniques [89]. The resulting DARP-LoPE protein possesses all the qualities needed for theranostics: it is capable of targeted interaction with target cells and is cytotoxic upon binding to cells.

Exotoxin A of *Pseudomonas aeruginosa* (PE, ETA) is one of the most efficient apoptosis inducers owing to its enzymatic activity, which inhibits translation. PE consists of three domains: domain I is responsible for toxin binding and penetration into the cell; domain II participates in the intracellular transport of the toxin; and domain III possesses intrinsic enzymatic activity. It catalyzes the ADP-ribosylation of eukaryotic eEF2, thus inhibiting protein biosynthesis in the cell and eventually causing its death [90]. The truncated variants of this toxin (namely, the catalytic domain coupled to targeting modules characterized by different specificities) are used for designing efficient PE-based immunotoxins. HER2-recognizing DARPin-based immunotoxins coupled to a variant of the C-terminal (effector) fragment of PE (LoPE), with mutations in immunodominant human B-cell epitopes, have been obtained [91]. The immunogenicity and systemic toxicity of this fragment are lower than those of the unmodified fragment.

DARP-LoPE immunotoxin, a targeting cytotoxic protein, was conjugated to the surface of nanosized anti-Stokes phosphors using carbodiimide and an intermediate linker, polyethylene glycol. The as-synthesized nanosized phosphors were coated with PMAO, an alternating maleic anhydride–1-octadecene copolymer, and polyethylene glycol to ensure a greater colloidal stability [89]. The cytotoxicity of the targeting nanosized phosphor–PEG–DARP–LoPE complexes was studied for SK-BR-3-Kat cells. The half-maximum inhibitory concentration (IC50) of these complexes is 0.4 μg/mL, while IC50 = 200 μg/mL in the control CHO cells not expressing HER2, which proves that the resulting compounds exhibit targeted cytotoxicity.

Targeted cytotoxicity was significantly enhanced by using yttrium-90 as a beta emitter in nanosized phosphors. Radioactive nanosized anti-Stokes phosphors with a beta emitter (having a half-life of 63 h, which is optimal for biomedicine applications) and those modified with a DARP 9_29 fusion protein carrying a fragment of pseudomonad exotoxin A (PE) were synthesized [92]. Combining the two therapeutic modalities in a single nanoparticle yields a strong synergistic effect: the IC50 values of the targeted nanoparticles and nanoparticles doped with yttrium-90 were 5.2 and 140 μg/mL, respectively; the half-maximal inhibitory concentration of the nanoparticles containing a targeting module and yttrium-90 decreased significantly: IC50 = 0.0024 μg/mL [92].

3.4. Lipid nanostructures conjugated to DARPins

Lipid structures such as single-layered liposomes and exosomes were used as study objects to solve the problems of cancer theranostics.

Liposomes (117 ± 41 nm in size) loaded with an RNase barnase and chemically conjugated to anti-HER2 DARPin 9_29 were obtained [93, 94]. There is interest in RNases as a non-mutagenic alternative to the conventional chemotherapeutics. However, many mammalian RNases are not potent toxins, since they are significantly suppressed by the ribonuclease inhibitor that is present in the cytoplasm of mammalian cells. The ribonuclease barnase stands out, because it is not mutagenic, does not have severe toxic side effects, and once it has penetrated the cell, it cleaves RNA and causes cell death. The human ribonuclease inhibitor does not suppress barnase activity. Barnase causes degradation of low-molecular-weight RNAs (namely, tRNA and 5.8S rRNA, but not 5S rRNA). Upon internalization, barnase causes plasma membrane blebbing and apoptosis via internucleosomal chromatin cleavage. Therapy of HER2-positive BT474 xenograft tumors using liposomes loaded with barnase and modified with anti-HER2 DARPin in laboratory animals proved effective. The IC50 of barnase within the targeted liposomes was 0.11 nM for a BT474 cell culture *in vitro*; the *in vivo* efficacy of tumor growth inhibition was 84%. A combined treatment with the targeted liposomes and the targeted immunotoxin based on LoPE and DARPin EC1 inhibited tumor growth by 91.8% and completely prevented the appearance of metastases [94].

DARP EC1 binds to the EpCAM receptor with a picomolar affinity (K_d = 68 pM). EpCAM, a transmembrane glycoprotein with a molecular weight of 40 kDa and consisting of 314 amino acid residues, was first discovered as a tumor antigen in colon cancer cells in 1979. The key function of EpCAM is to provide intercellular communication. The EpCAM molecule is also often expressed in human breast cancer cells, which is associated with a poor prognosis. Thus, the findings of an extensive study showed that EpCAM expression is detected in 48% of human breast cancer cases [95]. Similarly to HER2, EpCAM is already employed as a target in monoclonal antibody-based immunotherapy (using Removab). In connection to this, it seems promising to combine different methods of affecting malignant tumors using scaffold proteins that target

both HER2 and EpCAM to develop effective cancer treatment strategies.

Along with barnase-loaded liposomes, 90-nm liposomes loaded with PE40 and modified with DARP 9_29 were obtained [96]. These liposomes were used to selectively kill HER2-overexpressing cells (IC50 = 0.17 nM for SK-BR-3 cells and 0.21 nM for SK-OV-3 cells) [96].

An elegant approach to designing targeted lipid nanoparticles is to employ natural mechanisms for obtaining nanoparticles that have already been modified and do not require chemical conjugation. In particular, exosomes from HEK293T cells transduced with lentivirus, with the gene encoding HER2-detecting DARPin DARP G3 inserted, have been obtained [97]. These exosomes bound specifically to SK-BR-3 cells and have ensured targeted delivery of small interfering RNAs against the TPD52 gene, thus down-regulating the gene's expression by 70% [97].

3.5. Nucleic acid delivery using DARPins

It has been demonstrated that DARPins can be used for the targeted delivery of genetic material into eukaryotic cells. Lentiviruses displaying HER2-targeting DARPins DARP G3, DARP H14R, DARP 9_29, DARP 9_26, DARP 9_16, and DARP 9_01 on their surface have been obtained [98]. DARPin 9_29 turned out to be the most effective DARPin both in terms of its content on the virus surface and the transduction of HER2-positive cells. DARPins were more effective than the previously used scFv mini-antibody, a HER2-targeting single-chain fragment of the light and heavy chains of 4D5 immunoglobulin [98].

DARPins were used to deliver small interfering RNAs complementary to mRNA of the Bcl-2 apoptosis regulator [99]. Dimers of DARPin EC1 fused with protamine 1, a small protein that forms a complex with nucleic acids, were used. Protamine 1 bound four to five small interfering RNA molecules and retained its specificity of binding to the EpCAM receptor on the MCF-7 cell surface. This made it possible to perform targeted transfection of exclusively EpCAM-overexpressing cancer cells and effectively inhibit the biosynthesis of Bcl-2 [98].

4. AFFIBODIES AS A TOOL FOR TARGETED NANOPARTICLE DELIVERY

Affibodies contain the Z domain of *Staphylococcus aureus* protein A, which consists of 58 amino acid residues forming three α-helices arranged as a barrel. Affibodies are able to withstand high temperatures (~ 90°C) and are resistant to proteolysis and to acidic and alkaline conditions (pH ranging from 2.5 to 11). A range of affibodies specific to a number of molecular targets (HER1, HER2, and TNF-α) has recently been obtained. The $Z_{HER2:342}$ affibody (also known as ABY-002), which recognizes HER2 with K_d = 22 pM, is the one that has been studied most intensively [26]. The $Z_{HER2:342}$ affibody binds to subdomain I of HER2 without competing with other compounds targeting HER2 (antibodies trastuzumab or pertuzumab), thus opening up great avenues in the theranostics of cancer.

4.1. Modification of magnetic nanostructures with affibodies

Affibodies are among the most efficient scaffold proteins used for targeting nanoparticles to eukaryotic cells. A comparative study addressing the efficiency of various anti-HER2-targeting molecules in delivering carboxymethyl dextran-stabilized magnetic nanoparticles (sized 25 nm) to HER2-positive cells has been conducted [66]. The affibody-modified nanoparticles are most suitable for both the magnetic detection and fluorescence imaging of cells using nanoparticles. The reason for that is the small size of $Z_{HER2:342}$ affibody (8 kDa) compared to that of other molecules: DARPin DARP G3 (14 kDa) and trastuzumab antibody (150 kDa); so, a greater number of active molecules can be bound to the nanoparticle surface [66].

The effectiveness of affibodies is confirmed by the findings of numerous fundamental studies [100, 101]. A set of particles was produced to perform visualization and contrast-enhanced magnetic resonance imaging of EGFR- and HER2-positive cells both *in vitro* and *in vivo*. Lanthanide-doped superparamagnetic iron oxide nanoparticles sized 27 nm were obtained to perform a multiplex assay of nanoparticle–cell binding by inductively coupled plasma mass spectrometry. Anti-HER2 affibodies were conjugated to these nanoparticles using the copper-free click-chemistry method [102].

Click reactions (biorthogonal reactions) are characterized by an extremely high yield; they are regioselective and proceed under various conditions, including physiological ones. Azide-alkyne cycloaddition, with copper (I) used as a catalyst, is among the most common click reactions [103–105]. Since protein molecules typically contain neither azide nor alkyne moieties, by inserting these groups into the conjugated components and using this reaction, one obtains full control over conjugation selectivity and efficiency.

Superparamagnetic iron oxide (SPIO) nanoparticles sized 7 nm within 50-nm microemulsions formed by amphiphilic dyes (including photosensitizers), indocyanine green (ICG) and protoporphyrin

IX (PpIX), were used for *in vitro* targeted delivery [106]. SPIO nanoparticles (sized 30 nm) modified with the anti-HER2 affibody using the click chemistry approach were employed for contrast-enhanced magnetic resonance imaging of HER2-overexpressing T6-17 tumors [107]. The number of affibody molecules bound to nanoparticles needed to be optimal, so that target recognition could be ensured and maximum contrast enhancement in MRI achieved. Thus, it was shown by determining the number of affibody molecules on the nanoparticle's surface after the click reaction that 30-nm SPIO nanoparticles carrying 23 anti-HER2 affibody molecules on their surface (the tested range being 6–36 molecules) are the most effective ones [108].

The multifunctionality of magnetic nanostructures was also used for trimodal imaging by 24-nm ^{64}Cu-chelated heterostructures consisting of iron oxide (Fe_3O_4) and gold nanoparticles. Optical, PET, and MRI imaging of EGFR-overexpressing tumors in laboratory animals was carried out using nanoparticles conjugated to the $Z_{EGFR:1907}$ anti-EGFR affibody via the carbodiimide method [109]. Trimodal imaging of tumors by computed tomography, ultrasound imaging, and MRI was also performed. Magnetic nanoparticles sized 10 nm conjugated to $Z_{HER2:342}$ anti-HER2 affibody and labeled with the NIR-830 near-infrared dye were used for this purpose [110, 111]. These particles, loaded with cisplatin, were subsequently used for the *in vivo* photothermal therapy of HER2-positive tumors [112].

Magnetic particles modified with the IGF-1R-targeted $Z_{IGF1R:4551}$ affibody were used for both contrast-enhanced MRI and photoinduced hyperthermia of SW620 tumors upon irradiation with 808-nm light [113].

4.2. Modification of gold nanostructures with affibodies

Silicon-coated gold nanoparticles (sized 140 nm) modified with the $Z_{EGFR:1907}$ anti-EGFR affibody through a heterobifunctional maleimide derivative of PEG were used to selectively label a EGFR-overexpressing cell culture and for *ex vivo* tumor imaging [114]. Complexes that had formed between nanoparticles and cells were detected by both fluorescence microscopy and surface-enhanced Raman scattering [114]. These nanoparticles were shown to be weakly toxic for healthy mice as confirmed by measurement of the biochemical parameters, performance of a immunohistochemical analysis, and measurement of cardiac parameters for 2 weeks after systemic delivery of nanoparticles [115]. Targeted gold nanoparticles have been designed in a number of studies for the diagnosis [110, 116] and therapy of HER2-overexpressing tumors [112, 117].

Along with their contrast-enhancement ability in Raman spectroscopy, gold nanoparticles are efficient X-ray sensitizers. Gold nanoparticles (sized 56 nm) coated with the anti-HER2 affibody were obtained using the carbodiimide method in [118]. When exposed to X-rays (at a dose of 10 Gy), these particles exhibit HER2-specific cytotoxicity; HER2-positive SK-OV-3 cells turned out to be the most sensitive cell line among the ones tested (SK-BR-3, SK-OV-3, HN-5, and MCF-7): their survival rate upon exposure to targeted nanoparticles and X-rays decreased by 63 % [118].

Au-Fe_2C Janus particles sized 12 nm were synthesized to achieve the maximum efficiency in diagnosis (trimodal imaging) and therapy (photo-induced hyperthermia of the tumor). These particles were coated with the $Z_{HER2:342}$ anti-HER2 affibody and used for *in vivo* trimodal tumor detection (MRI, photoacoustic imaging and computed tomography) and for *in vivo* 808-nm induced hyperthermia of cancer cells in HER2-overexpressing xenograft models [119].

A more elegant approach to obtaining nanoparticles with a narrow size distribution was developed based on protein nanoparticles formed by the hepatitis B virus capsid displaying affibody molecules on its surface. Gold was reduced, giving rise to gold nanoparticles sized 1–3 nm on the surface of the viral particles that had already been obtained. These EGFR-specific heterostructures sized 40 nm are effective both for cancer cell imaging via Cy5.5 labeling and for the hyperthermic effect on EGFR-overexpressing MDA-MB-468 tumor cells [120].

4.3. Modification of the anti-Stokes nanostructures of affibodies

Upconversion nanoparticles are efficient diagnostic tools. They allow the high-sensitivity visualization of biological objects without significant autofluorescence interference [121]. $NaYF_4:Tm^{+3},Yb^{+3}$ nanoparticles covalently modified with anti-EGFR affibodies have been obtained for the visualization of EGFR-expressing tumors *in vivo* [122]. Upconversion nanoparticles with a more complex architecture have been synthesized for photodynamic therapy of EGFR-overexpressing tumors [123]. Complex superstructures with an upconverting $NaYF_4$,Yb,Er core surrounded by zinc-based organometallic framework structures were obtained. The self-assembly of such structures was performed using complementary DNA strands. When these structures are excited by external IR light, the upconverting core emits visible light, thereby exciting the organometallic frameworks that can

produce reactive oxygen species and act as therapeutic agents [123].

4.4. Affisomes

Compounds based on affibody-conjugated liposomes are known as affisomes [124, 125]. A number of liposomes covalently modified with the $Z_{HER2:342}$ anti-HER2 affibody [126] and via a polyethyleneglycol linker ($Z_{HER2:477}$ anti-HER2 affibody [124], $(Z_{00477})_2$-Cys [127], and $(Z_{EGFR:955})_2$ anti-EGFR affibody [128]) have been obtained and used to treat HER2- and EGFR-positive tumors.

4.5. Complexes of polymeric nanostructures and affibodies

Various materials (gold, carbon, magnetite, silicon, etc.) are used for synthesizing nanoparticles. Biocompatible polymers stand out in terms of their structural and functional characteristics: e.g., poly(lactic-co-glycolic acid) (PLGA), which is already used in diagnosis and therapy. PLGA is gradually degraded to lactic and glycolic acids and is excreted from the body. Various PLGA polymers containing free carboxyl and amino groups have been synthesized, opening up avenues for particle modification with molecules that recognize tumor antigens. PLGA nanoparticles sized 140 nm and loaded with the Nile Red fluorescent dye and doxorubicin were obtained. These nanoparticles were stabilized with chitosan and conjugated to the $Z_{HER2:342}$ anti-HER2 affibody by EDC/sulfo-NHS coupling. The PLGA–$Z_{HER2:342}$ nanoparticles were used to label HER2-overexpressing cancer cells both *in vitro* and *in vivo*. The specificity of these nanoparticles was higher than that of the control non-targeted nanoparticles more than 60-fold. The PLGA–$Z_{HER2:342}$ nanoparticles were used to affect the cells either alone or in combination with the DARP-LoPE-targeted bifunctional immunotoxin (42 kDa). Combination therapy using DARP-LoPE and PLGA–$Z_{HER2:342}$ was shown to reduce the effective immunotoxin concentration 1,000-fold *in vitro*. This dual-targeting strategy improved the efficacy of the anti-tumor therapy of HER2-positive cells *in vivo* [6]. The synthesis and surface modification method was further employed to design nanoparticles loaded with a rose bengal photosensitizer agent. When irradiated at the 532-nm wavelength, these nanoparticles produce reactive oxygen species, killing HER2-overexpressing cancer cells [129].

Nanoparticles consisting of hybrid polymers are also being intensively studied. Polymeric nanoparticles formed by poly(lactide-co-glycolide)-block-poly(ethylene glycol) have been obtained, modified with the $Z_{HER2:342}$ anti-HER2 affibody by maleimide-based chemical conjugation, and loaded with paclitaxel. These nanoparticles were used to selectively kill HER2-overexpressing cells *in vitro* [130].

A large number of nanoparticles (in which a polymer is the matrix for synthesizing and incorporating both soluble and insoluble compounds) have been developed. Meanwhile, the polymeric materials can *per se* have a diagnostic and therapeutic significance: they can possess fluorescence properties or photothermal conversion ability [131]. Thus, 30-nm nanoparticles based on polymers poly[9,9-bis(2-(2-(2-methoxyethoxy)ethoxy)ethyl)fluoroenyldivinylene]-alt-4,7-(2,1,3-benzothiadiazole) exhibiting fluorescent properties in the near-red spectral range and photosensitizing properties and poly[(4,4,9,9-tetrakis(4-(octyloxy)phenyl)-4,9-dihydro-s-indacenol-dithiophene-2,7-diyl)-alt-co-4,9-bis(thiophen-2-yl)-6,7-bis(4-(hexyloxy)phenyl)thiadiazole-quinoxaline] possessing strong near-infrared absorption and excellent photothermal conversion ability have been designed for theranostic purposes. These particles are characterized by a quantum yield of 60.4% and efficient photothermal conversion of 47.6%. The use of two types of impact (photodynamic and photothermal) was shown to have a synergistic effect in tumor therapy [132, 133]. Fluorescent hyperbranched polyelectrolyte core/shell complexes sized 30 nm were also obtained. A fluorescent polymer with the emission maximum at 565 nm, produced by polycyclotrimerization of alkynes, was used as a core; polyethylene glycol was used as a shell. These polyelectrolyte complexes were coated with an anti-HER2 affibody by carbodiimide conjugation and used as efficient fluorescent tags for the imaging of SK-BR-3 cells [134].

Nanobubbles, a unique class of contrast agents used for *in vivo* contrast-enhanced ultrasound imaging, stand out among polymeric nanomaterials [135]. Thus, 480-nm nanobubbles consisting of the phospholipid shell, filled with C_3F_8 gas and coated with anti-HER2 affibody using the streptavidin–biotin system have been obtained [136].

Particles of different shapes (80×320 and 55×60 nm) synthesized using the PRINT technology (particle replication in nonwetting templates) were modified with anti-EGFR affibodies with different affibody densities on the nanoparticle surface. Significant differences in the accumulation of both types of nanoparticles in the tumor depending on the affibody density were observed *in vivo*. The maximum ratio between the nanoparticle contents in the tumor and in blood was achieved for the particles where the amount of the ligand was maximal [137].

4.6. Complexes of protein nanoparticles and affibodies

In clinical practice, the biocompatibility and biodegradability of protein nanoparticles make them the leading diagnostic and therapeutic drugs. Meanwhile, the advances in genetic engineering allow us to generate fully genetically encoded fusion proteins with the desired functional characteristics without the need to use chemical conjugation techniques.

Albumin-based nanoparticles are among the most popular protein nanoparticles. They were modified with an anti-HER2 affibody using a bacterial superglue, the SpyTag (ST)/SpyCatcher (SC) protein adapter system derived from the split protein CnaB2 of *Streptococcus pyogenes*. SpyTag (a 13-amino acid peptide) and SpyCatcher (a 15-kDa protein) bind through a covalent peptide bond. The SpyTag/SpyCatcher system was used as a molecular mediator between the nanoparticle surface and the affibody molecule, thus ensuring that the affibody is attached regioselectively to the nanoparticle with an almost 100% efficiency. These nanoparticles were loaded with an indocyanine green photosensitizer and used for photothermally induced death of HER2-overexpressing cancer cells [138].

The SpyTag/SpyCatcher system was also successfully used to modify nanoparticles based on encapsulin [139, 140] and lumazine synthase [141]. Encapsulin (Encap) is a nanoparticle-forming protein isolated from the thermophilic bacteria *Thermotoga maritima*, the study of which began relatively recently. The encapsulin-SpyTag fusion protein has been obtained; this protein forms 35-nm nanoparticles with one of the elements of the adaptor system, ST [140]. Anti-HER2–anti-EGFR affibody proteins fused with the second component of the protein pair (SC) were also obtained. These fusion proteins were fluorescently tagged with two different dyes and doped with nanoparticles; specific bimodal fluorescence detection of cells characterized by different levels of HER2 and EGFR expression was then performed [140]. In a similar manner, nanoparticles based on lumazine synthase from *Aquifex aeolicus* (AaLS) and loaded with the gadolinium complex (Gd(III)-DOTA) were used for contrast-enhanced MRI of tumors characterized by different HER2 and EGFR expressions in mice [141].

Self-assembled protein nanoparticles (e.g., those based on hepatitis B virus capsid) are often used for both gene and protein delivery [142–148]. Viral capsid-based nanoparticles (sized 28 nm) loaded with the mCardinal far-red fluorescent protein and modified with the anti-HER2 affibody were engineered. *In vivo* tests showed that the particles actively accumulated in the tumor, while accumulating in the liver much less intensively compared to nanoparticles loaded with the conventional dyes (namely, Cy5.5) [142].

Human ferritin nanoparticles (sized 12 nm) consisting of 24 subunits of ferritin heavy chains fused with an anti-EGFR affibody by the genetic engineering technique have been obtained. These particles were labeled with a Cy5.5 near-red dye and used to visualize EGFR-overexpressing cells [149]. To ensure longer term *in vivo* circulation of ferritin nanostructures in the bloodstream, the following modifications were made: hydrophobic sequences were inserted into the structure so that a hydration shell was formed (this effect was similar to that of nanoparticle PEGylation) [150]. This approach has enhanced the accumulation of nanoparticles in the tumor twofold as confirmed by intravital imaging using the Cy5.5 dye [150].

It was found that 90-nm camptothecin-loaded mesoporous silicon nanoparticles coated with a protein corona formed by a glutathione-S-transferase/anti-HER2 affibody fusion protein bind to serum proteins to a significantly lower extent, thus minimizing the nanoparticle uptake by macrophages [151]. Such particles labeled with a DiI fluorescent dye and loaded with camptothecin, a cytotoxic quinoline alkaloid inhibiting topoisomerase I, were used for imaging and inhibiting tumor growth *in vivo* with 90% efficiency [151].

4.7. Modification of tetrahedral DNA complexes with affibody molecules

Many publications have addressed the development of systems for the targeted delivery of genetic material. For example, $Z_{HER2:2891}$ anti-HER2 affibody molecules bound to the polyethylene glycol–polyethyleneimine copolymer were used to deliver the luciferase gene into HER2-overexpressing BT474 cells. The luminescence intensity of the transfected HER2-overexpressing cells was shown to be higher than that of the control MDA-MB-231 cells, characterized by a moderate HER2 expression of more than 300-fold [152].

DNA can carry not only genetic information, but also chemotherapeutic drugs. In particular, DNA tetrahedra (3D structures produced from 20 bp DNA double helices using the DNA origami method) act as scaffolds. DNA tetrahedra chemically modified with the anti-HER2 affibody via maleimide conjugation and loaded with doxorubicin (53 doxorubicin molecules per complex) [153] inhibited cell growth significantly stronger compared to doxorubicin, while being much less toxic to cells with a normal HER2 expression level. Similar cisplatin-loaded nanoparticles (68 cisplatin

molecules per nanoparticle) were used to selectively kill HER2-positive cells with an almost 100% efficiency level [154].

A fusion protein consisting of the $Z_{HER2:342}$ affibody and RALA peptide, an efficient nonviral agent for nucleic acid delivery into cells, was also obtained. The affibody and the peptide were connected by a flexible protease-resistant glycine–serine linker $(G_4S)_3$. The resulting fusion peptide is associated with $FUdR_{15}$, a sequence of 15 residues of 5-fluorodeoxyuridine that is metabolized into a 5-fluorouracil chemotherapeutic agent [155]. The resulting system has a targeted impact on HER2-overexpressing N87 cells and leads to their apoptosis [155]. Subsequently, the targeted delivery mechanisms elaborated in the reviewed studies [154, 155] were combined into the DNA tetrahedron-based system for the delivery of FUdR to the cells of a tumor induced by the injection of BT474 cells; this system slowed down tumor progression approximately 2.5-fold [156].

4.8. Modification of quantum dots with affibodies

Quantum dots are fluorescent semiconductor nanocrystals (with a core sized 1–12 nm) synthesized from group II and VI elements (e.g., ZnS, CdSe or CdTe) or, less frequently, group III and V (InP) or group IV and VI (PbS, PbSe, or PbTe) elements. They differ from the conventional fluorophores such as organic dyes and fluorescent proteins in terms of their broad absorption band, significant Stokes shift, narrow emission spectrum, and high quantum yield (up to 80%), as well as high photostability [157, 158]. The significant dependence of the emission wavelength on the particle size makes it possible to perform multicolor labeling and simultaneous identification of different biological objects. However, the toxicity of QDs significantly limits the scope of their *in vivo* application for therapeutic purposes. The use of QDs for sentinel lymph node mapping is much more promising, since in this case the drug is injected locally and the metastatic lymph node is subsequently resected.

In particular, quantum dots QD655 modified with the $Z_{HER2:477}$ anti-HER2 affibody through the streptavidin–biotin system have been used for diagnostic purposes. These quantum dots have been applied for the immunohistochemical staining of tumor cross-sections to successfully identify the HER2 status of the tumor, as well as the presence and localization of HER2 homodimers, by confocal and electron microscopy [159, 160].

Quantum dots QD800 sized 5 nm (core/shell/shell = InAs/InP/ZnSe) conjugated to the $Z_{HER2:342}$ anti-HER2 affibody through a heterobifunctional PEG derivative carrying a terminal amino group were used for *in vivo* imaging. The affibody was modified with cysteine at its N-terminus, and the chemical conjugation reaction was performed using 4-maleimidobutyric acid N-succinimidyl ester. Anti-HER2 quantum dots were employed for selective real-time imaging of SK-OV-3 tumors in immunodeficient mice using an intravital imaging system [161]. The accumulation of targeted quantum dots in the tumor was shown to be approximately threefold higher than that of non-targeted ones [161].

$Z_{EGFR:1907}$ anti-EGFR affibody was adsorbed onto the surface of 8 nm silver sulfide (Ag_2S) quantum dots, and the modified particles were used for photoacoustic imaging of EGFR-overexpressing tumors [162]. The same quantum dots coated with IGF-1R-recognizing affibody, ZIGF1R, were used *in vivo* for bimodal photoacoustic imaging and near-infrared imaging of tumors in immunodeficient animals [163].

Carbon dots possessing a broad range of unique optical characteristics have found a wide application. Thus, not only do 20 nm gadolinium-encapsulated Gd@C carbon dots possess bright fluorescence, but they also exhibit MRI contrast properties [164]. These dots were coated with $Z_{EGFR:1907}$ anti-EGFR affibody and used for both *in vitro* and *in vivo* targeted delivery. It was shown *in vitro* that the MRI signal for HCC827 cells ($EGFR^+$) is significantly higher than that for NCI-H520 cells ($EGFR^-$). These structures are also efficient for *in vivo* targeted tumor imaging 1 h post-injection (MRI signals for HCC827 and NCI-H520 tumors differed by a factor of 1.5). Furthermore, Gd@C quantum dots with $Z_{EGFR:1907}$ are efficiently excreted by the kidneys, unlike Gd@C dots [164].

5. TARGETED ANTIBODIES BASED ON ADAPT PROTEINS

The high affinity constants of proteins based on albumin-binding domains (ABDs) ADAPT have made it possible to design an ultrasensitive method for detecting HER2 in the samples containing 10% of serum. Thus, QD625 quantum dots have been obtained and modified by HER2-targeting ADAPT6 via self-assembly. The threshold of HER2 detection using these quantum dots was 40×10^{-12} M (≈ 8 ng/mL) [165].

6. CONCLUSIONS

Scaffold proteins can be called next-generation proteins [166–169]. An appreciably large number of medications based on these proteins are currently undergoing clinical trials [170–175], and some of them are already used in theranostics (e.g., ecallantide, a protein based on the Kunitz domain).

Despite such advantages as small size, stable structure, and the simplicity of large-scale biotechnological production, these proteins also have shortcomings when used in combination with functional nanostructures, which are related to regioselective binding to the surface of nanostructures, while the recognition properties are retained. The problems of this kind are solved using various molecular mediators between the nanoparticle surface and protein molecules (e.g., SpyTag–SpyCatcher, barnase/barstar, and streptavidin/biotin), as well as genetic engineering techniques (e.g., incorporation of DARPins into the viral envelope).

Our advances in chemical modification and genetic engineering allow one to produce nanoparticles that are maximally effective only *in vitro*. When targeted nanoparticles are injected systemically into the bloodstream, their accumulation in the tumor is often no more than 2.5 times greater than that in the case of non-targeted nanoparticles; the total accumulation in the tumor is no greater than 0.7% of the injected dose.

Along with the development of targeted agents for the therapy and diagnosis of cancer (as well as cancer theranostics), designing novel methods for nanoparticle administration and delivery is an equally important task in nanobiomedicine. This has received much less attention thus far. In particular, methods for prolonging nanoparticle circulation in the bloodstream are being developed: the mononuclear phagocyte system is suppressed temporarily without any serious side effects.

Since solid tumors are dense heterogeneous structures, the *in vivo* impact of targeted therapeutic agents on cancer cells is meaningful only for the uppermost tumor layers, while deep-lying cells remain viable, thereby neutralizing the effect of the targeted action. Angiogenesis needs to be inhibited (through their impact on endothelial markers), thus disrupting the blood supply to deep-lying cancer cells. ●

This work was supported by the Russian Foundation for Basic Research (project No. 20-14-50514).

REFERENCES

1. Deyev S.M., Lebedenko E.N. // Russ. J. Bioorg. Chem. 2015. V. 41. № 5. P. 481–493.
2. Shilova O.N., Deyev S.M. // Acta Naturae. 2019. V. 11. № 4. P. 42–53.
3. Danhier F. // J. Control. Release. 2016. V. 244. № A. P. 108–121.
4. Lammers T., Kiessling F., Hennink W.E., Storm G. // J. Control. Release. 2012. V. 161. № 2. P. 175–187.
5. Wilhelm S., Tavares A.J., Dai Q., Ohta S., Audet J., Dvorak H.F., Chan W.C.W. // Nat. Rev. Mater. 2016. V. 1. № 5. P. 751.
6. Shipunova V.O., Komedchikova E.N., Kotelnikova P.A., Zelepukin I.V., Schulga A.A., Proshkina G.M., Shramova E.I., Kutscher H.L., Telegin G.B., Kabashin A.V., et al. // ACS Nano. 2020. V. 14. № 10. P. 12781–12795.
7. Nikitin M.P., Shipunova V.O., Deyev S.M., Nikitin P.I. // Nat. Nanotechnol. 2014. V. 9. № 9. P. 716–722.
8. Stepanov A.V., Belogurov A.A., Ponomarenko N.A., Stremovskiy O.A., Kozlov L.V., Bichucher A.M., Dmitriev S.E., Smirnov I.V., Shamborant O.G., Balabashin D.S., et al. // PLoS One. 2011. V. 6. № 6. P. e20991.
9. Zelepukin I.V., Yaremenko A.V., Shipunova V.O., Babenyshev A.V., Balalaeva I.V., Nikitin P.I., Deyev S.M., Nikitin M.P. // Nanoscale. 2019. V. 11. № 4. P. 1636–1646.
10. Zelepukin I.V., Yaremenko A.V., Ivanov I.N., Yuryev M.V., Cherkasov V.R., Deyev S.M., Nikitin P.I., Nikitin M.P. // ACS Nano. 2021. doi: 10.1021/acsnano.1c00687
11. Zelepukin I.V., Yaremenko A.V., Yuryev M.V., Mirkasymov A.B., Sokolov I.L., Deyev S.M., Nikitin P.I., Nikitin M.P. // J. Control. Release. 2020. V. 326. P. 181–191.
12. Nikitin M.P., Zelepukin I.V., Shipunova V.O., Sokolov I.L., Deyev S.M., Nikitin P.I. // Nat. Biomed. Eng. 2020. V. 4. № 7. P. 717–731.
13. Mirkasymov A.B., Zelepukin I.V., Nikitin P.I., Nikitin M.P., Deyev S.M. // J. Control. Release. 2021. V. 330. P. 111–118.
14. Deyev S.M., Lebedenko E.N., Petrovskaya L.E., Dolgikh D.A., Gabibov A.G., Kirpichnikov M.P. // Rus. Chem. Rev. 2015. V. 84. № 1. P. 1–26.
15. Tregubov A.A., Sokolov I.L., Babenyshev A.V., Nikitin P.I., Cherkasov V.R., Nikitin M.P. // J. Magn. Magn. Mat. 2018. V. 449. P. 590–596.
16. Shipunova V.O., Nikitin M.P., Zelepukin I.V., Nikitin P.I., Deyev S.M., Petrov R.V. // Dokl. Biochem. Biophys. 2015. V. 464. P. 315–318.
17. Silverman J., Liu Q., Lu Q., Bakker A., To W., Duguay A., Alba B.M., Smith R., Rivas A., Li P., et al. // Nat. Biotechnol. 2005. V. 23. № 12. P. 1556–1561.
18. Nord K., Nilsson J., Nilsson B., Uhlén M., Nygren P.A. // Protein Eng. 1995. V. 8. № 6. P. 601–608.
19. Tiede C., Tang A.A.S., Deacon S.E., Mandal U., Nettleship J.E., Owen R.L., George S.E., Harrison D.J., Owens R.J., Tomlinson D.C., et al. // Protein Eng. Des. Sel. 2014. V. 27. № 5. P. 145–155.
20. Miller C.J., McGinnis J.E., Martinez M.J., Wang G., Zhou J., Simmons E., Amet T., Abdeen S.J., van Huysse J.W., Bowsher R.R., et al. // New Biotechnol. 2021. V. 62. P. 79–85.
21. Sha F., Salzman G., Gupta A., Koide S. // Protein Sci. 2017. V. 26. № 5. P. 910–924.
22. Koide A., Bailey C.W., Huang X., Koide S. // J. Mol. Biol. 1998. V. 284. № 4. P. 1141–1151.
23. Zelensky A.N., Gready J.E. // FEBS J. 2005. V. 272. № 24. P. 6179–6217.

24. Deuschle F.-C., Ilyukhina E., Skerra A. // Expert Opin. Biol. Ther. 2021. V. 21. № 4. P. 509–518.
25. Rothe C., Skerra A. // BioDrugs. 2018. V. 32. № 3. P. 233–243.
26. Orlova A., Magnusson M., Eriksson T.L.J., Nilsson M., Larsson B., Höidén-Guthenberg I., Widström C., Carlsson J., Tolmachev V., Ståhl S., et al. // Cancer Res. 2006. V. 66. № 8. P. 4339–4348.
27. Ebersbach H., Fiedler E., Scheuermann T., Fiedler M., Stubbs M.T., Reimann C., Proetzel G., Rudolph R., Fiedler U. // J. Mol. Biol. 2007. V. 372. № 1. P. 172–185.
28. Settele F., Zwarg M., Fiedler S., Koscheinz D., Bosse-Doenecke E. // Methods Mol. Biol. 2018. V. 1701. P. 205–238.
29. Kyle S. // Trends Biochem. Sci. 2018. V. 43. № 4. P. 230–232.
30. Markland W., Ley A.C., Ladner R.C. // Biochemistry. 1996. V. 35. № 24. P. 8058–8067.
31. Krehenbrink M., Chami M., Guilvout I., Alzari P.M., Pécorari F., Pugsley A.P. // J. Mol. Biol. 2008. V. 383. № 5. P. 1058–1068.
32. Crook Z.R., Nairn N.W., Olson J.M. // Trends Biochem. Sci. 2020. V. 45. № 4. P. 332–346.
33. Huet S., Gorre H., Perrocheau A., Picot J., Cinier M. // PLoS One. 2015. V. 10. № 11. P. e0142304.
34. Steiner D., Forrer P., Plückthun A. // J. Mol. Biol. 2008. V. 382. № 5. P. 1211–1227.
35. Stefan N., Martin-Killias P., Wyss-Stoeckle S., Honegger A., Zangemeister-Wittke U., Plückthun A. // J. Mol. Biol. 2011. V. 413. № 4. P. 826–843.
36. Stahl A., Stumpp M.T., Schlegel A., Ekawardhani S., Lehrling C., Martin G., Gulotti-Georgieva M., Villemagne D., Forrer P., Agostini H.T., et al. // Angiogenesis. 2013. V. 16. № 1. P. 101–111.
37. Amstutz P., Koch H., Binz H.K., Deuber S.A., Plückthun A. // Protein Eng. Des. Sel. 2006. V. 19. № 5. P. 219–229.
38. Gracy J., Chiche L. // Curr. Pharm. Des. 2011. V. 17. № 38. P. 4337–4350.
39. Steemson J.D., Baake M., Rakonjac J., Arcus V.L., Liddament M.T. // PLoS One. 2014. V. 9. № 1. P. e86050.
40. Hosse R.J., Rothe A., Power B.E. // Protein Sci. 2006. V. 15. № 1. P. 14–27.
41. Škrlec K., Štrukelj B., Berlec A. // Trends Biotechnol. 2015. V. 33. № 7. P. 408–418.
42. Lee S.-C., Park K., Han J., Lee J.-j., Kim H.J., Hong S., Heu W., Kim Y.J., Ha J.-S., Lee S.-G., et al. // Proc. Natl. Acad. Sci. USA. 2012. V. 109. № 9. P. 3299–3304.
43. Grabulovski D., Kaspar M., Neri D. // J. Biol. Chem. 2007. V. 282. № 5. P. 3196–3204.
44. Diem M.D., Hyun L., Yi F., Hippensteel R., Kuhar E., Lowenstein C., Swift E.J., O'Neil K.T., Jacobs S.A. // Protein Eng. Des. Sel. 2014. V. 27. № 10. P. 419–429.
45. Garousi J., Lindbo S., Mitran B., Buijs J., Vorobyeva A., Orlova A., Tolmachev V., Hober S. // Sci. Rep. 2017. V. 7. № 1. P. 14780.
46. Suderman R.J., Rice D.A., Gibson S.D., Strick E.J., Chao D.M. // Protein Expr. Purif. 2017. V. 134. P. 114–124.
47. Coates J. // Trends Cell Biol. 2003. V. 13. № 9. P. 463–471.
48. Schneider S., Buchert M., Georgiev O., Catimel B., Halford M., Stacker S.A., Baechi T., Moelling K., Hovens C.M. // Nat. Biotechnol. 1999. V. 17. № 2. P. 170–175.
49. Kim D., Seo H.-D., Ryu Y., Kim H.-S. // Anal. Chim. Acta. 2020. V. 1126. P. 154–162.
50. Kim J.-W., Heu W., Jeong S., Kim H.-S. // Anal. Chim. Acta. 2017. V. 988. P. 81–88.
51. Lee J.-j., Kang J.A., Ryu Y., Han S.-S., Nam Y.R., Rho J.K., Choi D.S., Kang S.-W., Lee D.-E., Kim H.-S. // Biomaterials. 2017. V. 120. P. 22–31.
52. Khaled Y.S., Shamsuddin S., Tiernan J., McPherson M., Hughes T., Millner P., Jayne D.G. // Eur. J. Surg. Oncol. 2018. V. 44. P. S1.
53. Gaspar D.P., Faria V., Quintas J.P., Almeida A.J. // Curr. Org. Chem. 2017. V. 21. № 23.
54. Resnier P., Lepeltier E., Emina A.L., Galopin N., Bejaud J., David S., Ballet C., Benvegnu T., Pecorari F., Chourpa I., et al. // RSC Adv. 2019. V. 9. № 47. P. 27264–27278.
55. Vukojicic P., Béhar G., Tawara M.H., Fernandez-Villamarin M., Pecorari F., Fernandez-Megia E., Mouratou B. // ACS Appl. Mater. Interfaces. 2019. V. 11. № 24. P. 21391–21398.
56. Klem R., de Ruiter M.V., Cornelissen J.J.L.M. // Mol. Pharm. 2018. V. 15. № 8. P. 2991–2996.
57. Grove T.Z., Cortajarena A.L., Regan L. // Curr. Opin. Struct. Biol. 2008. V. 18. № 4. P. 507–515.
58. Gebauer M., Skerra A. // Annu. Rev. Pharmacol. Toxicol. 2020. V. 60. P. 391–415.
59. Kobe B., Kajava A.V. // Trends Biochem. Sci. 2000. V. 25. № 10. P. 509–515.
60. Grönwall C., Ståhl S. // J. Biotechnol. 2009. V. 140. № 3–4. P. 254–269.
61. Zahnd C., Kawe M., Stumpp M.T., de Pasquale C., Tamaskovic R., Nagy-Davidescu G., Dreier B., Schibli R., Binz H.K., Waibel R., et al. // Cancer Res. 2010. V. 70. № 4. P. 1595–1605.
62. Binz H.K., Amstutz P., Kohl A., Stumpp M.T., Briand C., Forrer P., Grütter M.G., Plückthun A. // Nat. Biotechnol. 2004. V. 22. № 5. P. 575–582.
63. Schilling J., Schöppe J., Plückthun A. // J. Mol. Biol. 2014. V. 426. № 3. P. 691–721.
64. Li D.-L., Tan J.-E., Tian Y., Huang S., Sun P.-H., Wang M., Han Y.-J., Li H.-S., Wu H.-B., Zhang X.-M., et al. // Biomaterials. 2017. V. 147. P. 86–98.
65. Kotelnikova P.A., Shipunova V.O., Aghayeva U.F., Stremovskiy O.A., Nikitin M.P., Novikov I.A., Schulga A.A., Deyev S.M., Petrov R.V. // Dokl. Biochem. Biophys. 2018. V. 481. № 1. P. 198–200.
66. Shipunova V.O., Kolesnikova O.A., Kotelnikova P.A., Soloviev V.D., Popov A.A., Proshkina G.M., Nikitin M.P., Deyev S.M. // ACS Omega. 2021. V. 6. № 24. P. 16000–16008.
67. Shipunova V.O., Kotelnikova P.A., Aghayeva U.F., Stremovskiy O.A., Novikov I.A., Schulga A.A., Nikitin M.P., Deyev S.M. // J. Magn. Magn. Mat. 2019. V. 469. P. 450–455.
68. Shipunova V.O., Zelepukin I.V., Stremovskiy O.A., Nikitin M.P., Care A., Sunna A., Zvyagin A.V., Deyev S.M. // ACS Appl. Mater. Interfaces. 2018. V. 10. № 20. P. 17437–17447.
69. Plückthun A. // Annu. Rev. Pharmacol. Toxicol. 2015. V. 55. P. 489–511.
70. Ignatiadis M., van den Eynden G., Roberto S., Fornili M., Bareche Y., Desmedt C., Rothé F., Maetens M., Venet D., Holgado E., et al. // J. Natl. Cancer Inst. 2019. V. 111. № 1. P. 69–77.
71. Nahta R., Hung M.-C., Esteva F.J. // Cancer Res. 2004. V. 64. № 7. P. 2343–2346.
72. Shipunova V.O., Nikitin M.P., Mironova K.E., Deyev S.M., Nikitin P.I. // IEEE 15th International Conference. Rome, Italy. 2015. P. 13–16.
73. Deyev S.M., Waibel R., Lebedenko E.N., Schubiger A.P., Plückthun A. // Nat. Biotechnol. 2003. V. 21. № 12. P. 1486–1492.
74. Sreenivasan V.K.A., Ivukina E.A., Deng W., Kelf T.A., Zdobnova T.A., Lukash S.V., Veryugin B.V., Stremovskiy

O.A., Zvyagin A.V., Deyev S.M. // J. Mater. Chem. 2011. V. 21. № 1. P. 65–68.
75. Kabashin A.V., Kravets V.G., Wu F., Imaizumi S., Shipunova V.O., Deyev S.M., Grigorenko A.N. // Adv. Funct. Mater. 2019. V. 29. № 26. P. 1902692.
76. Zelepukin I.V., Popov A.A., Shipunova V.O., Tikhonowski G.V., Mirkasymov A.B., Popova-Kuznetsova E.A., Klimentov S.M., Kabashin A.V., Deyev S.M. // Mater. Sci. Eng. C. 2021. V. 120. P. 111717.
77. Belova M.M., Shipunova V.O., Kotelnikova P.A., Babenyshev A.V., Rogozhin E.A., Cherednichenko M.Y., Deyev S.M. // Acta Naturae. 2019. V. 11. № 2. P. 47–53.
78. Zelepukin I.V., Shipunova V.O., Mirkasymov A.B., Nikitin P.I., Nikitin M.P., Deyev S.M. // Acta Naturae. 2017. V. 9. № 4 (35). P. 58–65.
79. Deyev S., Proshkina G., Ryabova A., Tavanti F., Menziani M.C., Eidelshtein G., Avishai G., Kotlyar A. // Bioconjugate Chem. 2017. V. 28. № 10. P. 2569–2574.
80. Proshkina G., Deyev S., Ryabova A., Tavanti F., Menziani M.C., Cohen R., Katrivas L., Kotlyar A. // ACS Appl. Mater. Interfaces. 2019. V. 11. № 38. P. 34645–34651.
81. Grebenik E.A., Kostyuk A.B., Deyev S.M. // Rus. Chem. Rev. 2016. V. 85. № 12. P. 1277–1296.
82. Khaydukov E.V., Mironova K.E., Semchishen V.A., Generalova A.N., Nechaev A.V., Khochenkov D.A., Stepanova E.V., Lebedev O.I., Zvyagin A.V., Deyev S.M., et al. // Sci. Rep. 2016. V. 6. P. 35103.
83. Guller A.E., Generalova A.N., Petersen E.V., Nechaev A.V., Trusova I.A., Landyshev N.N., Nadort A., Grebenik E.A., Deyev S.M., Shekhter A.B., et al. // Nano Res. 2015. V. 8. № 5. P. 1546–1562.
84. Grebenik E.A., Nadort A., Generalova A.N., Nechaev A.V., Sreenivasan V.K.A., Khaydukov E.V., Semchishen V.A., Popov A.P., Sokolov V.I., Akhmanov A.S., et al. // J. Biomed. Opt. 2013. V. 18. № 7. P. 76004.
85. Generalova A.N., Kochneva I.K., Khaydukov E.V., Semchishen V.A., Guller A.E., Nechaev A.V., Shekhter A.B., Zubov V.P., Zvyagin A.V., Deyev S.M. // Nanoscale. 2015. V. 7. № 5. P. 1709–1717.
86. Guryev E.L., Shilyagina N.Y., Kostyuk A.B., Sencha L.M., Balalaeva I.V., Vodeneev V.A., Kutova O.M., Lyubeshkin A.V., Yakubovskaya R.I., Pankratov A.A., et al. // Toxicol. Sci. 2019. V. 170. № 1. P. 123–132.
87. Mironova K.E., Khochenkov D.A., Generalova A.N., Rocheva V.V., Sholina N.V., Nechaev A.V., Semchishen V.A., Deyev S.M., Zvyagin A.V., Khaydukov E.V. // Nanoscale. 2017. V. 9. № 39. P. 14921–14928.
88. Guryev E.L., Smyshlyaeva A.S., Shilyagina N.Y., Sokolova E.A., Shanwar S., Kostyuk A.B., Lyubeshkin A.V., Schulga A.A., Konovalova E.V., Lin Q., et al. // Molecules. 2020. V. 25. № 18. P. 4302.
doi: 10.3390/molecules25184302.
89. Guryev E.L., Smyshlyaeva A.S., Shilyagina N.Y., Shanwar S., Kostyuk A.B., Shulga A.A., Konovalova E.V., Zvyagin A.V., Deyev S.M., Petrov R.V. // Dokl. Biochem. Biophys. 2020. V. 491. № 1. P. 73–76.
90. Shapira A., Benhar I. // Toxins (Basel). 2010. V. 2. № 11. P. 2519–2583.
91. Liu W., Onda M., Lee B., Kreitman R.J., Hassan R., Xiang L., Pastan I. // Proc. Natl. Acad. Sci. USA. 2012. V. 109. № 29. P. 11782–11787.
92. Guryev E.L., Volodina N.O., Shilyagina N.Y., Gudkov S.V., Balalaeva I.V., Volovetskiy A.B., Lyubeshkin A.V., Sen' A.V., Ermilov S.A., Vodeneev V.A., et al. // Proc. Natl. Acad. Sci. USA. 2018. V. 115. № 39. P. 9690–9695.
93. Shipunova V.O., Shramova E.I., Schulga A.A., Shilova M.V., Deyev S.M., Proshkina G.M. // Rus. J. Bioorg. Chem. 2020. V. 46. № 6. P. 1156–1161.
94. Shramova E., Proshkina G., Shipunova V., Ryabova A., Kamyshinsky R., Konevega A., Schulga A., Konovalova E., Telegin G., Deyev S. // Cancers (Basel). 2020. V. 12. № 10. P. 3014.
doi: 10.3390/cancers12103014.
95. Soysal S.D., Muenst S., Barbie T., Fleming T., Gao F., Spizzo G., Oertli D., Viehl C.T., Obermann E.C., Gillanders W.E. // Br. J. Cancer. 2013. V. 108. № 7. P. 1480–1487.
96. Deyev S., Proshkina G., Baryshnikova O., Ryabova A., Avishai G., Katrivas L., Giannini C., Levi-Kalisman Y., Kotlyar A. // Eur. J. Pharm. Biopharm. 2018. V. 130. P. 296–305.
97. Limoni S.K., Moghadam M.F., Moazzeni S.M., Gomari H., Salimi F. // Appl. Biochem. Biotechnol. 2019. V. 187. № 1. P. 352–364.
98. Münch R.C., Mühlebach M.D., Schaser T., Kneissl S., Jost C., Plückthun A., Cichutek K., Buchholz C.J. // Mol. Ther. 2011. V. 19. № 4. P. 686–693.
99. Winkler J., Martin-Killias P., Plückthun A., Zangemeister-Wittke U. // Mol. Cancer Ther. 2009. V. 8. № 9. P. 2674–2683.
100. Pala K., Jakimowicz P., Cyranka-Czaja A., Otlewski J. // Mater. Res. Express. 2015. V. 2. № 4. P. 45403.
101. Vargo K.B., Zaki A.A., Warden-Rothman R., Tsourkas A., Hammer D.A. // Small. 2015. V. 11. № 12. P. 1409–1413.
102. Elias A., Crayton S.H., Warden-Rothman R., Tsourkas A. // Sci. Rep. 2014. V. 4. P. 5840.
103. Kolb H.C., Finn M.G., Sharpless K.B. // Angew. Chem. 2001. V. 40. № 11. P. 2004–2021.
104. Rostovtsev V.V., Green L.G., Fokin V.V., Sharpless K.B. // Angew. Chem. Int. Ed. 2002. V. 41. № 14. P. 2596–2599.
105. Tornøe C.W., Christensen C., Meldal M. // J. Org. Chem. 2002. V. 67. № 9. P. 3057–3064.
106. Amirshaghaghi A., Altun B., Nwe K., Yan L., Stein J.M., Cheng Z., Tsourkas A. // J. Am. Chem. Soc. 2018. V. 140. № 42. P. 13550–13553.
107. Elias D.R., Cheng Z., Tsourkas A. // Small. 2010. V. 6. № 21. P. 2460–2468.
108. Elias D.R., Poloukhtine A., Popik V., Tsourkas A. // Nanomedicine. 2013. V. 9. № 2. P. 194–201.
109. Yang M., Cheng K., Qi S., Liu H., Jiang Y., Jiang H., Li J., Chen K., Zhang H., Cheng Z. // Biomaterials. 2013. V. 34. № 11. P. 2796–2806.
110. Satpathy M., Zielinski R., Lyakhov I., Yang L. // Methods Mol. Biol. 2015. V. 1219. P. 171–185.
111. Satpathy M., Wang L., Zielinski R., Qian W., Lipowska M., Capala J., Lee G.Y., Xu H., Wang Y.A., Mao H., et al. // Small. 2014. V. 10. № 3. P. 544–555.
112. Satpathy M., Wang L., Zielinski R.J., Qian W., Wang Y.A., Mohs A.M., Kairdolf B.A., Ji X., Capala J., Lipowska M., et al. // Theranostics. 2019. V. 9. № 3. P. 778–795.
113. Liu J., Chen H., Fu Y., Li X., Chen Y., Zhang H., Wang Z. // J. Mater. Chem. B. 2017. V. 5. № 43. P. 8554–8562.
114. Jokerst J.V., Miao Z., Zavaleta C., Cheng Z., Gambhir S.S. // Small. 2011. V. 7. № 5. P. 625–633.
115. Thakor A.S., Luong R., Paulmurugan R., Lin F.I., Kempen P., Zavaleta C., Chu P., Massoud T.F., Sinclair R., Gambhir S.S. // Sci. Transl. Med. 2011. V. 3. № 79. P. 79ra33.
116. Ravalli A., da Rocha C.G., Yamanaka H., Marrazza G. // Bioelectrochemistry. 2015. V. 106. Pt B. P. 268–275.
117. Zhang C., Zhang F., Han M., Wang X., Du J., Zhang H., Li W. // Sci. Rep. 2020. V. 10. № 1. P. 22015.

118. Pourshohod A., Jamalan M., Zeinali M., Ghanemi M., Kheirollah A. // J. Drug Deliv. Sci. Technol. 2019. V. 52. № 9524. P. 934–941.
119. Ju Y., Zhang H., Yu J., Tong S., Tian N., Wang Z., Wang X., Su X., Chu X., Lin J., et al. // ACS Nano. 2017. V. 11. № 9. P. 9239–9248.
120. Kwon K.C., Ryu J.H., Lee J.-H., Lee E.J., Kwon I.C., Kim K., Lee J. // Adv. Mat. 2014. V. 26. № 37. P. 6436–6441.
121. Lucky S.S., Idris N.M., Huang K., Kim J., Li Z., Thong P.S.P., Xu R., Soo K.C., Zhang Y. // Theranostics. 2016. V. 6. № 11. P. 1844–1865.
122. Badieirostami M., Carpenter C., Pratx G., Xing L., Sun C. // MRS Adv. 2019. V. 4. № 46–47. P. 2461–2470.
123. He L., Brasino M., Mao C., Cho S., Park W., Goodwin A.P., Cha J.N. // Small. 2017. V. 13. № 24. doi: 10.1002/smll.201700504.
124. Akhtari J., Rezayat S.M., Teymouri M., Alavizadeh S.H., Gheybi F., Badiee A., Jaafari M.R. // Int. J. Pharm. 2016. V. 505. № 1–2. P. 89–95.
125. Smith B., Lyakhov I., Loomis K., Needle D., Baxa U., Yavlovich A., Capala J., Blumenthal R., Puri A. // J. Control. Release. 2011. V. 153. № 2. P. 187–194.
126. Moballegh-Nasery M., Mandegary A., Eslaminejad T., Zeinali M., Pardakhti A., Behnam B., Mohammadi M. // J. Liposome Res. 2021. V. 31. № 2. P. 189–194.
127. Alavizadeh S.H., Akhtari J., Badiee A., Golmohammadzadeh S., Jaafari M.R. // Expert Opin. Drug Deliv. 2016. V. 13. № 3. P. 325–336.
128. Beuttler J., Rothdiener M., Müller D., Frejd F.Y., Kontermann R.E. // Bioconjugate Chem. 2009. V. 20. № 6. P. 1201–1208.
129. Shipunova V.O., Sogomonyan A.S., Zelepukin I.V., Nikitin M.P., Deyev S.M. // Molecules. 2021. V. 26. № 13. P. 3955.
130. Alexis F., Basto P., Levy-Nissenbaum E., Radovic-Moreno A.F., Zhang L., Pridgen E., Wang A.Z., Marein S.L., Westerhof K., Molnar L.K., et al. // Chem. Med. Chem. 2008. V. 3. № 12. P. 1839–1843.
131. Narsireddy A., Vijayashree K., Adimoolam M.G., Manorama S.V., Rao N.M. // Int. J. Nanomedicine. 2015. V. 10. P. 6865–6878.
132. Feng G., Fang Y., Liu J., Geng J., Ding D., Liu B. // Small. 2017. V. 13. № 3. doi: 10.1002/smll.201602807.
133. Liu J., Feng G., Ding D., Liu B. // Polym. Chem. 2013. V. 4. № 16. P. 4326.
134. Pu K.-Y., Shi J., Cai L., Li K., Liu B. // Biomacromolecules. 2011. V. 12. № 8. P. 2966–2974.
135. Du J., Li X.-Y., Hu H., Xu L., Yang S.-P., Li F.-H. // Sci. Rep. 2018. V. 8. № 1. P. 3887.
136. Yang H., Cai W., Xu L., Lv X., Qiao Y., Li P., Wu H., Yang Y., Zhang L., Duan Y. // Biomaterials. 2015. V. 37. P. 279–288.
137. Reuter K.G., Perry J.L., Kim D., Luft J.C., Liu R., DeSimone J.M. // Nano Lett. 2015. V. 15. № 10. P. 6371–6378.
138. Lee C., Kang S. // Biomacromolecules. 2021. V. 22. № 6. P. 2649–2658.
139. Choi H., Eom S., Kim H.-U., Bae Y., Jung H.S., Kang S. // Biomacromolecules. 2021. V. 22. № 7. P. 3028–3039.
140. Bae Y., Kim G.J., Kim H., Park S.G., Jung H.S., Kang S. // Biomacromolecules. 2018. V. 19. № 7. P. 2896–2904.
141. Kim H., Jin S., Choi H., Kang M., Park S.G., Jun H., Cho H., Kang S. // J. Control. Release. 2021. V. 335. P. 269–280.
142. Kim S.-E., Jo S.D., Kwon K.C., Won Y.-Y., Lee J. // Adv. Sci. 2017. V. 4. № 5. P. 1600471.
143. Nishimura Y., Mimura W., Mohamed Suffian I.F., Amino T., Ishii J., Ogino C., Kondo A. // J. Biochem. 2013. V. 153. № 3. P. 251–256.
144. Nishimura Y., Ishii J., Okazaki F., Ogino C., Kondo A. // J. Drug Target. 2012. V. 20. № 10. P. 897–905.
145. Nishimura Y., Ezawa R., Ishii J., Ogino C., Kondo A. // Bioorg. Med. Chem. Lett. 2017. V. 27. № 2. P. 336–341.
146. Nishimura Y., Takeda K., Ezawa R., Ishii J., Ogino C., Kondo A. // J. Nanobiotechnology. 2014. V. 12. P. 11.
147. Nishimura Y., Mieda H., Ishii J., Ogino C., Fujiwara T., Kondo A. // J. Nanobiotechnology. 2013. V. 11. P. 19.
148. Shishido T., Mieda H., Hwang S.Y., Nishimura Y., Tanaka T., Ogino C., Fukuda H., Kondo A. // Bioorg. Med. Chem. Lett. 2010. V. 20. № 19. P. 5726–5731.
149. Kwon K.C., Ko H.K., Lee J., Lee E.J., Kim K., Lee J. // Small. 2016. V. 12. № 31. P. 4241–4253.
150. Lee N.K., Lee E.J., Kim S., Nam G.-H., Kih M., Hong Y., Jeong C., Yang Y., Byun Y., Kim I.-S. // J. Control. Release. 2017. V. 267. P. 172–180.
151. Oh J.Y., Kim H.S., Palanikumar L., Go E.M., Jana B., Park S.A., Kim H.Y., Kim K., Seo J.K., Kwak S.K., et al. // Nat. Commun. 2018. V. 9. № 1. P. 4548.
152. Joubran S., Zigler M., Pessah N., Klein S., Shir A., Edinger N., Sagalov A., Razvag Y., Reches M., Levitzki A. // Bioconjugate Chem. 2014. V. 25. № 9. P. 1644–1654.
153. Zhang Y., Jiang S., Zhang D., Bai X., Hecht S.M., Chen S. // Chem. Comm. 2017. V. 53. № 3. P. 573–576.
154. Zhang C., Zhang H., Han M., Yang X., Pei C., Xu Z., Du J., Li W., Chen S. // RSC Adv. 2019. V. 9. № 4. P. 1982–1989.
155. Zhang F., Yin J., Zhang C., Han M., Wang X., Fu S., Du J., Zhang H., Li W. // Macromol. Biosci. 2020. V. 20. № 7. P. e2000083.
156. Zhang C., Han M., Zhang F., Yang X., Du J., Zhang H., Li W., Chen S. // Int. J. Nanomedicine. 2020. V. 15. P. 885–900.
157. Balalaeva I.V., Zdobnova T.A., Krutova I.V., Brilkina A.A., Lebedenko E.N., Deyev S.M. // J. Biophotonics. 2012. V. 5. № 11–12. P. 860–867.
158. Generalova A.N., Sizova S.V., Zdobnova T.A., Zarifullina M.M., Artemyev M.V., Baranov A.V., Oleinikov V.A., Zubov V.P., Deyev S.M. // Nanomedicine. 2011. V. 6. № 2. P. 195–209.
159. Peckys D.B., Hirsch D., Gaiser T., de Jonge N. // Mol. Med. 2019. V. 25. № 1. P. 42.
160. Peckys D.B., Korf U., de Jonge N. // Sci. Adv. 2015. V. 1. № 6. P. e1500165.
161. Gao J., Chen K., Miao Z., Ren G., Chen X., Gambhir S.S., Cheng Z. // Biomaterials. 2011. V. 32. № 8. P. 2141–2148.
162. Zhang Y., Zhao N., Qin Y., Wu F., Xu Z., Lan T., Cheng Z., Zhao P., Liu H. // Nanoscale. 2018. V. 10. № 35. P. 16581–16590.
163. Sun R., Zhao Y., Wang Y., Zhang Q., Zhao P. // Nanotechnology. 2021. V. 32. № 20. P. 205103.
164. Wu Y., Li H., Yan Y., Wang K., Cheng Y., Li Y., Zhu X., Xie J., Sun X. // Int. J. Nanomedicine. 2020. V. 15. P. 4691–4703.
165. Wu Y.-T., Qiu X., Lindbo S., Susumu K., Medintz I.L., Hober S., Hildebrandt N. // Small. 2018. V. 14. № 35. P. e1802266.
166. Binz H.K., Plückthun A. // Curr. Opin. Biotechnol. 2005. V. 16. № 4. P. 459–469.
167. Löfblom J., Frejd F.Y., Ståhl S. // Curr. Opin. Biotechnol. 2011. V. 22. № 6. P. 843–848.
168. Martin H.L., Bedford R., Heseltine S.J., Tang A.A., Haza K.Z., Rao A., McPherson M.J., Tomlinson D.C. // New Biotechnol. 2018. V. 45. P. 28–35.
169. Nygren P.-A., Skerra A. // J. Immunol. Methods. 2004. V. 290. № 1–2. P. 3–28.

170. Renders L., Budde K., Rosenberger C., van Swelm R., Swinkels D., Dellanna F., Feuerer W., Wen M., Erley C., Bader B., et al. // PLoS One. 2019. V. 14. № 3. P. e0212023.
171. Mross K., Richly H., Fischer R., Scharr D., Büchert M., Stern A., Gille H., Audoly L.P., Scheulen M.E. // PLoS One. 2013. V. 8. № 12. P. e83232.
172. Bragina O., von Witting E., Garousi J., Zelchan R., Sandström M., Orlova A., Medvedeva A., Doroshenko A., Vorobyeva A., Lindbo S., et al. // J. Nucl. Med. 2021. V. 62. № 4. P. 493–499.
173. Tolcher A.W., Sweeney C.J., Papadopoulos K., Patnaik A., Chiorean E.G., Mita A.C., Sankhala K., Furfine E., Gokemeijer J., Iacono L., et al. // Clin. Cancer Res. 2011. V. 17. № 2. P. 363–371.
174. Sandström M., Lindskog K., Velikyan I., Wennborg A., Feldwisch J., Sandberg D., Tolmachev V., Orlova A., Sörensen J., Carlsson J., et al. // J. Nucl. Med. 2016. V. 57. № 6. P. 867–871.
175. Sörensen J., Velikyan I., Sandberg D., Wennborg A., Feldwisch J., Tolmachev V., Orlova A., Sandström M., Lubberink M., Olofsson H., et al. // Theranostics. 2016. V. 6. № 2. P. 262–271.

Tandem Exon Duplications Expanding the Alternative Splicing Repertoire

T. M. Ivanov, D. D. Pervouchine*
Center of Life Sciences, Skolkovo Institute of Science and Technology, Moscow, 121205 Russia
*E-mail: d.pervouchine@skoltech.ru
Received: September 06, 2021; in final form, January 17, 2022
DOI: 10.32607/actanaturae.11583

ABSTRACT **Tandem exon duplications play an important role in the evolution of eukaryotic genes, providing a generic mechanism for adaptive regulation of protein function. In recent studies, tandem exon duplications have been linked to mutually exclusive exon choice, a pattern of alternative splicing in which one and only one exon from a group of tandemly arranged exons is included in the mature transcript. Here, we revisit the problem of identifying tandem exon duplications in eukaryotic genomes using bioinformatic methods and show that tandemly duplicated exons are abundant not only in the coding parts, but also in the untranslated regions. We present a number of remarkable examples of tandem exon duplications, identify unannotated duplicated exons, and provide statistical support for their expression using large panels of RNA-seq experiments.**
KEYWORDS **Alternative splicing, gene structure, tandem exon duplications, RNA-sec.**
ABBREVIATIONS **CDS – coding DNA sequence; UTR – untranslated region.**

INTRODUCTION

The major driving force of molecular evolution is mutation, a process that introduces changes to the genomic sequences that are transmissible through generations. While the most frequent type of mutations are single-nucleotide polymorphisms, which affect single bases, genomic duplications are another important type of DNA changes. A particular subtype are the so-called tandem genomic duplications, which are represented by DNA sequences typically more than 1 kb long, are immediately adjacent to each other, and have a high level of sequence identity [1, 2].

Tandem genomic duplications may affect entire genes, either protein-coding or non-coding, or only gene parts. In the latter case, the duplication leads to propagation of only a portion of the gene sequence, thus affecting the exon-intron structure [3]. The process where the same exon of a gene is duplicated or two or more exons from different genes are brought together ectopically is called exon shuffling [4, 5]. In many cases, exon shuffling through tandem exon duplication has been linked to mutually exclusive exon choice, a regulated pattern of alternative splicing in which only one exon from a group of exons is included in the mature transcript [6, 7]. Mutually exclusive exons (MXEs) are found in the genes across diverse phylae; e.g., cadherin-N (*CadN*) [8, 9], myosin heavy chain (*MHC*) [10], *14-3-3ζ* [11], *srp* [12], multidrug resistance-associated protein (*MRP*) [13] genes in *D. melanogaster*, mammalian forkhead box (*FOX*) transcription factor [14] and tropomyosin gene families [15]. Perhaps the most fascinating example of MXE that resulted from tandem duplications is *D. melanogaster* down syndrome cell adhesion molecule 1 (*DSCAM1*) gene, which contains 4 groups of MXE clusters, which in total can lead to up to 38,016 distinct protein isoforms [16, 17, 18, 19, 20, 21].

In 2002, a systematic study of common exon duplications and their role in alternative splicing reported that about 10% of animal genes contain tandemly duplicated exons and discovered more than 2,000 unannotated candidate MXEs by similarity searches identifying homology to neighboring exons or within DNA adjacent to exons [22]. However, tandem exon duplications may also affect the intronic and untranslated regions (UTRs) that are not immediately adjacent to annotated exons, and genome annotation databases have significantly expanded. This has motivated us to revisit this question by detecting homology between annotated exons and the entire gene sequences and their genomic neighborhoods. We found that, indeed, tandem exon duplications span far beyond the protein-coding part of gene sequence and are also quite frequent in the untranslated regions. We present a

dynamic picture of the abundance of exon duplications as a function of nucleotide sequence homology and report a number of characteristic examples of such duplications.

METHODS

Genome sequences and annotations

The February 2009 (hg19, GRCh37.p13) assembly of the human genome was downloaded from the Genome Reference Consortium [23]. GENCODE comprehensive gene annotation version 19 was downloaded from the GENCODE consortium website [24]. *D. melanogaster* BDGP Release 6 (dm6) and *C. elegans* WBcel235 (ce11) genome assemblies were downloaded from the UCSC Genome Browser website [25]. ENSEMBL transcript annotations for *D. melanogaster* were imported from FlyBase, release dmel_r6.32 [26]. ENSEMBL transcript annotations for *C. elegans* release 104 were imported from Wormbase [27]. RefSeq transcript annotations for all organisms were downloaded from NCBI RefSeq database [28]. Records other than protein coding genes were excluded from all annotation databases. The numbers of unique exons in the human, *D. melanogaster*, and *C. elegans* databases were 329,983; 83,276; and 172,984, respectively.

Exon homology search

The homology search was carried out using the EMBL-EBI's exonerate tool to identify tandem exon duplication [29]. The nucleotide sequence of each exon was aligned to the nucleotide sequence of its parent gene that was extended in both directions by 15% of the gene length in a strand-specific way. We chose to use a percent of the gene length rather than a fixed window around the gene, since human genes are substantially longer than *D. melanogaster* genes. The choice of 15% cutoff was motivated by the fact that the distance from a gene to its neighbor genes does not exceed 15% of the gene length for approximately one half of *D. melanogaster* genes. The program was executed in the exhaustive mode to obtain a more accurate alignment. The minimal percent identity cutoff was set to 50%; however, exonerate did not detect sequence homology below 57%. The sequences of the alignments were extracted using the getfasta tool from the bedtools package [30]. The alignments were organized in a bed12 table, in which each line corresponds to one query-target pair (including self-hits). After discarding self-hits, the table contained 116,320; 5,244; and 5,605 query-target pairs for the human, *D. melanogaster*, and *C. elegans genes*, respectively.

Filtering procedure for query-target pairs

To identify unannotated tandem exon duplications, we filtered the table of query-target pairs using the bedtools intersect utility as follows. We removed the query-target pairs in which the target sequence intersects at least one annotated exon by more than 5% if its length. Additionally, we removed the query-target pairs in which the target sequence intersects at least one annotated interspersed repeat or low-complexity DNA sequence by more than 10% if its length, according to multiple repeats tracks from the UCSC Genome browser [25].

RNA-seq data

The RNA-seq data from 6,625 samples in the Genotype-Tissue Expression (GTEx) consortium v7 data were analyzed using the procedure described previously [31]. Short reads were mapped to the human genome using STAR aligner v2.4.2a by the data providers [32]. Split reads supporting splice junctions were extracted using the IPSA package with the default settings [33] (Shannon entropy threshold 1.5 bit). Only split reads with the canonical GT/AG dinucleotides were considered. Uniquely mapped reads were selected based on the presence of NH:1 tag in the BAM files. The average read coverage and PhastCons conservation scores were calculated using the Deeptools software package [34].

RESULTS

Nucleotide increase ratio

In order to detect exonic duplications, we used the largest to-date exon annotation datasets, including the GENCODE [35] and RefSeq [28] databases, and performed a sequence similarity search for each exon within the extended nucleotide sequence of its parent gene using exonerate software [29]. In what follows, we refer to the annotated exons as query sequences, and their respective homologs that were found by exonerate as target sequences (*Fig. 1*). Each query-target pair is characterized by the covariates related to the query (e.g., location within CDS or UTR), the covariates related to the target (e.g., whether or not it overlaps an annotated exon), and percent sequence identity between the query and the target. Since many exons are alternatively spliced and, thus, contribute as overlapping regions to the exon annotation sets, we introduced the Nucleotide Increase Ratio (NIR) score, which is defined as the total number of nucleotides covered by the target set as a fraction of the total number of nucleotides covered by the query set in the similarity search with the given or higher percent of sequence identity. By construction, NIR

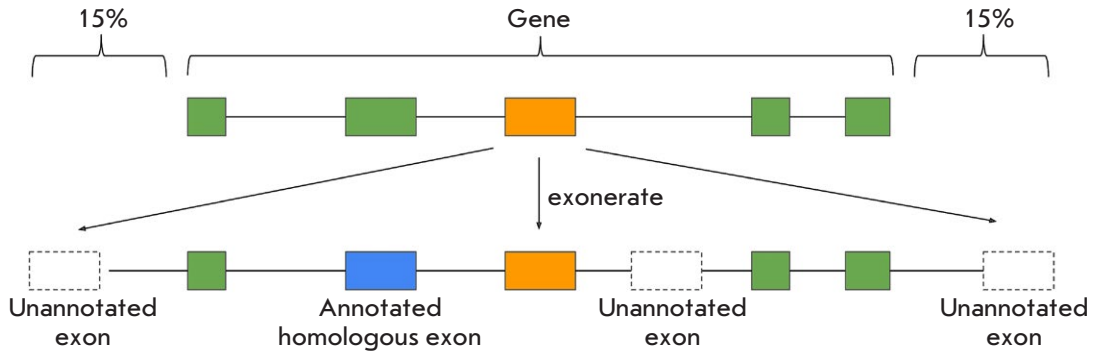

Fig. 1. A schematic representation of the tandem exon duplication search. The nucleotide sequence of each exon of every gene is aligned to the nucleotide sequence of its parent gene that is extended 15% in length upstream and downstream

is always greater than 1 since each query serves as its own target with 100% sequence identity. NIR can be computed for all query exons as well as for coding and UTR queries separately. Tables of query-target pairs are available through the online repository https://zenodo.org/record/5474863.

As expected, the NIR values decrease with increasing sequence identity threshold (*Fig. 2A*). Despite the 50% threshold on minimal sequence identity, exonerate did not detect any query-target pair with sequence homology below 57%. Considering 80% sequence identity cutoff as the midpoint in the 60%–100% interval, which contains all the targets, we observed that approximately 2% of human exonic nucleotides were found to have homologs when performing the similarity search with 80% sequence identity or larger, while only 0.08% of *D. melanogaster* and 0.06% of *C. elegans* exonic nucleotides did so. Obviously, this has to do with the fact that the targets of exonic nucleotides beyond the annotated exons belong to intronic regions, and human introns are much longer than those of *D. melanogaster* and *C. elegans*. Remarkably, when considering only exons that are located in UTRs, almost 15% of human exonic nucleotides were found to have homologs when performing the similarity search with 80% sequence identity or larger (*Fig. 2A*). The respective proportions for *D. melanogaster* and *C. elegans* were 0.3% and 0.2%, indicating a substantially larger frequency of exon duplications in UTRs.

Next, we asked whether some genes are more prone to tandem exon duplications than the others. To address this question, we computed the NIR values for each annotated gene separately and plotted the NIR frequency distributions (*Fig. 2B*). The NIR frequencies followed a power law distribution as evidenced by a nearly linear dependence of the logarithm of frequency on the logarithm of the NIR, with a substantial decline towards higher frequencies for larger NIR values in some genes. Interestingly, the human genes with declining NIR values for CDS exons included *CAMK1D* (Calcium/Calmodulin Dependent Protein Kinase ID), *CLYBL* (Citramalyl-CoA Lyase), and *NBPF20* (Neuroblastoma breakpoint family member 20) genes; however, some genes also had declining NIR values for the UTRs; e.g., *OBSCN* (Obscurin, Cytoskeletal Calmodulin and Titin-Interacting RhoGEF) and *NEB* (Nebulin). In *D. melanogaster*, the remarkable outliers were the *dpy*, *hydra*, and *heph* genes.

The difference in the propensity of tandem duplications in the genes with large NIR compared to other genes could potentially arise from differences in their exon lengths. To address this, we compared the NIR values in groups of exons equally spaced in ten bins by length. We found that the NIR values decrease approximately fourfold as exon length increases from 20 to 220 nucleotides, thus indicating that longer exons do not contribute to larger NIR values. Indeed, the longer the target, the smaller the likelihood of finding a homolog at 80% sequence identity cutoff should be. Additionally, the average exon length for the top 200 genes with the largest NIR values did not differ significantly from the average exon length in the population of all exons (Wilxcoxon test, P value = 0.2). Therefore, exon lengths do not significantly affect the propensity of tandem duplications. The Gene Ontology analysis of the top 200 genes with large NIR values revealed a statistical enrichment of GO categories related to cell adhesion and nervous system development (biological function), ion binding and receptor activities (molecular function), and membrane localization (cellular compartment).

To further investigate the structure of exonic duplications in these genes, we created a track hub for the UCSC Genome browser as a visualization tool for all query-target pairs. As a positive control, we confirmed that our procedure successfully identified clus-

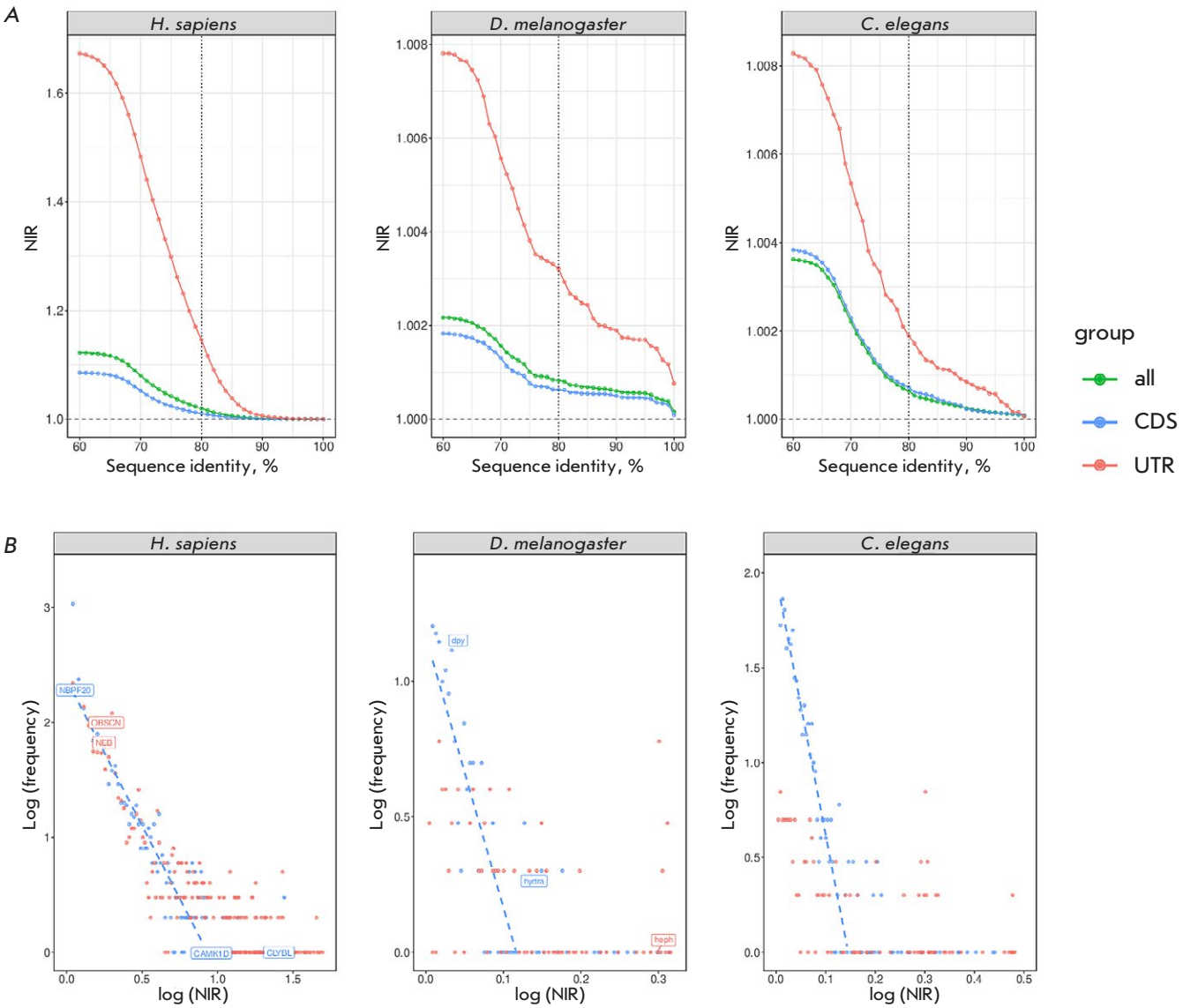

Fig. 2. (*A*) The Nucleotide Increase Ratio (NIR) in human, *D. melanogaster*, and *C. elegans* genes as a function of query-target nucleotide sequence identity. (*B*) The frequency distribution of NIR in human, *D. melanogaster*, and *C. elegans* genes (sequence identity threshold 80%). Gene names are shown for remarkable outliers. The insets list the genes with large NIR (cutoffs are shown)

ters of tandemly duplicated exons in the genes known from the literature [10, 11, 12, 13] (data not shown). In order to discover novel, unannotated tandem exon duplications, we excluded the query-target pairs that overlap any annotated exon from consideration and filtered out the targets intersecting the annotated repeats or low-complexity regions, since they could have originated through a different mechanism; e.g., exonization of transposed elements [36]. As statistical evidence for the expression of the newfound exons, we computed the read coverage and splice junction support using RNA-seq data from the Genotype Tissue Expression project [31].

CASE STUDIES

Obscurin (*OBSCN*)

Obscurin (*OBSCN*) is a remarkable example of a human gene broadly affected by tandem exon duplications. It spans more than 150 kb and contains over 80 exons [37]. The protein encoded by this gene belongs to the family of giant sacromeric signaling proteins,

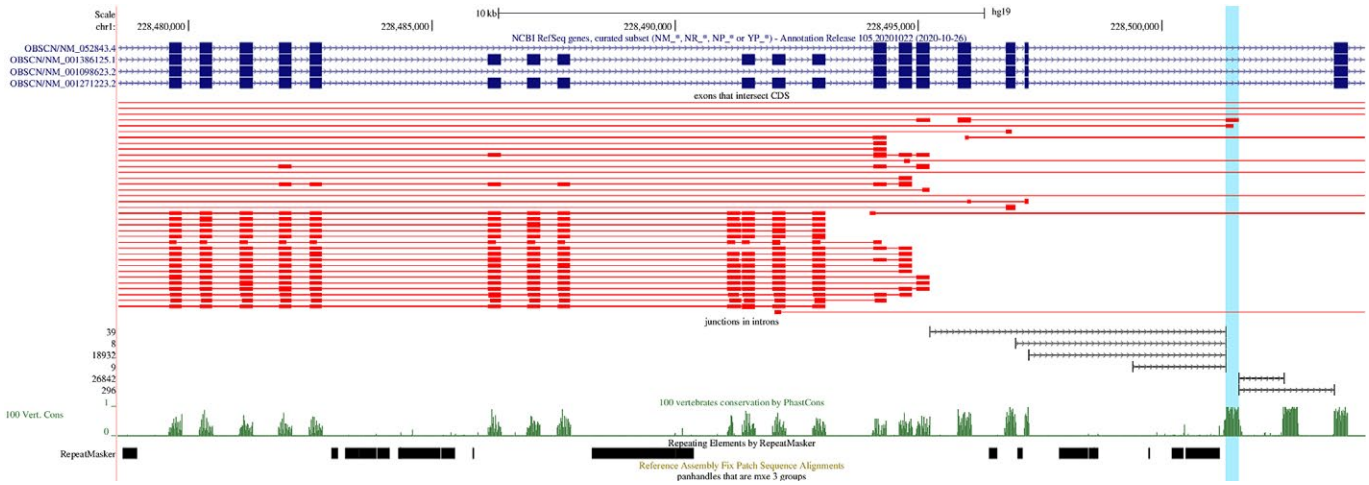

Fig. 3. A Genome Browser diagram of tandem exon duplications in *OBSCN*. The annotated transcripts (GENCODE and RefSeq) are shown in dark blue. The query-target pairs with 80% sequence identity are shown in red; query exons are thick, and their targets are thin. The track below query-target pairs represents split reads supporting splice junctions. The PhastCons score over 100 vertebrates is shown in green

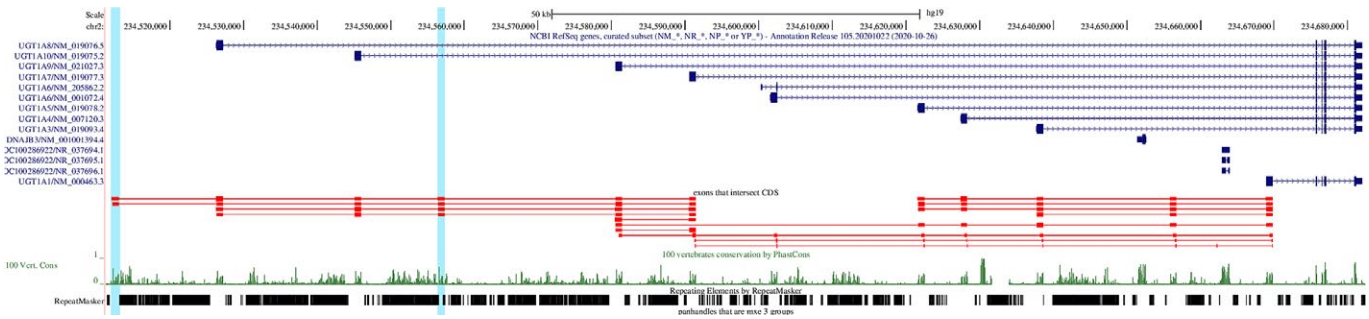

Fig. 4. A Genome Browser diagram of tandem exon duplications in *UGT1A*. The color codes in this legend are identical to those in *Fig. 3*

which also includes titin and nebulin [38]. *OBSCN* is expressed in the heart (RPKM 8.6), prostate (RPKM 2.9), and other tissues [31].

Our analysis has shown that the vast majority of *OBSCN* exons are homologous to each other and similar in length, being indicative of their origin in tandem duplication (*Fig. 3*). The presence of repeated elements in the intervening introns further suggests that they originated through several rounds of genomic duplications, most likely, via non-homologous recombination. Remarkably, one of the intervening introns contains a region that is homologous to other exons but is not annotated as exon (*Fig. 3*, blue). The functionality of this region is supported by a peak of phastCons score and the existence of split reads aligning to exon–exon junctions. Interestingly, the same intervening intron contains another peak of phastCons score downstream of the shaded exon that is also supported by split reads; however, it does not show sufficient sequence homology to other exons (percent sequence identity 62.4% vs. 78.9% for the other regions).

UDP Glucuronosyltransferase Family 1 Member A (*UGT1A*)

The human *UGT1A* gene encodes UDP Glucuronosyltransferase Family 1 Member A group of proteins, which is represented by thirteen unique alternate first exons followed by four common exons. *UGT1A* is associated with diseases including Gilbert syndrome [39] and Crigler–Najjar syndrome [40]. Each first exon encodes the substrate binding site, giving rise to proteins with different N-termini and identical C-termini, and is regulated by its own promoter. According to

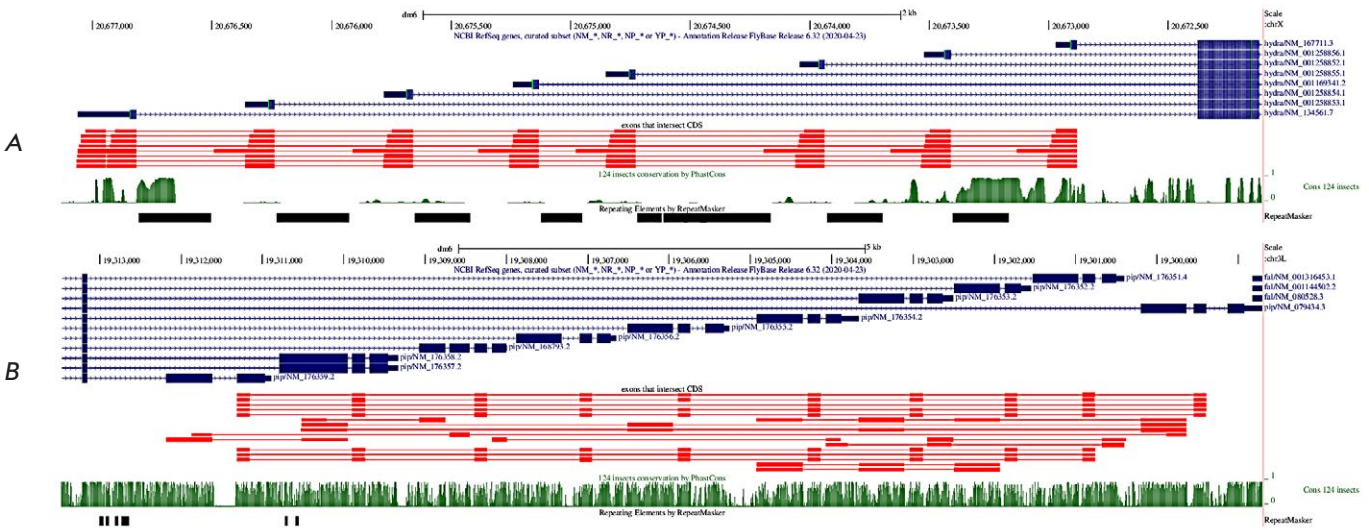

Fig. 5. A Genome Browser diagram of tandem exon duplications in *D. melanogaster* genes *hydra* (*A*) and *pip* (*B*) . The color codes in this legend are identical to those in *Fig. 3*

our analysis, the variable initial exons of these genes are homologous to each other (*Fig. 4*), thus likely being generated by tandem exon duplications. There is a region in the 5'-UTR of this gene that contains a region that is homologous to the initial exons, but not annotated as an exon. This region is also supported by a peak of phastCons score (*Fig. 4*, blue). A remarkable feature of this exon cluster is the mutually exclusive choice of the initial exons in the mature transcripts of this gene.

Examples of tandem exon duplications in *D. melanogaster* UTRs

Two remarkable examples of tandem exon duplications in UTRs of *D. melanogaster* are the *hydra* (*Fig. 5A*) and *pip* (*Fig. 5B*) genes. In *hydra*, nine homologous initial exons are spliced in a mutually exclusive manner, while in *pip* we observe eight tandemly repeated homologous clusters of mutually exclusive terminal exons. It was shown that the initial exon of *hydra* has undergone recurrent duplications, and seven of these alternative initial exons are flanked on their 3'-side by the transposon DINE-1 (Drosophila interspersed element-1) [41]. At least four of the nine duplicated initial exons can function as alternative transcription start sites [41]. The 3'-UTRs of *pip*, which encodes sulfotransferase that contributes to the formation and polarity of the embryonic dorsal-ventral axis, have been studied in much less detail. A similar pattern of mutually exclusive usage of 3'-UTRs has been recently reported to be dependent on competing RNA secondary structures, including the 3-UTR of *pip* [42].

Expression support by RNA-seq data

To assess the expression of tandem exon duplications using RNA-seq data, we considered query-target pairs in the human genes in which the target region does not intersect any annotated exon or any annotated repeat element, and merged the remaining targets using the bedtools merge program. This procedure yielded 4,027 intronic targets. Each of these targets was matched randomly to a control region of the same length that was located 30 nt upstream or downstream.

One inherent problem in assessing the expression of tandem exon duplications using RNA-seq data is that in the case of high nucleotide sequence identity, short reads align equally well to the query and target regions, thus confounding the analysis. We, therefore, filtered out all short reads that aligned to more than one position in the genome and computed the average read coverage for the target and control regions in each of the 53 tissue transcriptomes within the Genotype Tissue Expression (GTEx) project [31] using only uniquely mapped reads. Next, we computed the score $\log FC_i = \log_{10}(1 + target_i) - \log_{10}(1 + control_i)$, where $target_i$ is the average target read coverage in the tissue i and $control_i$ is the average control read coverage in the tissue i. Tissues with an insufficient number of $\log FC_i$ values (Bladder, Cervix - Endocervix, Cervix - Ectocervix) were excluded from further analysis. In a group of targets that showed at least 80% nucleotide sequence homology to the query, we observed a significant positive departure of the $\log FC_i$ metric from zero (Wilcoxon signed rank test), which remained significant in some tissues af-

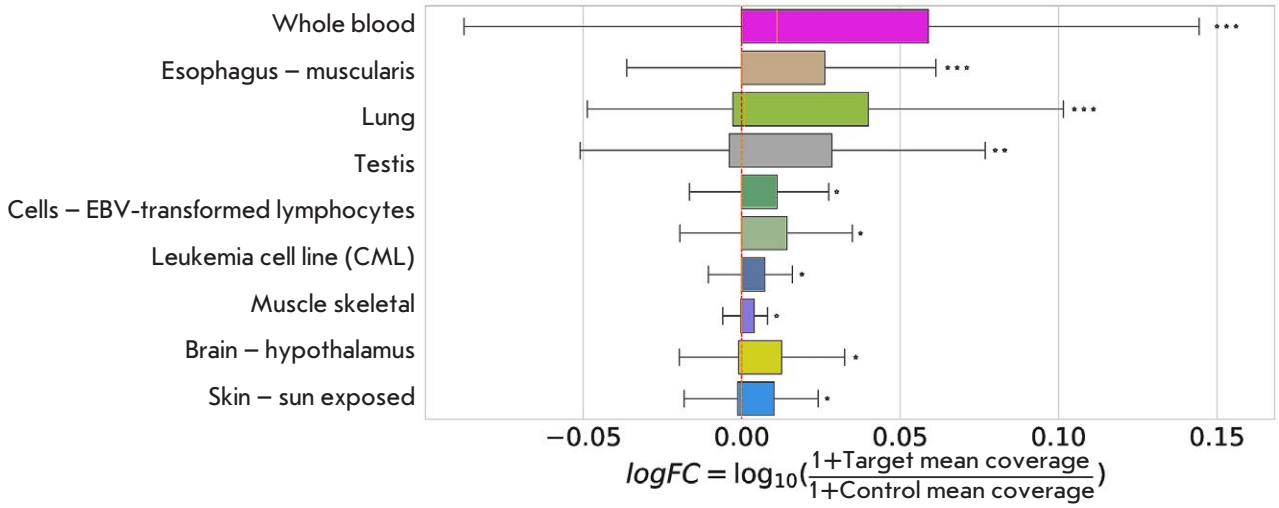

Fig. 6. The distribution of the log FC$_i$ read coverage metric in GTEx tissues for targets with at least 80% nucleotide sequence homology to the query. The standard color coding of GTEx tissues from [31] was used. Only tissues with significant departure of log FC$_i$ from zero are shown (by descending statistical significance). Significance levels were assigned by Wilcoxon signed rank test after the Benjamini-Hochberg correction criteria for multiple testing had been applied

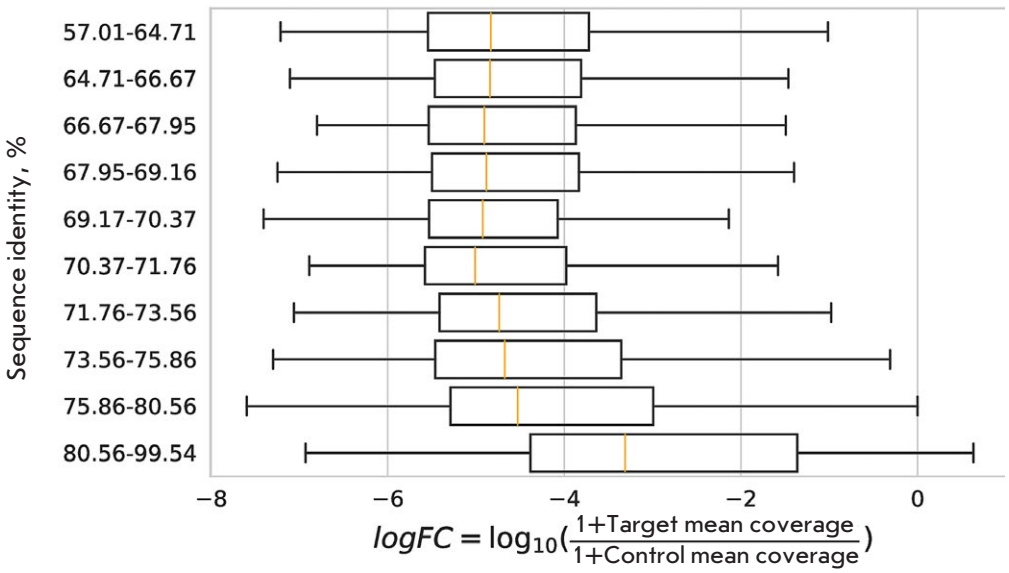

Fig. 7. The distribution of the log FCi split read metric. The log FC$_i$ metric was computed as log FC$_i$ = log$_{10}$(1 + target$_i$) – log$_{10}$(1 + control$_i$), where target$_i$ (control$_i$) is the total number of uniquely mapped split reads supporting the inclusion of target (control) region in tissue i

ter Benjamini-Hochberg correction for multiple testing (*Fig. 6*); e.g. Whole Blood, Esophagus, Lung, Testis, Muscle, Brain, and also some of the transformed cells. Remarkably, the Wilcoxon signed rank test indicated a statistically significant departure from zero even in the cases when the median was close to zero, which indicates the prevalence of large positive differences in the sample. We also observed an increase in the number of split reads supporting exon–exon junctions for tandemly duplicated exons with higher nucleotide sequence identity (*Fig. 7*). These results demonstrate that at least some of the unannotated tandemly duplicated exons may indeed be expressed, but in a tissue-specific manner.

Finally, we calculated the difference between average PhastCons [43] scores obtained from the multiple alignments of 100 vertebrate species between the target and control regions. The target regions were on average more evolutionarily conserved than the control regions (Wilcoxon signed rank test, P value = 0.009), which additionally supports their functionality.

DISCUSSION

An interesting observation made in this work is that tandem exon duplications are prevalent not only in the coding regions, but also in the UTRs of eukaryotic genes and, moreover, they seem to be associated with a mutually exclusive choice of tandemly duplicated initial and terminal exons. A recent study has shown that the regulatory mechanism underlying the mutually exclusive choice of 3' variable regions in *D. melanogaster PGRP-LC* pre-mRNA involves competing RNA structures [42]. These RNA structures jointly regulate the 3' UTR selection through activating the proximal 3' splice site and concurrently masking the intron-proximal 5' splice site, together with physical competition of RNA pairing [42]. A similar regulatory program also operates in 3' variable regions of *D. melanogaster CG42235* and *pip* genes. This observation raises an intriguing question of whether tandem exon duplications in UTRs can generally be controlled by competing RNA structures.

Recently, we have proposed an evolutionary mechanism for the generation of competing RNA structures associated with mutually exclusive splicing via genomic duplications that affect not only exons but also their adjacent introns with stem-loop structures [44]. According to this hypothesis, if one of the two arms of an intronic stem-loop is duplicated, it will automatically generate two sequences that compete for base pairing with another sequence, a pattern that is associated with MXE splicing [13, 14, 15, 21]. This model implies that the mutually exclusive splicing pattern is an inevitable consequence of tandem exon duplications. Considering the high abundance of conserved complementary regions in the UTRs of human genes [45], it appears plausible that tandem exon duplications within UTRs also could generate competing RNA structures leading to mutually exclusive exon inclusion.

CONCLUSIONS

Tandem exon duplications are abundant not only in the coding parts, but also in the untranslated regions of eukaryotic genes. It still remains an open question whether or not competing RNA structures are broadly involved in the regulation of mutually exclusive splicing of these exons, as well as whether they could be generated as a byproduct of tandem genomic duplications. ●

We thank Marina Kalinina, Dmitry Skvortsov, and Olga Dontsova for insightful discussions on mutually exclusive splicing.

This work was supported by the Russian Foundation for Basic Research grants Nos. 19-34-90174 and 18-29-13020-MK. The analysis of RNA-seq data was supported by the Russian Science Foundation grant No. 21-64-00006.

The authors declare that they have no competing interests.

D.P. designed and supervised the study; T.I. performed the data analysis. D.P. and T.I. wrote the manuscript. All authors have read and approved the manuscript.

REFERENCES

1. Emanuel B.S., Shaikh T.H. // Nat. Rev. Genet. 2001. V. 2. № 10. P. 791–800.
2. Mehan M.R., Freimer N.B., Ophoff R.A. // Hum. Genomics. 2004. V. 1. № 5. P. 335–344.
3. Ma M.Y., Lan X.R., Niu D.K. // Peer J. 2016. V. 4. P. e2272.
4. Kolkman J.A., Stemmer W.P. // Nat. Biotechnol. 2001. V. 19. № 5. P. 423–428.
5. Patthy L. // Gene. 1999. V. 238. № 1. P. 103–114.
6. Suyama M. // Bioinformatics. 2013. V. 29. № 17. P. 2084–2087.
7. Kondrashov F.A., Koonin E.V. // Hum. Mol. Genet. 2001. V. 10. № 23. P. 2661–2669.
8. Nern A., Nguyen L.V., Herman T., Prakash S., Clandinin T.R., Zipursky S.L. // Proc. Natl. Acad. Sci. USA. 2005. V. 102. № 36. P. 12944–12949.
9. Ting C.Y., Yonekura S., Chung P., Hsu S.N., Robertson H.M., Chiba A., Lee C.H. // Development. 2005. V. 132. № 5. P. 953–963.
10. George E.L., Ober M.B., Emerson C.P. // Mol. Cell. Biol. 1989. V. 9. № 7. P. 2957–2974.
11. Messaritou G., Leptourgidou F., Franco M., Skoulakis E.M. // FEBS Lett. 2009. V. 583. № 17. P. 2934–2938.
12. Waltzer L., Bataillé L., Peyrefitte S., Haenlin M. // EMBO J. 2002. V. 21. № 20. P. 5477–5486.
13. Grailles M., Brey P.T., Roth C.W. // Gene. 2003. V. 307. P. 41–50.
14. Gabut M., Samavarchi-Tehrani P., Wang X., Slobodeniuc V., O'Hanlon D., Sung H.K., Alvarez M., Talukder S., Pan Q., Mazzoni E.O., et al. // Cell. 2011. V. 147. № 1. P. 132–146.
15. Gooding C., Smith C.W. // Adv. Exp. Med. Biol. 2008. V. 644. P. 27–42.
16. Chen B.E., Kondo M., Garnier A., Watson F.L., Püettmann-Holgado R., Lamar D.R., Schmucker D. // Cell. 2006. V. 125. № 3. P. 607–620.
17. He H., Kise Y., Izadifar A., Urwyler O., Ayaz D., Parthasarthy A., Yan B., Erfurth M.L., Dascenco D., Schmucker D. // Science. 2014. V. 344. № 6188. P. 1182–1186.
18. Hughes M.E., Bortnick R., Tsubouchi A., Bäumer P., Kondo M., Uemura T., Schmucker D. // Neuron. 2007. V. 54. № 3. P. 417–427.
19. Hummel T., Vasconcelos M.L., Clemens J.C., Fishilevich Y., Vosshall L.B., Zipursky S.L. // Neuron. 2003. V. 37. № 2. P. 221–231.

20. Matthews B.J., Kim M.E., Flanagan J.J., Hattori D., Clemens J.C., Zipursky S.L., Grueber W.B. // Cell. 2007. V. 129. № 3. P. 593–604.
21. Soba P., Zhu S., Emoto K., Younger S., Yang S.J., Yu H.H., Lee T., Jan L.Y., Jan Y.N. // Neuron. 2007. V. 54. № 3. P. 403–416.
22. Letunic I., Copley R.R., Bork P. // Hum. Mol. Genet. 2002. V. 11. № 13. P. 1561–1567.
23. Church D.M., Schneider V.A., Graves T., Auger K., Cunningham F., Bouk N., Chen H.C., Agarwala R., McLaren W.M., Ritchie G.R., et al. // PLoS Biol. 2011. V. 9. № 7. P. e1001091.
24. Harrow J., Frankish A., Gonzalez J.M., Tapanari E., Diekhans M., Kokocinski F., Aken B.L., Barrell D., Zadissa A., Searle S., et al. // Genome Res. 2012. V. 22. № 9. P. 1760–1774.
25. Kent W.J., Sugnet C.W., Furey T.S., Roskin K.M., Pringle T.H., Zahler A.M., Haussler D. // Genome Res. 2002. V. 12. № 6. P. 996–1006.
26. Marygold S.J., Crosby M.A., Goodman J.L. // Meth. Mol. Biol. 2016. V. 1478. P. 1–31.
27. Harris T.W., Arnaboldi V., Cain S., Chan J., Chen W.J., Cho J., Davis P., Gao S., Grove C.A., Kishore R., et al. // Nucl. Acids Res. 2020. V. 48. № D1. P. D762–D767.
28. O'Leary N.A., Wright M.W., Brister J.R., Ciufo S., Haddad D., McVeigh R., Rajput B., Robbertse B., Smith-White B., Ako-Adjei D., et al. // Nucl. Acids Res. 2016. V. 44. № D1. P. D733– D745.
29. Slater G.S., Birney E. // BMC Bioinformatics. 2005. V. 6. P. 31.
30. Quinlan A.R., Hall I.M. // Bioinformatics. 2010. V. 26. № 6. P. 841–842.
31. Mele M., Ferreira P.G., Reverter F., DeLuca D.S., Monlong J., Sammeth M., Young T.R., Goldmann J.M., Pervouchine D.D., Sullivan T.J., et al. // Science. 2015. V. 348. № 6235. P. 660–665.
32. Dobin A., Davis C.A., Schlesinger F., Drenkow J., Zaleski C., Jha S., Batut P., Chaisson M., Gingeras T.R. // Bioinformatics. 2013. V. 29. № 1. P. 15–21.
33. Pervouchine D.D., Knowles D.G.., Guigó R. // Bioinformatics. 2013. V. 29. № 2. P. 273–274.
34. Ramírez F., Dündar F., Diehl S., Grüning B.A., Manke T. // Nucl. Acids Res. 2014. V. 42 (Web Server issue). P. W187–191.
35. Frankish A., Diekhans M., Ferreira A.M., Johnson R., Jungreis I., Loveland J., Mudge J.M., Sisu C., Wright J., Armstrong J., et al. // Nucl. Acids Res. 2019. V. 47. № D1. P. D766–D773.
36. Schmitz J., Brosius J. // Biochimie. 2011. V. 93. № 11. P. 1928–1934.
37. Fukuzawa A., Idowu S., Gautel M. // J. Muscle Res. Cell. Motil. 2005. V. 26. № 6–8. P. 427–434.
38. Kontrogianni-Konstantopoulos A., Bloch R.J. // J. Muscle Res. Cell. Motil. 2005. V. 26. № 6–8. P. 419–426.
39. Landerer S., Kalthoff S., Paulusch S., Strassburg C.P. // Sci. Rep. 2020. V. 10. № 1. P. 8689.
40. Strassburg C.P., Kalthoff S., Ehmer U. // Crit. Rev. Clin. Lab. Sci. 2008. V. 45. № 6. P. 485–530.
41. Chen S.T., Cheng H.C., Barbash D.A., Yang H.P. // PLoS Genet. 2007. V. 3. № 7. P. e107.
42. Pan H., Shi Y., Chen S., Yang Y., Yue Y., Zhan L., Dai L., Dong H., Hong W., Shi F., et al. // RNA. 2018. V. 24. № 11. P. 1466–1480.
43. Siepel A., Bejerano G., Pedersen J.S., Hinrichs A.S., Hou M., Rosenbloom K., Clawson H., Spieth J., Hillier L.W., Richards S., et al. // Genome Res. 2005. V. 15. № 8. P. 1034–1050.
44. Ivanov T.M., Pervouchine D.D. // Genes (Basel). 2018. V. 9. № 7. P. 356.
45. Kalmykova S., Kalinina M., Denisov S., Mironov A., Skvortsov D., Guigo R., Pervouchine D. // Nat. Commun. 2021. V. 12. № 1. P. 2300.

Effect of Additional Amino Acid Replacements on the Properties of Multi-point Mutant Bacterial Formate Dehyderogenase PseFDH SM4S

A. A. Pometun[1,2,3], P. D. Parshin[2,3], N. P. Galanicheva[2], L. A. Shaposhnikov[2], D. L. Atroshenko[1,2,3], E. V. Pometun[4], V. V. Burmakin[2], S. Yu. Kleymenov[1,5], S. S. Savin[2,3], V. I. Tishkov[1,2,3*]

[1]Bach Institute of Biochemistry, Federal Research Center of Biotechnology of the Russian Academy of Sciences, Moscow, 119071 Russia

[2]Lomonosov Moscow State University, Department of Chemistry, Moscow, 119991 Russia

[3]Innovations and High Technologies MSU Ltd., Moscow, 109559 Russia

[4]Sechenov First Moscow State Medical University, Moscow, 119991 Russia

[5]Koltzov Institute of Developmental Biology of the Russian Academy of Sciences, Moscow, 119334 Russia

*E-mail: vitishkov@gmail.com

Received: December 17, 2021; in final form, February 11, 2022

DOI: 10.32607/actanaturae.11665

ABSTRACT **Formate dehydrogenase from *Pseudomonas* sp. 101 bacterium (PseFDH, EC 1.2.1.2) is a research model for the elucidation of the catalytic mechanism of 2-oxyacid D-specific dehydrogenases enzyme superfamily. The enzyme is actively used for regeneration of the reduced form of NAD(P)H in chiral synthesis with oxidoreductases. A multi-point mutant PseFDH SM4S with an improved thermal and chemical stability has been prepared earlier in this laboratory. To further improve the properties of the mutant, additional single-point replacements have been introduced to generate five new PseFDH mutants. All new enzymes have been highly purified, and their kinetic properties and thermal stability studied using analysis of thermal inactivation kinetics and differential scanning calorimetry. The E170D amino acid change in PseFDH SM4S shows an increase in thermal stability 1.76- and 10-fold compared to the starting mutant and the wild-type enzyme, respectively.**

KEYWORDS **formate dehydrogenase, *Pseudomonas* sp. 101, catalytic properties, thermal stability, site-directed mutagenesis.**

ABBREVIATIONS **FDH – formate dehydrogenase; NAD(P)$^+$ – nicotinamide adenine dinucleotide (phosphate).**

INTRODUCTION

NAD$^+$-dependent formate dehydrogenase (FDH, EC 1.2.1.2) from methylotrophic bacterium *Pseudomonas* sp. 101 (PseFDH) is one of the best studied enzyme in the group. PseFDH is the first formate dehydrogenases obtained in a highly purified form and characterized [1]. The gene coding for the enzyme, *psefdh*, has been the first bacterial formate dehydrogenase gene cloned and overexpressed in *Escherichia coli* [2, 3]. Crystal structures for apo- and holo-forms of PseFDH have been determined (PDB2NAC, PDB2NAD, PDB2GO1, and PDB2GUG structures). Despite the fact that many novel formate dehydrogenases have been cloned, isolated, and characterized in the last decades, PseFDH is still the one with the highest thermal stability [4], and high catalytic activity and efficiency [5, 6]. Formate dehydrogenase from pathogenic bacterium *Staphylococcus aureus* (SauFDH) has been recently isolated and crystallized in this laboratory [7]; this enzyme is comparable to PseFDH in its thermal stability [4] and exhibits a higher catalytic activity, but not efficiency [6].

We systematically study structure-function relationships in formate dehydrogenases. The importance of His332-Gln313 pair and Arg284 residue in the catalytic mechanism of PseFDH has been confirmed [8, 9]. Hydrophobization of alpha-helices with single-point replacement resulted in the production of mutant forms with improved thermal stability [10]. The experiments aimed at changing the coenzyme specific-

ity have been initiated [11]; the mutants with changed isoelectric point have been constructed [12]. The effect of N-terminal His-tag on the properties of the wild-type enzyme and its $NADP^+$-specific mutants has been studied by site-directed mutagenesis [13]. Chemical stability of PseFDH has been improved as well, and the mutants with an increased stability in the presence of hydrogen peroxide have been produced [14, 15].

As seen from above, to construct a novel biocatalyst with just one improved parameter, one needs to introduce a set of amino acid replacements. In some cases, combination of mutations results in synergy. For example, such effect has been observed while improving thermal stability of soybean FDH [16]. In case of PseFDH SM4S mutant, replacements in 311th position generate enzymes with a 2.4-fold improved thermal stability with respect to the initial mutant, and more than 7-fold if compared to the wild-type PseFDH [17].

By combining replacements improving catalytic activity, as well as thermal and operational stability, we have generated PseFDH SM4S variant. Here we continued experiments to improve properties of the above mutant. Additional single-point amino acid substitutions were introduced in PseFDH SM4S. Previously it have been shown that these changes provided positive effect on the properties of the wild-type enzyme.

EXPERIMENTAL

Site-directed mutagenesis

Single point amino acid substitutions were introduced using a two-step polymerase chain reaction (PCR). The pPseFDH8_SM4S plasmid, with *psefdh* gene under control of a strong T7 phage RNA polymerase promoter, was used as a template. To introduce mutations, forward (T7_for) and reverse (T7_rev) primers for the gene ends, as well as forward and reverse primers carrying the required substitution in the *psefdhsm4* gene were used:

T7_for	5'-TAA TAC GAC TCA CTA TAG GG-3'
T7_rev	5'-GCT AGT TAT TGC TCA GCG G-3'
K61R_for	5'-GGC CTG CGC CGT TAT CTC GAA TCC AAC GGC CAC ACC CTG-3'
K61R_rev	5'-GAT TCG AGA TAA CGG CGC AGG CCG AGC TCG CCG G-3'
K61P_for	5'-GGC CTG CGC CGT TAT CTC GAA TCC AAC GGC CAC ACC CTG-3'
K61P_rev	5'-GAT TCG AGA TAC GGG CGC AGG CCG AGC TCG CCG G-3'
S131A_for	5'-GTC GAT CTT CAG GCG GCT ATC GAC CGT AAC GTC ACC-3'
S131A_rev	5'-GAT AGC CGC CTG AAG ATC GAC GTG GTC-3'
S160A_for	5'-GAT GAT CCT GGC GCT GGT GCG CAA CTA TCT GCC CTC-3'
S160A_rev	5'-GCA CCA GCG CCA GGA TCA TCA TCA CCA CAT G-3'
E170D_for	5'-CCT CGC ACG ATT GGG CGC GGA AGG GCG GCT G-3'
E170D_rev	5'-CTT CCG CGC CCA ATC GTG CGA GGG CAG ATA GTT GCG CAC-3'.

The PCR reaction mixture contained 2.5 μL of 10x *Pfu* DNA polymerase buffer (200 mM Tris-HCl (pH 8.8 at 25°C), 100 mM $(NH_4)_2SO_4$, 100 mM KCl, 1 mg/mL BSA, 1% (v/v) Triton X-100, 20 mM $MgSO_4$); 2.5 μL of dNTP mix (dATP, dGTP, dTTP, dCTP, concentration of each 2.5 mM); 1 μL DNA template (≈10 ng/μL); 2 μL of primers (10 nmol/mL); 0.5 μL of *Pfu* DNA polymerase (2.5 U/μL) and deionized water to a total mixture volume of 25 μL. PCR was performed in a 0.5 mL thin-walled plastic tube (SSI, USA) on a Tertsik device ("DNA-Technologies", Russia).

To prevent evaporation of the reaction mixture, 30 μL of mineral oil was added to the tube. The tube was heated for 5 min at 95°C and then the reaction was carried out according to the following program: denaturation, 95°C, 30 s; primer binding, 54–58°C; elongation, 72°C, 2 min, 25–35 cycles in total. After the last cycle, the reaction mixture was additionally left for 5 min at 72°C. The temperature at the second stage was chosen to be 3–5°C lower than the melting temperature of duplexes (Tm) formed by the primers.

To obtain fragments containing the desired substitution, two PCRs were performed using primer pairs: 1) forward PseFor containing the required nucleotide(s) substitution(s) and reverse standard primer T7_rev (fragment 1); standard forward primer T7_for and reverse primer PseRev, also containing the required nucleotide(s) substitution(s) (fragment 2). The products of two PCRs were purified by electrophoresis in 1% agarose gel followed by isolation of DNA fragments from the gel. At the next stage, the third combining PCR was performed with primers T7_for and T7_rev, where both previously obtained fragments were used as a DNA template.

The product of the third PCR was purified in the same manner and then digested with restriction endonucleases NdeI and XhoI. The PseFDH_SM4S plasmid was treated with the same restrictases to remove the gene fragment with the introduced mutation. The digested PCR product and plasmid were purified by electrophoresis and ligated. The mixture obtained after the ligation reaction was transformed into *E. coli* DH5α cells. The introduction of the required mutations was controlled by plasmid DNA sequencing at the Genome Center of Collective Use, Engelhardt Institute of Molecular Biology, Russian Academy of Sciences or at the Industrial Biotechnology Center of Collective Use, Federal Research Center for Biotechnology, Russian Academy of Sciences.

Expression of new PseFDH mutants in *E. coli* cells

PseFDH wild-type and mutant variants were expressed in *E. coli* BL21(DE3)/pLysS cells. Cells were transformed with the corresponding plasmid and plated on Petri dishes with agar medium containing ampicillin (100 μg/mL) and chloramphenicol

(25 μg/mL). To prepare the inoculum, a single colony was taken from the dish and cultured in 5 mL of 2YT medium (yeast extract 10 g/L, bactotrypton 16 g/L, sodium chloride 5 g/L, pH 7.0) in the presence of 150 μg/mL ampicillin and 25 μg/mL chloramphenicol for 7–9 hrs at 30°C and 180 rpm until the absorption at a wavelength of 600 nm was A600 ≈ 0.6–0.8. Then, 2 mL of the overnight culture were transferred into 100 mL shaked flasks containing 20 mL of 2YT medium and 150 μg/mL ampicillin and the cells were cultured at 37°C and 120 rpm until the absorbance of A600 = 0.6–0.8 was reached. Then cells were reseeded into flasks containing 230 ml of 2YT medium without antibiotics and cultivated at 30°C until the absorbance value A600 ≈ 0.6–0.8. Protein synthesis was induced by adding a lactose solution (300 g/L) to the culture medium to a final concentration of 20 g/L. After induction, the cells were incubated for 17 hrs at 120 rpm and 30°C. The cell biomass after cultivation was collected on a Beckman J-21 centrifuge (USA) at 7500 rpm for 20 min at 4°C. The supernatant was removed and the cells were resuspended in 0.1 M sodium phosphate buffer pH 8.0 in a ratio of 1 : 4 (w/w). The resulting suspension was frozen and stored at –20°C.

Isolation and purification

Cells after cultivation were disintegrated by sonication. Cellular debris was precipitated by centrifugation (Eppendorf 5804R, 40 min, +4°C, 12000 rpm), and a saturated solution of ammonium sulfate was added to the supernatant to final concentration 35% of saturation (0.1 M sodium phosphate buffer, 0.01 M EDTA, pH 7.0 (solution A)) and the final solution was incubated for 4–8 h at +4°C. Undissolved proteins were precipitated in 50 ml tubes on an Eppendorf 5804 R centrifuge (11,000 rpm, +4°C), and the resulting supernatant was applied to a 1.0 × 10 cm column with Phenyl Sepharose FastFlow (Pharmacia Biotech, Austria) equilibrated with solution A. After applying the enzyme, the column was washed with solution A until absorption at 280 nm disappeared. The enzyme was eluted from the column with a linear ammonium sulfate gradient (35–0% saturation, 0.1 M phosphate buffer, 0.01 M EDTA, pH 7.0, total volume 150 mL). 5 mL fractions were collected, absorbance at 280 and 260 nm (A_{280} and A_{260}, respectively) and enzymatic activity (A) were measured. Fractions with the maximum ratio (A/A_{280}) were combined. Desalting was performed on a 2.5 × 10 cm column (volume 25 mL) with Sephadex G25 (Pharmacia Fine Chemicals, Sweden) equilibrated with 0.1 M Na-phosphate, 0.01 M EDTA, pH 7.0. Fractions of 0.5 mL were collected, and enzymatic activity and absorbance at 280 nm were determined in each fraction. The purity of the preparations was controlled by analytical electrophoresis in 12% polyacrylamide gel in the presence of 0.1% sodium dodecyl sulfate on a BioRad MiniProtean II electrophoresis device according to the manufacturer's protocol. The enzyme concentration in the samples was calculated from the absorption value of 1.6 for a 0.1% solution of purified PseFDH at a wavelength of 280 nm.

Measurement of formate dehydrogenase activity

FDH activity was determined spectrophotometrically by the accumulation of NADH (NADPH) at a wavelength of 340 nm (ε_{340} = 6,220M^{-1} cm^{-1}) on a Schimadzu UV1800 PC spectrophotometer at 30°C in 0.1 M sodium phosphate buffer, pH 7.0. The concentration of sodium formate and $NAD(P)^+$ in the cuvette was 0.6 M and 1 mg/mL, respectively.

Determination of Michaelis constants

The Michaelis constants for NAD^+ and formate were determined from the dependences of the enzyme activity on the concentration (0.4–6 K_M) of the corresponding substrate. The concentration of the second substrate was saturating (>15 K_M). The exact concentration of the stock NAD^+ solution was determined spectrophotometrically at a wavelength of 260 nm (ε_{260} = 17,800 $M^{-1}cm^{-1}$).

A solution of sodium formate with a given concentration was prepared by dissolving the required amount of the substrate in 0.1 M sodium phosphate buffer, pH 7.0. The volume of the solution was controlled in a volumetric flask. The K_M values were calculated from the experimental dependences by the method of non-linear regression using the Origin Pro 2015 program.

Thermal inactivation kinetics

Thermal stability of enzymes was measured in 0.1 M sodium phosphate buffer, pH 7.0 at several temperatures. Test tubes (0.5 mL volume) with 100 μL of the enzyme solution (0.2 mg/mL) were placed in a water thermostat preheated to the required temperature (temperature control accuracy ±0.1°C). At certain time points, one tube was taken and transferred to ice for 5 min, then the tube was centrifuged for 3 min at 12,000 rpm in an Eppendorf 5415D centrifuge. A residual FDH activity was measured in triplicate as described above. The thermal inactivation rate constant (k_{in}) was determined as the slope of the direct dependence of the natural logarithm of the residual activity on time (semilogarithmic coordinates $\ln(A/A_0)$ – t) by linear regression using the Origin Pro 8.1 program.

Determination of temperature stability by differential scanning calorimetry

Temperature stability was studied on a Nano DSC differential adiabatic scanning microcalorimeter (TA Instruments, USA). The working volume of capillary calorimetric platinum cells was 300 μL. To prevent the formation of bubbles and boiling of solutions with increasing the temperature, an excess pressure of 3 atm was maintained in the cells of the calorimeter. Before the experiment, the instrumental baseline was recorded and then subtracted from the data obtained for the protein. During measurements, a buffer solution was placed in the control cell, and FDH solution in the same buffer was placed in the working cell. The enzyme concentration was 1–2 mg/mL, and the heating rate was 1°C/min.

RESULTS AND DISCUSSION

Selection of residues for directed mutagenesis

C145S, C255A, and A198G mutations are the key amino acid replacements in PseFDH SM4S mutant. The first two protect the active site of PseFDH from chemical modification and/or oxidation of essential cysteine residues. The C255A replacement results in preservation of 60% of the enzyme activity after 90-day storage at 25°C, whereas the wild-type PseFDH becomes completely inactive at this point [14]. The double replacement C145S/C255A decreases the enzyme inactivation rate constant in the presence of 100 mM hydrogen peroxide by almost 100 times [15]. The A198G replacement provides a decrease in structural tension in the polypeptide chain turn connecting βA beta-sheet and αB helix in the coenzyme binding domain of PseFDH active site. This replacement improves the enzyme thermal stability 2.6-fold, and Michaelis constant for NAD^+ almost 2 times [11]. The present work focuses on the improvement of the thermal stability of PseFDH SM4S mutant.

Lys61 replacements

A shift in the medium pH from 7.0 to 8.0 increases the rate constant of PseFDH thermal inactivation by 6 times [18]. This fact may be interpreted by ionic pairs disruption in alkaline pH, for example, by losing the positive charge on ε-amino group of lysine residue. In the previous work on FDH from *Mycobacterium vaccae* N10 (MycFDH), which has 4 times worse thermal stability than PseFDH but differs from PseFDH by two amino acid residues, with one being Glu61 instead of K61 in PseFDH, the introduced mitations Glu61K (like in PseFDH) or Glu61Pro yield mutant MycFDHs close in their stability to PseFDH [19]. The analysis of apo- and holo-PseFDH structures (PDB2NAC and PDB2NAD, respectively) points to the ionic pair formed by K61 amino group and Asp43 carboxyl. The same stabilization effect of the introduced Pro61 to that of Lys61 means that the ionic pair, responsible for the support of the enzyme structural stability, is preserved in the K61P mutant with the increase in pH. Additionally, K61R replacement can be introduced, since guanidine group will preserve the positive charge up to at least pH 12.

Hydrophobization of S131 and S160 residues

An approach to proteins stabilization based on hydrophobization of protein α-helices, is known for a while [20]. The most frequent Ser/Ala replacement in α-helices is a universal and effective approach for majority of proteins. For example, using this approach, we increased the thermal stability of *D*-amino acid oxidase by several fold [21]. The analysis of PseFDH structure revealed five Ser residues located in α-helices, among which only one was conserved. Mutations of the other four residues showed that the highest stabilization effect (ca. 20% each) was observed for S131A and S160A replacements [10]. These particular replacements were selected for introduction into PseFDH SM4S.

Glu170Asp replacement

The Glu170 residue is located at the center of the protein globule, at the subunit interface (*Fig. 1*), and the negatively charged oxygen atoms of Glu170A carboxyl group of the first subunit are only 2.67 Å far from the oxygen atoms of Glu170B carboxyl group of the second subunit. A removal of carboxylic groups is inappropriate, since these groups participate in electrostatic interactions, and in particular with Arg173 guanidine groups from both A and B subunits (2.64 Å distance). To decrease the mutual repulsion of Glu170 residues without disrupting the whole system of Glu170 interactions, Asp residue can be introduced, because it is shorter by one CH_2-gropup than Glu residue [22]. Of note, *Moraxella* sp. C2 FDH (84% homologous to PseFDH) does have Asp residues in position 170 [23, 24]. The E170D replacement in PseFDH resulted in a 40% increase in the enzyme thermal stability [22].

Thus, the structural analysis allowed us to choose 5 amino acid replacements in 4 positions for directed mutagenesis as shown in *Fig. 1*. Of note, they are located both on the surface and inside the protein globule, including the subunit interface, which is not accessible for solvent molecules. Each replacement in the wild-type PseFDH did not give a significant improvement in stability (max to 40%), however, our

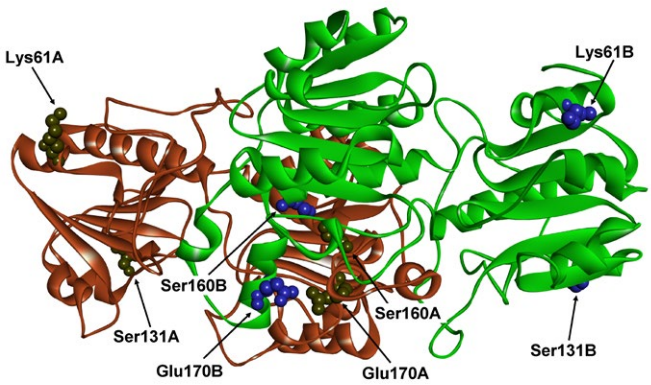

Fig. 1. Positions of Lys61, Ser131, Ser160 and Glu170 in the structure of apo-form of FDH from *Pseudomonas* sp. 101 (PDB2NAC)

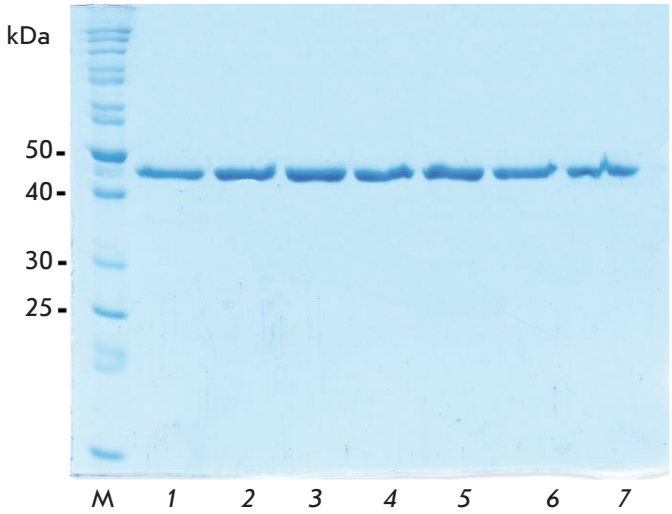

Fig.2. Analytical electrophoresis in 12% polyacrylamide gel in the presence of SDS-Na of enzyme preparations after purification. M – molecular weight marker; 1 – PseFDH wild type; 2 – PseFDH SM4S; 3 – PseFDH SM4S K61P; 4 – PseFDH SM4S E170D; 5 – PseFDH SM4S K61R; 6 – PseFDH SM4S S131A; 7 – PseFDH SM4S S160A

previous mutagenesis experience let us expect synergy for the introduced replacements, and the combined effect could be sufficiently high.

Production of PseFDH SM4S mutant forms

New mutants of PseFDH SM4S have been constructed in accordance with the protocol described in the Experimental Section. Gene sequencing shows that only target mutations have been introduced. The expression results are summarized in *Table 1*. Expression of PseFDH SM4S and wild-type enzyme PseFDH are used as control. The data obtained allow us to conclude that the protocol developed for wild-type PseFDH expression is applicable for production of all new enzyme forms. Isolation and purification of mutant PseFDH forms has been performed using the method developed by us earlier [8]. The results of analytical electrophoresis of PseFDH mutants shown in *Fig. 2* confirm that each preparation contains only one lane and no impurities. Thus, the enzyme preparations obtained are no less than 99% pure.

Table 1. Expression of mutant forms of PseFDH and wild-type enzyme in *E. coli* cells

Enzyme	Enzyme yield, activity, U/L of medium	Biomass yield, g/L of medium	Yield of enzyme by mass*, mg/L of medium	Enzyme content in cells, U/g
PseFDH wt	3875	13.5	388	287
PseFDH SM4S	5430	12.0	543	462
PseFDH SM4S K61P	4865	17.0	487	300
PseFDH SM4S K61R	4575	17.2	458	265
PseFDH SM4S S131A	5200	20.0	520	213
PseFDH SM4S S160A	5450	17.0	545	315
PseFDH SM4S E170D	6300	17.0	630	358

*Enzyme yield per 1 liter of medium was calculated based on activity yield (column 2) and specific activity value of 10 U/mg of protein.

Table 2. Kinetic parameters of mutant PseFDHs and wild-type enzyme

Enzyme	k_{cat}, s^{-1}	$K_M^{HCOO^-}$, mM	$K_M^{NAD^+}$, μM	$k_{cat}/K_M^{NAD^+}$, $(M^{-1}s^{-1})\times10^6$	$k_{cat}/K_M^{HCOO^-}$, $(M^{-1}s^{-1})\times10^3$
PseFDH wt	7.3 ± 0.3	1.63 ± 0.08	52.5 ± 2.5	0.14	4.47
PseFDH SM4S	7.3 ± 0.3	1.36 ± 0.14	35.5 ± 1.5	0.21	5.37
PseFDH SM4S K61P	7.3 ± 0.3	1.19 ± 0.08	48.3 ± 1.7	0.15	6.13
PseFDH SM4S K61R	7.7 ± 0.4	1.89 ± 0.11	45.8 ± 2.0	0.17	4.07
PseFDH SM4S S131A	7.5 ± 0.4	2.31 ± 0.15	48.6 ± 1.6	0.15	3.25
PseFDH SM4S S160A	7.3 ± 0.3	1.22 ± 0.12	48.6 ± 2.7	0.15	5.98
PseFDH SM4S E170D	7.3 ± 0.3	1.11 ± 0.08	41.0 ± 1.7	0.18	6.58

Note. 0.1 M sodium phosphate buffer, 0.01 M EDTA, pH 7.0, 30°C.

Kinetic properties of enzyme mutants

The values of catalytic and Michaelis constants for NAD^+ and $HCOO^-$ for all PseFDH mutants obtained are summarized in *Table 2*. Of note, the apparent value of the catalytic constant for all PseFDH mutants remains unchanged within the experimental error. A small increase in Michaelis constant for formate is observed for S131A change (60% and 40% as compared to PseFDH SM4S and wild-type PseFDH, respectively). The K61R replacement has a similar effect on K_M for formate. The values of Michaelis constants for NAD^+ for the mutants obtained remain unchanged within the experimental error (a 10–20% increase and 15–35% decrease in comparison with K_M for PseFDH SM4S and wild-type PseFDH, respectively). As a consequence of these subtle changes, the catalytic efficiency $k_{cat}/K_M^{NAD^+}$ for all mutants is 1.4-fold lesser than that for PseFDH SM4S and equals to that of wild-type PseFDH. The value of $k_{cat}/K_M^{HCOO^-}$ is slightly increased as the result of K61P and S160A replacements in PseFDH SM4S. Overall, the introduced replacements do not cause noticeable effects on the enzyme catalytic properties.

Thermal stability of PseFDH mutant forms

Thermal stability of PseFDH mutants has been studied in the temperature range of 65–69°C, where thermal inactivation of the wild-type enzyme proceeds irreversibly in accordance with a monomolecular mechanism and first-order reaction kinetics [19]. An example of a dependence of the enzyme residual activity on time in a semi-logarithmic coordinates is shown in *Fig. 3A* for PseFDH SM4S E170D. As seen, the semi-logarithmic plot shows a linear dependence, and thus, the inactivation process obeys first-order re-

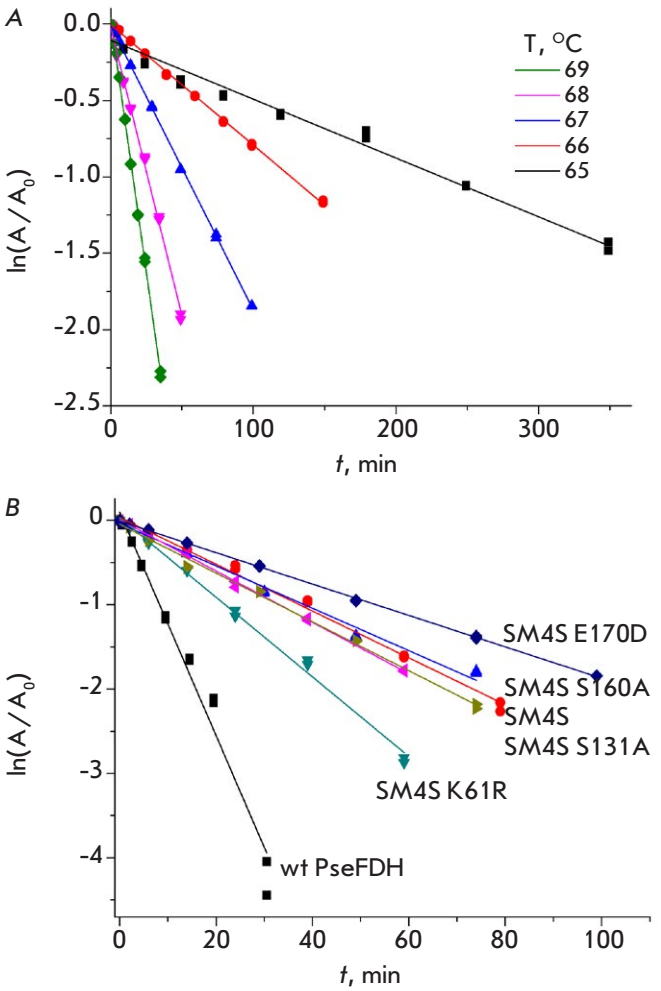

Fig. 3. (*A*) Dependence of the residual activity of PseFDH SM4S E170D on time in coordinates $\ln(A/A_0)$ – t, at several temperatures. (*B*) Time dependence of the residual activity of wild-type PseFDH and its mutant forms in coordinates $\ln(A/A_0)$ – t (s) at 67°C, 0.1 M sodium phosphate buffer, pH 7.0

action kinetics. The apparent first-order rate constant for thermal inactivation, k_{in}, is calculated from the slope of the linear dependence. The residual activity at 67°C for all enzyme forms studied plotted *versus* time in the semi-logarithmic coordinates is shown in *Fig. 3B*. It is clear that the highest stabilization effect is observed for E170D replacement in PseFDH SM4S. The K61R replacement slightly destabilizes PseFDH SM4S, however, the K61R PseFDH SM4S is still more stable than the wild-type enzyme. All other mutants exhibit the stability similar to that of PseFDH SM4S (*Fig. 3B*).

The analysis of the temperature dependence of the apparent rate constant of thermal inactivation gives an answer to the thermodynamic origin of the improved stability of PseFDH SM4S E170D mutant. The true monomolecular character of PseFDH inactivation in the whole range of the temperatures studied allows us to apply the transition state theory for the analysis of the inactivation process.

According to the theory, the equation for the apparent rate constant of thermal inactivation has the following dependence on the temperature:

$$k_{in} = \frac{k_B T}{h} \cdot e^{-\left(\frac{\Delta G^{\neq}}{RT}\right)} = \frac{k_B T}{h} \cdot e^{-\left(\frac{\Delta H^{\neq}}{RT} - \frac{\Delta S^{\neq}}{R}\right)},$$

where k_B = 1.238 × 10^{-23} J/K – is Bolzmann's constant;
h = 6.634 × 10^{-34} J/s^{-1} – is Plank's constant;
R = 8.314 J/mol/K – is universal gas constant.

The linearized equation looks as:

$$\ln\left(\frac{k_{in}}{T}\right) = \ln\left(\frac{k_B}{h}\right) + \frac{\Delta S^{\neq}}{R} - \frac{\Delta H^{\neq}}{RT} = const - \frac{\Delta H^{\neq}}{R}\frac{1}{T},$$

where $const = \ln\left(\frac{k_B}{h}\right) + \frac{\Delta S^{\neq}}{R}$.

The dependence in ln(k_{in}/T) – 1/T coordinates is linear with the slope equal to -$\Delta H^{\neq}/R$. The experimental data on the dependence of the apparent rate constant for thermal inactivation for all PseFDH mutants are plotted in *Fig. 4*. As one can see, in all cases the character of the dependence is the same as for PseFDH SM4S. Using the transition state theory, the values of enthalpy ($\Delta H^{\neq}$) and entropy ($\Delta S^{\neq}$) have been calculated. The value of $\Delta S^{\neq}$ can be obtained from the slope of the dependence of $\Delta G^{\neq}$ on temperature in accordance with the equation:

$$\Delta G^{\neq} = \Delta H^{\neq} - T\Delta S^{\neq}$$

The value of activation Gibbs energy can be calculated from:

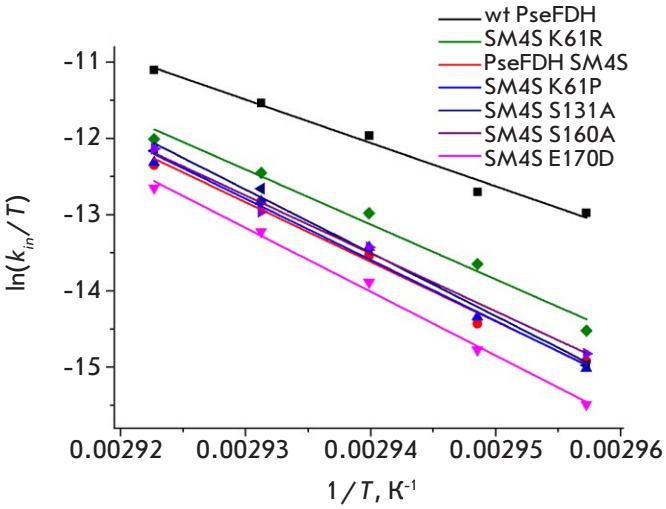

Fig. 4. Temperature dependences of the observed thermal inactivation rate constants for wild-type and mutant PseFDHs in coordinates ln(k_{in}/T) – 1/T. 0.1 M sodium phosphate buffer, pH 7.0

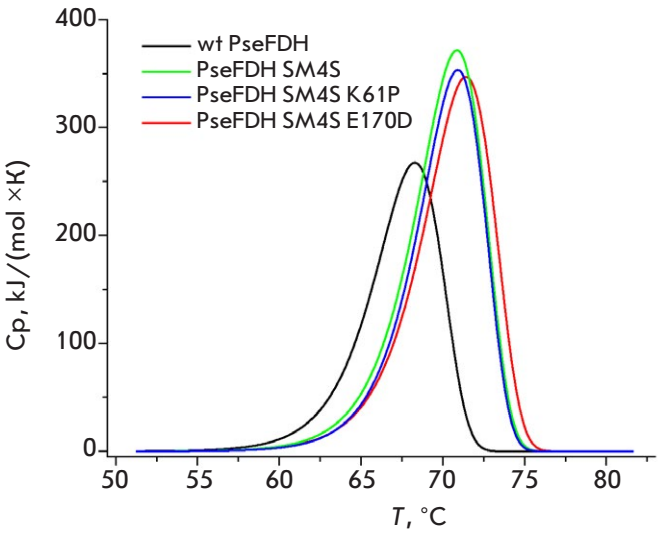

Fig. 5. DSC melting curves for mutant and wild-type PseFDH, 0.1 M sodium phosphate buffer, 0.01 M EDTA, pH 7.0. Protein concentration 2 mg/mL, scanning speed 1 °C/min

$$\Delta G^{\neq} = RT\left[\ln\left(\frac{k_B}{h}\right) - \ln\left(\frac{k_{in}}{T}\right)\right] = RT\ln\left(\frac{k_B T}{k_m h}\right)$$

As seen in *Table 3*, $\Delta H^{\neq}$ and $\Delta S^{\neq}$ for the mutants and PseFDH SM4S have the close values and they are higher than for the wild-type enzyme. The highest value of $\Delta H^{\neq}$ is observed for the mutant with the highest stabilization effect, PseFDH SM4S E170D (*Table 3*).

Table 3. Parameters for thermal inactivation process of mutant PseFDHs and wild-type enzyme

Enzyme	$\Delta H^{\neq}$, kJ/mol	$\Delta S^{\neq}$, J/mol/K	ΔH_{DSC}, kJ/mol	Phase transition temperature, T_m, °C
PseFDH wt	470 ± 35	1100 ± 100	1470	68.3
PseFDH SM4S	650 ± 40	1600 ± 100	1975	70.9
PseFDH SM4S K61P	665 ± 40	1650 ± 100	1880	70.9
PseFDH SM4S K61R	600 ± 40	1450 ± 100	nd	nd
PseFDH SM4S S131A	630 ± 50	1720 ± 100	nd	nd
PseFDH SM4S S160A	690 ± 35	1550 ± 100	nd	nd
PseFDH SM4S E170D	700 ± 30	1730 ± 100	2070	71.4

Note. nd – no data. 0.1 M sodium phosphate buffer, pH 7.0.

Thermal stability of some most interesting PseFDH mutant forms has been also studied using differential scanning calorimetry. Since the mutants exhibit similar stability, the above method has been used for the wild-type enzyme, PseFDH SM4S and two its variants with additional replacements E170D and K61P (S131A and S160A exhibit close stabilization effects), as shown in *Fig. 5*. The numeric values of the heat capacity and phase-transition temperature calculated from the melting curves are shown in *Table 3*. As seen from *Table 3* and *Fig. 5*, E170D replacement results in the highest increase in the maximum temperature at the melting curve (0.5°C) as compared to the one for PseFDH SM4S. Such increase is in agreement with the magnitude of the stabilization effect observed in kinetic experiments on thermal inactivation. The E170D substitution also causes an increase in the specific heat of phase transition in comparison with the other mutants studied and the wild-type enzyme (*Table 3*), being in agreement with the analysis of thermal inactivation kinetics with the help of the transition state theory. Thus, there is a good agreement in the results obtained by two independent approaches to the study of thermal stability of PseFDH mutants.

CONCLUSION

The values of relative thermal stability of the newly obtained mutants with respect to the wild-type PseFDH and the starting PseFDH SM4S mutant (value in brackets) at different temperatures are shown in *Table 4*. The comparison of the stabilization effects leads us to a number of conclusions.

1. Replacements in position 61 confirmed the importance of K61 residue in supporting the active PseFDH structure. Despite the fact that K61R substitution results in destabilization of PseFDH SM4S, the additional mutation still results in the variant with a higher stability that the wild-type. As mentioned above, the replacement of Lys61 with Pro aimed at the removal of the ionic pair without compromising the stability. The results obtained confirm the validity of our hypothesis at pH 7.0. It has been also proposed that the removal of the ionic pair could increase the enzyme thermal stability at an increased pH of 8.0. Preliminary experiments show that K61P change in PseFDH SM4S at pH 8.0 and the standard 0.1 M phosphate buffer actually results in a decrease in the apparent thermal inactivation rate constant, in comparison with the starting PseFDH SM4S enzyme form. The further work will be performed in a wider range of buffer concentrations, because A198G substitution results in the change of the profile of the dependence of the thermal inactivation rate constant on the buffer concentration compared to the wild-type enzyme [18].

2. Replacements S131A and S160A cause no measurable change in the thermal stability of PseFDH SM4S. This is likely the result of the mild stabilization effect even for the wild-type enzyme (no more than 20%), which is negligibly small and falls within the experimental error when one studies PseFDH SM4S, which thermal stability at 65–69°C is 3.6–7.0 times higher than for the wild-type PseFDH.

3. The E170D replacement in the highly stable PseFDH SM4S results in a 2-fold stronger stabilization effect than that for the wild-type enzyme, hence, we do observe a strong synergy effect (200%). In addition, a higher enthalpy of activation ($\Delta H^{\neq}$ = 700 and 470 kJ/mol for PseFDH SM4S E170D and wild-type

Table 4. Values of the stabilization effect* of mutant enzymes with respect to wild-type PseFDH and PseFDH SM4S at various temperatures

Enzyme	Stabilization effect, k_{in}^{wt}/k_{in}^{mut} ($k_{in}^{SM4S}/k_{in}^{mut}$)				
	Temperature, °C				
	65	66	67	68	69
PseFDH wt	1.0	1.0	1.0	1.0	1.0
PseFDH SM4S	7.03(1.0)	5.59(1.0)	4.86(1.0)	3.78(1.0)	3.62(1.0)
PseFDH SM4S K61R	4.43(0.63)	2.58(0.56)	2.75(0.57)	2.5(0.59)	2.48(0.61)
PseFDH SM4S K61P	7.70(1.1)	5.16(0.92)	4.30(0.90)	3.5(0.97)	3.4(0.97)
PseFDH SM4S S131A	7.39(1.05)	4.13(0.93)	4.5(0.93)	4.2(1.15)	2.9(0.83)
PseFDH SM4S S160A	6.35(0.90)	4.13(0.93)	4.3(0.90)	3.1(0.95)	2.81(0.81)
PseFDH SM4S E170D	12.40(1.76)	7.95(1.41)	6.85(1.42)	5.4(1.49)	4.7(1.35)

*Stabilization effect calculated as the ratio of the observed inactivation rate constant of the mutant enzyme to the observed inactivation rate constant of wild-type PseFDH at a given temperature (k_{in}^{wt}/k_{in}^{mut}). Values in parentheses show the corresponding $k_{in}^{SM4S}/k_{in}^{mut}$ ratios, in which the observed rate constant of thermal inactivation of PseFDH SM4S was taken as the baseline.
0.1 M sodium phosphate buffer, 0.01 M EDTA, pH 7.0.

PseFDH, respectively) leads to the values of apparent rate constants of the new mutant enzyme inactivation at application temperatures (25–40°C) thousand times lesser than those for the wild-type enzyme. The mutant obtained at these temperatures will be hundreds times more stable than the starting PseFDH SM4S mutant.

4. Since four single-point substitutions, e.g. K61P, S131A, S160A, E170D, do no change or even slightly increase thermal stability, and barely affect the kinetic parameters in comparison with PseFDH SM4S, they open a possibility of combining all the amino acid changes into a multi-point mutant. Strong synergy observed upon introducing E170D replacement into PseFDH SM4S supports the need in producing multi-point mutants, because by analogy, one may expect a similar synergic effect for combination of the other three mutations. Preliminary modeling and calculations (to be published in separate) demonstrate that there is one more possible replacement that could improve chemical stability and Michaelis constants for both NAD^+ and formate. The work in this direction is underway. ●

The work was partly supported by the grant of the President of the Russian Federation for state support of young Russian scientists – Doctors of Science (contract – MD-2021) MD-349.2021.1.4 and partly within the framework of the state task.

REFERENCES

1. Egorov A.M., Avilova T.V., Dikov M.M., Popov V.O., Rodionov Y.V., Berezin I.V. // Eur. J. Biochem. 1979. V. 99(3), P. 569–576. https://doi.org/10.1111/j.1432-1033.1979.tb13289.x
2. Tishkov V.I., Galkin A.G., Egorov A.M. // Dokl. USSR Acad. Sci. 1991. V. 317. № 3. P. 745–748.
3. Tishkov V.I., Galkin A.G., Marchenko G.N., Tsygankov Y.D., Egorov A.M. // Biotechnol. Appl. Biochem. 1993. V. 18. P. 201–207. DOI: 10.1111/j.1470-8744.1993.tb00266.x
4. Pometun A.A., Kleymenov S.Yu., Zarubina S.A., Kargov I.S., Parshin P.D., Sadykhov E.G., Savin S.S., Tishkov V.I. // Moscow Univ. Chem. Bull. 2018. V. 73. № 2. P. 80–84. DOI: 10.3103/S002713141802013X
5. Tishkov V.I., Popov V.O. // Biomol. Eng. 2006. V. 23. № 2–3. P. 89–110. DOI: 10.1016/j.bioeng.2006.02.003
6. Tishkov V.I., Pometun A.A., Stepashkina A.V., Fedorchuk V.V., Zarubina S.A., Kargov I.S., Atroshenko D.L., Parshin P.D., Kovalevski R.P., Boiko K.M., et al. // Moscow Univ. Chem. Bull. 2018. V. 73. № 2. P. 1–6. DOI: 10.3103/S0027131418020153
7. Pometun A.A., Boyko K.M., Yurchenko T.S., Nikolaeva A.Yu., Atroshenko D.L., Savin S.S., Popov V.O., Tishkov V.I. // Biochemistry (Moscow). 2020. V. 85. № 6. P. 689–696. DOI: 10.1134/S0006297920060061
8. Tishkov V.I., Matorin A.D., Rojkova A.M., Fedorchuk V.V., Savitsky A.P., Dementieva L.A., Lamzin V.S., Mezentzev

A.V., Popov V.O. // FEBS Lett. 1996. V. 390. № 1. P. 104–108. DOI: 10.1016/0014-5793(96)00641-2
9. Galkin A.G., Kutsenko A.S., Bajulina N.P., Esipova N.G., Lamzin V.S., Mezentzev A.V., Shelukho D.V., Tikhonova T.V., Tishkov V.I., Ustinnikova T.B., et al. // Biochim. Biophys. Acta. 2002. V. 1594. № 1. P. 136–149. DOI: 10.1016/s0167-4838(01)00297-7
10. Rojkova A.M., Galkin A.G., Kulakova L.B., Serov A.E., Savitsky P.A., Fedorchuk V.V., Tishkov V.I. // FEBS Lett. 1999. V. 445. № 1. P. 183–188. DOI: 10.1016/S0014-5793(99)00127-1
11. Alekseeva A.A., Fedorchuk V.V., Zarubina S.A., Sadykhov E.G., Matorin A.D., Savin S.S., Tishkov V.I. // Acta Naturae 2015. V. 7. № 1(24). P. 60–69. DOI: 10.32607/20758251-2015-7-3-55-64
12. Alekseeva A.A., Petrov A.S., Fedorchuk V.V., Fedorchuk E.A., Osipova T.A., Tishkov V.I. // Moscow Univ. Chem. Bull. 2014. V. 69. № 2. P. 73–79. DOI: 10.3103/S0027131414020023
13. Pometun A.A., Parshin P.D., Galanicheva N.P., Uporov I.V., Atroshenko D.L., Savin S.S., Tishkov V.I. // Moscow Univ. Chem. Bull. 2020. V. 75. № 4. P. 250–257. DOI: 10.3103/S0027131420040057
14. Odintseva E.R., Popova A.S., Rozhkova A.M., Tishkov V.I. // Moscow Univ. Chem. Bull. 2002. V. 43. № 6. P. 356–359 (rus).
15. Savin S.S., Tishkov V.I. // Acta Naturae 2010. V. 2. № 1(4). P. 97–101. DOI: 10.32607/20758251-2010-2-1-97-101
16. Alekseeva A.A., Kargov I.S., Kleimenov S.Yu., Savin S.S., Tishkov V.I. // Acta Naturae 2015. V. 7. № 3(26). P. 55–64. DOI: 10.32607/20758251-2015-7-3-55-64
17. Tishkov V.I., Goncharenko K.V., Alekseeva A.A., Kleymenov S.Yu., Savin S.S. // Biochemistry (Moscow). 2015. V. 80. № 13. P. 1690–1700. DOI: 10.1134/S000629791513005
18. Voinova N.S., Savin S.S., Alekseeva A.A., Skirgello O.E., Tishkov V.I. // Moscow Univ. Chem. Bull. 2008. V. 63. № 2. P. 60–62. DOI: 10.3103/S0027131408020028
19. Fedorchuk V.V., Galkin A.G., Yasny I.E., Kulakova L.B., Rojkova A.M., Filippova A.A., Tishkov V.I. // Biochemistry (Moscow) 2002. V. 67. № 10. P. 1145–1151. DOI: 10.1023/A:1020915324159
20. Munoz V., Serrano L. // J. Mol. Biol. 1995. V. 245. № 3. P. 275–296. DOI: 10.1006/jmbi.1994.0023
21. Golubev I.V., Komarova N.V., Ryzhenkova K.V., Chubar T.A., Savin S.S., Tishkov V.I. // Acta Naturae. 2014. V. 6. № 3(22). P. 76–88. DOI: 10.32607/20758251-2014-6-3-76-88
22. Fedorchuk V.V. Increasing the thermal stability of bacterial formate dehydrogenase by site-directed mutagenesis: PhD thesis. M.: M.V. Lomonosov Moscow State University, 2000.
23. Shabalin I.G., Filippova E.V., Polyakov K.M., Sadykhov E.G., Safonova T.N., Tikhonova T.V., Tishkov V.I., Popov V.O. // Acta Crystallogr. D Biol. Crystallogr. 2009. V. 65. № 12. P. 1315–1325. DOI: 10.1107/S0907444909040773
24. Shabalin I.G., Polyakov K.M., Tishkov V.I., Popov V.O. // Acta Naturae. 2009. V. 1. № 3. P. 89–93. DOI: 10.32607/20758251-2009-1-3-89-93

3D Models of Cellular Spheroids As a Universal Tool for Studying the Cytotoxic Properties of Anticancer Compounds *In Vitro*

A. S. Sogomonyan[1,2], V. O. Shipunova[1,2,3,4*], V. D. Soloviev[1,4], V. I. Larionov[1], P. A. Kotelnikova[1,4], S. M. Deyev[1,2]

[1]Shemyakin–Ovchinnikov Institute of Bioorganic Chemistry, Russian Academy of Sciences, Moscow, 117997 Russia

[2]MEPhI (Moscow Engineering Physics Institute), Institute of Engineering Physics for Biomedicine, (PhysBio), Moscow, 115409 Russia

[3]Sirius University of Science and Technology, Sochi, 354340 Russia

[4]Moscow Institute of Physics and Technology (National Research University), Dolgoprudny, Moscow Region, 141701 Russia

*E-mail: viktoriya.shipunova@phystech.edu

Received September 23, 2021; in final form, January 26, 2022

DOI: 10.32607/actanaturae.11603

ABSTRACT **The aim of this work is to develop a 3D cell culture model based on cell spheroids for predicting the functional activity of various compounds *in vivo*. Agarose gel molds were made using 3D printing. The solidified agarose gel is a matrix consisting of nine low-adhesive U-shaped microwells of 2.3 × 3.3 mm for 3D cell spheroid formation and growth. This matrix is placed into a single well of a 12-well plate. The effectiveness of the cell culture method was demonstrated using human ovarian carcinoma SKOVip-kat cells stably expressing the red fluorescent protein Katushka in the cytoplasm and overexpressing the membrane-associated tumor marker HER2. The SKOVip-kat cell spheroids were visualized by fluorescence microscopy. The cell concentration required for the formation of same-shape and same-size spheroids with tight intercellular contacts was optimized. To verify the developed model, the cytotoxicity of the targeted immunotoxin anti-HER2 consisting of the anti-HER2 scaffold DARP 9_29 and a fragment of the *Pseudomonas aeroginosa* exotoxin, DARP-LoPE, was studied in 2D and 3D SKOVip-kat cell cultures. The existence of a difference in the cytotoxic properties of DARP-LoPE between the 2D and 3D cultures has been demonstrated: the IC50 value in the 3D culture is an order of magnitude higher than that in the monolayer culture. The present work describes a universal tool for 3D cultivation of mammalian cells based on reusable agarose gel molds that allows for reproducible formation of multicellular spheroids with tight contacts for molecular and cell biology studies.**

KEYWORDS **3D printing, 3D cell culture models, DARPin, TurboFP635.**

ABBREVIATIONS **MTT – 3-(4,5-dimethylthiazol-2-yl)-2,5-diphenyltetrazolium bromide; FITC – fluorescein isothiocyanate; DARPin – designed ankyrin repeat protein; LoPE – low immunogenic exotoxin A fragment of the gram-negative bacteria *Pseudomonas aeruginosa*; HER2 – human epidermal growth factor receptor 2.**

INTRODUCTION

In vitro culturing of mammalian cells remains one of the most valuable tools in molecular and cell biology. In 1885, Wilhelm Roux developed a cell culture method by incubating live chick embryo cells in saline for several days. In 1906, American zoologist Ross Granville Harrison became the first scientist to grow an artificial tissue culture [1]. Cell cultures began to be used as a tool to study the interaction of various substances with living objects as the 19th century was coming to an end [2]. Two-dimensional (2D) cell models, which are currently the main tool employed in *in vitro* experiments, are widely used in fundamental and applied research; in particular, in developing antitumor therapy methods using various hybrid assemblies [3] and nanoparticles loaded with active

substances [4–9]. Studies in 2D cultures take into account differences from *in vivo* animal models; however, in order to predict what effect this will have on the body, a large number of cell culture experiments is required. Other disadvantages of monolayer cultures include the lack of a tissue structure and unlimited access of cells to such growth medium components as oxygen, nutrients, and metabolites, while access of a tumor tissue to these substances is, on the contrary, more variable. These limitations have led to the need for an alternative system resembling organs that allows one to perform a large number of routine experiments without laboratory animals. Such systems are spherical clusters of interacting cells: three-dimensional (3D) models [10] such as dense cell aggregations; spheroids grown on the surface of either low-adhesion plastic [11] or agarose [12]; and those obtained using hanging drops [13], alginate capsules [14], and other 3D systems.

Tumor 3D spheroids are closer to *in vivo* cell models compared to 2D cultures, since the latter do not reflect the architecture of animal organs, which have a specific structure and spatial organization. Spheroids are used to create organelles and organs mimicking the heterogeneity and pathophysiology of oncological processes in a living organism and also test potential drugs [11, 15, 16].

Tumor tissue consists not only of cancer cells but also of stromal cells, such as fibroblasts, vascular endothelial cells, pericytes, adipocytes, lymphatic endothelial cells, and the cells of the immune system. These cells contribute to tumor formation and growth and participate in cancer drug resistance [17]. Spheroids consisting of tumor cells only form cell–cell and cell–extracellular matrix interactions and, thus, create a barrier for the substances to be tested [18]. Therefore, the results of studies of cytotoxic compounds in 3D models differ from those obtained in monolayer cultures. Thus, 3D cultures are most suitable for *in vitro* studies aimed at predicting and modeling the tumor response to drug exposure. For this reason, introduction of these objects into laboratory practice will save time and costs in identifying new drug candidates, accelerate clinical trials, and reduce the development time to market [18, 19].

This paper presents a simple and universal method for creating 3D spheroids (same-shape and same-size cell clusters) to study the activity of substances in both fundamental and preclinical studies. The 3D printing technique was used to make gel molds from a photopolymer resin. Molds were filled with agarose, which served as the well matrix for cell spheroid formation. Fluorescent microscopy showed the presence of numerous live cells, outnumbering dead ones, during spheroid growth. Comparison of 2D and 3D cell cultures revealed significant differences in the cytotoxicity of the original targeted immunotoxin DARP-LoPE [20]. For instance, the half-maximum inhibitory concentration (IC50) value for the immunotoxin in the 3D culture is approximately an order of magnitude higher than that in the 2D culture, which must be taken into account when selecting drug doses for therapeutic injections *in vivo*.

EXPERIMENTAL

Cell culture conditions

Fluorescent ovarian carcinoma SKOVip-kat cells have been previously obtained to study the effect of antitumor compounds in the intraperitoneal metastasis model in immunodeficient animals [20]. CHO cells were obtained from the collection of the Laboratory of Molecular Immunology of the Institute of Bioorganic Chemistry of the Russian Academy of Sciences. SKOVip-kat and CHO cells were cultured in cell culture flasks (Nunc, Denmark) containing a DMEM medium (Gibco, USA) supplemented with 10% fetal bovine serum (FBS, Capricorn, Germany) in a CO_2 incubator (BINDER, Germany) at 37°C and 5% CO_2. The cells were detached from the surface of culture flasks using a Versen solution (PanEco, Russia).

Formation of fluorescent SKOVip-kat cell spheroids

Agarose molds were made of a FormLabs Gray Resin 1L photopolymer resin (USA) using a FormLabs Form3 3D printer (USA). Agarose (1%; PanEco) diluted in a colorless Fluorobrite DMEM medium (Gibco) without FBS was used as a mold material for spheroid formation. The spheroids were obtained by adding SKOVip-kat cell suspension to agarose gel wells in a 12-well plate (Nunc) containing the DMEM medium (Gibco) supplemented with 10% FBS (Capricorn) and further culturing of cells for five days in a CO_2 incubator (BINDER, Germany) at 37°C and 5% CO_2. The resulting spheroids were stained with fluorescent dyes and visualized using fluorescence microscopes Leica DMI6000B (Leica Microsystems, Germany) and Axiovert 200 (Carl Zeiss, Germany).

Fluorescence microscopy

The cells were visualized using fluorescent dyes Hoechst 33342 (PanEco), propidium iodide, and acridine orange (Sigma-Aldrich, USA).

Labeled SKOVip-kat spheroids were visualized using the inverted fluorescence microscopes Leica DMI6000B and Axiovert 200. The Katushka (TurboFP635) protein fluorescence was excited with the HBO 100W mercury lamp of an Axiovert 200 flu-

orescence microscope with excitation and emission wavelengths of 565/30 and 620/60 nm, respectively; the excitation and emission wavelengths for fluorescent dyes were 365/12 and 397/LP nm for Hoechst 33342 and 565/30 and 620/60 nm for propidium iodide, respectively. The Katushka protein fluorescence was also excited using the metal halide lamp of a Leica DMI6000B fluorescence microscope with excitation and emission wavelengths of 545/30 and 610/75 nm, respectively; the excitation and emission wavelengths for fluorescent dyes were 405/10 and 460/40 nm for Hoechst 33342, 545/30 and 610/75 nm for propidium iodide, and 470/40 and 525/50 nm for acridine orange, respectively. Plastic 96-well plates (Nunc) were used to visualize the 2D SKOVip-kat and CHO cell cultures. The cells were incubated in 100 μL of a colorless DMEM medium (Gibco) with FBS (Capricorn) for 12 h at 37°C and 5% CO_2. Then, either the monoclonal antibody trastuzumab or DARP-LoPE immunotoxin conjugated to the fluorescent dye fluorescein 5(6)-isothiocyanate (FITC) was added to a final concentration of 2 μg/mL [7] in a volume of 100 μL. The cells were washed to remove unbound proteins and resuspended in a 1% bovine serum albumin in phosphate buffer. A Leica DMI6000B fluorescence microscope was used for visualization.

Cell viability assay

The cytotoxicity of the SKOVip-kat [20] and CHO cells incubated with DARP-LoPE immunotoxin [21] was analyzed using the colorimetric MTT assay (MTT is a yellow tetrazolium dye that is reduced to purple formazan by live cells) [22].

The assay was performed in a 96-well plate (Nunc). The SKOVip-kat and CHO cells (3.5×10^3 cells per well) were incubated in 100 μL of a phenol-red free DMEM medium (Gibco (Thermo Scientific), USA) supplemented with 10% FBS (Capricorn) for 12 h at 37°C and 5% CO_2. Then, 100 μl of DARP-LoPE immunotoxin was added and the cells were incubated for 72 h. After this, the medium underwent shaking and 100 μl of 0.5 g/L MTT were added. The MTT solution underwent shaking after 1 h, and 100 μL of DMSO (Panreac-AppliChem, USA) was added to the wells to dissolve formazan. The optical density was measured using an Infinite M1000 Pro microplate reader (Tecan, Austria) at a wavelength of 570 nm and a reference wavelength of 630 nm. The IC50 values of DARP-LoPE in SKOVip-kat and CHO cells were determined using the GraphPad Prism 8.0.1 software.

RESULTS AND DISCUSSION

The aim of the current work is to produce reproducible 3D spheroids *in vitro* that mimic the characteristics of tumor tissues to test various active substances, including drugs. We used human ovarian carcinoma SKOVip-kat cells overexpressing the HER2 receptor, a diagnostic and therapeutic marker of some cancers, on its surface. This cell line has been previously obtained by stably transfecting SKOV3-1ip cells with the gene of the red fluorescent protein Katushka [23]. The Katushka fluorescence excitation and emission wavelengths are in the near infrared region (588 and 635 nm, respectively) [24]; this region falls in the tissue transparency window, which makes it possible to visualize these cells both *in vitro* and *in vivo* with equal efficiency.

Formation of 3D spheroids using agarose molds

Agarose, which is a natural biodegradable, non-adhesive, and non-toxic polysaccharide derived from seaweed, was used as the matrix for the 3D spheroids [25]. Agarose has the characteristic necessary for creating three-dimensional cell culture models: high porosity (average pore size, 100–300 nm), which allows for the renewal of nutrient media for 3D cell growth [25] and provides access to gases and small molecules [26]. Since agarose is an optically transparent material, it is suitable for the microscopic visualization of spheroids. Agarose gel solidifies in molds at room temperature, which makes it possible to perform experiments under sterile conditions without significant difficulties, while the accessibility of the resulting gel wells to a pipette tip makes it possible to introduce cells and conduct other mold manipulations.

The resulting agarose molds have nine identical wells, 2.3 mm in diameter and 3.3 mm in height, in which spheroids with the same size and shape are formed. The designed mold is an open system that allows one to analyze spheroid formation and test various compounds using light and fluorescence microscopy.

Figure 1 presents the design of SKOVip-kat cell spheroids. Molds for the agarose gel were printed on a FormLabs Form3 3D printer (USA) using the FormLabs Gray Resin (USA). The agarose volume in the mold is 1,200 μl; the volume of a single agarose well is 10 μl. The agarose surface is non-adhesive to cells, which allows for spheroid self-formation. Spheroids formed in five days, which was confirmed visually by the presence of intercellular contacts [26] (*Fig. 2*). *Figure 2* shows the viability of the cells inside the spheroids assessed using a Leica DMI6000B fluorescence microscope. Three representative spheroids stained with fluorescent dyes were visualized along the Z axis with a 200-nm step. The fluorescent dye acridine orange stains nucleic acids in living cells; propidium iodide stains nucleic acids in dead cells,

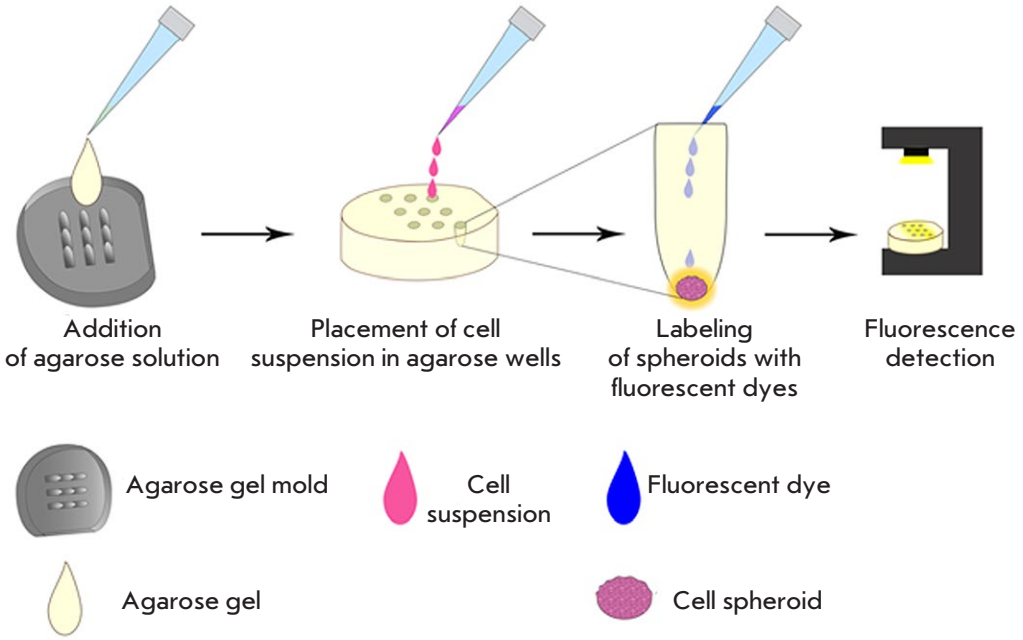

Fig. 1. Design of 3D SKOVip-kat cell spheroids. An agarose solution was added to the molds for solidification at room temperature. A suspension of SKOVip-kat cells was added to the gel-containing wells. After the spheroids had formed, the cells were labeled with fluorescent dyes and analyzed by fluorescence microscopy

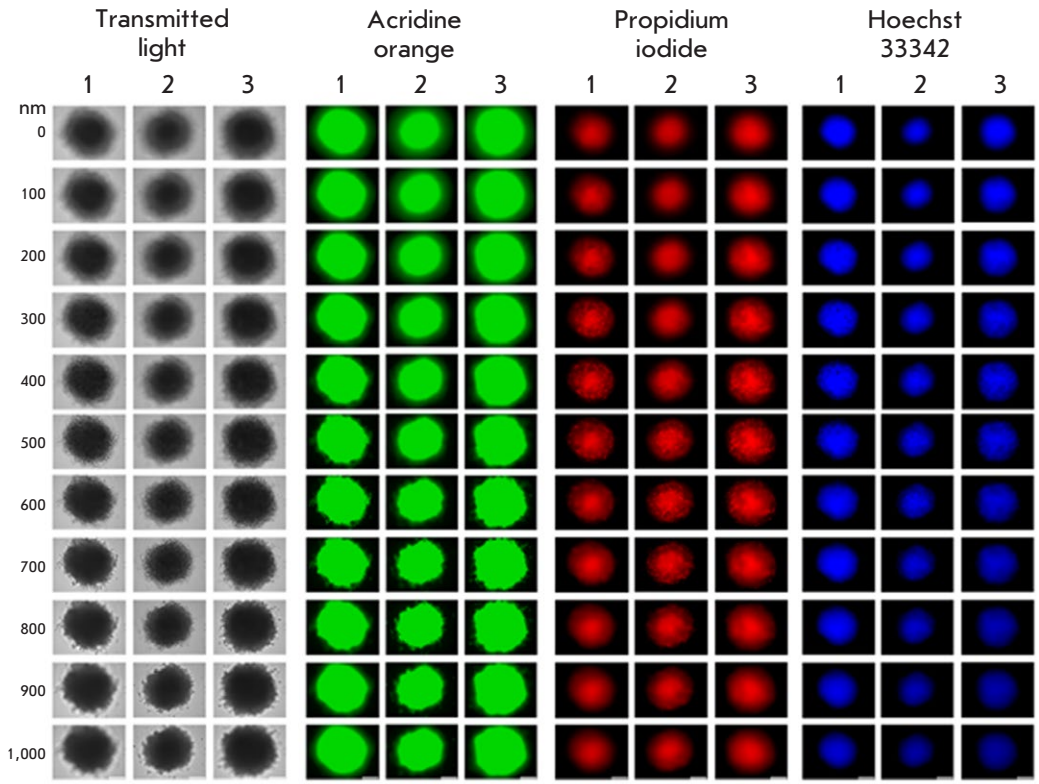

Fig. 2. Imaging of SKOVip-kat spheroids. Imaging of three representative spheroids stained with the fluorescent dyes acridine orange, Hoechst 33342, and propidium iodide with a Z-axis step of 200 nm. The excitation and emission wavelengths for fluorescence detection were as follows: 470/40 and 525/50 nm for acridine orange, 545/30 and 610/75 nm for propidium iodide, and 405/10 and 460/40 nm for Hoechst 33342, respectively. Scale: 250 μm

since the membranes of living cells are impermeable to the dye [27]; Hoechst 33342 stains nucleic acids in nuclei [28] by passing through the membranes of living cells [29]. Staining with acridine orange and Hoechst 33342 showed that there are more live cells than dead cells stained with propidium iodide both inside and outside the spheroid. Thus, the 3D cell cultures obtained by us are most suitable for testing drugs, since the cells in a spheroid create intercellular contacts and create an approximate model of cancer tissues; i.e., they represent a more adequate *in vitro* system than 2D cultures.

Evaluation of HER2 receptor expression on the SKOVip-kat cell surface

HER2 (human epidermal growth factor receptor 2) is a well-known membrane-associated tumor marker [30–32]. Expression of this receptor is often high in mammary, ovarian, endometrial, gastric, and esophageal cancers and low in normal cells [33]. For example, this tumor marker is found in 30% of breast cancers [34]; for this reason, HER2 is considered an important target in tumor diagnosis and therapy. HER2 expression on the surface of SKOVip-kat cells was evaluated using the monoclonal antibody trastuzumab conjugated to FITC. Chinese hamster ovary CHO cells lacking HER2 on their cell surface were used as a negative control (*Fig. 3*). Both cell cultures were incubated with a trastuzumab–FITC conjugate and then visualized on a Leica DMI6000B fluorescence microscope. The data presented in *Fig. 3* confirm the presence of HER2 on the SKOVip-kat cell surface.

DARP-LoPE immunotoxin cytotoxicity in the 2D culture

In order to validate the developed 3D model as a tool for studying the antitumor efficacy of the compounds, we evaluated the cytotoxicity of the targeted antitumor compound, DARP-LoPE immunotoxin.

Immunotoxins are targeted proteins fused to the toxin isolated from either bacteria or poisonous plants [35, 36]; they are considered one of the most promising targeted molecules in oncotherapy. The immunotoxin DARP-LoPE has previously been genetically engineered using the non-immunoglobulin designed ankyrin repeat protein DARP 9_29 that binds to the HER2 receptor [37, 38], and the low-immunogenic variant of the exotoxin A region (LoPE) isolated from the Gram-negative bacterium *Pseudomonas aeruginosa* [21]. This immunotoxin binds specifically to HER2 and induces tumor cell death *in vitro* [21]. Moreover, DARP-LoPE effectively inhibits the growth of HER2-positive human ovarian carcinoma xenografts, which confirms the effectiveness of DARPin-based targeted drugs [5, 20, 21, 39].

Figure 4 shows DARP-LoPE cytotoxicity analysis results and fluorescence microscopy data confirming the specificity of immunotoxin binding to SKOVip-kat cells. Cytotoxicity was evaluated using the MTT assay; the data was processed using the OriginPro 2015 software. The obtained results indicate the targeted cytotoxicity of DARP-LoPE in SKOVip-kat cells and the absence of DARP-LoPE cytotoxicity in CHO. The IC50 value for DARP-LoPE in SKOVip-kat cells was 41.9 pM (*Fig. 4A*).

Tumor cells were visualized by labeling HER2 on the surface of SKOVip-kat cells with the monoclonal antibody trastuzumab and FITC-conjugated DARP-LoPE. It was shown that both immunotoxin

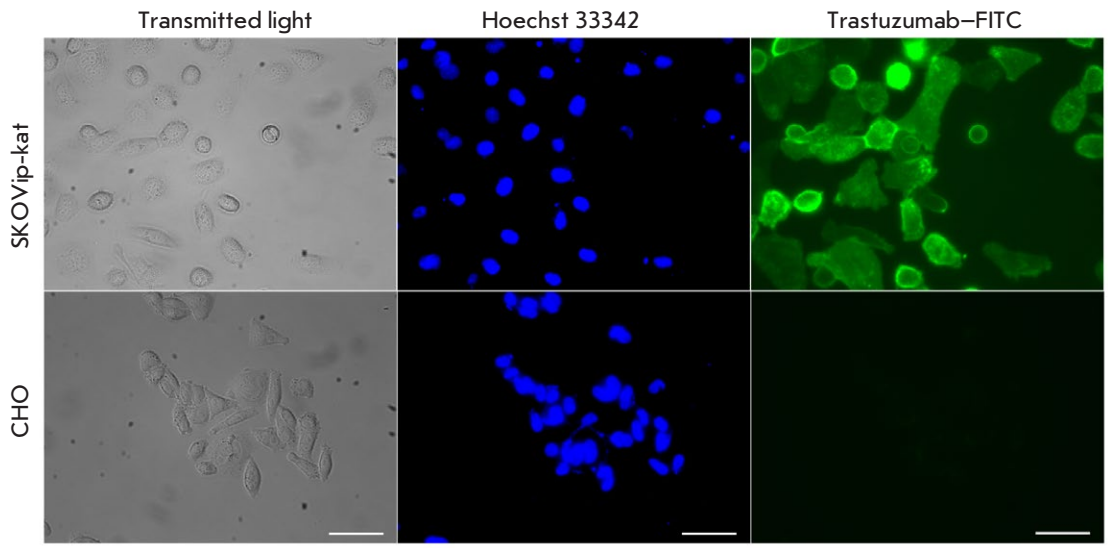

Fig. 3. Imaging of the HER2 receptor expression in SKOVip-kat (HER2-positive) and CHO (HER2-negative) cells using the monoclonal antibody trastuzumab conjugated to the fluorescent dye FITC. Expression of HER2 on the SKOVip-kat cell surface was confirmed by intense staining of the cell membrane with the anti-HER2 antibody. Cell nuclei were stained with Hoechst 33342. The excitation and emission wavelengths for fluorescence detection were as follows: 405/10 and 460/40 nm Hoechst 33342 and 470/40 and 525/50 nm for FITC, respectively. Scale: 50 μm

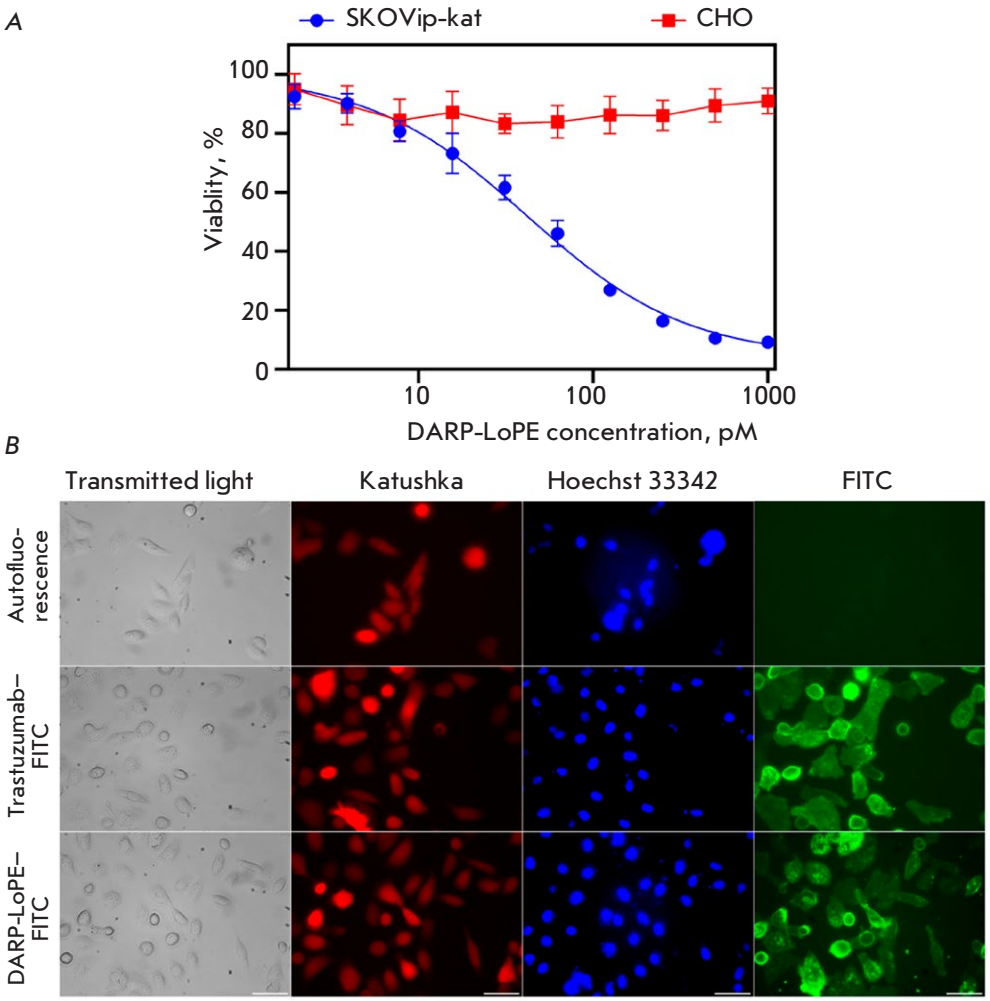

Fig. 4. Interaction of the targeted immunotoxin DARP-LoPE with SKOVip-kat cells. (*A*) – evaluation of DARP-LoPE cytotoxicity in SKOVip-Kat and CHO cells using the MTT assay. Cell viablity in the absence of DARP-LoPE immunotoxin was considered as 100%. (*B*) – visualization of live cells using the Katushka protein (TurboFP635) and Hoechst 33342 dye; visualization of HER2 receptor expression in SKOVip-kat cells incubated with the monoclonal antibody trastuzumab–FITC and immunotoxin DARP-LoPE–FITC. The excitation and emission wavelengths were as follows: 545/30 and 610/75 nm for Katushka protein, 405/10 and 460/40 nm for Hoechst 33342, and 470/40 and 525/50 nm for FITC, respectively. Scale: 50 μm

and trastuzumab effectively interact with HER2 on the tumor cell surface (*Fig. 4B*).

DARP-LoPE immunotoxin cytotoxicity in SKOVip-kat spheroids

In order to select the optimal number of cells in the spheroid wells, the concentration range from 1,500 to 15,000 cells per well was tested. Optimal concentrations were determined on day 3 of cell incubation in the agarose wells by transmitted light microscopy and fluorescence visualization of the Katushka protein in SKOVip-kat. Reproducibility of our results and formation of cell contacts (the absence of cell fragmentation) [26] were observed in wells containing 15,000 cells per spheroid (*Fig. 5*).

Along with selection of the cell concentrations, DARP-LoPE cytotoxicity was studied by incubating the spheroids with various concentrations of DARP-LoPE. After incubation with the protein and staining with Hoechst 33342 and propidium iodide, the samples were analyzed by fluorescence microscopy (*Fig. 5*). Visually determined IC50 of DARP-LoPE in the 3D culture was 0.3 nM, which is about eight times greater than that in the 2D culture (41.9 pM). Since the structural organization of 3D cell models is closer to animal models *in vivo* than that of 2D models, the visualization and cytotoxicity results in the 3D culture should presumably be similar to those obtained in animal objects *in vivo*.

CONCLUSION

The transition from 2D to 3D models is necessary due to the insufficient information value of 2D systems when studying various effects and testing drugs for the diagnosis and treatment of various diseases. The creation of 3D spheroids imitating solid tumors and their introduction in research practice can also be rationalized on ethical grounds: the results obtained by using these systems are closer to *in vivo* results [40]. Thus, the use of these models may reduce the num-

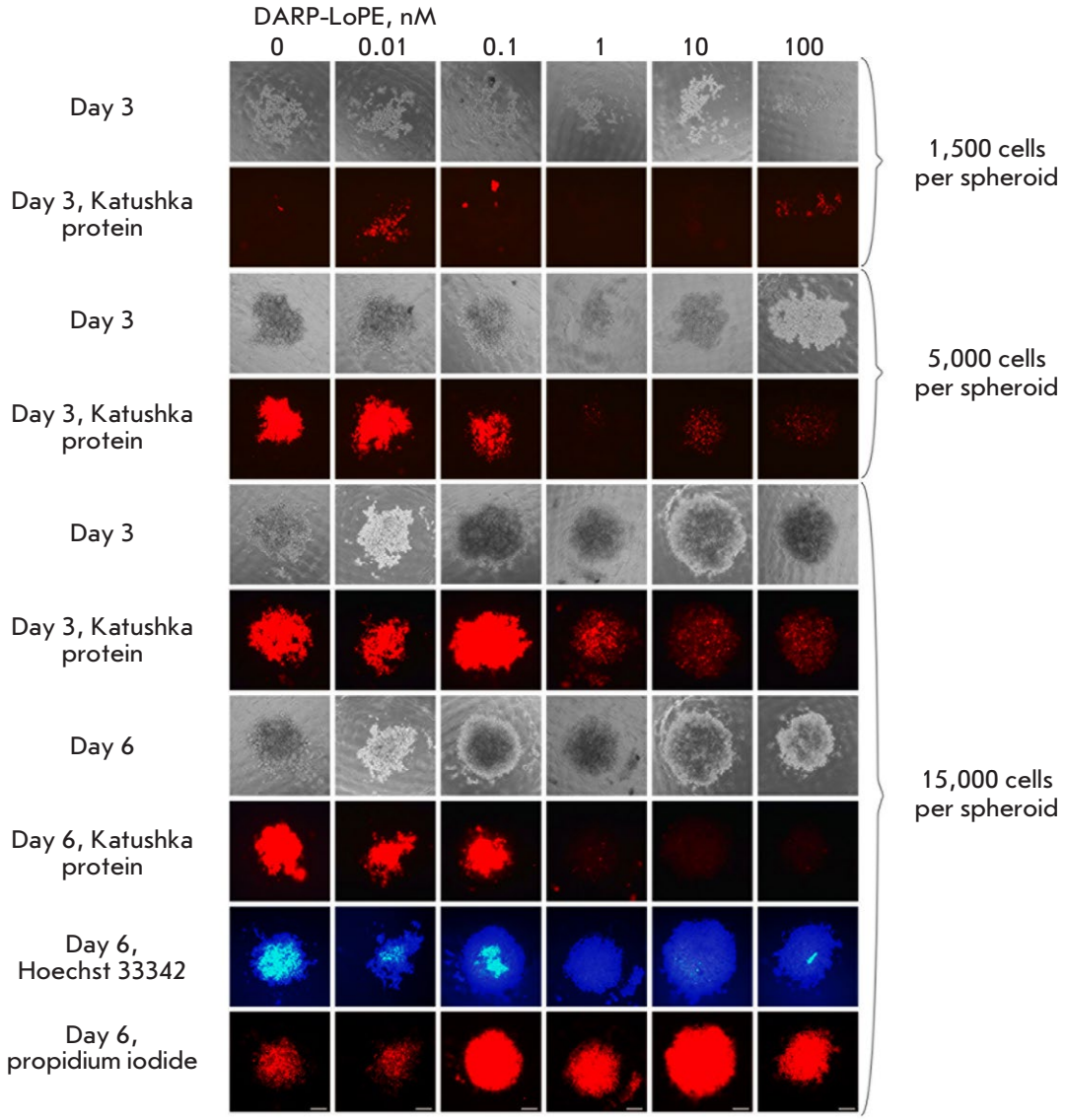

Fig. 5. Imaging of SKOVip-kat spheroids and analysis of DARP-LoPE immunotoxin cytotoxicity in the 3D culture. The cells were incubated with various concentrations of immunotoxin; cell viability was analyzed for six days. The cytotoxicity of DARP-LoPE immunotoxin in the 3D cell culture containing spheroids comprised of a different number of SKOVip-kat cells was analyzed. The optimal number of cells for creating a 3D culture was shown to be 15,000 cells per spheroid. The viability of SKOVip-kat cells was assessed based on the fluorescence of the Katushka protein using real-time fluorescence microscopy on days 3 and 6. On day 6, the spheroids were incubated with dyes: live and dead cells were visualized using Hoechst 33342 and propidium iodide, respectively. The Excitation and emission wavelengths were as follows: 565/30 and 620/60 nm for Katushka, 365/12 and 397/LP nm for Hoechst 33342, and 565/30 and 620/60 nm for propidium iodide, respectively. Scale: 250 μm

ber of animal experiments required for drug screening [41].

Three-dimensional cell spheroids form a specific microenvironment with characteristics different from those of 2D structures: pH value, presence and concentration of autocrine factors, as well as oxygen and CO_2 concentrations; cells in this microenvironment have their own morphology, ability to differentiate, proliferate, and respond to various stimuli, thereby imitating the *in vivo* behavior. These properties of cells in a spheroid are important in order to study the effect of various drugs, since the artificial microenvi-

ronment limits penetration of the latter; therefore, a higher substance concentration is required to achieve the desired effect [18].

In our work, we present a method for creating cancer cell spheroids based on 3D printing of photopolymer resin molds and their filling with agarose. It is a simple and reproducible method for drug testing; it allows one to obtain cytotoxicity analysis results that are close to those obtained *in vivo*. Today, 3D printing is becoming an affordable means for obtaining molds with the desired characteristics; it is widely used in various fields, such as regenerative medicine [42], engineering [43], architecture [44], and manufacturing [45]. To date, 3D printers and materials for creating the desired objects have become more affordable [46], which makes it possible to use the technique in many laboratories. The use of agarose as the matrix for spheroid formation makes this method as effective as possible for routine experiments. Since agarose is low adhesive to cells, interactions in a spheroid occur only between cells, which promotes cell growth in all directions instead of just one. In addition, since agarose is a transparent polymer, it can be used in various studies: in particular, in photodynamic therapy. Furthermore, the developed spheroid model is an open system that allows one to perform such cell manipulations as medium change and washoff of various components, external exposure to electromagnetic radiation, introduction of other cell types (endothelium cells and fibroblasts), and placement of biopsy specimens into a separate well.

Using the developed method, we obtained reproducible same-shape and same-size 3D spheroids from fluorescent SKOVip-kat cells. Significant differences were revealed in the effect of the targeted immunotoxin between 2D and 3D models using the colorimetric toxicity assay and fluorescence microscopy. Thus, we have developed a simple and effective method for obtaining representative 3D spheroid models for molecular biological and cellular studies [47, 48]. ●

This study was supported by the RFBR grant No. 19-29-04012 MK (development of a 3D model of ErbB2-positive tumors) and the Russian Science Foundation, RSF No. 17-74-20146 (isolation and purification of targeted immunotoxin, evaluation of its cytotoxicity).

REFERENCES

1.Harrison R.G. // Exp. Biol. Med. 1906. V. 4. № 1. P. 140–143.
2.Yao T., Asayama Y. // Reprod. Med. Biol. 2017. V. 16. № 2. P. 99–117.
3.Grebenik E.A., Kostyuk A.B., Deyev S.M. // Russ. Chem. Rev. 2016. V. 85. № 12. P. 1277–1296.
4.Shipunova V.O., Sogomonyan A.S., Zelepukin I.V., Nikitin M.P., Deyev S.M. // Molecules. 2021. V. 26. № 13. P. 3955. doi: 10.3390/molecules26133955.
5.Shramova E., Proshkina G., Shipunova V., Ryabova A., Kamyshinsky R., Konevega A., Schulga A., Konovalova E., Telegin G., Deyev S. // Cancers (Basel). 2020. V. 12. № 10. P. 3014. doi: 10.3390/cancers12103014.
6.Shipunova V.O., Komedchikova E.N., Kotelnikova P.A., Zelepukin I.V., Schulga A.A., Proshkina G.M., Shramova E.I., Kutscher H.L., Telegin G.B., Kabashin A.V., et al. // ACS Nano. 2020. V. 14. № 10. P. 12781–12795.
7.Shipunova V.O., Kolesnikova O.A., Kotelnikova P.A., Soloviev V.D., Popov A.A., Proshkina G.M., Nikitin M.P., Deyev S.M. // ACS Omega. 2021. V. 6. № 24. P. 16000–16008.
8.Zelepukin I.V., Popov A.A., Shipunova V.O., Tikhonowski G.V., Mirkasymov A.B., Popova-Kuznetsova E.A., Klimentov S.M., Kabashin A.V., Deyev S.M. // Mater. Sci. Eng. C. 2021. V. 120. P. 111717.
9.Kabashin A.V., Kravets V.G., Wu F., Imaizumi S., Shipunova V.O., Deyev S.M., Grigorenko A.N. // Adv. Funct. Mater. 2019. V. 29. № 26. P. 1902692.
10. Kapałczyńska M., Kolenda T., Przybyła W., Zajączkowska M., Teresiak A., Filas V., Ibbs M., Bliźniak R., Łuczewski Ł., Lamperska K. // Arch. Med. Sci. 2016. V. 14. № 4. P. 910–919.
11. Zanoni M., Piccinini F., Arienti C., Zamagni A., Santi S., Polico R., Bevilacqua A., Tesei A. // Sci. Rep. 2016. V. 6. P. 19103.
12.Liao W., Wang J., Xu J., You F., Pan M., Xu X., Weng J., Han X., Li S., Li Y., et al. // J. Tissue Eng. 2019. V. 10. P. 2041731419889184. doi: 10.1177/2041731419889184.
13.Białkowska K., Komorowski P., Bryszewska M., Miłowska K. // Int. J. Mol. Sci. 2020. V. 21. № 17. P. 6225. doi: 10.3390/ijms21176225.
14. Andersen T., Auk-Emblem P., Dornish M. // Microarrays. 2015. V. 4. № 2. P. 133–161.
15. Zhang C., Yang Z., Dong D.-L., Jang T.-S., Knowles J.C., Kim H.-W., Jin G.-Z., Xuan Y. // J. Tissue Eng. 2020. V. 11. P. 1–17.
16. Balalaeva I.V., Sokolova E.A., Puzhikhina A.D., Brilkina A.A., Deyev S.M. // Acta Naturae. 2017. V. 9. № 1. P. 38–44.
17. Zanoni M., Cortesi M., Zamagni A., Arienti C., Pignatta S., Tesei A. // J. Hematol. Oncol. 2020. V. 13. № 1. P. 97.
18. Sant S., Johnston P.A. // Drug Discov. Today Technol. 2017. V. 23. P. 27–36.
19. Godugu C., Patel A.R., Desai U., Andey T., Sams A., Singh M. // PLoS One. 2013. V. 8. № 1. P. e53708.
20.Sokolova E.A., Shilova O.N., Kiseleva D.V., Schulga A.A., Balalaeva I.V., Deyev S.M. // Int. J. Mol. Sci. 2019. V. 20. № 10. P. 2399. doi: 10.3390/ijms20102399.
21. Proshkina G.M., Kiseleva D.V., Shilova O.N., Ryabova A.V., Shramova E.I., Stremovskiy O.A., Deyev S.M. // Mol. Biol. 2017. V. 51. № 6. P. 865–873.
22. Mosmann T. // J. Immunol. Methods. 1983. V. 65. № 1–2. P. 55–63.
23. Zdobnova T., Sokolova E., Stremovskiy O., Karpenko D., Telford W., Turchin I., Balalaeva I., Deyev S. // Oncotarget. 2015. V. 6. № 31. P. 30919–30928.
24. Shcherbo D., Merzlyak E.M., Chepurnykh T.V., Fradkov A.F., Ermakova G.V., Solovieva E.A., Lukyanov K.A., Bogdanova E.A., Zaraisky A.G., Lukyanov S., et al. // Nat.

Methods. 2007. V. 4. № 9. P. 741–746.
25. Shin S., Ikram M., Subhan F., Kang H.Y., Lim Y., Lee R., Jin S., Jeong Y.H., Kwak J.-Y., Na Y.-J., et al. // RSC Adv. 2016. V. 6. № 52. P. 46952–46965.
26. Tang Y., Liu J., Chen Y. // Microelectron. Eng. 2016. V. 158. P. 41–45.
27. Nicoletti I., Migliorati G., Pagliacci M.C., Grignani F., Riccardi C. // J. Immunol. Methods. 1991. V. 139. № 2. P. 271–279.
28. Arndt-Jovin D.J., Jovin T.M. // J. Histochem. Cytochem. 1977. V. 25. № 7. P. 585–589.
29. Purschke M., Rubio N., Held K.D., Redmond R.W. // Photochem. Photobiol. Sci. 2010. V. 9. № 12. P. 1634–1639.
30. Krishnamurti U., Silverman J.F. // Adv. Anat. Pathol. 2014. V. 21. № 2. P. 100–107.
31.Carlsson J., Nordgren H., Sjöström J., Wester K., Villman K., Bengtsson N.O., Ostenstad B., Lundqvist H., Blomqvist C. // Br. J. Cancer. 2004. V. 90. № 12. P. 2344–2348.
32.Murphy C.G., Modi S. // Biologics. 2009. V. 3. P. 289–301.
33. Iqbal N., Iqbal N. // Mol. Biol. Int. 2014. V. 2014. P. 852748.
34. Mitri Z., Constantine T., O'Regan R. // Chemother. Res. Pract. 2012. V. 2012. P. 743193.
35. Stepanov A.V., Belogurov A.A., Ponomarenko N.A., Stremovskiy O.A., Kozlov L.V., Bichucher A.M., Dmitriev S.E., Smirnov I.V., Shamborant O.G., Balabashin D.S., et al. // PLoS One. 2011. V. 6. № 6. P. e20991.
36. Pastan I., Hassan R., FitzGerald D.J., Kreitman R.J. // Annu. Rev. Med. 2007. V. 58. P. 221–237.
37. Boersma Y.L., Plückthun A. // Curr. Opin. Biotechnol. 2011. V. 22. № 6. P. 849–857.
38. Dreier B., Honegger A., Hess C., Nagy-Davidescu G., Mittl P.R.E., Grütter M.G., Belousova N., Mikheeva G., Krasnykh V., Plückthun A. // Proc. Natl. Acad. Sci. USA. 2013. V. 110. № 10. P. E869–877.
39. Plückthun A. // Annu. Rev. Pharmacol. Toxicol. 2015. V. 55. P. 489–511.
40.de Dios-Figueroa G.T., Aguilera-Marquez J.D.R., Camacho-Villegas T.A., Lugo-Fabres P.H. // Biomedicines. 2021. V. 9. № 6. P. 602. doi: 10.3390/biomedicines9060602.
41.Jensen C., Teng Y. // Front. Mol. Biosci. 2020. V. 7. P. 33.
42.Nakayama Y., Takewa Y., Sumikura H., Yamanami M., Matsui Y., Oie T., Kishimoto Y., Arakawa M., Ohmuma K., Tajikawa T., et al. // J. Biomed. Mater. Res. B. 2015. V. 103. № 1. P. 1–11.
43.Kun K. // Procedia Eng. 2016. V. 149. № 2. P. 203–211.
44.Nicholas P., Rossi G., Williams E., Bennett M., Schork T. // Int. J. Archit. Comput. 2020. V. 18. № 4. P. 371–384.
45. Murphy S.V., Atala A. // Nat. Biotechnol. 2014. V. 32. № 8. P. 773–785.
46.Wang L., Pumera M. // Trends Analyt. Chem. 2021. V. 135. P. 116151.
47. Tolmachev V.M., Chernov V.I., Deyev S.M. // Russ. Chem. Rev. 2022. V. 91. RCR5034. https://doi.org/10.1070/RCR5034
48. Shipunova V.O., Deyev S.M. // Acta Naturae. 2022. V. 14. № 1(52). P. 54–72.

Analysis of the TREC and KREC Levels in the Dried Blood Spots of Healthy Newborns with Different Gestational Ages and Weights

D. A. Cheremokhin[1,2*], K. Shinwari[3], S. S. Deryabina[1,2,3], M. A. Bolkov[1,3], I. A. Tuzankina[1,3], D. A. Kudlay[4,5]

[1]Institute of Immunology and Physiology of the Ural Branch of the Russian Academy of Sciences, Yekaterinburg, 620049 Russia

[2]Medical Center "Healthcare of mother and child", Yekaterinburg, 620041 Russia

[3]Department of Immunochemistry, Institute of Chemical Engineering of the Ural Federal University, Yekaterinburg, 620083 Russia

[4]I.M. Sechenov First Moscow State Medical University (Sechenov University), Moscow, 119991 Russia

[5]National Research Center, Institute of Immunology Federal Medical-Biological Agency of Russia, Moscow, 115522 Russia

*E-mail: dimacheremokhin@gmail.com

Received: July 04, 2021; in final form, January 12, 2022

DOI: 10.32607/actanaturae.11501

ABSTRACT **Inborn errors of immunity can be detected by evaluating circular DNA (cDNA) fragments of T- and B-cell receptors (TREC and KREC) resulting from the receptor gene rearrangement in T and B cells. Maturation and activation of the fetal immune system is known to proceed gradually according to the gestational age, which highlights the importance of the immune status in premature infants at different gestational ages. In this article, we evaluated TREC and KREC levels in infants of various gestational ages by real-time PCR with taking into account the newborn's weight and sex. The 95% confidence intervals for TREC and KREC levels (expressed in the number of cDNA copies per 10^5 cells) were established for different gestational groups. The importance of studying immune system development in newborns is informed by the discovered dependence of the level of naive markers on the gestational stage in the early neonatal period.**

KEYWORDS **T-cell receptor excision circles, K-deleting recombination excision circles, primary immunodeficiency, inborn error of immunity, severe combined immunodeficiency, reference value.**

ABBREVIATIONS **TREC – T-cell receptor excision circles; KREC – K-deleting recombination excision circles; TCR – T-cell receptor; BCR – B-cell receptor; PID – primary immunodeficiency; IEI – innate errors of immunity; SCID – severe combined immunodeficiency; DBS – dried blood spot.**

INTRODUCTION

Innate errors of immunity (IEI), which are also known as primary immunodeficiency (PID), are a group of genetic diseases that manifest themselves as various developmental defects and immune system dysfunction. In 2019, the International Union of Immunological Societies classified and listed more than 450 individual IEI [1]. Thanks to advances in our understanding of their pathogenetic basis and improvement in laboratory diagnostic methods, it has become possible to provide a large number of patients with a clinical diagnosis confirmed by the results of molecular genetic studies. The IEI prevalence currently stands at 1.27 per 10,000 cases [2, 3].

V(D)J recombination is one of the most important events taking place in a functional immune system, during which diverse and functional variants of T- and B-cell receptors (TCR and BCR, respectively)

and antibodies are formed. These processes are essential stages in adaptive immunity development [4]. The recombinases RAG1 and RAG2 play an important role in this process [5]. These proteins catalyze the rearrangement of the DNA fragments of TCR genes during T cell maturation and the B cell response at the stage of selection of variable regions of immunoglobulins.

T-cell receptor excision circles (TREC) are DNA fragments resulting from the *TCR* gene rearrangement in thymocytes. TREC are transported as episomal DNA from the nucleus to the cytoplasm of independent, although still naive, T cells, where they persist without being involved in replication during mitosis. The resulting TREC concentration indicates the number of naive T cells, which is, apparently, an important diagnostic criterion [6–8]. Double-stranded DNA circles similar to TREC are formed during *BCR* gene rearrangement in naive B cells; they are called kappa-deleting recombination excision circles (KREC) [9]. KREC resulting from intron RSS–Kde rearrangement at the IGK locus is used to assess B-cell neogenesis in the bone marrow [10, 11]. Both TREC and KREC are non-replicative and stable; their levels do not change during cell proliferation (e.g., clonal expansion) [12, 13]. Because of that, quantification of TREC and KREC molecules is widely used to assess the state of the thymus and bone marrow in various physiological and pathological conditions. The blood levels of TREC and KREC can be a criterion of high diagnostic significance in various immunodeficient states. A method for multiplex real-time PCR that makes it possible to detect defects in T and B cells generation by simultaneously measuring TREC and KREC copy numbers has been developed [14, 15]. Mass screening for the TREC/KREC level could help us classify an infant as a risk group patient based on their immunological profile as early as in the neonatal period; this will increase the survival rate of infants with an immune-related pathology and reduce expenses [16–18]. This approach has other advantages, including high sensitivity, high throughput capacity, relatively low cost, and the possibility of using DNA isolated from the minimum volume of a blood sample collected using Guthrie cards [6, 16, 19]. This allows for using TREC and KREC molecules as functional markers of the thymus and bone marrow in various clinical conditions and, in particular, IEI. However, in order to characterize IEI patients, one has to know the state of these immunity markers in a healthy individual, especially with taking into account his/her age and sex [20]. Quantification of TREC and KREC in a newborn's blood remains topical.

EXPERIMENTAL

Dried blood spot samples

Our study included 80 dried blood spot (DBS) samples obtained from otherwise healthy (no deviations according to the results of large neonatal screening and blood transfusion data) infants (40 boys and 40 girls) collected onto Perkin Elmer 226 Guthrie cards (Perkin Elmer Health Sciences, USA). The Guthrie cards were stored at the Neonatal Screening Laboratory of the Medical Center "Healthcare of mother and child" (Yekaterinburg) at room temperature before use.

DNA isolation

DNA was isolated from seven DBS discs 3.2 mm in diameter (20 μl) by magnetic sorting on the Magna Pure LC 2.0 Instrument using the MagNA Pure LC DNA Isolation Kit I (Roche Diagnostics GmbH, Germany) according to the standard DNA I Blood_Cells_High_Performance protocol. The DBS pretreatment step included sample lysis using the buffer from the Magna Pure LC DNA Isolation Kit II (Tissue). A total of 260 μl of the lysis buffer and 40 μl of proteinase K were added to the DBS samples. The resulting mixtures were thoroughly vortexed and incubated at 65°C for 20 min with occasional tube shaking and, then, at 95°C for 10 min with shaking on a vortex every five min. The samples were cooled to room temperature, and the extract was transferred to the Sample Cartridge and loaded into the workstation.

PCR analysis of TREC and KREC

The TREC and KREC molecules were quantified by PCR with real-time detection of the fluorescent signal. The study was conducted on a CFX96 qPCR Detection System (Bio-Rad, USA) using the Immuno-BiT reagent kit (ABV-test, Russia) according to the manufacturer's instructions. The number of TREC and KREC molecules per 10^5 nucleated cells (leukocytes) was calculated relative to the *ALB* gene copy number using the following formula:

$$TREC\left(KREC\right)copies/\left(10^5\ leukocytes\right)=$$

$$=\frac{TREC\left(KREC\right)\frac{copies}{ml}}{ALB\frac{copies}{ml}}\times 200\ 000.$$

In the case of an *ALB* copy number < 10^5, the result was considered invalid, and the study was repeated, starting from the DNA isolation stage.

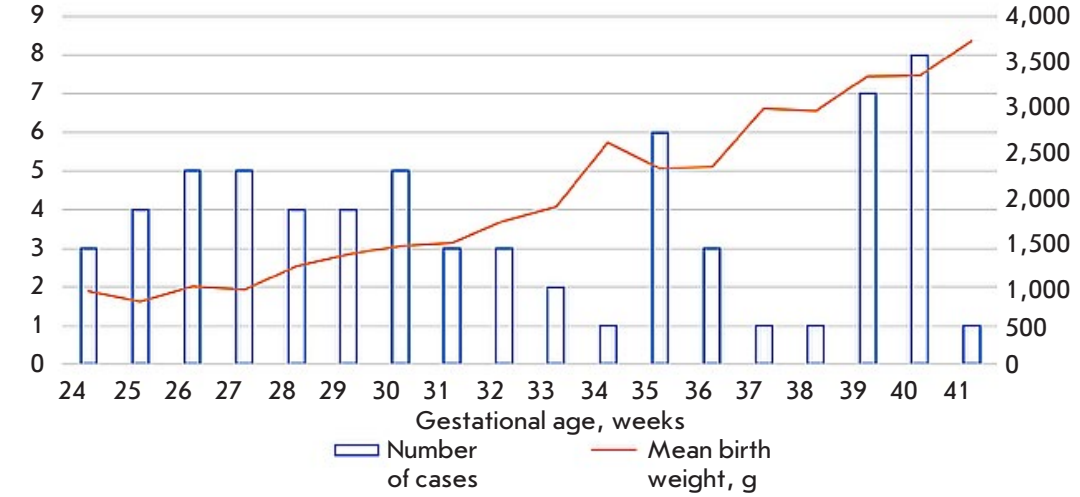

Fig. 1. Distribution of healthy infants based on gestational age and birth weight

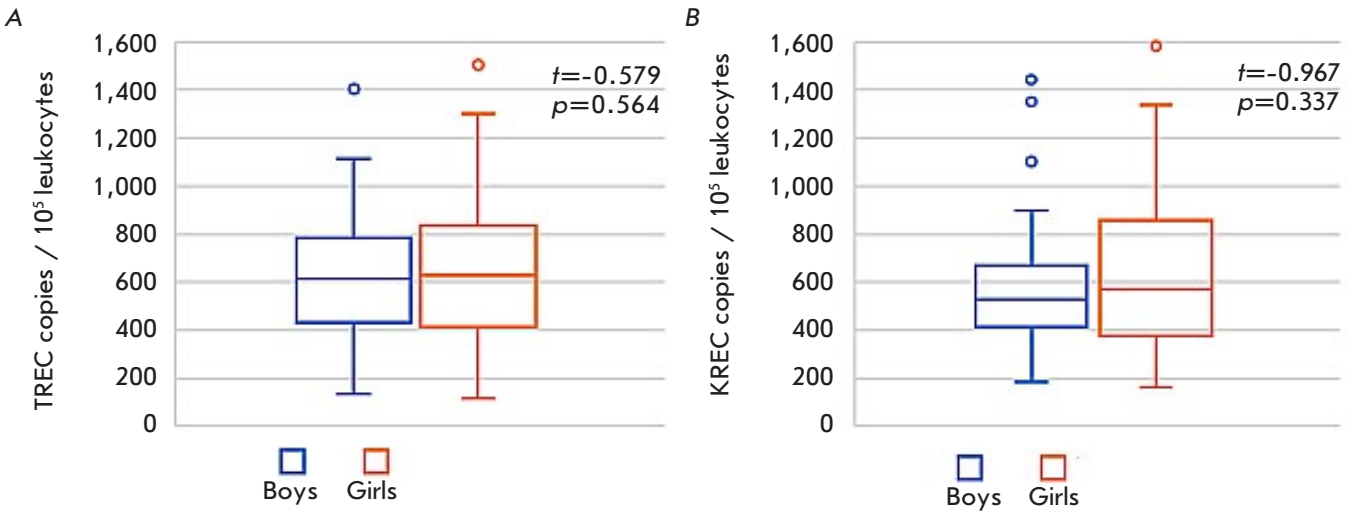

Fig. 2. TREC (*A*) and KREC (*B*) levels in the DBS samples of healthy infants depending on gender. *Note:* hereinafter, the median, interquartile, and maximum range are shown

Statistical data analysis

The data were analyzed mathematically using the Microsoft Excel (Microsoft Office 365, USA) and IBM SPSS Statistics V21.0 (IBM Corp., USA) statistical software packages. The normality of the data distribution was assessed using the Shapiro–Wilk test; the arithmetic mean and standard error of the mean (m ± SEM) were used for descriptive characterization. Student's *t*-test for independent samples and Pearson's correlation coefficient (p) were used to analyze the statistical significance of the differences between the mean values and the presence of correlations, respectively. Differences were considered significant at $p < 0.05$.

RESULTS

The study included 80 apparently healthy infants (40 boys and 40 girls) of different gestational ages born in the Sverdlovsk region in 2020 (*Fig. 1*).

Gender differences in the TREC and KREC levels

An analysis of the TREC and KREC levels in the DBS samples of the presumably healthy boys and girls revealed no statistically significant differences (*Fig. 2*),

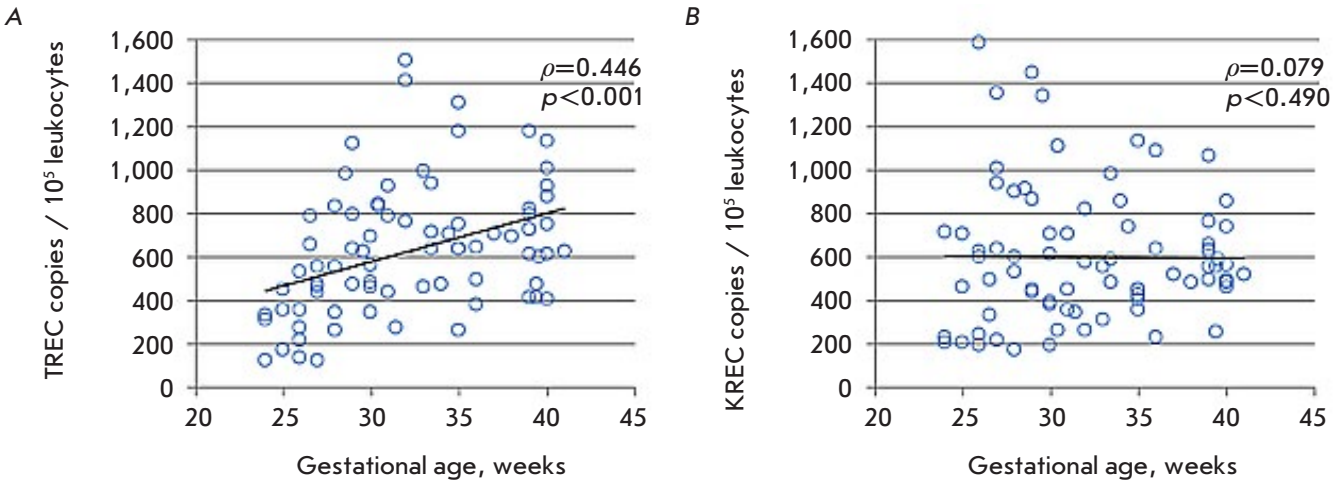

Fig. 3. TREC (*A*) and KREC (*B*) levels in the DBS samples of healthy infants depending on gestational age in the early neonatal period

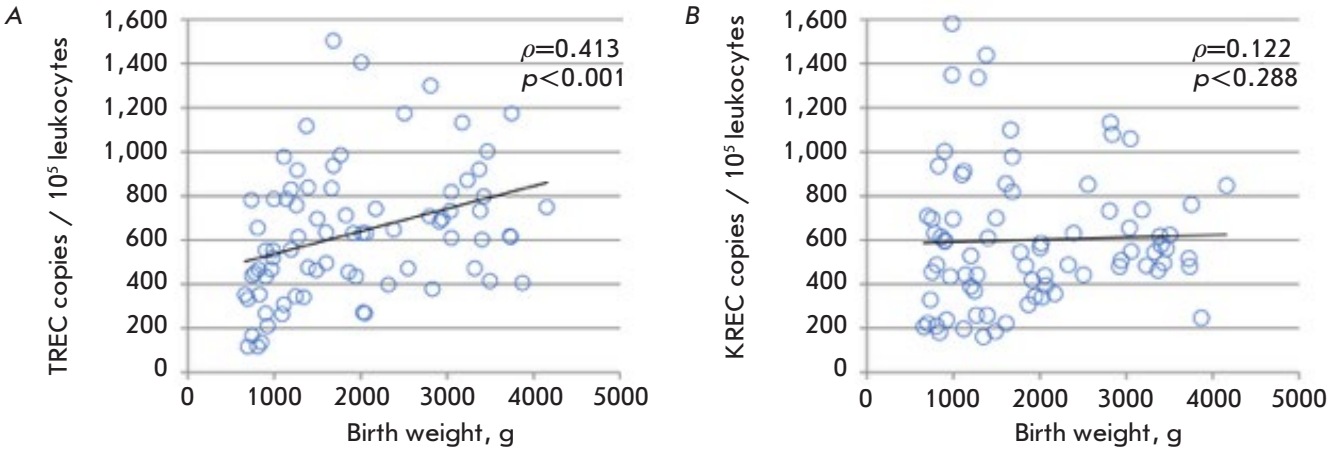

Fig. 4. TREC (*A*) and KREC (*B*) levels in the DBS samples of healthy infants depending on birth weight

which corresponds to the results obtained by other researchers [21].

TREC and KREC levels in preterm infants of different gestational ages

A statistical analysis based on correlation data was conducted to determine possible variations in the TREC and KREC copy numbers associated with a newborn's gestational age. A statistically significant positive correlation (ρ = 0.446 (p < 0.001)) was established between the gestational age and the TREC level. No relationship was found between an infant's age and the level of KREC, which is a marker of naive B cells (*Fig. 3*).

TREC and KREC levels in preterm infants with different birth weight

The relationship between naive T- and B-cell marker levels and a newborn's weight was also analyzed. Naturally, the fetus develops during pregnancy. All internal organs and, in particular, the thymus, develop according to the gestational period. During their growth and differentiation, thymogenic tissues are enriched with lymphocyte precursors and, in particular with ones that have already passed double recognition; i.e., positive and negative selection. This is denoted by a positive correlation (ρ = 0.413 (p < 0.001)) between an infant's birth weight and the TREC level in their DBS sample. No such correlation

was found between the birth weight and KREC level (*Fig. 4*).

Analysis of TREC and KREC levels in infants of different preterm birth categories

Having discovered a positive correlation between the newborn's gestational age and TREC level, we decided to evaluate the possibility of significant differences in the TREC level of infants of different preterm birth categories. In order to do this, we decided to divide newborns into four groups according to the preterm birth category: extremely preterm (< 28 weeks), very preterm (28–32 weeks), moderate to late preterm (33–38 weeks), and term-birth (39–41 weeks) infants (*Fig. 5*, *Table*).

Figure 1 shows a trend towards an increase in the TREC marker level during fetus growth and development; however, there was no statistically significant correlation between the preterm category and TREC level. Since no statistically significant relationship was found between the KREC copy number in the DBS sample and such parameters as a newborn's body weight and gestational age in infants of different preterm categories, the newborns were not divided into separate groups. An average of 599.9 KREC copies per 10^5 leukocytes (*SE* = 34.9) were found per sample; however, one needs to know the lower limits of the obtained reference intervals for practical use. The lowest KREC value in the group of apparently healthy infants was 162.8 copies/10^5 leukocytes, while the lower limit of the 95% confidence interval was 210.9 copies/10^5 leukocytes (the results of descriptive statistics are presented in the *Table*).

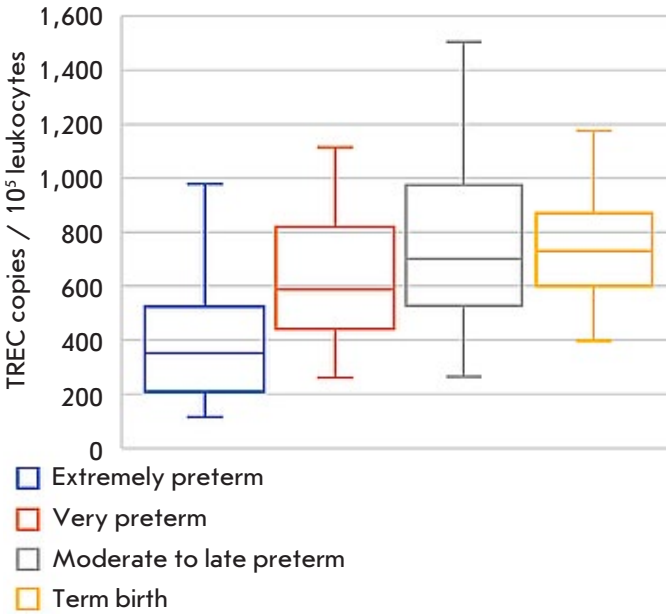

Fig. 5. TREC levels in the DBS samples of infants of different gestational ages in the early neonatal period

DISCUSSION

To date, there have been numerous attempts at TREC/KREC quantification in different age groups, ranging from infants and older children to adult populations. The main goal of most of these studies was to assess the changes in the functional activity of naive immunity during organism maturation and aging [21–23]. According to Douek et al., the TREC and KREC copy numbers in the blood samples of older children and adults are 10 and 100 times lower than those in healthy term-birth newborns, respectively. These data indicate a reduced thymic output owing to the age-related decrease in the functional thymus tissue [24]. The study of patients with combined variable immunodeficiency and healthy control donors revealed a stable KREC level, while TREC levels reduced with age in both patients with an immune-related pathology and the control group; this confirms the independence of the decrease in the level of naive T-cell markers from the disease and dependence

TREC and KREC levels (copies/10^5 leukocytes) in the DBS samples of apparently healthy infants of different gestational ages in the early neonatal period

Preterm birth category	Mean	95% confidence interval	SEM	MIN	MAX
TREC					
Extremely preterm (< 28 weeks)	402.7	116.6–784.0	52.8	115.9	978.0
Very preterm (28–32 weeks)	611.1	271.0–917.9	52.5	261.4	1115.6
Moderate to late preterm (33–38 weeks)	776.1	378.2–1405.5	76.5	263.6	1505.6
Term birth (39–41 weeks)	723.9	406.1–1133.2	52.2	398.1	1174.0
KREC					
	599.9	210.9–1103.5	34.9	162.8	1584.0

on age [23, 25–27]. The TREC and KREC levels may also decrease because of dilution. Nuclear DNA replicates only during an active immune response at the stage of cellular expansion of functionally active lymphocyte clones. Since TREC and KREC are episomal molecules, they remain only in precursor cells, which leads to a relative decrease in the parameters [28]. Despite numerous data on age-related changes in T- and B-cell immunity, it is also important to study TREC and KREC level alternations not only in the early neonatal period, but at different fetal development stages as well. This will allow for assessing the immune state at different stages of human embryonic development.

The main goal of our study was to determine the TREC and KREC levels in the blood of newborns delivered at different gestational ages. However, for greater informational value, we decided to analyze gender differences in the levels of naive immunocompetent cell markers. We have not found any significant differences in the TREC and KREC levels between boys and girls, which is consistent with the results obtained by other researchers [29, 30]. However, some works indicate a higher TREC level in the blood of females [31–33].

To date, data have been published on the relationship between an infant's birth weight and his/her TREC level [34–36]. A recent study of DBS samples of preterm infants revealed a positive correlation between the TREC and KREC levels and birth weight [5]. Another work studied the relationship not only between birth weight, but also gestational age at the time of birth. Based on the analysis results in that work, newborns were divided into three groups: infants with very low, low, and normal birth weight [32]. Data have also been published on the existence of a relationship between the immune state and growth of adult individuals [36, 37].

All internal organs, in particular, the thymus, develop in accordance with the gestational period. During growth and differentiation, thymogenic tissues are enriched with lymphocyte precursors and, in particular, with the ones that have already passed double recognition: i.e., positive and negative selection. This is indicated by a positive correlation ($\rho = 0.413$ ($p < 0.001$)) between the infant's birth weight and the TREC level in his/her DBS sample. [21, 26, 27].

We also analyzed the relationship between the quantitative content of B-cell markers, gestational age, and newborn's weight; however, the relationship between these parameters was not statistically significant. These results show that the KREC level in the DBS of a newborn delivered at a gestational age $\geqslant$ 28 weeks, which corresponds to normative values, is an indicator of proper B cell maturation in the bone marrow. Pre-B-cells are found in the fetal liver at week eight of pregnancy, where they already express class M immunoglobulins on their surface by that period. This indicates that the system of humoral parameters of immunity functions with high efficiency by that early stages of human development, which probably determines the relatively high KREC level in the DBS of newborns delivered at different gestational ages [23, 27].

IEI usually remain undiagnosed until clinical signs begin to appear. These signs are, mainly, chronic and recurrent infections. In order to diagnose PID, a clinical blood analysis, lymphocyte phenotyping, determination of various types of immunoglobulins, functional tests for determining immunocompetent cells, and a genetic analysis are used. Functional tests for determining immunocompetent cells and a genetic analysis are currently the most promising and important approaches. The analysis of the TREC and KREC levels is a fast and sensitive tool for screening for severe combined immunodeficiency (SCID) and diagnosing other IEI, especially considering the fact that a small sample volume is required for DNA extraction, which reduces the risk of harm to the infant. The impossibility of collecting the required amount of biological sample is often an insurmountable barrier in laboratory diagnostics. The use of different protocols for TREC and KREC level analysis in different laboratories contributes to the wide spread of thresholds for newborn screening programs among different countries. Genetic differences between populations may also play a role. Therefore, our results in determining TREC and KREC intervals with taking into account the patient's age and sex are of no small importance for diagnosing IEI in infants.

PIDs are still considered rare diseases, although they are not orphan. In 2019, a total of 2,798 patients with IEI were registered in the Russian Federation, with 60% of them being children [38]. The introduction of programs for mass newborn screening based on an evaluation of the TREC and KREC levels will significantly increase the risk group for SCID and other severe PIDs that cause death at an early age. Early diagnosis will ensure the possibility of timely application of pathogenetically appropriate therapy. This also relates to the use of radical transplantation technologies during the opportunity window before the onset of severe clinical manifestations; this will not only improve the quality of life of patients with this pathology and save their lives, but also reduce the financial and economic costs in the treatment and life support of patients [39–45].

CONCLUSION

The results of our studies suggest that the gestational age should be considered as an important factor affecting the TREC and KREC levels. In order to interpret the results of newborn screening, we calculated the reference ranges of these parameters for different gestational groups. This also has the potential to allow us to monitor immune changes in T and B cells during immunotherapy, including monitoring after hematopoietic stem cell transplantation.

Early diagnosis and treatment are important in all IEI variants. The use of the method of quantitative assessment of the T- and B-cell markers TREC and KREC, respectively, has made it possible to develop screening programs for SCID and agammaglobulinemia detection in many countries of the world. However, other PIDs such as immunodeficiency disorders with normal levels of peripheral T and B cells, defects in phagocyte count and function, complement deficiency, and diseases associated with immune dysregulation remain unaddressed. Further search for effective disease markers; development of strategies for cellular, genetic, and functional diagnostics; as well as adaptation of these tolls to mass diagnostic programs for various PIDs are required. ●

This study was carried out within the framework of the AAAA-A21-121012090091-6 project at the Institute of Immunology and Physiology of the Ural Branch of the Russian Academy of Sciences.

REFERENCES

1. Tangye S.G., Al-Herz W., Bousfiha A., Chatila T., Cunningham- Rundles C., Etzioni A., Franco J.L., Holland S.M., Klein C., Morio T., et al. // J. Clin. Immunol. 2020. V. 40. P. 24–64.
2. Rubin Z., Pappalardo A., Schwartz A., Antoon J.W. // J. Allergy Clin. Immunol. Pract. 2018. V. 6. P. 1705–1710.
3. Modell V., Knaus M., Modell F., Roifman C., Orange J., Notarangelo L.D. // Immunol. Res. 2014. V. 60. P. 132–144.
4. Jung D., Alt F.W. // Cell. 2004. V. 116. P. 299–311.
5. Ye P., Kirschner D.E. // Crit. Rev. Immunol. 2002. V. 22. № 5–6. P. 483–497.
6. Nourizadeh M., Borte S., Fazlollahi M.R., Hammarstrom L., Pourpak Z. // Iran J. Allergy Asthma Immunol. 2015. V. 14. № 4. P. 457–461.
7. Ye P., Kirschner D.E. // J. Immunol. 2002. V. 168. P. 4968–4979.
8. Hazenberg M.D., Verschuren M.C., Hamann D., Miedema F., van Dongen J.J. // J. Mol. Med. 2001. V. 79. P. 631–640.
9. Barbaro M., Ohlsson A., Borte S., Jonsson S., Zetterstrom R.H., King J., Winiarski J., von Döbeln U., Hammarström L. // J. Clin. Immunol. 2017. V. 37. P. 51–60.
10. Siminovitch K.A., Bakhshi A., Goldman P., Korsmeyer S.J. // Nature. 1985. V. 316. P. 260–262.
11. van Zelm M.C., van der Burg M., Langerak A.W., van Dongen J.J. // Front. Immunol. 2011. V. 2. P. 12.
12. van Zelm M.C., Szczepanski T., van der Burg M., van Dongen J.J. // J. Exp. Med. 2007. V. 204. P. 645–655.
13. Kong F.K., Chen C.L., Six A., Hockett R.D., Cooper M.D. // Proc. Natl. Acad. Sci. USA. 1999. V. 96. P. 1536–1540.
14. Livak F., Schatz D.G. // Mol. Cell. Biol. 1996. V. 16. P. 609–618.
15. Borte S., von Dobeln U., Fasth A., Wang N., Janzi M., Winiarski J. // Blood. 2012. V. 119. № 11. P. 2552–2555.
16. Puck J.M., Group SNSW. // J. Clin. Immunol. 2007. V. 120. № 4. P. 760–768.
17. Puck J.M. // J. Allergy Clin. Immunol. 2012. V. 129. № 3. P. 607–616.
18. Korsunsky I.A., Kudlay D.A., Prodeus A.P., Shcherbina A.Yu., Rumyantsev A.G. // Pediatria n.a. G.N. Speransky. 2020. V. 99. № 2. P. 8–15.
19. King J.R., Hammarstrom L. // J. Clin. Immunol. 2018. V. 38. № 1. P. 56–66.
20. Claustres M., Kozich V., Dequeker E., Fowler B., Hehir-Kwa J.Y., Miller K. // Eur. J. Hum. Genet. 2014. V. 22. № 2. P. 160–170.
21. de Felipe B., Olbrich P., Lucenas J.M., Delgado-Pecellin C., Pavon-Delgado A., Marquez J. // Pediatr. Allergy Immunol. 2016. V. 27. № 1. P. 70–77.
22. Castermans E., Morrhaye G., Marchand S., Martens H., Moutschen M., Geenen V. // Revue Med. de Liege. 2007. V. 62. № 12. P. 725–729.
23. Geenen V., Poulin J.F., Dion M.L., Martens H., Castermans E., Hansenne I. // J. Endocrinol. 2003. V. 176. № 3. P. 305–311.
24. Sempowski G.D., Gooding M.E., Liao H.X., Le P.T., Haynes B.F. // Mol. Immunol. 2002. V. 38. № 11. P. 841–848.
25. Douek D.C., McFarland R.D., Keiser P.H., Gage E.A., Massey J.M., Haynes B.F. // Nature. 1998. V. 396. № 6712. P. 690–695.
26. Olbrich P., de Felipe B., Delgado-Pecellin C., Rodero R., Rojas P., Aguayo J. // Ann. Pediatr. (Barc.). 2014. V. 81. № 5. P. 310–317.
27. Moro-Garcia M.A., Alonso-Arias R., Lopez-Larrea C. // Curr. Genomics. 2012. V. 13. № 8. P. 589–602.
28. Palmer S., Albergante L., Blackburn C.C., Newman T.J. // Proc. Natl. Acad. Sci. USA. 2018. V. 115. № 8. P. 1883–1888.
29. Goronzy J.J., Shao L., Weyand C.M. // Rheum. Dis. Clin. North Am. 2010. V. 36. № 2. P. 297–310.
30. Sottini A., Serana F., Bertoli D., Chiarini M., Valotti M., Vaglio Tessitore M. // J. Vis. Exp. 2016. V. 6. P. 94.
31. Shakerian L., Pourpak Z., Shamlou S. // Iran J. Allergy Asthma Immunol. 2019. V. 18. № 2. P. 143–152.
32. Yoshida K., Nakashima E., Kubo Y., Yamaoka M., Kajimura J., Kyoizumi S. // PLoS One. 2014. V. 9. № 3. e91985.
33. Rechavi E., Lev A., Simon A.J., Stauber T., Daas S., Saraf-Levy T. // Front. Immunol. 2017. V. 8. P. 1448.
34. Serana F., Chiarini M., Zanotti C., Sottini A., Bertoli D., Bosio A. // J. Transl. Med. 2013. V. 11. P. 119.
35. Raqib R., Alam D.S., Sarker P., Ahmad S.M., Ara G., Yunus M. // Am. J. Clin. Nutr. 2007. V. 85. № 3. P. 845–852.
36. Pawlowski B., Nowak J., Borkowska B., Augustyniak D., Drulis-Kawa Z. // Proc. Biol. Sci. 2017. V. 284. P. 1859.
37. Krams I.A., Skrinda I., Kecko S., Moore F.R., Krama T.,

Kaasik A. // Sci. Rep. 2014. V. 4. P. 6223.
38. Mukhina A.A., Kuzmenko N., Rodina Y.A., Kondratenko I.V., Bologov A.A., Latysheva T.V., Prodeus A.P., Pampura A.N., Balashov D.N., Ilyina N.I., at al. // Front. Immunol. 2020. V. 11. P. 1491.
39. Buckley R.H., Schiff S.E., Schiff R.I., Markert L., Williams L.W., Roberts J.L. // N. Engl. J. Med. 1999. V. 340. P. 508–516.
40. Castagnoli R,, Delmonte O.M., Calzoni E., Notarangelo L.D. // Front. Pediatr. 2019. V. 7. P. 295.
41. Pai S.Y., Logan B.R., Griffith L.M., Buckley R.H., Parrott R.E., Dvorak C.C. // N. Engl. J. Med. 2014. V. 371. P. 434–446.
42. Gardulf A., Winiarski J., Thorin M., Heibert Arnlind M., von Dobeln U., Hammarstrom L. // J. Allergy Clin. Immunol. 2017. V. 139. P. 1713–1716.
43. Bessey A., Chilcott J., Leaviss J., de la Cruz C., Wong R. // Int. J. Neonat. Screen. 2019. V. 5. P. 28.
44. Thomas C., Durand-Zaleski I., Frenkiel J., Mirallie S., Leger A., Cheillan D. // Clin. Immunol. 2019. V. 202. P. 33–39.
45. Kozlov V.A., Tikhonova E.P., Savchenko A.A., Kudryavtsev I.V., Andronova N.V., Anisimova E.N., Golovkin A.S., Demina D.V., Zdzitovetsky D.E., Kalinina Yu.S., et al. Clinical Immunology. A practical guide for infectious disease specialists. Krasnoyarsk: Polikor, 2021. 563 p.

Genomic Estimated Breeding Value of Milk Performance and Fertility Traits in the Russian Black-and-White Cattle Population

F. S. Sharko[1*], A. Khatib[2,3,4], E. B. Prokhortchouk[1,2]

[1]Laboratory of vertebrate genomics and epigenomics, Federal Research Centre "Fundamentals of Biotechnology" of the Russian Academy of Sciences, Moscow, 119071 Russia

[2]Laboratory I-Gene, ZAO "Genoanalytica", Moscow, 119234 Russia

[3]Department of biotechnology, faculty of Biology, Lomonosov Moscow State University, Moscow, 119234 Russia

[4]Atomic Energy Commission of Syria (AECS), Department of Agriculture, Damascus, 6091 Syria

[*]E-mail: fedosic@gmail.com

Received: November 30, 2021; in final form, January 14, 2022

DOI: 10.32607/actanaturae.11648

ABSTRACT **A breakthrough in cattle breeding was achieved with the incorporation of animal genomic data into breeding programs. The introduction of genomic selection has a major impact on traditional genetic assessment systems and animal genetic improvement programs. Since 2010, genomic selection has been officially introduced in the evaluation of the breeding and genetic potential of cattle in Europe, the U.S., Canada, and many other developed countries. The purpose of this study is to develop a system for a genomic evaluation of the breeding value of the domestic livestock of Black-and-White and Russian Holstein cattle based on 3 milk performance traits: daily milk yield (kg), daily milk fat (%), and daily milk protein content (%) and 6 fertility traits: age at first calving (AFC), calving interval (CI), calving to first insemination interval (CFI), interval between first and last insemination (IFL), days open (DO), and number of services (NS). We built a unified database of breeding animals from 523 breeding farms in the Russian Federation. The database included pedigree information on 2,551,529 cows and 69,131 bulls of the Russian Holstein and Black-and-White cattle breeds, as well as information on the milk performance of 1,597,426 cows with 4,771,366 completed lactations. The date of birth of the animals included in the database was between 1975 and 2017. Genotyping was performed in 672 animals using a BovineSNP50 v3 DNA Analysis BeadChip microarray (Illumina, USA). The genomic estimated breeding value (GEBV) was evaluated only for 644 animals (427 bulls and 217 cows) using the single-step genomic best linear unbiased prediction – animal model (ssGBLUP-AM). The mean genetic potential was +0.88 and +1.03 kg for the daily milk yield, -0.002% for the milk fat content, and –0.003 and 0.001% for the milk protein content in the cows and bulls, respectively. There was negative genetic progress in the fertility traits in the studied population between 1975 and 2017. The reliability of the estimated breeding value (EBV) for genotyped bulls ranged from 89 to 93% for the milk performance traits and 85 to 90% for the fertility traits, whereas the reliability of the genomic estimated breeding value (GEBV) varied 54 to 64% for the milk traits and 23 to 60% for the fertility traits. This result shows that it is possible to use the genomic estimated breeding value with rather high reliability to evaluate the domestic livestock of Russian Holstein and Black-and-White cattle breeds for fertility and milk performance traits. This system of genomic evaluation may help bring domestic breeding in line with modern competitive practices and estimate the breeding value of cattle at birth based on information on the animal's genome.**

KEYWORDS **GEBV, Russian Black-and-White cattle, genotyping, TD ssGBLUP-AM, test-day, milk performance, fertility.**

INTRODUCTION

One of the most challenging stages in the selection of farm animals is the assessment of their breeding value. To evaluate the breeding value, it is necessary to compare and analyze the breeding characteristics of the animals being evaluated, their closest relatives, offspring, and ancestors. At the initial stages of the development of livestock breeding, the breeding value was assessed by phenotypic indicators: in particular, milk performance indicators were used in dairy cattle breeding [1, 2]. However, more efficient methods based on molecular genetic markers have been developed in the last decade in order to assess the breeding value. Significant progress has been achieved thanks to success in deciphering the genome of the main agricultural animals (cattle, pigs, and sheep) [3], as well as the use of statistical analysis, in particular the best linear, unbiased prediction (BLUP) method. Calculation of the breeding value using the BLUP method makes it possible to exclude the influence of non-genetic factors on the variability of the selected traits in a population, as well as to identify and evaluate the genetic component with a high degree of reliability [4]. The use of molecular genetic markers improves reliability in the assessment of the breeding value of young animals, reduces the generation interval, and expands the capabilities of intensive selection. In addition, the use of genomic assessment leads to an increase in the rate of genetic improvement of economically useful traits in cows and to a decrease in material and technical costs in assessing the genetic potential of sires [5, 6]. Genomic assessment is of particular importance for health and fertility indicators, because the reliability of a genomic assessment of the breeding value is only slightly inferior to the reliability of these indicators for the quality of offspring. To date, there has been no significant genetic progress in the assessment of fertility traits, because, for a long time, many of these traits have not received the appropriate level of attention in breeding programs [7]. The reliability of the genomic estimated breeding value of young animals depends on the reliability of the assessment of the animals included in the reference population – a population of sires with a highly reliable assessment of the offspring and available genomic information [8]. Because obtaining information about the genome is a standardized and proven technology, the reliability of the genomic estimated breeding value largely depends on the reliability of the assessment of the animals included in the reference population based on the offspring. In practice, assessment of the breeding value for milk performance traits by offspring is based on the use of a 305-day lactation yield [9]. The 305-day milk yield is calculated using daily measurements of milk production and the percentage of milk fat and protein for a month. These measurements are called test days [10]. The use of the 305-day milk yield to evaluate the estimated breeding value not only has some advantages, but also a number of disadvantages. First, the procedure for calculating the milk yield [11] is based on plotting the lactation curve using the test day results with fixed parameters, which leads to an underestimation of milk performance during the first months of lactation and to its overestimation during the last months of lactation. These wrinkles may lead to an incorrect calculation of the 305-day milk yield and a decrease in the reliability of the estimated breeding value based on these source data and, therefore, to a decrease in the reliability of the genomic estimated breeding value. Second, when using the 305-day milk yield in linear and non-linear mathematical models as a fixed factor influencing the variability of this value, an averaged effect of the environment for this lactation (herd–year–calving season effect) is used, which means that the effect is constant throughout lactation [12]. In practice, this effect may vary greatly from one lactation day to the next [13]. Ignoring the variability of the environmental effect on the daily milk yield leads to incorrect calculation of genetic and paratypic parameters upon assessment of the breeding value and also introduces an error in the assessment of the breeding value by the offspring and genome. Using the daily milk yield results directly in the generation of mathematical models for the assessment of the breeding value solves all the problems mentioned above [14]. These mathematical models are called test day models or TD models [15]. The purpose of this study was to develop a system for genomic evaluation of the breeding value of the domestic stock of Holstein and Black-and-White cattle using the TD ssGBLUP-AM method based on a set of milk performance traits (daily milk yield (kg), milk fat (%), milk protein (%)) and the ssGBLUP-AM method for fertility traits: age at first calving (AFC, days), calving interval (CI, days), calving to first insemination interval (CFI, days), interval between first and last insemination (IFL, days), days open (DO, days), and number of services (NS).

EXPERIMENTAL

Database of breeding animals

We developed a unified database on the phenotypic indicators of the studied traits and the pedigree of animals from 12 regions of the Russian Federation. To develop the unified database, we used primary databases about animals from 523 farms included in

the register of breeding organizations of the Ministry of Agriculture of the Russian Federation. Primary raw data were obtained as databases generated using the SELEX software package [16], which is related to RDBMS Firebird 2.5. Operating the databases and unloading the necessary information were performed using the Python 2.7 programming language and FDB package. Information on fertility and milk performance indicators and the pedigree of each animal with completed lactation from 523 local databases was uploaded. Information about milk performance for each animal included information about TD (the day of collection of animal milk performance at the control milking day) for each lactation: daily milk yield, daily fat percentage, and daily protein percentage. Information for the database of phenotypic data on fertility traits included information about the date of calving for each animal, age at calving, and date and number of services. Also, we uploaded all primary information about the pedigree of all animals with known productivity and information about all known generations of ancestors on the paternal and maternal lines.

System for assessing the reliability of the phenotypic data of the breeding animals included in the created database

An analysis of the unified database of the breeding animals revealed that the primary data contain numerous errors and inaccuracies. This prevented the use of these data in further research. To correct the situation, a unique multi-stage system for checking the reliability of milk performance data was developed. It included six main stages: checking data for critical values, checking the duration of pregnancy, checking the variability of milk performance data within each farm, checking the number of test days in lactation, and analyzing the reliability of milk performance data within each lactation. All lactations included in the created unified database were checked sequentially at each stage. Lactations that did not pass quality control were removed from further analysis.

First, milk performance data whose values were less than or equal to 0 were removed from the database. Next, the milk performance data were checked for falling into the interval $(\mu - 3\sigma, \mu + 3\sigma)$, and those that did not fall in the interval were removed. It should be noted that not only daily milk yield values, but also data on milk fat and milk protein content were deleted, regardless of whether they passed the test or not.

At the next stage, the duration of pregnancy for each lactation was also checked using the three-sigma rule [17]. Erroneous non-positive values were preliminarily removed. As a result, lactations that corresponded to a pregnancy duration of 268 to 317 days were tested. Lactations whose duration of pre-pregnancy did not fall within the confidence interval were excluded from further analysis.

At the third checking stage, the variability of the traits within the herd at each farm was controlled to exclude data obtained by copying one-shot values. This checking eliminated trait values at each farm from further analysis if the same values were found in the data of the farm for each control dairy day, week, or month.

The next step in checking milk performance data was to check the number and quality of the test days in each lactation. According to the accepted rules for assessing the milk performance of cows [18], the data were checked for meeting the following conditions:

1) there should be data on at least three test days in lactation;

2) there should be no more than 70 days between the calving date and the first TD date;

3) there should be no more than 70 days between adjacent TDs.

Lactations that did not fit these rules were removed. It should be noted that if the "daily milk yield in kg" data were deleted, then the entire lactation was deleted.

At the next checking stage, a lactation curve was built using internationally recognized methods [19, 20] for each lactation for which the information on daily milk yields passed the previous checking stages. For each plotted lactation curve, the mean absolute approximation error (MAE) was calculated for each trait. The results obtained for each trait form a normally distributed sample of values. On the basis of the analysis of the calculated mean absolute approximation errors for each lactation, lactations that had too large an approximation error (were not within the interval $(0, \mu + 3\sigma)$) were excluded from further calculations.

Primary data on fertility traits were checked for each trait separately. Regarding the age at first calving, data whose values did not fall into an interval of 18–30 months were deleted. Regarding calving interval data, the database included only those lactations that corresponded to a calving interval of 300 to 600 days. Also, the database included data whose values ranged from 25 to 360 days for the calving interval trait – first insemination (CFI) and 25 to 500 days for first–last insemination (IFL) and days open (DO) traits. The reliability of the data on the number of services (NS) was checked for compliance with the condition that this value should not exceed 10 inseminations per lactation.

System for assessing the reliability of information on the pedigree of the breeding animals

Information about the pedigree of all animals whose lactation data were deleted during checking of the reliability of fertility and milk performance data was deleted from the unified database. A primary analysis showed that the quality of the data on the pedigree of the animals precluded their further analysis because of a large number of duplicates, errors, and inaccuracies.

At the first stage of correcting the data on the pedigree of the animals, a unique algorithm for correcting loops in the existing primary database was developed. The main idea behind the algorithm is to assign a generation number to an animal and analyze its changes. Initially, each animal in the kinship table has a value of 1. If sequential passing through the table encounters descendants of an animal, then the number of the appropriate generation is increased by one. If the offspring of an animal has a higher generation number, then the generation number of the animal should be proportionally increased. The algorithm operates until the numbers of animal generations stop changing. Accordingly, the animal with the highest generation number is the ancestor. If there are errors in the data of some animal and there are cycles, its generation number will not stop increasing. Animals with this anomaly were removed from the pedigree database. The developed algorithm enabled the removal of erroneous data of this kind.

The next step in adjusting the constituted kinship database was the formation of a combined database on the pedigree of the animals using a reference database. This stage included integrating animals from the created database into the CDCB (Council of Dairy Cattle Breeding, USA) [21], which is publicly available and is the most complete database of dairy breeds in the world. Information on the animal pedigree obtained from this database was considered as the reference. Further, data on the pedigree of animals obtained from Russian and foreign sources were used to generate two genealogical trees and perform a search for matches at the tops of these trees. Search conditions were matching of gender + part of the number + date of birth or matching of gender + number with a length of more than 7 digits. If the vertices coincided, all records about the ancestors of the animal, which were obtained from Russian sources, were replaced with reference ones. This, among other things, satisfied the lack of information in the databases and the combined branches of the genealogical tree built based on Russian data, which would never have crossed without a foreign database.

After developing the combined database on the pedigree of the animals, grouping of duplicates of the same ancestors of the animals with completed lactation was performed. First, records that had not been replaced at the previous stage were pooled according to the coincidence of nickname + date of birth, or inventory number + nickname, or inventory number + date of birth. Each group of records was assigned a unique number in chronological order. Erroneous data were deleted if two or more unique numbers were assigned to parents (father or mother) in one group of records. Further, the data were grouped with allowance for sibling relationships (match of father or mother + match of any personal data (nicknames, numbers or dates of birth)).

We also tested a method for the recovery of some missing information in the relationship matrix by iteratively estimating the matrix R (covariance matrix of the residual error e) for the *AM* model. We applied the *EM algorithm* [22], an algorithm used in mathematical statistics to find maximum likelihood estimates for the parameters of probabilistic models when the model depended on some hidden variables. First, latent variables are estimated by the current approximation of parameters and, then, the parameter estimate that maximizes the likelihood of the latent variable is estimated and repeated until it converges to the maximum likelihood. As a first approximation, we assumed that the matrix R was diagonal. By solving the *AM* model with it, we obtained an estimate of the internal parameters (β and u) of the model; in the next iteration, we found the next approximation of the estimate of the matrix R using the same *AM* model, thereby improving the accuracy of our *AM* model estimate.

Animal genotyping

We genotyped 672 animals. DNA was isolated from blood and skin notches according to the standard QIAamp® DNA Investigator protocol. Samples containing 4 μl of a DNA solution with a concentration of 50 ng/μl were genotyped using a BovineSNP50 v3 DNA Analysis BeadChip microarray (Illumina, USA), according to the manufacturer's instruction. Only genotypes with a call rate > 90% were used to develop a system for genomic evaluation of the breeding value. All SNP markers with a minor allele frequency of less than 5% were excluded from the analysis.

Determination of breed by Principal Component Analysis (PCA)

Using the PCA method, we were able to tentatively identify the breeds of the animals, information on which was not available in our database. In this meth-

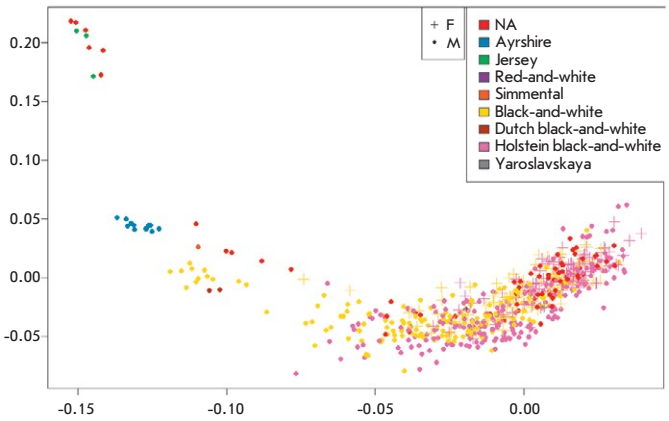

Fig. 1. Principal component analysis PC1 and PC2 (PCA) for the genotyped animals

od, we used the genotypes of 672 animals of various breeds and the plink program.

Thus, *Fig. 1* shows a clear separation of Jersey and Ayrshire animals and a large cluster of animals from the Black-and-White family. The method enabled the identification of 644 animals (427 sires and 217 cows) belonging to the Holstein (392) and Black-and-White (252) breeds, which were subsequently used to assess the breeding value.

Estimation of the breeding value and genetic parameters of the Black-and-White animal population

The breeding value of the animals was assessed using the TD ssGBLUP AM method [23, 24] for milk performance traits and the ssGBLUP AM method [25] for fertility traits. The following fixed models were created:

$$Y = X_1A + X_2HYSc + X_3L + X_4\ TD + Z_1a + Z_2p + e$$
$$AFC = X_1RYSb + X_2H + Z_1a + e$$
$$CI = X_1RYSc + X_2H + X_3LA + Z_1a + Z_2p + e$$
$$OFI = X_1RYSc + X_2H + X_3LA + Z_1a + Z_2p + e$$
$$FLI = X_1RYSi + X_2H + X_3LA + Z_1a + Z_2p + e$$
$$DO = X_1RYSc + X_2H + X_3LA + Z_1a + Z_2p + e$$
$$NS = X_1RYSi + X_2H + LA + Z_1a + Z_2p + e,$$

where Y is a vector of the milk performance traits (milk yield (kg), fat content (%), milk fat yield (kg); protein content (%), and milk protein yield (kg)); AFC is the vector of the age at first calving trait (days); CI is the vector of the calving interval trait (days); CFI is the vector of the calving to first insemination interval trait (days); IFL is the vector of the interval between first and last insemination trait (days); DO is the vector of the days open trait (days); NS is the vector of the number of services trait; A is the fixed effect vector of animal age; HYSc is the fixed effect vector of farm–year–calving season; RYSb is the fixed effect vector of region–year–season of birth; L is the fixed effect vector of lactation number; H is the fixed effect vector of farm; TD is the fixed effect vector of control milk day; RYSc is the fixed effect vector of region–year–calving season; RYSi is the fixed effect vector of region–year–season of insemination; LA is the fixed effect vector of lactation–animal age; a is the vector of animal randomized additive effects; p is the vector of randomized environmental effects; e is the residual effect vector; and X_1, X_2, X_3, Z_1, and Z_2 are unit diagonal matrices relating the vector of observation to the fixed and random effect vectors.

The genetic parameters (heritability and repeatability coefficients) were calculated according to the following formulas [26]:

$$h^2 = \frac{\sigma_a^2}{\sigma_a^2 + \sigma_p^2 + \sigma_e^2}$$

$$R = \frac{\sigma_a^2 + \sigma_p^2}{\sigma_a^2 + \sigma_p^2 + \sigma_e^2},$$

where h^2 is the heritability coefficient; R is the repeatability factor; σ_a^2 is the additive genetic variance; σ_p^2 is the environment variance; and σ_e^2 is the residual effect variance.

The reliability of the estimated breeding value was calculated using the following formula [27]:

$$REL = 1 - \frac{PEV}{(1+F)\sigma_a^2},$$

where REL is the reliability of the estimated breeding value, PEV is the predicted error variance; F is the inbreeding coefficient and σ_a^2 is the additive genetic variance.

RESULTS

Characterization of the database of breeding animals of the Russian Black-and-White cattle population

The developed system was used to form a unique, consolidated database on the pedigree of breeding animals on the paternal and maternal lines, which included information on 69,131 bulls and 251,529 cows of the Black-and-White dairy breed. The developed system enables a combination of heterogeneous information on the pedigree of dairy breeding animals from 523 farms in the Russian Federation. The birth dates of the animals according to lactations included in the database were distributed between 1975 and 2017; the mean number of test days per lactation was

9. The distribution of the animals in the developed database and the distribution of genotyped animals by date of birth are shown in *Figs. 2* and *3*.

After a test of the system for checking phenotypic data and the data on the pedigree of the animals, the final database included information on 1,597,426 cows with 4,771,366 completed lactations. There are data on the daily milk yield, milk fat, and milk protein in 1,047,224, 1,033,839, and 1,046,148 animals, respectively. The number of test day records for the daily milk yield, milk fat, and milk protein content was 29,735,417, 26,393,276, and 26,955,476, respectively. The kinship table for three milk performance traits contained information on 1,983,031 animals, of which 51,810 were sires. The mean performance value of the entire livestock was 20.9 ± 8.433 kg for the daily milk yield, 3.90 ± 0.46% for the milk fat content, and 3.18 ± 0.24% for the milk protein content. The mean age at first calving was 836.06 ± 117.32 days. For other fertility indicators, the mean value was: 401.79 ± 67.098 days for the calving interval, 90.713 ± 53.425 days for the calving–first insemination interval, 41.685 ± 79.243 days for the interval between first–last insemination, 140.18 ± 89.805 days for days open, and 1.80 ± 1.39 for the number of services (*Table 1*).

Evaluation of the genetic parameters of breeding traits in the Holstein and Black-and-White cattle population

To assess the breeding value of animals in a cattle population, it is necessary to determine the parameters of breeding traits in the animals in the population. The following genetic parameters of the Russian Holstein and Black-and-White cattle populations were evaluated: phenotypic variance, genetic variance, en-

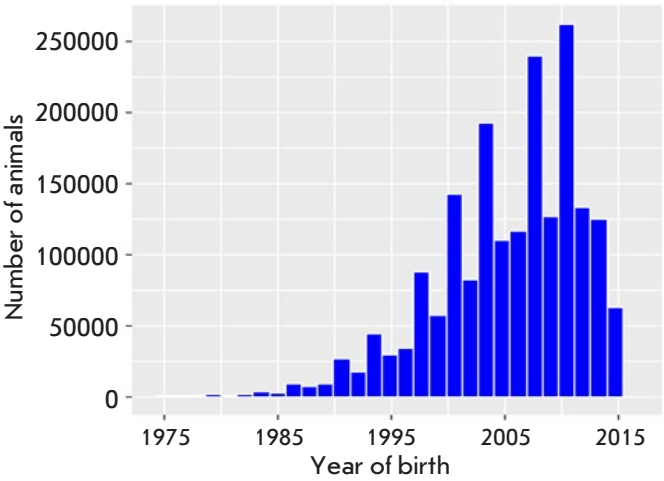

Fig. 2. Distribution of animals in the database by date of birth

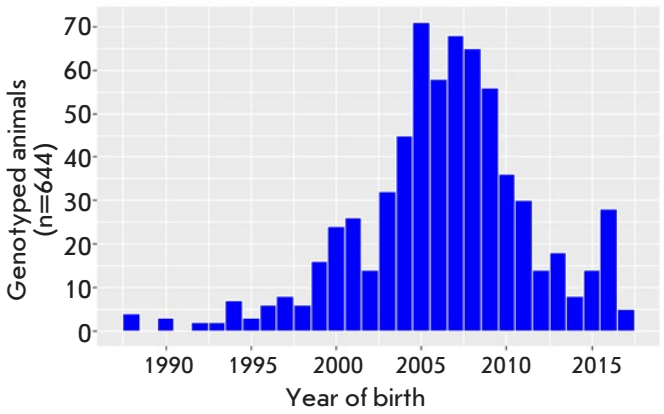

Fig. 3. Distribution of the genotyped animals by date of birth

Table 1. Indicators of breeding animals from the Russian Holstein and Black-and-White cattle populations

Trait	Number of animals	Number of records	Number of animals in kinship table	Number of bulls	Min	Max	Mean	Standard deviation
Daily yield, kg	1,047,224	29,735,417	1,983,031	51,810	0.2	46.211	20.90	8.43
Milk fat, %	1,033,839	26,393,276	1,983,031	51,810	2.38	5.47	3.90	0.46
Milk protein, %	1,046,148	26,955,476	1,983,031	51,810	2.31	4.08	3.18	0.24
AFC, days	937,175	937,175	1,434,321	49,644	540	1230	836.06	117.32
CI, days	763,773	2,026,259	1,247,553	46,371	300	600	401.79	67.1
CFI, days	904,999	2,535,158	1,409,240	49,111	25	360	90.713	53.43
IFL, days	787,536	3,174,412	1,214,206	47,352	0	720	41.685	79.24
DO, days	898,131	2,539,399	1,400,007	48,964	25	500	140.18	89.81
NS	959,501	3,575,124	1,447,815	49,781	1	10	1.80	1.39

Table 2. Calculation of the genetic variance (σ^2_a), environment variance (σ^2_p), residual variance (σ^2_e), repeatability coefficient (R), and heritability coefficient (h^2)

Trait	σ^2_a	σ^2_p	σ^2_e	h^2	R
Daily milk yield, kg	4.644 ± 0.783	5.278 ± 0.545	13.536 ± 0.112	0.20	0.427
Milk fat, %	0.108 ± 0.189	0.109 ± 0.130	0.127 ± 0.610	0.31	0.631
Milk protein, %	0.221 ± 0.431	0.261 ± 0.302	0.364 ± 0.172	0.26	0.569
AFC, days	2,025 ± 24.12	–	7,515 ± 19.09	0.21	–
CI, days	215.98 ± 4.896	334.3 ± 4.762	3,736.6 ± 4.646	0.05	0.13
CFI, days	232.02 ± 3.172	147.42 ± 2.569	2,187.5 ± 2.375	0.09	0.15
IFL, days	296.58 ± 5.141	438.19 ± 4.523	4,861.7 ± 4.462	0.05	0.13
DO, days	505.30 ± 9.534	1,070.8 ± 8.925	6,183.1 ± 6.994	0.07	0.2
NS	0.961± 0.423	0.522 ± 0.341	0.731 ± 0.254	0.11	0.19

Table 3. Evaluation of the breeding value of cows and sires for the main breeding traits of fertility and milk performance in the Holstein and Black-and-White cattle populations

Trait	EBV (cows)				EBV (bulls)			
	Min	Max	Mean	Reliability (mean)	Min	Max	Mean	Reliability (mean)
Daily milk yield, kg	−11.23	13.98	0.88	0.38	−12.05	15.07	1.03	0.33
Milk fat, %	−0.55	0.69	-0.002	0.39	−0.97	0.73	−0.002	0.34
Milk protein, %	−0.22	0.31	−0.003	0.37	−0.18	0.30	0.001	0.32
AFC, days	−142.66	170.45	−11.35	0.35	−199.83	198.35	−10.67	0.32
CI, days	−34.37	49.54	2.76	0.28	−36.68	49.88	3.07	0.26
CFI, days	−51.45	56.24	−2.02	0.33	−66.5	73.9	−0.73	0.30
IFL, days	−40.38	82.07	5.93	0.30	−48.52	94.69	5.85	0.27
DO, days	−53.94	72.18	3.25	0.29	−68.83	106.07	4.14	0.27
NS	−1.03	2.18	0.14	0.23	−1.08	1.66	0.05	0.21

vironment variance, residual variance, repeatability coefficient, and heritability coefficient. To calculate the dispersion components, the AIREMLF90 module was used, which, in turn, is based on the AI-REML (Average Information-Residual Maximal Likelihood) algorithm. The calculated genetic parameters are presented in *Table 2*.

The calculation of variance components shows that the variability of the fertility and milk performance traits in the Holstein and Black-and-White cattle populations in Russia is quite high, which makes targeted breeding for these traits quite effective. The heritability coefficient was 0.20 for the daily milk yield, 0.31 for the milk fat content, and 0.26 for the milk protein content. For all fertility traits, except for AFC, the heritability coefficient was low; < 0.11. This indicates a low genotypic diversity of the animal population and a high impact of environmental conditions on the variability of these traits.

Evaluation of the breeding value of cows and sires of Holstein and Black-and-White breeds

We calculated the genomic breeding value of all the animals born between 1975 and 2017 and represented in the developed database. The estimated breeding value (EBV) was calculated using the ssGBLUP-AM method. This method enables the inclusion of information about the phenotype and genotype of the animals and the pedigree of the animals into a single model. The BLUPF90 software [27] was used at all steps of breeding value assessment. The result of the breeding value evaluation is provided in *Table 3*.

The mean genetic potential was 0.88 kg in cows and 1.03 kg in bulls for the daily milk yield, –0.002% for the milk fat content, and –0.003 and 0.001% for the milk protein content in cows and the progeny of bulls, respectively. It should be noted that the mean assessment values for each trait are close to zero, and that the distribution of the animals relative to

Table 4. Calculation of the reliability of the genomic-estimated breeding value for the main breeding traits of fertility and milk performance in the Black-and-White cattle population

Trait	Genotyped cows (n = 217)			Genotyped bulls (n = 427)		
	Number of offspring (mean)	Reliability of EBV	Reliability of GEBV*	Number of offspring (mean)	Reliability of EBV	Reliability of GEBV*
Daily milk yield, kg	1.02	0.59	0.98	583.2	0.93	0.65
Milk fat, %	1.02	0.59	0.97	583.2	0.92	0.54
Milk protein, %	1.02	0.57	0.97	583.2	0.89	0.54
AFC, days	0.08	0.21	0.82	358.2	0.89	0.24
CI, days	0.05	0.15	0.87	285.1	0.87	0.60
CFI, days	0.08	0.21	0.93	347.1	0.87	0.45
IFL, days	0.08	0.20	0.54	219.4	0.86	0.26
DO, days	0.08	0.20	0.93	345.5	0.90	0.56
NS	0.09	0.18	0.51	359.1	0.85	0.23

*Reliability of the estimate compared to the estimate for offspring (square of the rank correlation coefficient).

this value is almost symmetrical (1 : 1): i.e., 50% of the animals have positive values and the other 50% have negative values. The genetic trend for the main breeding traits of fertility and milk performance in the Black-and-White breed population is built using the mean calculated breeding value of the animals by year of birth and is shown in *Fig. 1* (Appendix).

A significant increase in the milk yield (4.4 kg/day) was observed between 1975 and 2017, while a decrease in the milk protein content was noted between 1975 and 2002. Then, between 2002 and 2017, the mean breeding value of the animals increased from –0.006 to 0.002%. After 2010, the genetic trend in the fat content shows a significant drop from –0.005 to –0.03%. A decrease in all fertility indicators, except for the age at first calving, occurred between 1975 and 2017.

One of the factors affecting the accuracy of the breeding value estimate is the level of trait heritability. The higher the heritability, the higher the estimate accuracy. In our study, the EBV accuracy for three milk performance traits and the AFC fertility trait is higher than the EBV accuracy for other fertility traits (CI, CFI, IFL, DO, and NS). However, the heritability coefficient varied from 0.20 to 0.31 for the AFC and milk traits and from 0.05 to 0.11 for other fertility traits.

Assessment of the effectiveness of the system for genomic evaluation of dairy cattle

The reliability of the genomic estimated breeding value was evaluated using cross-validation. Genotyped animals were randomly divided into 11 equal groups. Ten groups were used in turn to calculate the model. The remaining 11th group was a test group: data on the descendants of the animals in this group were deleted, and the breeding value was calculated only based on the genome. Then, the breeding value of the animals was compared to their breeding value using phenotypic data. The degree of correlation between the breeding value of the genotyped animals, which was calculated by offspring (EBV), and their breeding value calculated by genotype (GEBV) served as a criterion for the reliability of the genomic estimated breeding value. The result of our assessment of the reliability of the genomic prediction is presented in *Table 4*.

The accuracy in the assessment of the breeding value by offspring (EBV) was calculated based on the variational components and genetic variability of the traits using the REML method, and the accuracy of GEBV was calculated as the square of the rank correlation coefficient between the EBV and GEBV values. It is worth noting that bulls have significantly more offspring than cows. In this study, the mean number of offspring in the genotyped bulls ranged from 219.4 for IFL to 583.2 for milk performance traits. In the genotyped cows, the mean number of offspring did not exceed 1.02 for all the studied traits, while the reliability of EBV mainly depended on the number of offspring. As shown in *Table 4*, the reliability of EBV in the genotyped cows is less than that in the bulls. In the genotyped bulls, a high accuracy of EBV (> 85%) is observed for all fertility and milk performance traits; in the genotyped cows, the reliability

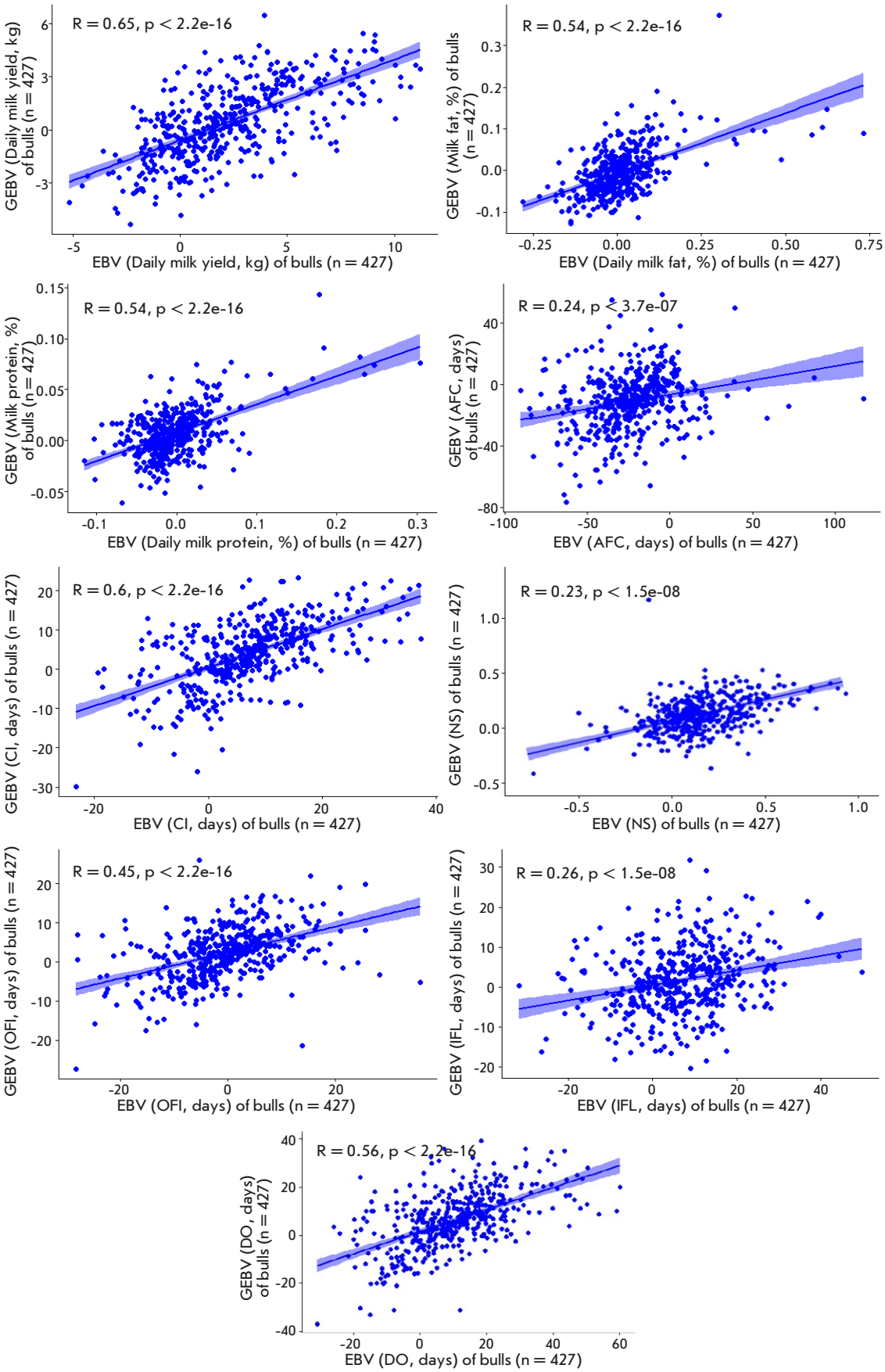

Fig. 4. Correlation between the estimated breeding values (EBV) of bulls and their genomic estimated breeding values (GEBV) for the fertility and milk performance traits

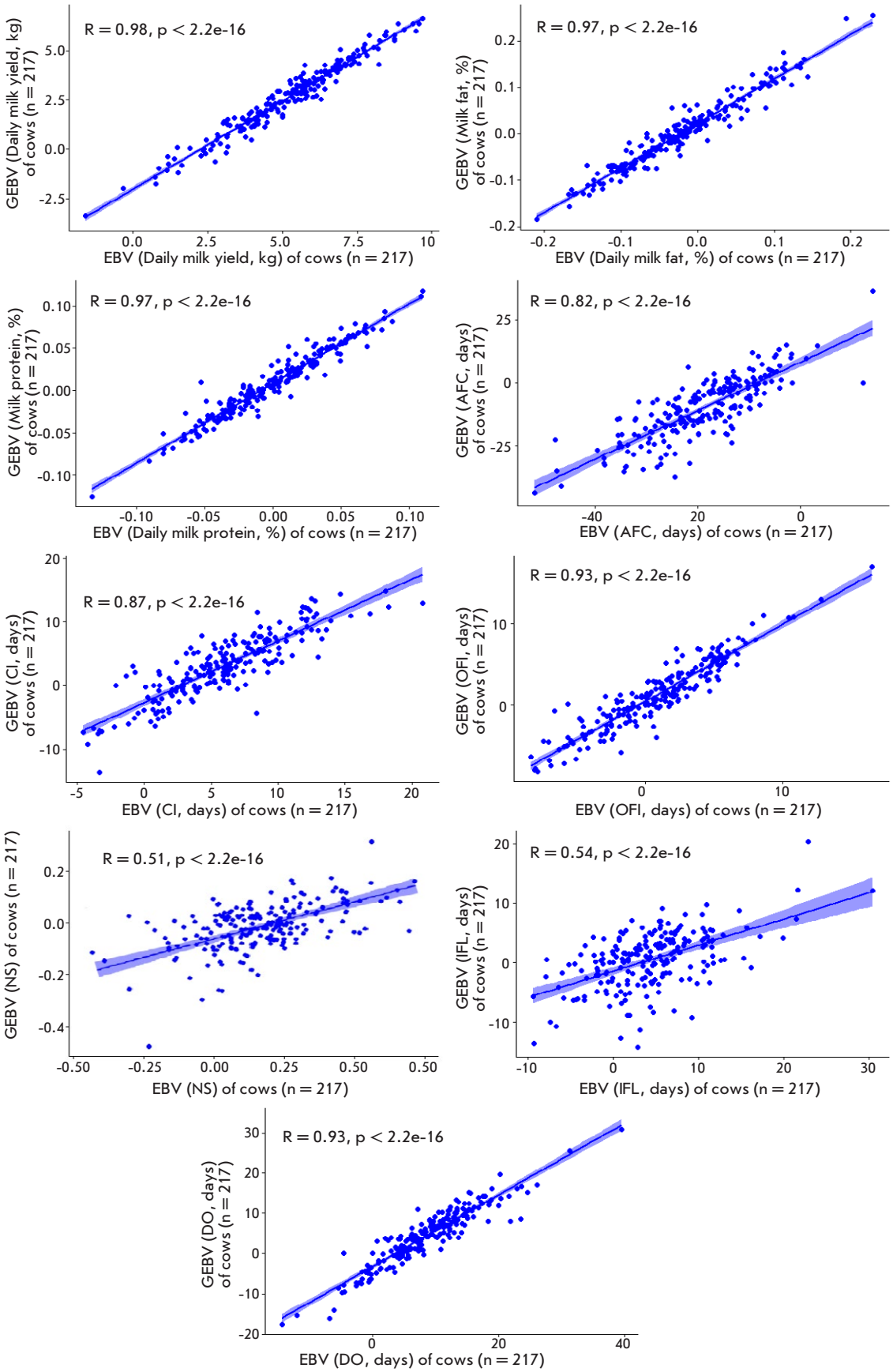

Fig. 5. Correlation between the estimated breeding values of the genotyped cows (EBV) and their genomic-estimated breeding values (GEBV) for the fertility and milk performance traits

Table 5. Comparison of the Black-and-White breed with various cattle breeds in the world

Breed	Number of cows		
	Milk yield, kg	Milk fat	Milk protein
Black-and-white	1,047,224	1,033,839	1,046,148
Nordic RDC	3,538,966	3,538,966	3,538,966
Holstein (Canada)	5,976,711	5,976,711	5,976,711
Ayrshire (Canada)	221,533	221,533	221,533
Jersey (Canada)	185,737	185,737	185,737
Portuguese Holstein	578,552	–	–
German Holstein	48,977	–	–
	Number of test days, million		
	Milk yield, kg	Milk fat	Milk protein
Black-and-white	29.7	26.4	27
Nordic RDC	95.6	95.6	95.6
Holstein (Canada)	72.4	72.4	72.4
Ayrshire (Canada)	2.4	2.4	2.4
Jersey (Canada)	1.7	1.7	1.7
Portuguese Holstein	11.4	–	–
German Holstein	0.106		
	Reliability of GEBV, %		
	Milk yield, kg	Milk fat	Milk protein
Black-and-white	65	54	54
Nordic RDC	40	50	40
Holstein (Canada)	65	58	67
Ayrshire (Canada)	39	43	54
Jersey (Canada)	58	62	68
Portuguese Holstein	52–72	–	–
German Holstein	81–88	–	–

of EBV ranges from 0.18 for NS to 0.59 for the milk yield and milk fat content.

The correlation of EBV and GEBV (reliability of GEBV) exceeded 80% in the genotyped cows for most of the studied traits and reached 98% for the daily milk yield.

When calculating GEBV, offspring data of genotyped animals were removed and the breeding value was assessed only by genotype. Genotyped cows have few offspring, so removal of offspring from the ssGBLUP model does not significantly affect the EBV values of the animals and, thus, there is a high correlation between the EBV and GEBV values. Therefore, unlike sires, the reliability of GEBV in genotyped cows may not reflect the effectiveness of the genomic scoring system.

In genotyped bulls, mean values of GEBV reliability were found for three milk performance traits. This result indicates the possibility of assessing the breeding value of the Black-and-White cattle population by genotype with a reliability of up to 65% for the daily milk yield and up to 54% for the milk fat and protein content. A rather high accuracy of GEBV was found for the CI, DO, and CFI traits: 60, 54, and 45%, respectively. The minimum GEBV accuracy was obtained for AFC (24%), IFL (26%), and NS (23%) traits.

The advent of genomic selection has reduced the requirements on traditional approaches to choosing

candidates for selection when many phenotypic traits of all close relatives of candidates should be determined. Genomic selection opens up the opportunity for selecting traits that are difficult or expensive to measure, such as fertility. This approach will be developed through new genomic studies (based on genomics, transcriptomics, and proteomics) aimed at identifying the genes and pathways that control fertility in cattle and will improve phenotyping for reproductive function.

The result of an evaluation of the reliability of the genomic prediction in genotyped bulls and cows is also shown in *Figs. 4* and *5*.

DISCUSSION

The breeding results confirmed that prediction of the cattle breeding value using genomic information is more accurate than kinship, alone [28–30]. In this study, the genomic estimated breeding value in the Russian Holstein and Black-and-White cattle populations was determined for the first time in Russia based on fertility traits. The reliability of the genomic estimated breeding value was 65% for the daily milk yield and 54% for the milk fat and protein content. The reliability of GEBV for fertility traits amounted to 60% (CI), 54% (DO), 45% (CFI), 24% (AFC), 26% (IFL), and 23% (NS). These values are slightly higher than those in Nordic Red dairy cattle (from 0.22 to 0.31%) for three fertility traits [31]. A similar result (28.9% reliability) was obtained by Su et al., who assessed the breeding value in Danish Jersey using a small reference population (1,250 Danish bulls) [32].

In addition, we used the TD ssGBLUP-AM test day model to assess the breeding value of cattle for milk traits. Currently, this model is used to officially assess the cattle breeding value in many countries: e.g., Nordic Red dairy cattle (RDC) [33]. The official RDC assessment data for March 2012 were obtained from a genetic assessment of Nordic cattle (NAV). To assess the breeding value of RDC, 3,538,966 cows were selected from 95.6 million records of test days and the total number of animals in the RDC pedigree was 477,468 (*Table 5*). Comparison of the results of our earlier study of the Holstein Dairy breed shows that despite a 2.5-fold difference in the size of the statistical sample, assessment of the breeding value of the Holstein and Black-and-White breeds by the TD ssGBLUP-AM method has a rather high prediction reliability (about 65%).

The calculated genomic prediction reliability of the breeding value is comparable with the estimated breeding value of Portuguese Holstein cows [34]. The mean reliability of the genomic-estimated breeding value of Portuguese Holstein bulls was 52% in young bulls and 72% in bulls with data on the performance of their daughters.

The test day model is likewise used for a genomic estimate of the breeding value in three dairy cattle populations in Canada (Holstein, Ayrshire, and Jersey). The prediction reliability of the breeding value for the milk yield is 65, 39, and 58% for Holstein, Ayrshire, and Jersey breeds, respectively [35]. In a study by Bohlouli *et al.*, 11.4 million test day records were used to estimate the breeding value of 48,977 Holstein cows in Germany. The reliability of the evaluation reached 88% [36].

CONCLUSION

In this study, despite a small number of genotyped sires in the reference population, an acceptable level of reliability in the genomic assessment of the cattle breeding value was achieved. Reliability may be improved by increasing the number of genotyped animals in the reference population. We have shown that there is a possibility to use the genomic-estimated breeding value in the domestic population of Holstein and Black-and-White cattle according to various fertility and milk performance traits. This system will take domestic breeding to a modern, competitive level and help evaluate the cattle breeding value at birth based on information about the animal's genome. ●

This study of FSh and EP was partly supported by the Russian Foundation for Basic Research (grant No. 17-29-08033) and state task of the Federal Research Center of Biotechnology RAS. The study of AKh was partially supported by the Russian Ministry of Education and Science under Agreement No. 14.579.21.0147 on the provision of a subsidy (unique identifier of works (project) RFMEFI57917X0147) and the Russian Foundation for Basic Research (grant No. 17-29-08033).

REFERENCES

1. Lukyanov K., Soloshenko V.A., Klimenok I.I., Yudin N.S. // Genetics and animal breeding. 2015. №. 3. P. 63–69.
2. Tanana L.A., Minina N.G., Klimov N.N., Korshun S.I., Peshko V.V. Fundamentals of farm animal breeding. GGAU, Grodno, 2011. 116 p.
3. Hayes B.J., Bowman P.J., Chamberlain A.J., Goddard M.E. // J. Dairy Sci. 2009. V. 92. № 2. P. 433–443.
4. Kuznetsov V.M. // Problems of biology of productive animals. 2012. №. 4. P. 18–57.
5. Pribyl J., Rehout V., Citek J., Pribylova J. // J. Sci. Food Agric. 2010. V. 90. № 11. P. 1765–1773.
6. Robinson G.K. // Statistical Sci. 1991. P. 15–32.
7. Ma L., Cole J., Da Y., VanRaden P. // J. Dairy Sci. 2019.

V. 102. № 4. P. 3735–3743.
8. Pryce J., Daetwyler H. // Animal Production Sci. 2011. V. 52. № 3. P. 107–114.
9. Schaeffer L., Jamrozik J., Kistemaker G., van Doormaal J. // J. Dairy Sci. 2000. V. 83. № 5. P. 1135–1144.
10. Jamrozik J., Schaeffer L., Dekkers J. // J. Dairy Sci. 1997. V. 80. № 6. P. 1217–1226.
11. Wiggans G., Goddard M. // J. Dairy Sci. 1997. V. 80. № 8. P. 1795–1800.
12. Meseret S., Tamir B., Gebreyohannes G., Lidauer M., Negussie E. // Asian-Australasian J. Animal Sci. 2015. V. 28. № 9. P. 1226.
13. Van Tassell C.P., Quaas R.L., Everett R.W. // Dairy Sci. 1992. Suppl 1. P. 251.
14. Ptak E., Schaeffer L. // Livestock Production Sci. 1993. V. 34. P. 23–34.
15. Swalve H. // Archiv für Tierzucht. 1995.
16. Nardin D.S., Malinina A.I. // Electronic scientific and methodological journal of Omsk State Agrarian University. 2015. №. 3.
17. Ivchenko G.I., Medvedev Yu.I. Introduction to mathematical statistics. M.: LKI, 2010. 600 p.
18. Arturovich L. // Department of animal husbandry and breeding of the Ministry of Agriculture of the Russian Federation. 1997 P. 23–97.
19. Wood P. // Nature. 1967. V. 216. № 5111. P. 164–165.
20. Wilmink J. // Livestock Production Sci. 1987. V. 16. № 4. P. 335–348.
21. https://queries.uscdcb.com/eval/summary/inbrd.cfm?R_Menu=HO#StartBody
22. Hastie T., Tibshirani R., Friedman J. // Springer. 2001. P. 236–243.
23. Koivula M., Strandén I., Pösö J., Aamand G., Mäntysaari E. // J. Dairy Sci. 2015. V. 98. № 4. P. 2775–2784.
24. Oliveira H., Lourenco D., Masuda Y., Misztal I., Tsuruta S., Jamrozik J., Brito L., Silva F., Schenkel F. // J. Dairy Sci. 2019. V. 102. № 3. P. 2365–2377.
25. Kuznetsov V.M. // Actual problems of pork production in the Russian Federation. BLUP animal model for breeding assessment of pigs: a basic model. 2010. P. 50–57.
26. Ayalew W., Aliy M., Negussie E. // Asian-Australasian J. Animal Sci. 2017. V. 30. № 11. P. 1550.
27. Misztal I., Tsuruta S., Strabel T., Auvray B., Druet T., Lee D. // Proc. 7th world congress on genetics applied to livestock production. 2002. V. 28. № 7.
28. Patry C., Ducrocq V. // Genet. Sel. Evol. 2011. V. 43. № 1. P. 1–9.
29. Lourenco D., Misztal I., Wang H., Aguilar I., Tsuruta S., Bertrand J. // J. Anim. Sci. 2013. V. 91. № 9. P. 4090–4098.
30. Naserkheil M., Lee D.H., Mehrban H. // BMC Genet. 2020. V. 21. № 1. P. 1–9.
31. Matilainen K., Strandén I., Aamand G.P., Mäntysaari E.A. // J. Anim. Breed. Genet. 2018. V. 135. № 5. P. 337–348.
32. Su G., Ma P., Nielsen U., Aamand G., Wiggans G., Guldbrandtsen B., Lund M. // Animal. 2016. V. 10. № 6. P. 1067–1075.
33. Koivula M., Strandén I., Pösö J., Aamand G.P., Mäntysaari E.A. // Interbull Bulletin. 2012. № 46. P. 115–120.
34. Silva A., Silva D., Silva F., Costa C., Lopes P., Caetano A., Thompson G., Carvalheira J. // J. Dairy Sci. 2019. V. 102. № 7. P. 6330–6339.
35. Oliveira H., Lourenco D., Masuda Y., Misztal I., Tsuruta S., Jamrozik J., Brito L., Silva F., Schenkel F. // J. Dairy Sci. 2019. V. 102. № 3. P. 2365–2377.
36. Bohlouli M., Alijani S., Naderi S., Yin T., König S. // J. Dairy Sci. 2019. V. 102. № 1. P. 488–502.

APPENDIX

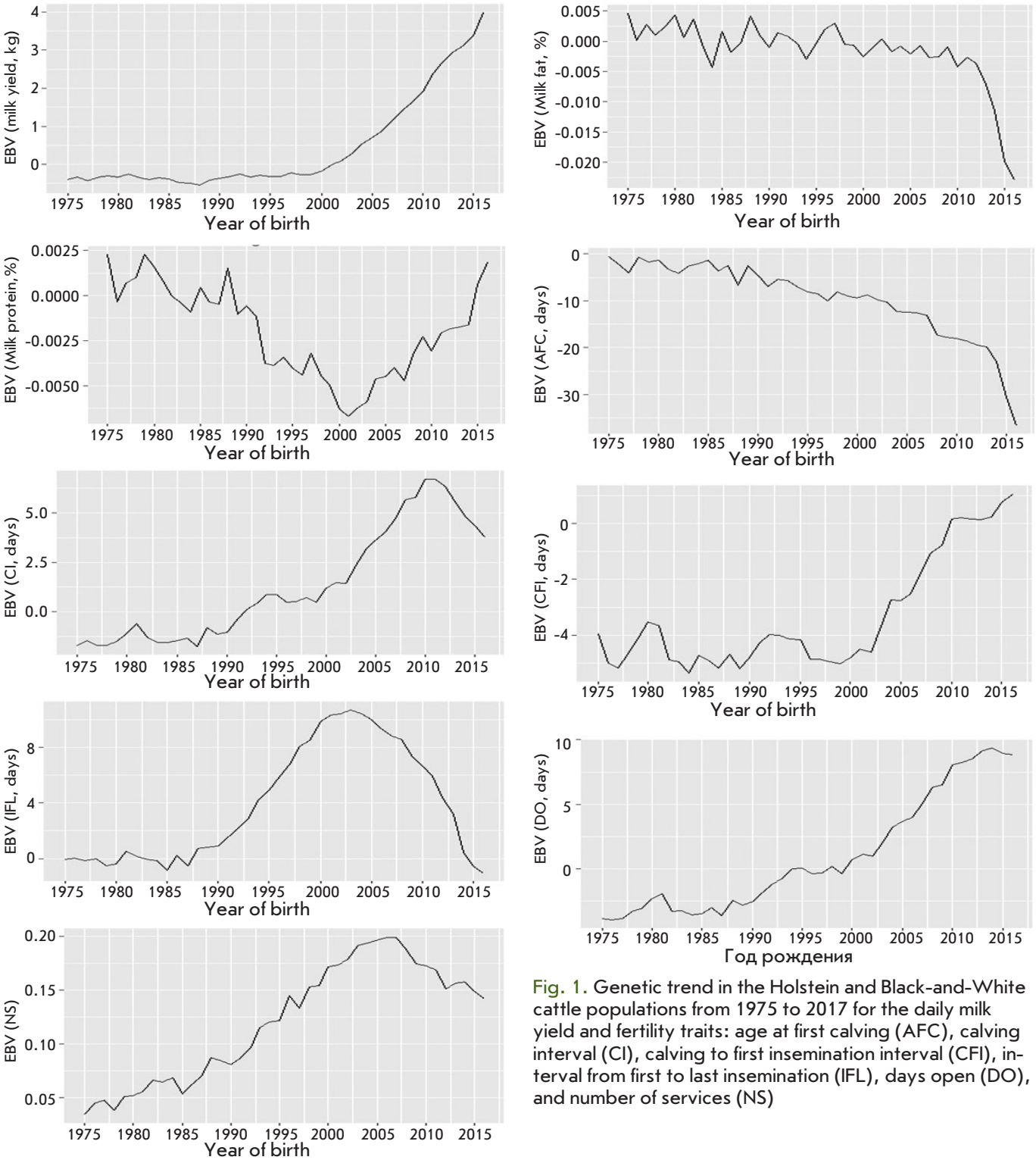

Fig. 1. Genetic trend in the Holstein and Black-and-White cattle populations from 1975 to 2017 for the daily milk yield and fertility traits: age at first calving (AFC), calving interval (CI), calving to first insemination interval (CFI), interval from first to last insemination (IFL), days open (DO), and number of services (NS)

GENERAL RULES

Acta Naturae publishes experimental articles and reviews, as well as articles on topical issues, short reviews, and reports on the subjects of basic and applied life sciences and biotechnology.

The journal *Acta Naturae* is on the list of the leading periodicals of the Higher Attestation Commission of the Russian Ministry of Education and Science. The journal Acta Naturae is indexed in PubMed, Web of Science, Scopus and RCSI databases.

The editors of *Acta Naturae* ask of the authors that they follow certain guidelines listed below. Articles which fail to conform to these guidelines will be rejected without review. The editors will not consider articles whose results have already been published or are being considered by other publications.

The maximum length of a review, together with tables and references, cannot exceed 50,000 characters with spaces (approximately 30 pages, A4 format, 1.5 spacing, Times New Roman font, size 12) and cannot contain more than 16 figures.

Experimental articles should not exceed 30,000 symbols (approximately 15 pages in A4 format, including tables and references). They should contain no more than ten figures.

A short report must include the study's rationale, experimental material, and conclusions. A short report should not exceed 12,000 symbols (5–6 pages in A4 format including no more than 12 references). It should contain no more than three figures.

The manuscript and all necessary files should be uploaded to www.actanaturae.ru:

1) text in Word 2003 for Windows format;
2) the figures in TIFF format;
3) the text of the article and figures in one pdf file;
4) the article's title, the names and initials of the authors, the full name of the organizations, the abstract, keywords, abbreviations, figure captions, and Russian references should be translated to English;
5) the cover letter stating that the submitted manuscript has not been published elsewhere and is not under consideration for publication;
6) the license agreement (the agreement form can be downloaded from the website www.actanaturae.ru).

MANUSCRIPT FORMATTING

The manuscript should be formatted in the following manner:

- Article title. Bold font. The title should not be too long or too short and must be informative. The title should not exceed 100 characters. It should reflect the major result, the essence, and uniqueness of the work, names and initials of the authors.
- The corresponding author, who will also be working with the proofs, should be marked with a footnote *.
- Full name of the scientific organization and its departmental affiliation. If there are two or more scientific organizations involved, they should be linked by digital superscripts with the authors' names. Abstract. The structure of the abstract should be very clear and must reflect the following: it should introduce the reader to the main issue and describe the experimental approach, the possibility of practical use, and the possibility of further research in the field. The average length of an abstract is 20 lines (1,500 characters).
- Keywords (3 – 6). These should include the field of research, methods, experimental subject, and the specifics of the work. List of abbreviations.
- INTRODUCTION
- EXPERIMENTAL PROCEDURES
- RESULTS AND DISCUSSION
- CONCLUSION

  The organizations that funded the work should be listed at the end of this section with grant numbers in parenthesis.
- REFERENCES

  The in-text references should be in brackets, such as [1].

RECOMMENDATIONS ON THE TYPING AND FORMATTING OF THE TEXT

- We recommend the use of Microsoft Word 2003 for Windows text editing software.
- The Times New Roman font should be used. Standard font size is 12.
- The space between the lines is 1.5.
- Using more than one whole space between words is not recommended.
- We do not accept articles with automatic referencing; automatic word hyphenation; or automatic prohibition of hyphenation, listing, automatic indentation, etc.
- We recommend that tables be created using Word software options (Table → Insert Table) or MS Excel. Tables that were created manually (using lots of spaces without boxes) cannot be accepted.
- Initials and last names should always be separated by a whole space; for example, A. A. Ivanov.
- Throughout the text, all dates should appear in the "day.month.year" format, for example 02.05.1991, 26.12.1874, etc.
- There should be no periods after the title of the article, the authors' names, headings and subheadings, figure captions, units (s – second, g – gram, min – minute, h – hour, d – day, deg – degree).
- Periods should be used after footnotes (including those in tables), table comments, abstracts, and abbreviations (mon. – months, y. – years, m. temp. – melting temperature); however, they should not be used in subscripted indexes (T_m – melting temperature; $T_{p.t}$ – temperature of phase transition). One exception is mln – million, which should be used without a period.
- Decimal numbers should always contain a period and not a comma (0.25 and not 0,25).
- The hyphen ("-") is surrounded by two whole spaces, while the "minus," "interval," or "chemical bond" symbols do not require a space.
- The only symbol used for multiplication is "×"; the "×" symbol can only be used if it has a number to its

right. The "·" symbol is used for denoting complex compounds in chemical formulas and also noncovalent complexes (such as DNA·RNA, etc.).
- Formulas must use the letter of the Latin and Greek alphabets.
- Latin genera and species' names should be in italics, while the taxa of higher orders should be in regular font.
- Gene names (except for yeast genes) should be italicized, while names of proteins should be in regular font.
- Names of nucleotides (A, T, G, C, U), amino acids (Arg, Ile, Val, etc.), and phosphonucleotides (ATP, AMP, etc.) should be written with Latin letters in regular font.
- Numeration of bases in nucleic acids and amino acid residues should not be hyphenated (T34, Ala89).
- When choosing units of measurement, SI units are to be used.
- Molecular mass should be in Daltons (Da, KDa, MDa).
- The number of nucleotide pairs should be abbreviated (bp, kbp).
- The number of amino acids should be abbreviated to aa.
- Biochemical terms, such as the names of enzymes, should conform to IUPAC standards.
- The number of term and name abbreviations in the text should be kept to a minimum.
- Repeating the same data in the text, tables, and graphs is not allowed.

GUIDENESS FOR ILLUSTRATIONS

- Figures should be supplied in separate files. Only TIFF is accepted.
- Figures should have a resolution of no less than 300 dpi for color and half-tone images and no less than 600 dpi.
- Files should not have any additional layers.

REVIEW AND PREPARATION OF THE MANUSCRIPT FOR PRINT AND PUBLICATION

Articles are published on a first-come, first-served basis. The members of the editorial board have the right to recommend the expedited publishing of articles which are deemed to be a priority and have received good reviews.

Articles which have been received by the editorial board are assessed by the board members and then sent for external review, if needed. The choice of reviewers is up to the editorial board. The manuscript is sent on to reviewers who are experts in this field of research, and the editorial board makes its decisions based on the reviews of these experts. The article may be accepted as is, sent back for improvements, or rejected.

The editorial board can decide to reject an article if it does not conform to the guidelines set above.

The return of an article to the authors for improvement does not mean that the article has been accepted for publication. After the revised text has been received, a decision is made by the editorial board. The author must return the improved text, together with the responses to all comments. The date of acceptance is the day on which the final version of the article was received by the publisher.

A revised manuscript must be sent back to the publisher a week after the authors have received the comments; if not, the article is considered a resubmission.

E-mail is used at all the stages of communication between the author, editors, publishers, and reviewers, so it is of vital importance that the authors monitor the address that they list in the article and inform the publisher of any changes in due time.

After the layout for the relevant issue of the journal is ready, the publisher sends out PDF files to the authors for a final review.

Changes other than simple corrections in the text, figures, or tables are not allowed at the final review stage. If this is necessary, the issue is resolved by the editorial board.

FORMAT OF REFERENCES

The journal uses a numeric reference system, which means that references are denoted as numbers in the text (in brackets) which refer to the number in the reference list.

For books: the last name and initials of the author, full title of the book, location of publisher, publisher, year in which the work was published, and the volume or issue and the number of pages in the book.

For periodicals: the last name and initials of the author, title of the journal, year in which the work was published, volume, issue, first and last page of the article. Must specify the name of the first 10 authors. Ross M.T., Grafham D.V., Coffey A.J., Scherer S., McLay K., Muzny D., Platzer M., Howell G.R., Burrows C., Bird C.P., et al. // Nature. 2005. V. 434. № 7031. P. 325–337.

References to books which have Russian translations should be accompanied with references to the original material listing the required data.

References to doctoral thesis abstracts must include the last name and initials of the author, the title of the thesis, the location in which the work was performed, and the year of completion.

References to patents must include the last names and initials of the authors, the type of the patent document (the author's rights or patent), the patent number, the name of the country that issued the document, the international invention classification index, and the year of patent issue.

The list of references should be on a separate page. The tables should be on a separate page, and figure captions should also be on a separate page.

The following e-mail addresses can be used to contact the editorial staff: actanaturae@gmail.com, tel.: (495) 727-38-60.

ActaNaturae

Fluorescence of cells after staining with various proteins. The mean values for the three experiments ± mean error are given

Sample	Fluorescence intensity measured in the FL1 channel	
	SK-BR-3 cells	CHO cells
Unstained cells	3700 ± 400	3700 ± 900
+ β-LG-FITC	5700 ± 600	3300 ± 400
+ 4D5scFv-FITC	$2.7\times10^4 \pm 7\times10^3$	3200 ± 500
+ 4D5scFv-miniSOG	$2.3\times10^4 \pm 3\times10^3$	4600 ± 400
+ DARPin-miniSOG	$1.71\times10^4 \pm 1.6\times10^3$	3000 ± 400

Hence, it has been demonstrated that the targeted recombinant proteins 4D5scFv-miniSOG and DARPin-miniSOG are capable of highly specific binding to the HER2/neu receptor on the surface of human breast adenocarcinoma SK-BR-3 cells.

It was revealed that receptor-mediated internalization of proteins did not take place after the DARPin-miniSOG and 4D5scFv-miniSOG proteins were bound to the receptor on the surface of SK-BR-3 cells at +4°C. However, the receptor–protein complex undergoes internalization at +37°C, as evidenced by the reduction in the fluorescence intensity ΔMFI (the difference between the average fluorescence intensities of stained and unstained cells) (*Fig. 1*). The DARPin-miniSOG recombinant protein as part of its complex with the receptor is internalized faster than 4D5scFv-miniSOG, since ΔMFI for DARPin-miniSOG decreases twofold as compared to its baseline during the first 10 min, while ΔMFI for 4D5scFv-miniSOG is 40 min. These findings are consistent with the published data: 4D5scFv-miniSOG has a higher cytotoxicity than DARPin-miniSOG [5, 6], because 4D5scFv-miniSOG resides on the membrane for a longer time. Since necrosis is the predominant death mechanism of cells irradiated in the presence of these phototoxins, membrane damage makes a crucial contribution to the toxicity of targeted proteins. However, the decline in the fluorescence intensity of miniSOG can be indicative of reactions involving chromophore, which is also expected to affect its efficiency as a phototoxin.

In order to elucidate the reasons for the decline in the fluorescence intensity and toxicity of miniSOG-based proteins observed during their internalization, we evaluated the effect of various factors on the fluorescent properties of miniSOG. A hypothesis has been put forward that quenching of DARPin-miniSOG

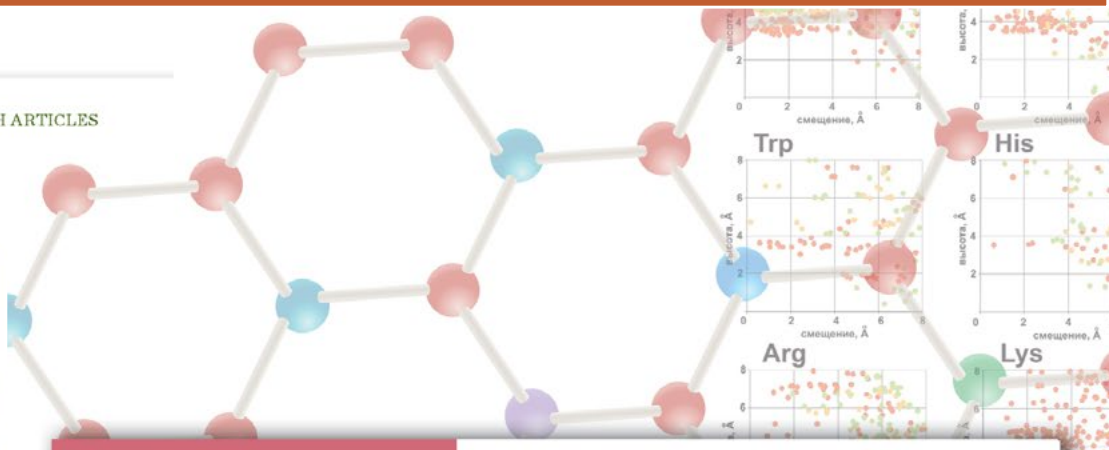

OCTOBER-DECEMBER 2018 VOL. 10 № 4 (39)
ISSN 2075-8251
ActaNaturae

The EIMB Hydrogel Microarray Technology: Thirty Years Later

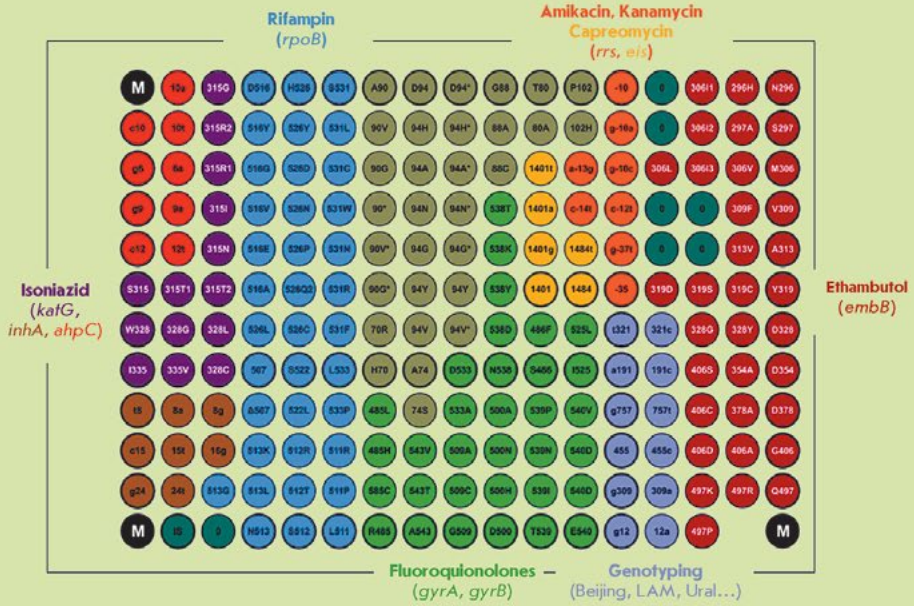

ActaNaturae

Acta Naturae journal places a special focus on interdisciplinary research lying at the interface of various biological disciplines: molecular biology, biochemistry, molecular genetics, and biomedicine.

Acta Naturae is published in Russian and English languages. It has been included in the List of the leading peer-reviewed journals of the Higher Attestation Commission of the Ministry of Science and Education of the Russian Federation and is indexed in the RSCI, PubMed, Web of Science, and Scopus databases.

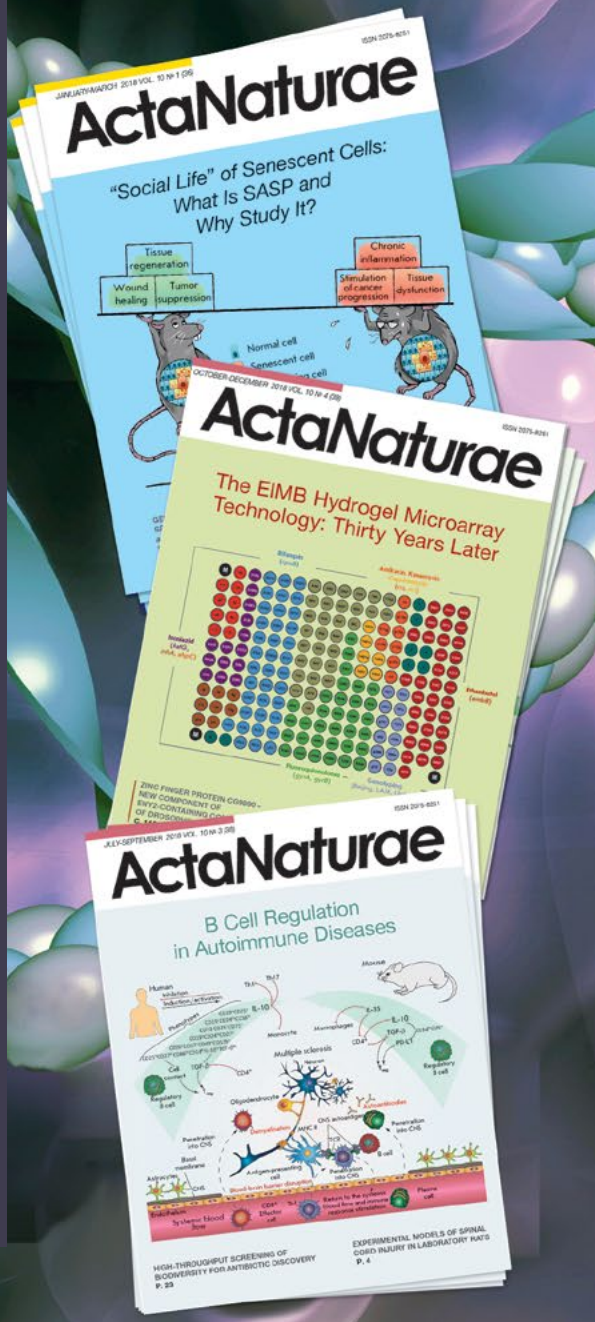

INFORMATION FOR AUTHORS

You can contact the Editorial Board via e-mail actanaturae@gmail.com and telephone +7 (495) 727-38-60.

The manuscript and supplementary files can be uploaded on the website www.actanaturae.ru.